La chasse aux modes-B du fond diffus cosmologique dans la jungle des contaminations systématiques

Josquin Errard

Laboratoire Astroparticule & Cosmologie
Université Paris VII - Denis Diderot
Ecole Doctorale 517 — Particules, Noyaux et Cosmos

A hunt for Cosmic Microwave Background B-modes in the systematic contaminants jungle

Josquin ERRARD

PhD advisor: Dr Radek STOMPOR

Une thèse présentée pour obtenir le titre de
Docteur de l'Université Paris VII - Denis Diderot
—
spécialité physique

18^{th} of September, 2012

Dr. Anthony J. Banday (examiner)

Prof. Pierre Binétruy (head of the committee)

Dr. Julian Borrill (examiner)

Prof. Andrew H. Jaffe (reviewer)

Dr. Juan Francisco Macías-Pérez (reviewer)

Dr. Radek Stompor (PhD advisor)

Prof. Benjamin Wandelt (examiner)

Day of the defense: Eighteenth of September, 2012.

Signature from head of PhD committee:

Abstract

This thesis presents a study of selected instrumental and astrophysical systematics, which may affect the performance of new generation of future observations of the Cosmic Microwave Background (CMB) polarization. It elaborates on their impact on the science goals of those observations and discusses techniques and approaches for their removal. Its focus is on general issues typical of entire classes of experiments, but also on specific problems as encountered in the context of a CMB B-mode experiment, POLARBEAR.

The main target of the CMB polarization effort undergoing currently in the field is a detection of the primordial B-modes anisotropies — a so far undetected signature of the inflationary theories. This would have far-reaching impact on our understanding of the universe but also fundamental laws of physics. Understanding, modelling, and ultimately removal of the systematics are essential steps in any modern CMB analysis pipeline and their successful accomplishment, together with a high instrumental sensitivity, will decide of a final success of the entire effort.

In this thesis I first describe optics of typical CMB experiments and introduce a parametrization of instrumental and cross-polarization effects particularly convenient for the analysis of their impact. Second, I present a model describing the atmospheric contamination and use it to provide some insights about the atmosphere's role and its impact on performance of ground-based experiments. I also outline how it could be used further to improve control of atmospheric effects in the CMB data analysis. Then, I discuss another source of sky systematics — the polarized astrophysical foregrounds. In this context I present on the one hand a new approach to forecasting performance of the future experiments, which accounts for the presence of the foregrounds, while on the other I propose a framework for optimizing hardware of such experiments to let them achieve better performance. This part of thesis stems from a common work with drs. F. Stivoli and R. Stompor. I finally present one of the leading CMB polarization experiment POLARBEAR, in which I have been involved in over the course of my PhD studies. I describe its current status and performance as well as selected steps of its data analysis pipeline. In particular, I show methods to estimate some of the parameters introduced for the systematics modeling from simulated

data. This work has been performed in collaboration with members of the POLARBEAR team.

Resumé

Cette thèse présente une étude de certains effets systématiques instrumentaux et astrophysiques, pouvant affecter les performances des nouvelles et futures générations d'observations de la polarisation du fond diffus cosmologique (CMB). Nous étudions l'impact de ces effets sur les objectifs scientifiques de ces observations, ainsi que les techniques pour leur élimination. Ce travail se concentre sur les problèmes généraux que rencontrent les expériences de manière générale, mais se penche également sur les questions plus spécifiques soulevées dans le cadre de l'expérience d'observation des modes-B du CMB, POLARBEAR.

L'objectif principal de l'effort actuel pour l'étude de la polarisation du CMB est une détection des anisotropies primordiales appelées modes-B — une signature des théories inflationnaires non détectée à ce jour. Cela aurait un grand impact sur notre compréhension de l'univers, mais aussi des lois fondamentales de la physique. Comprendre, modéliser, et, finalement, éliminer ces effets systématiques sont des éléments indispensables pour tout pipeline d'analyse moderne du CMB. Sa réussite, de concert avec une haute sensibilité instrumentale, décidera du succès final des efforts entrepris.

Dans cette thèse je décris tout d'abord l'optique des expériences typiques d'observation du CMB et propose un paramétrage des polarisations instrumentale et croisée. Deuxièmement, je présente un modèle décrivant la contamination atmosphérique et utilise celui-ci afin de donner quelques aperçus sur le rôle et l'impact de l'atmosphère sur les performances des expériences au sol. J'indique également comment ces résultats peuvent être utilisés pour améliorer le contrôle des effets atmosphériques dans l'analyse des données CMB. Ensuite, je discute d'une autre source d'effets systématiques venant du ciel — les avants-plans astrophysiques polarisés. Dans ce contexte, je présente d'une part une nouvelle approche pour prédire les performances des futures expériences prenant en compte la présence des avant-plans, et d'autre part je propose un cadre pour l'optimisation des expériences afin qu'elles puissent atteindre de meilleures performances. Cette partie de la thèse est issue d'un travail commun avec F. Stivoli et R. Stompor. Je présente enfin une expérience phare pour l'observation de la polarisation du CMB, POLARBEAR, dans laquelle j'ai été impliqué au cours de mes études doctorales. Je décris le statut actuel et les performances de l'instrument ainsi que quelques étapes de son pipeline d'analyse des données. En particulier, je montre des

méthodes d'estimation de certains des paramètres introduits pour la modélisation d'effets systématiques, à partir de données simulées. Ce travail a été réalisé en collaboration avec les membres de l'équipe POLARBEAR.

Acknowledgements

First of all, I would like to sincerely thank Radek Stompor, who advised me and directed my research during those last three years. He has been a caring advisor, a helpful educator and it has been a great privilege to learn and work in his team.

I thank Andrew H. Jaffe and Juan Francisco Macías-Pérez who accepted, during this summer, to report this thesis. I am very grateful for their efforts and the advices they have provided for the improvement of this manuscript. I thank Pierre Binétruy for giving me the honor of being at the head of the committee. I also thank Anthony J. Banday and Benjamin Wandelt for participating to the jury as examiners of my work. Many thanks to Julian Borrill, who comes from Berkeley for this defense, and who proposed me a postdoctoral position in his team for the next years. This opportunity allows me to continue my work on POLARBEAR, trying to extract science from the data during a very exciting period for the project.

My thanks to Adrian T. Lee and all the members of the POLARBEAR collaboration, with whom I have had the chance to travel for the commissioning and first lights of the instrument both in California and Chile. In addition to the discovery of fantastic persons and countries, I learnt all the basics of the instrument and its observation, essential knowledge for the analysis of the data.

I also thank my lab, the laboratoire Astroparticule & Cosmologie which is a place who gave me more than colleagues, from my first internship with a satellite dish on the roof of the lab trying to detect the CMB, up to this research thesis. Of course, I wish the best things to everyone from the third and fourth floors, with whom discussions were fruitful and life in the lab pleasant.

I thank my friends and family without whom nothing would have been possible. They have always been infallible supports and have always helped me in my projects. Finally, I address particular thanks to Solenne, a wonderful person who gave me more than assistance and support during those years.

Contents

List of Figures

LIST OF FIGURES

List of Tables

To Gab & Betty,

Introduction

Observational cosmology aims at understanding the history of the universe, its dynamics and evolution on the grounds of observational data. Among other approaches, the observation of the Cosmic Microwave Background (CMB) polarization provides a unique window onto the physics of the very early universe and an exceptional probe of the laws governing at the highest energies.

However, observing the CMB is a very challenging task and history shows that it has been possible thanks to a tremendous collaboration between theorists, experimentalists, data analysts at the junction between particle physics and astrophysics. After major discoveries, the adventure still continues nowadays as cosmological community faces many new challenges and the aims posed for the CMB research are continuously renewed. Among others, observational goals for the next years include the detection of primordial inflationary B-modes, primordial non-gaussianity, dark matter particles, signatures of modified gravity and the characterization of dark energy.

Theoretical challenges – In addition to the research on models about, for instance, the dark sector, and the trials to predict observables from high energy physics such as quantum gravity, theorists intensively study scenarios for inflation. Their research is based on either phenomenology or specific models (e.g. string theory) and especially aims at predicting levels for e.g. primordial gravitational waves or non-gaussianity. The constructed models are subsequently used to interpret the noisy data produced by observational experiments. Some current problems are related to the mechanisms generating inflation and their potential observational signatures.

Experimental challenges – New CMB polarization experiments need a very high sensitivity and strong control of systematic effects. Current problems are usually related to the production of large planar arrays, made of e.g. multichroic detectors. Furthermore, optimization of cryogenics systems as well as the improvements of the readout network are essential steps for future instruments. To reduce or control systematics at the experimental level, researchers look in particular for techniques in order to modulate the incoming polarization and attenuate potential polarized contaminants. However, those goals imply real challenges: for instance, developing mechanisms which could work for long periods of time, at very low temperature, is very difficult.

Data analysis challenges – The required improvements at the experimental level as well as new predictions from theories solicits new projects and approaches in the data analysts community. In particular, the main question is how to deal with huge data sets and be able to optimally extract reliable cosmological information in a reasonable time scale and to take into account systematic effects? In this thesis I define systematic effects as both instrumental (e.g. imperfect optics) and sky systematics (astrophysical

foregrounds, atmosphere, etc.): for instance, how to optimize and be as efficient as possible for the separation of sky components, i.e. the disentanglement of CMB from other astrophysical sources? Lastly, how to efficiently filter atmospheric contamination or estimate instrumental systematic effects in order to optimally extract scientific informations encoded in the observational data?

The research projects described in this thesis have been motivated by the data analysis challenges of the current (e.g. POLARBEAR) and future CMB experiments (POLARBEAR-II and nearly full-sky satellite experiment such as COrE or CMBpol). Their unifying theme can be formulated as: how to describe and control systematic effects at the data analysis level in a statistical robust way?

This thesis is organized as follows. In Part I, after a brief introduction of the concept of standard cosmology, I present the theory of inflation, the ultimate aim of this research. I also describe the observable signatures of the very early universe physics encoded in the CMB anisotropies, which are unique means to reach our science goal. Part II is a transition between the introduction and the presentation of my PhD work: I present the interest we have in observing the B-modes polarization anisotropies, what is the status of CMB polarization observation and how my projects are located in comparison to the contemporary challenges experimentalists and data analysts have to face. Part III introduces important sky and instrumental systematic effects potentially affecting new generation CMB polarization experiments. Part IV summarizes the work I have performed in collaboration with drs. F. Stivoli and R. Stompor about focal plane optimization for future nearly full-sky CMB experiments, in the presence of astrophysical foregrounds. Finally, in Part V, I present the CMB polarization instrument called POLARBEAR, mounted on the Huan Tran Telescope at Chajnantor plateau, 5200 m, Chile, which has begun its observations in January 2012. Then I introduce some of the algorithms and analysis I have developed and/or tested as a member of the international POLARBEAR collaboration.

Part I

Introduction to inflation and its observables

At large scales, our universe can be seen as an expanding homogeneous and isotropic medium. This simple description, combined with some thermal assumptions, allows us to describe, at first order, the physics of the primordial plasma and the creation of the different contents (light nuclei, radiation, etc.) of the universe. Especially, it predicts the existence of a background radiation, called the Cosmic Microwave Background (CMB) which is a gold mine for observational cosmologists. The standard cosmological model has serious limitations though, which can be solved by introducing an inflationary period occurring during the very early period of the universe. This mechanism, called inflation, has specific observational side effects, in particular the CMB B-modes anisotropies in polarization which detection is one of the most exciting goal for the new generation CMB experiments.

This first Part sets the background for the future discussion describing the standard cosmology, inflation, and its observational signatures onto the CMB. Chapter 1 presents the hot big bang model, which provides the framework within which most of the cosmological observations can be explained today. In chapter 2 I review the motivations for the inflation and briefly explain its dynamics and observational consequences. Finally, in chapter 3, I describe and analyze the signatures in the Cosmic Microwave Background radiation due to initial perturbations, emphasizing the existence of linearly polarized signals.

Chapter 1

The homogeneous universe

A spectacular development of our understanding of the universe happened during the twentieth century. This progress has only been possible thanks to achievements both in theory and experimentation, closely related to the development of new technologies.

In 1925, Edwin Hubble made an amazing discovery while using the most powerful telescope at the time at Mount Wilson: distant galaxies were isotropically receding away from us with speeds that only depended on the distance between them and us, see Hubble (67), Lemaître (82). Those observations, followed by others, had really strong theoretical implications and gave an observational evidence that our universe was expanding. In particular, the homogeneous and isotropic cosmic expansion could be extrapolated back in time, such that the observable universe was once hotter and denser, an initial state from which the present cold and rarefied universe emerged through a spectacular expansion. Theorists of the time, and in the next decades, used the then-new concepts of general relativity (GR) and particle physics to reproduce how the universe looked like during its first stages, predicting that this hot and young universe could be seen today as a highly homogeneous space-time filled with a blackbody radiation reaching us from all directions of the sky, in the microwave frequencies region, radiation which was eventually called the Cosmic Microwave Background (CMB). This prediction, made by R. Alpher, R. Herman and G. Gamow in the 1940s, remained a theoretical conjecture among many others, impossible to be verified until 40 years after Hubble's discovery, when A. A. Penzias and R. W. Wilson measured an excess of the sky temperature coming from all directions while testing their antenna working at 4.080 GHz, see Penzias and Wilson (105). Since then we had to wait another 30 years until a precise measurement of the CMB was achieved by the space mission COBE, and its absolute spectrometer FIRAS, which unambiguously showed that the CMB had a blackbody spectrum with a brightness temperature of 2.725 ± 0.002 K, see Fixsen et al. (48), Mather et al. (89).

Until the mid 1990s, the accepted view was that we live in an expanding universe in which gravitational forces dominate at large scales, mainly due to the non-baryonic dark matter, and the discussion was centered on whether there was enough matter to stop this expansion and eventually re-collapse it (the famous Big Crunch), or if the universe was going to grow forever. But this idea started changing upon better experimental constraints on the cosmological parameters, suggesting that another sort of energy dominates the universe at large scales, opposing gravity with an expansive effect. Extending Hubble's observation to much larger distances by using new techniques from the study of type Ia supernova events, and the use of bigger and more powerful telescopes, the High-z Supernova Search Team in 1998 (Riess et al. (113)), and the Supernova Cosmology Project in 1999 (Perlmutter et al. (107)) showed that the universe has been actually undergoing a recent accelerated expansion. This implied the existence of a new form of energy, often called "dark energy", or was due to a property of the vacuum itself, or a consequence of the modification of the gravity (see for instance Nojiri and Odintsov (101)), etc. It did not imply a fundamental flaw in the theoretical models accepted at the time. For instance, the observed effect is a simple consequence of general relativity when provided with a "cosmological constant" term, or for any scalar field model with an equation of state parameter less than $-1/3$ (equivalent to a negative pressure). Nowadays, one of our main scientific challenges is to explain the nature of this energy, why it constitutes nearly 72 % of the energy content of the universe. In addition, researchers try to understand why the acceleration of the expansion is happening now – this is what we call the coincidence problem.

We know that the universe is inhomogeneous today, and we expect some small perturbations at earlier times, visible on the CMB. The modeling of the initial conditions predicts the presence of tiny temperature fluctuations in angular space, of only one part in 10^5 of the average temperature. These fluctuations can be indeed derived from the fundamental properties of the early universe in some models, e.g. inflation, and contain valuable information about it. The first successful attempt to measure these fluctuations was done by COBE and its differential radiometer DMR, which measured the CMB dipole (produced by the relative motion of the Earth with respect to the rest frame of the CMB) and CMB fluctuations on a $\sim 7\,\mathrm{deg}$ scale and down to a level of $\sim 30\mu\mathrm{K}$. The precise measurement came from another satellite based on differential radiometer, the Wilkinson Microwave Anisotropy Probe (WMAP), which measured these anisotropies on a $\sim 0.5\,\mathrm{deg}$ scale, probing the available theory with unprecedented precision, and allowing the estimation of fundamental cosmological parameters like the energy content of the universe (Gold et al. (54)). COBE and WMAP, with dozens of other smaller experiments, opened a whole new field in observational cosmology: understanding the fundamental properties of our universe thanks to the CMB.

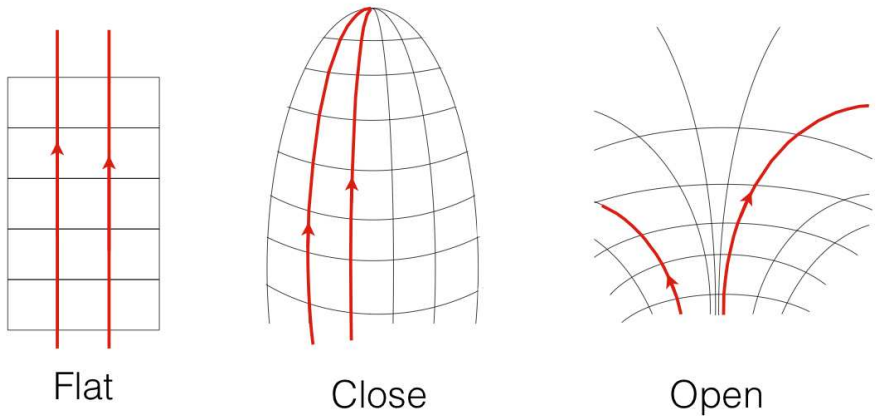

Figure 1.1: Scheme illustrating the different geometry of the universe: flat ($K = 0$), close ($K < 0$) or open ($K < 0$). Red lines are freely moving particles, with initially parallel directions at the beginning.

Throughout this thesis, if not specified, I adopt the convention $c = \hbar = k_B = 1$.

1.1 Cosmological principles and cosmography

The fundamental principle in cosmology is the assumption that the universe is, at least on large scale, homogeneous and isotropic. This idea was born at the beginning of the twentieth century: it was originally a concept motivated rather by philosophical considerations than observational reasons.

First of all, let us introduce the metric for our homogeneous and isotropic universe. Just after the birth of GR, A. Einstein was one of the first physicists to attempt to build a metric which could describe the entire universe. The starting idea was that the universe was homogeneous, isotropic and immutable with time. As I mentioned before, the abandonment of this latter hypothesis was primarily due to the discovery by E. Hubble of the galaxies movement of recession. However, it is only after 1965, when A. A. Penzias and R. W. Wilson discovered and characterized the Cosmic Microwave Background (CMB), that the Hot Big Bang model (the fact that the universe has experienced a hot phase in the past) won against the idea of an immutable universe, as described by the steady state model. We have today strong evidences for the homogeneity and isotropy, even if, for a long time, local observations of stars and galaxies were showing important inhomogeneities. As mentioned before, the strongest proof of isotropy nowadays is the CMB even if, as we will see in details in chapter 3, this latter has anisotropies at the 10^{-5} level.

In the GR frame, homogeneity and isotropy determine the general expression of the metric, encapsulated in the tensor $\mathbf{g}_{\mu\nu}$, e.g. Weinberg (146). This latter corresponds to

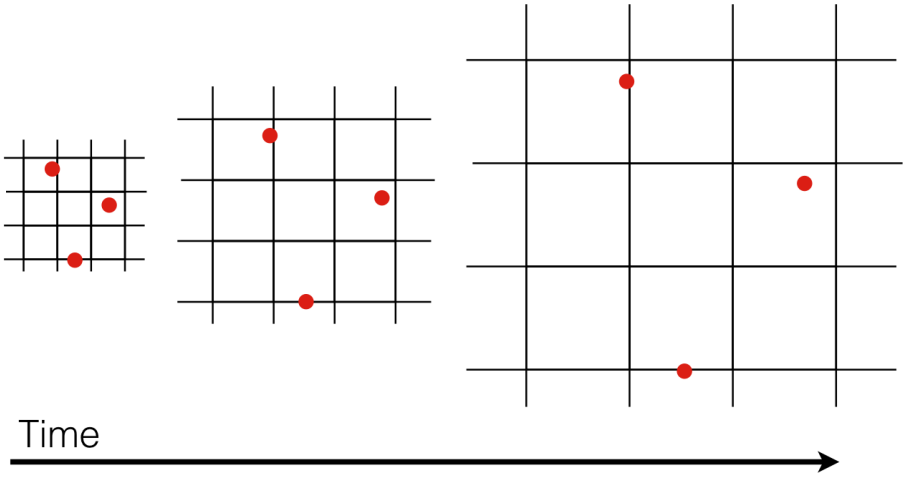

Figure 1.2: Scheme illustrating the expansion of the universe. Red spots could be seen as distant galaxies: through time, the comoving distances (difference between coordinates) do not vary but physical distances increase.

the Friedmann-Lemaitre-Robertson-Walker (FLRW) metric defined as

$$ds^2 \equiv \mathbf{g}_{\mu\nu} dx^\mu dx^\nu \tag{1.1}$$

$$\equiv -dt^2 + a(t)^2 \left[\frac{dr^2}{1 - Kr^2} + r^2 d\theta^2 + r^2 \sin^2(\theta) d\phi^2 \right] \tag{1.2}$$

where K is a parameter describing the spatial geometry of the universe: if $K = 0$, the spatial part of the metric is flat — if $K \neq 0$, curvature is not null. Consequently, universe can be either flat, open or close. As illustrated in Fig. 1.1, a spatially flat universe corresponds to an Euclidean geometry. Above (or below) a critical value for the total energy density ρ_{tot} ($\sim 10^{-29}\, g.cm^{-3}$), the universe is close (or open). These two last spatial geometries have positive and negative curvature respectively.

Secondly, we have strong evidence that the universe is expanding. This results in a continuous increase of the "physical" distance between us and distant galaxies since early times. In order to describe this dynamics, I introduce the so-called scale factor a, whose present value, a_0, is by convention set to 1 when $K = 0$, cf. Eq. (1.2). At earlier times, because of the expansion, a was smaller than today. Fig. 1.2 illustrates this expansion: notice that red dots, for instance distant galaxies, are moving with the grid – their comoving coordinates do not change. Therefore the difference between coordinates, called the comoving distance between two galaxies, remains constant with time. However, the physical distance is proportional to the scale factor, and consequently evolves with time. A way of quantifying the variation of the scale factor through the

time (and also its relation with the energy contents of the universe) is to use the Hubble rate defined as

$$H(t) \equiv \frac{\dot{a}}{a}, \tag{1.3}$$

which gives a measure of how rapidly the scale factor a changes. Throughout this thesis, I will use $\dot{x}$ to denote the derivative of x with respect to the time t. Let us imagine that a photon travels from (r_1, t_1) and reaches us today $(0, t_0)$. In this case, Eq. (1.2) reads

$$ds^2 = 0 \quad \text{which defines a geodesic, i.e. the path followed by a massless particle without interaction} \tag{1.4}$$

$$= dt^2 - a(t)^2 \left[\frac{dr^2}{1 - Kr^2}\right] \tag{1.5}$$

Therefore we can write

$$\int_{t_1}^{t_0} \frac{dt}{a(t)} = \int_0^{r_1} \frac{dr}{\sqrt{1 - Kr^2}}. \tag{1.6}$$

If the starting point (r_1, t_1) is supposed to be at rest ($\dot{r}_1 = 0$), then two events separated by a time Δt_1 at the starting time will be separated by a time interval Δt_0 at the reception, such as

$$\frac{\Delta t_0}{a(t_0)} = \frac{\Delta t_1}{a(t_1)}. \tag{1.7}$$

This implies that, specifically, electromagnetics wavelengths λ_1 and λ_0 verify

$$\frac{\lambda_0}{\lambda_1} = \frac{a(t_0)}{a(t_1)}. \tag{1.8}$$

As a consequence of Eq. (1.8), the expansion of the universe translates into a shift toward red wavelengths — this corresponds to what we call a redshift z, defined as

$$1 + z \equiv \frac{a(t_0)}{a(t_1)}. \tag{1.9}$$

Assuming a cosmology (a set of cosmological parameters, see e.g. section 3.4), z is finally a way of measuring distances. It is important to understand that the proportionality relation between distance and velocity is only true in the local universe: as soon as $z \gtrsim 1$, we have to be careful with which distance definition we use (angular, luminous, parallax, etc.).

1.2 Evolution of the scaling factor a

To understand the history of the universe, we must determine the evolution of the scale factor a with the cosmic time t. GR provides the connection between this evolution and the energy, i.e. the contents, of the universe. Einstein equations reads (Einstein (37))

$$\mathbf{G}_{\mu\nu} = 8\pi G \mathbf{T}_{\mu\nu} + \Lambda \mathbf{g}_{\mu\nu}, \tag{1.10}$$

where we set $\mathbf{G}_{\mu\nu} \equiv \mathbf{R}_{\mu\nu} - \frac{1}{2}\mathbf{g}_{\mu\nu}R$, corresponding to the geometrical part including the metric tensor $\mathbf{g}_{\mu\nu}$ and the r.h.s. of Eq. (1.10) corresponds to the energy contents of the cosmos. Isotropy of a perfect cosmic fluid implies that the energy-momentum tensor, $\mathbf{T}_{\mu\nu}$, reads

$$\mathbf{T}_{\mu\nu} \equiv \begin{bmatrix} \rho & 0 & 0 & 0 \\ 0 & p & 0 & 0 \\ 0 & 0 & p & 0 \\ 0 & 0 & 0 & p \end{bmatrix} \tag{1.11}$$

where ρ is the energy density of the cosmic fluid and p its pressure. Of course, this solution is a simplified modeling of the universe and we could consider perturbations to this tensor as explained in the next chapter. From the energy-momentum conservation laws (covariant derivative of $\mathbf{T}_{\mu\nu}$ is equal to 0), we have

$$a^3 \frac{\partial p}{\partial t} = \frac{\partial}{\partial t}\left[a^3(\rho + p)\right] \tag{1.12}$$

$$\Rightarrow \frac{\partial}{\partial t}\left(\rho a^3\right) = -3pa^3 \tag{1.13}$$

To simplify, it is common to assume the following equation of state, parametrized by a constant w,

$$p \equiv w\rho, \tag{1.14}$$

which relates the local pressure p to the energy density ρ. This assumption is true for each component (radiation, matter, etc.) but is not true for the total fluid. However, each component dominate the total energy at different period of the cosmic history. For instance, when ultra-relativistic particles dominate the universe, $w = 1/3$, and when matter dominates, $w = 0$ (dust without pressure). Energy conservation applied to each fluid leads to the density evolution of each of those,

$$\rho_\gamma \propto a^{-4} \text{ for radiation} \tag{1.15}$$

$$\rho_m \propto a^{-3} \text{ for matter} \tag{1.16}$$

$$\rho_\Lambda \propto \text{ constant for the cosmological constant } \Lambda. \tag{1.17}$$

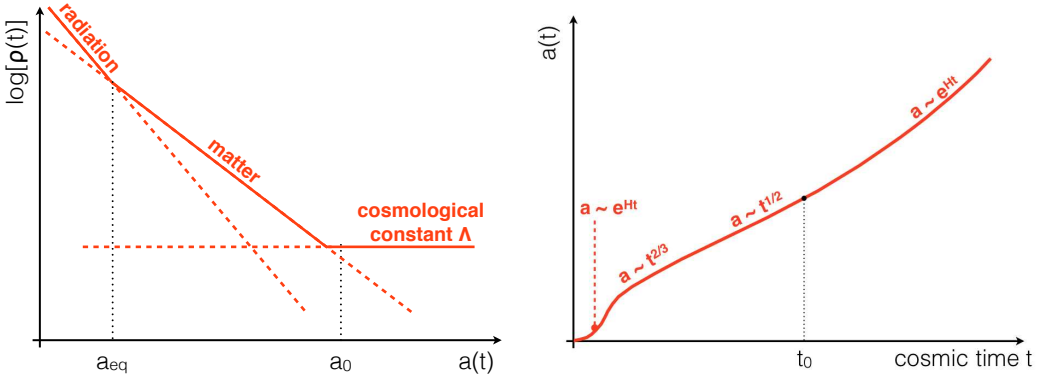

Figure 1.3: **Left panel:** energy density ρ as a function of the scale factor a. Different constituents of the universe dominates at different time of the history: radiation, non-relativistic matter and a potential cosmological constant. **Right panel:** behavior of the scale factor a as a function of the cosmic time t, in the frame of the ΛCDM model.

Furthermore, under the assumptions of homogeneity and isotropy, Eq. (1.10) leads to the equations of the evolution of a, the so-called Friedman equations:

$$3\frac{\ddot{a}}{a} = -4\pi G\rho(1+3w)+\Lambda \tag{1.18}$$

$$\left(\frac{\dot{a}}{a}\right)^2 = \frac{8\pi G}{3}\rho - \frac{K}{a^2} + \frac{\Lambda}{3}. \tag{1.19}$$

If $K = 0$ and $\Lambda = 0$, solution of Eqs. 1.18 and 1.19 are of the form, cf. Fig. 1.3:

$$a \propto t^{2/3} \text{ for the matter dominated period for which } \dot{a} \propto \frac{1}{a} \tag{1.20}$$

$$a \propto t^{1/2} \text{ for the radiation dominated period for which } \dot{a} \propto \frac{1}{a^2}. \tag{1.21}$$

Let us have a look at Eq. (1.19): if we assume that a increases with time, we can note that the terms in ρ, K and Λ dominate successively the r.h.s.. At early times, universe is dominated by radiation energy, and we saw that $a \propto t^{1/2}$. Later, nonrelativistic matter dominates and this implies that $a \propto t^{2/3}$. One way to explore the energy content of the universe is to measure changes in the scale factor (thanks to, for instance, Supernovae observation, which measures the deceleration $\propto \ddot{a}$). As a result of such research, we now believe that the scale factor a has stopped growing as $t^{2/3}$, which can be interpreted as the existence of a new form of energy starting dominating, of unknown fundamental nature at the time of writing this thesis — the so-called dark energy.

For definiteness, we set the following quantities:

$$\Omega_i \equiv \frac{\rho_i}{\rho_c} \tag{1.22}$$

where i is a component of the universe and ρ_c is the critical energy density defined as

$$\rho_c \equiv \frac{3H_0^2}{8\pi G} \text{ and} \tag{1.23}$$

$$\Omega_\Lambda \equiv \frac{\Lambda}{3H_0^2} \tag{1.24}$$

Therefore, Eq. (1.19) gives $\Omega + \Omega_\Lambda = 1 + K/\dot{a}^2$. If $K \sim 0$, as suggested by the most recent observations, $\Omega_{tot} \equiv \Omega + \Omega_\Lambda$ should be equal to 1.

1.3 Thermal history of the universe

The universe, dominated by CMB photons, is considered to be adiabatically expanding, with microphysical interactions rate being much more quicker than the typical expansion rate. We then usually associate the CMB temperature to the cosmic fluid, i.e.

$$T(t) = T(z) = T(a). \tag{1.25}$$

The interested reader will refer to e.g. Kolb and Turner (73) or Mukhanov (94) for more detailed informations.

1.3.1 Overview

The temperature of the cosmic radiation decreases as the universe expands. It is unambiguously related to the redshift,

$$T(z) = T_0 \times (1 + z), \tag{1.26}$$

and can be used as an alternative to the cosmic time t to parameterize the history of the universe. To obtain an estimate for the temperature expressed in MeV, at the time t measured in seconds, we can use the fact that

$$T(t) \propto \frac{1}{\sqrt{t}} \tag{1.27}$$

which is valid during the radiation-dominated epoch. Below we briefly summarize the sequence of the main events constituting the history of our universe, in chronological order, as illustrated in Fig. 1.4:

- around 10^{-43} sec ($\sim 10^{19}$ GeV) — near the Planckian scale, quantum gravity dominates and GR is not valid. We expected that all the problems raising at these huge energies will find answers in a still unknown non-perturbative string/quantum gravity theory, e.g. Vey (143).

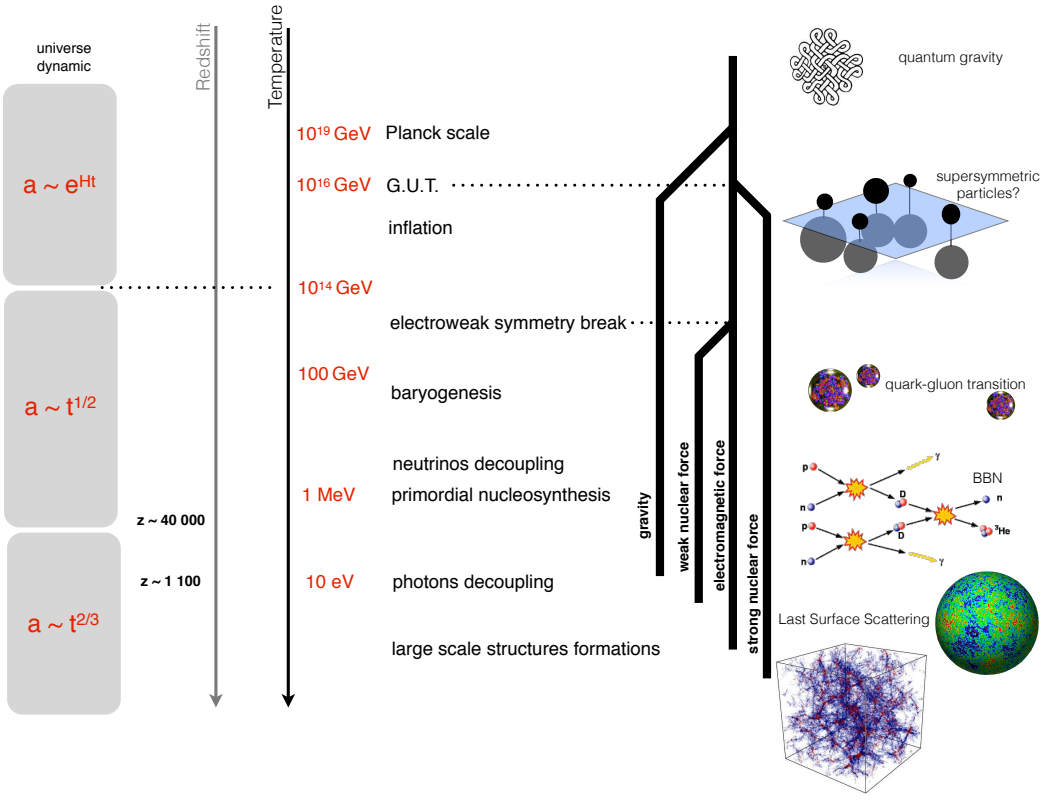

Figure 1.4: Scheme illustrating the thermal history of the early universe.

- $10^{-43} \rightarrow 10^{-14}$ sec (10^{19} GeV $\rightarrow$ 10 TeV) — because this energy range will probably not be reached by accelerators in the near future, constraints on this period give unique information about fundamental physics. In addition, even if GR is considered to be valid at these energies, uncertainties remains about the nature of the basic elements composing the cosmic fluid at those times. Among other things, we expect baryon asymmetry, not explained by the standard model, to occur at the highest energies of this range. Besides, supersymmetry theory proposes the existence of all the super-particles in this period (including weakly interacting and massive particles, candidates for dark matter, still being hunted by the Large Hadron Collider (LHC)). As illustrated in Fig. 1.4, there are good reasons that a unification (GUT) of the electroweak and strong interactions took place around $\sim 10^{16}$ GeV. Cosmic strings, monopoles and other topological defects are also created during this period. Independently from any particle physics, as we will see in the next chapter, it is also the period of an inflationary phase of expansion, where the scale factor verify $a(t) \sim \exp(Ht)$. This stage has important observational consequences, such as imprints in the CMB fluctuations or in the large structures formation and is expected to solve many fundamental problems such as the horizon problem, the flatness of the universe spatial geometry, etc., see chapter 2.

- $10^{-14} \rightarrow 10^{-10}$ sec (100 TeV $\rightarrow$ 10 GeV) — LHC is able to probe energies within this range. The standard model of particle physics starts being valid. At temperatures above $\sim$ 100 GeV, the electroweak symmetry is restored and the gauge bosons are massless.

- 10^{-5} sec ($T \sim 200$ MeV) — the quark-gluon transition takes place, which means that free quarks and gluons become confined within baryons and mesons. The physics of the quark-gluon transition is not yet completely understood, and is currently studied by several experiments such as the LHC-project ALICE.

- 0.2 sec ($T \sim 1 - 2$ MeV) — primordial neutrinos decouple from the other particles and propagate without further scatterings. Second, the ratio of neutrons to protons "freezes out" because the interactions that keep neutrons and protons in chemical equilibrium become inefficient. Subsequently, the number of the left neutrons determines the abundances of the primordial elements.

- 1 sec ($T \sim 0.5$ MeV) — electron-positron pairs present in the very early universe begin to annihilate when the temperature becomes lower than their rest mass. Only a small excess of electrons over positrons, roughly one per billion photons, are left after annihilation. The photons produced by this process are in thermal equilibrium. The universe enters in the radiation-dominated era.

- $200 - 300$ sec ($T \sim 0.05$ MeV) — nuclear formation starts at this energy. As a result, free protons and neutrons form helium and other light nuclei. The abundances of the light elements resulting from primordial nucleosynthesis are in very good agreement with available observational data and consists in one of the main observational pillar of the hot big bang theory.

- 10^{11} sec ($T \sim 1$ eV) — this corresponds to the time of matter-radiation equality, separating the radiation-dominated epoch from the matter-dominated one, cf. a_{eq} in Fig. 1.3.

- $10^{12} \rightarrow 10^{13}$ sec ($T \sim 0.5$ eV) — free electrons and protons combine and form the lightest atom: neutral hydrogen. This phenomenon is called recombination. The universe becomes transparent to photons —radiation emitted at this time defines the CMB. Its temperature fluctuations, induced by the small inhomogeneous matter distribution at recombination, see chapter 3, give us unique and direct information about the state of the universe at the last scattering surface.

- $10^{16} \rightarrow 10^{17}$ sec ($T \sim 5$ meV) — galaxies and clusters of galaxies starts to form as a result of gravitational instability. Structure formation can be well described using Newtonian gravity but remains a very complicated nonlinear problem, which can only be solved numerically, e.g. Bernardeau et al. (11). Of course, one of the main unresolved fundamental issues regarding this formation process is the nature of dark matter and dark energy.

1.3.2 Boltzmann equation in an expanding universe

Even if I implicitly assumed in Eq. (1.25) that thermal equilibrium is a good approximation to describe the universe — today its temperature is $T_0^{\rm CMB} \sim 2.725$ K — there have been important departures from thermal equilibrium such as neutrino and photon decouplings, Big Bang Nucleosynthesis (BBN), baryogenesis, inflation, etc. These deviations from equilibrium have led to some relics such as light elements (H, He, ...), a neutrino and radiation backgrounds, etc.

Once a particle species ψ decouples from the primordial plasma, its number density goes like $n_\psi \propto 1/a^3$ and its momentum $p_\psi \propto 1/a$. The criterion for particles to decouple is the comparison of their interaction rate (per particle) Γ with the typical expansion rate of the universe, parametrized by the Hubble constant H. If $\Gamma \gtrsim H$, species remains coupled with the plasma. On the contrary, if $\Gamma \lesssim H$, species decouple. Physically, this means that if the mean free path $\sim 1/\Gamma$ becomes bigger than the length c/H, particles cannot interact anymore.

To properly treat the decoupling process, we should look into the energy and density distribution of each of the particles species, thanks to the Boltzmann equation

$$\mathbf{L}[f] = \mathbf{C}[f], \tag{1.28}$$

where $\mathbf{L}$ is the Liouville operator given by

$$\mathbf{L} \equiv p^\alpha \frac{\partial}{\partial x^\alpha} - \Gamma^\alpha_{\beta\gamma} p^\beta p^\gamma \frac{\partial}{\partial p^\alpha}, \tag{1.29}$$

in which expression f is the phase space density and $\mathbf{C}$ is the collision operator. In the case of the isotropic and homogeneous FLRW universe, $f = f(|\mathbf{p}|, t) = f(E, t)$, and then $\mathbf{L}[f]$ reads

$$\mathbf{L} = E\frac{\partial f}{\partial t} - H\,|\mathbf{p}|^2\,\frac{\partial f}{\partial E}, \tag{1.30}$$

with $H \equiv \dot{a}/a$ is the Hubble parameter, cf. Eq. 1.3. Therefore, Eq. (1.28) gives

$$\dot{n} + 3Hn = \frac{g}{(2\pi)^3}\int \mathbf{C}[f]\frac{d\mathbf{p}}{E}, \tag{1.31}$$

where n is the density number defined as $n(t) = \left(g/(2\pi)^3\right)\int d\mathbf{p} f(E,t)$ and g counts for internal degrees of freedom. The second factor on the l.h.s. accounts for the dilution effect due to the expansion of the universe and the r.h.s. term accounts for the interactions that change the number of particles.

Now I present some specific applications of this formalism.

1.3.3 Freeze-out

In this section, I describe the relic abundance today, after their decoupling, i.e.

$$\Gamma \lesssim H. \tag{1.32}$$

Let us consider the interaction

$$a \;+\; b \;\leftrightarrow\; c \;+\; d \tag{1.33}$$

Using Eq. (1.31), it can be shown that

$$\dot{n_a} + 3Hn_a = -n_a n_b \langle\sigma_{ab\to cd} v_{ab}\rangle + n_c n_d \langle\sigma_{cd\to ab} v_{cd}\rangle \tag{1.34}$$

and equivalent equations for b, c and d. σ_X denotes the cross-section of the process X. At thermal equilibrium, we have

$$n_a^{eq} n_b^{eq} \langle\sigma_{ab\to cd} v_{ab}\rangle_{TE} = n_c^{eq} n_d^{eq} \langle\sigma_{cd\to ab} v_{cd}\rangle_{TE} \tag{1.35}$$

We make the approximation that $\langle \sigma v \rangle \sim \langle \sigma v \rangle_{TE}$ when we are close to the equilibrium, so that Eq. (1.34) reads

$$\dot{n_a} + 3Hn_a = -\langle \sigma_{ab\to cd} v_{ab} \rangle_{TE} \left[n_a n_b - n_a^{eq} n_b^{eq} \right] + \langle \sigma_{cd\to ab} v_{cd} \rangle_{TE} \left[n_c n_d - n_c^{eq} n_d^{eq} \right] \quad (1.36)$$

When decoupling occurs, let us assume that c and d stays at equilibrium and that $n_a \sim n_b$ (as it is the case for e.g. particles and antiparticles when $\mu/T \ll 1$). It can be shown that

$$\frac{d\left[\log(a^3 n_a)\right]}{d\left[\log(a^3)\right]} = -\frac{\Gamma}{H}\left(1 - \left(\frac{n_a^{eq}}{n_a}\right)^2\right), \quad (1.37)$$

where $a^3 n_a$ corresponds to the number of particles in a comoving volume. Because of the fact that $T \propto 1/a$, cf. Eq. (1.26), and thanks to statistical distribution equations, we can write

$$n^{eq} \propto T^3 \propto \frac{1}{a^3} \quad \text{if particles are relativistic} \quad (1.38)$$

$$n^{eq} \propto T^3 \left(\frac{m}{T}\right)^{3/2} e^{(m-\mu)/T} \quad \text{if particles are non} - \text{relativistic} \quad (1.39)$$

If particles are relativistic, Eq. (1.37) is satisfied at the thermal equilibrium for any value of Γ/H. On the contrary, if particles are non-relativistic, Eq. (1.37) is only true for $\Gamma/H \gg 1$.

1.3.4 Recombination

With the universe expanding, particles interact progressively less, which is especially relevant in the case of photons, electrons and protons. One can imagine that below a given energy, corresponding roughly to the 13.6 eV of the binding energy of an electron around a proton, photons would stop interacting with matter. As mentioned in paragraph 1.3.1, at this particular moment of the universe history, the plasma becomes transparent and light can freely travel through space-time.

After nucleosynthesis, the universe is composed of protons p, helium nuclei ${}^4_2H_e$, photons γ, electrons e^-, decoupled neutrinos ν, some light nuclei like D, Li, etc., potentially dark matter particles, etc. Because of the efficiency of their interactions, we only consider here the presence of p, e^- and γ. Those latter are in equilibrium through Compton scattering, such as

$$\gamma + e^- \leftrightarrow \gamma + e^- \quad (1.40)$$

$$\gamma + p \leftrightarrow \gamma + p. \quad (1.41)$$

As soon as the temperature $T \sim$ eV, electrons can combine with protons and start forming the first H atoms

$$p + e^- \leftrightarrow H + \gamma, \quad (1.42)$$

and this is what we call the recombination. Furthermore, the process

$$\gamma + H \leftrightarrow \gamma + H \tag{1.43}$$

is not efficient enough and photons escape the plasma: this is what we call the decoupling. If the process (1.42) is in equilibrium, i.e. $\Gamma \gtrsim H$, then the electrons density is given by the Saha equation

$$\frac{1-x_e}{x_e} = n_\gamma \left(\frac{m_e\, T}{2\pi}\right)^{-3/2} e^{E_B/T} \tag{1.44}$$

where

$$x_e \equiv \frac{n_{e^-}}{n_b} = \frac{n_p}{n_b} \equiv \frac{n_p}{n_p + n_H},\ \mathrm{n_b}\ \text{being the baryonic number} \tag{1.45}$$

$$E_B = 13.6\ \text{eV},\ \text{corresponds to the binding energy of H} \tag{1.46}$$

We can then write Eq. (1.44) as

$$\frac{1-x_e}{x_e} = x_e n_b \left(\frac{m_e T}{2\pi}\right)^{-3/2} e^{E_B/T} \tag{1.47}$$

where n_b can be measured[1] and leads to

$$\frac{1-x_e}{x_e^2} \approx 3.84\eta \left(\frac{T}{m_e}\right)^{3/2} e^{E_B/T} \tag{1.48}$$

with $\eta \equiv N_b/N_\gamma$, as measured today. Solving Eq. (1.48) for a 50% yield leads to a temperature of roughly

$$T_{dec} \sim 4000\mathrm{K} \sim 0.5\ \text{eV}. \tag{1.49}$$

One should notice that $T_{dec} < E_B = 13.6$ eV, and this is due to the fact that the density of photons is so important at this early stage of the universe, that a population of photons at the tail of the energy distribution is large enough to keep the primordial plasma ionized. The average energy is therefore around 0.5 eV but the distribution of photons still permits the ionization of the first hydrogen nuclei.

Moreover, because $T = T_0(1+z)$, cf. Eq. (1.26), we can estimate that the photons decoupling corresponds to a redshift of

$$z_{dec} \sim 1100. \tag{1.50}$$

[1]The primordial ratio of deuterium to hydrogen nuclei $\equiv D/H$, both created during the BBN, provides a measure of the cosmological density of baryons, n_b. Measurements of the D/H ratio in the interstellar medium of our Galaxy provides a lower limit on the primordial ratio, because processing of gas by stars reduces the abundance of D relative to H. In addition, absorption of radiation from distant quasars by intervening clouds of gas offers a way of probing D/H ratios at large redshifts, where the effects of stellar processing are assumed to be negligible.

Chapter 2

Toward the initial conditions

2.1 Some limits of the Standard Model

Standard cosmology (without inflation, radiation being dominant at the beginning, followed by a matter-dominated period) is a very good framework for interpreting many observations. However, in the 1980s, some observational results did not have explanations in this approach. Some of these classical problems are listed below:

- **Horizon problem** – in the framework of the standard cosmology, we can derived the comoving radius of the horizon defined as

$$r_H = \int_0^t \frac{c\,dt}{a(t)} \tag{2.1}$$

  where c is the speed of light and $a(t)$ is the scale factor parametrizing the expansion of the universe, introduced in section 1.1. This horizon is also called the particle horizon, and corresponds to the maximum distance a particle can travel since the beginning of the universe, after a time t. The horizon, at the decoupling[1], was only about 100 Mpc, which corresponds nowadays to a ~ 1 deg angular distance on the sky. However, we observe, as a first approximation, that the CMB is almost perfectly isotropic. How can several different regions across the sky could share the same properties if they were causally disconnected at the recombination?

- **Flatness problem** – recent observations show that $\Omega_{tot} \sim 1$. However, it can be proved that this condition corresponds to an unstable solution for the universe and would have required an extremely fine tuning in the past. For example, at the Planck time, this is equivalent to a deviation of only 10^{-60} from $\Omega_{tot} = 1$.

[1] As introduced in section 1.3, decoupling is defined as the moment during recombination when the interaction rate between photons and matter became lower than the expansion of the universe. At that moment, radiation nearly stopped interacting with charged matter and decoupled, producing the CMB.

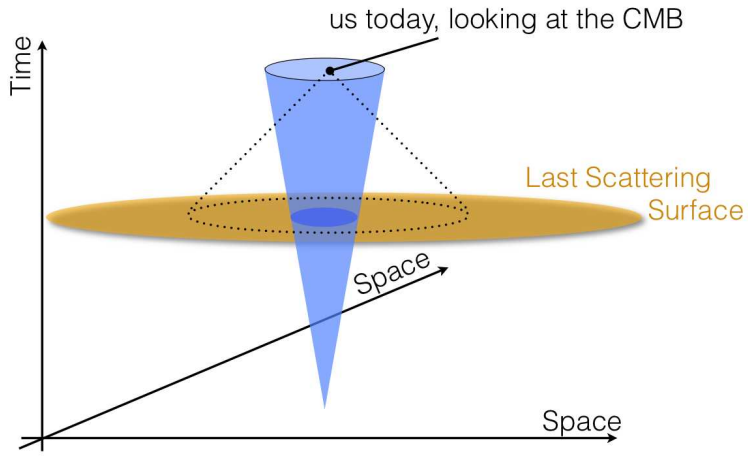

Figure 2.1: Scheme illustrating the horizon problem. The region inside the cone in blue is causally connected to us (it is our light cone). However, photons emitted from the Last Surface Scattering reach us today, started outside the blue region (e.g. dots limited region) and have temperatures that are almost identical. How is that possible?

This fine tuning requires a very precise mechanism which is not explained in the standard cosmology.

- **Monopoles problem** – in the context of unified gauge theories, many very massive stable particles must have been created during phase transitions which happened at early times of the universe — and could contribute in a significant way to the energy density nowadays i.e. $\Omega_X \gg 1$. The case of monopoles is the best known. In addition, particles with high masses have cross sections of annihilation even smaller. The "old" cosmology could not explain the non observation of such particles.

- **Origins of structures** – the universe is only statistically homogeneous on large scales ($\sim$ 100 Mpc). It is generally assumed that galaxies and galaxy clusters are formed by gravitational instability from initial perturbations. Inflation is, as explained below, a mechanism which could explain the origin to those fluctuations.

2.2 Mechanism for the inflation

This section describes the mechanism of inflationary models which has been proposed to solve the previous observational problems, see Guth (57).

2.2.1 Equation of state for the inflation

Inflation consider the possibility for a very particular equation of state in the first moments after the Big Bang. To solve the problem of the horizon and to allow for

causal contact between two points of the sky that are a priori causally disconnected, we must imagine a universe that could grow faster than the light i.e. such that the scale factor $a(t)$ satisfies $a(t \sim 0) \sim t^{\alpha}$ with $\alpha > 1$. The basic idea is to "decouple" the causal size r_H from the Hubble radius[1], so that the physical size of the horizon in the standard radiation-dominated era is much larger than the Hubble radius. Such a situation can occur if the comoving Hubble radius decreases sufficiently in the very early universe, which implies

$$\ddot{a} > 0, \tag{2.2}$$

corresponding to a phase of acceleration. Assuming this specific dynamics, the Friedman equations, Eqs. 1.18 and 1.19, give the following condition on the equation of state

$$p < -\frac{\rho}{3}. \tag{2.3}$$

This criterion may allow us to solve the flatness problem. Considering again Friedman equations leads to

$$\dot{a}^2 = \frac{8\pi G\rho a^2}{3} - K, \tag{2.4}$$

where K is the curvature coefficient involved in the expression of the metric. Since inflation is a process in which the quantity ρa^2 increases dramatically, we can reasonably neglect the curvature term in K — at least if inflation lasts long enough, as explained in the next paragraph.

2.2.2 De Sitter space and inflation

As previously mentioned, inflation needs an equation of state with a negative pressure, and the first idea is a vacuum energy satisfying

$$p = -\rho. \tag{2.5}$$

This equation of state is also satisfied in the case of a universe dominated by a cosmological constant, cf. the Λ terms in Eqs. 1.18 and 1.18. In this case, Friedman equations have three solutions depending on the geometry of the universe:

$$a(t) \propto \sinh(\bar{H}t) \text{ if } K = -1 \tag{2.6}$$

$$\propto \exp(\bar{H}t) \text{ if } K = 0 \tag{2.7}$$

$$\propto \cosh(\bar{H}t) \text{ if } K = -1 \tag{2.8}$$

[1]It corresponds to the distance beyond which objects recede from a given observer, because of the expansion of the universe, at a rate greater than the speed of light. The comoving Hubble radius at a time t is given by $d_H(t) = c/H(t)$.

with $\bar{H} \equiv \sqrt{\Lambda/3} = \sqrt{8\pi G\rho_\Lambda/3}$, cf. Eq. (1.24). All solutions tend towards the behavior of the exponential (K = 0), which corresponds to the de Sitter space. This latter is the maximally symmetric, vacuum solution of Einstein equations with a cosmological constant Λ verifying $p = -\rho$. $\bar{H}$ is not the usual Hubble parameter H, but it becomes so asymptotically. Moreover, the density parameter Ω_{tot} tends to 1 when $\bar{H}$ goes to H. If we assume that the universe is not fine tuned initially, then, for an expansion by a factor e^{N_e}, we can show that

$$\Omega_{tot} - 1 \sim e^{-2N_e}. \tag{2.9}$$

This may solve the problem of flatness, at least if e^{N_e} is sufficiently large. If we want $\Omega_{tot} - 1 \sim 0$ today, it is necessary that, at the GUT time[1], we have $|\Omega_{tot} - 1| \leq 10^{-52}$ and therefore the number N_e, introduced in Eq. (2.9) and named number of e-foldings[2], satisfies

$$N_e \geq 60. \tag{2.11}$$

It will be shown later that this is also the requirement to solve the problem of horizon. Thus, we have demonstrated an important prediction of inflation: the universe becomes spatially flat i.e. $K = 0$.

2.2.3 Reheating

A difficulty remains in this theory: how does the transition take place from an universe which has an equation of state with negative pressure to a universe with a "standard" equation of state? In other words, how did the universe switch from inflation to the standard Hot Big Bang model? We have seen in the previous chapter that Guth's invention in 1981 had to wait for some developments in quantum field theory to find the mechanisms for an adequate phase transition. This is what we see briefly in section 2.3.3. If we consider a field with a temperature T, then the energy density is $\sim T^4$ in the form of a vacuum energy. Naively, a phase transition setting the vacuum energy to zero will transfer, if it is instantaneous (this is not exactly the case in all the models), a latent heat with an energy $\sim T^4$ giving birth to matter and radiation. The universe is then reheated: it goes back to a state with the initial temperature T and with the expected

[1] As mentioned in the previous chapter, the Grand Unified Theory (GUT) is the model in which at very high-energy, the three gauge interactions of the Standard Model — the electromagnetic, weak, and strong interactions — are merged into one single interaction characterized by one larger gauge symmetry and thus one unified coupling constant.

[2] The number of e-folding is simply defined by

$$N_e \equiv \log\left[\frac{a(t_f)}{a(t_i)}\right], \tag{2.10}$$

where t_i and t_f are two given times, and therefore N_e has sense in a given period of time, here $\Delta t \equiv t_f - t_i$.

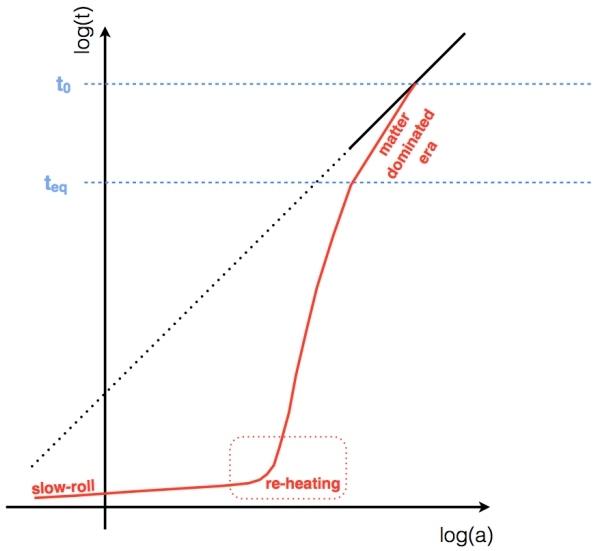

Figure 2.2: Evolution of the scale factor (x-axis) as a function of time (y-axis) in the case of a simple inflationary model.

conditions for the "standard" expansion. Fig. 2.2 illustrates the behavior of the scale factor during the inflation period.

2.3 Inflationary fields dynamics

The general concept of inflation is based on an equation of state with negative pressure, Eq. (2.3). This can be achieved naturally in the early universe using quantum fields.

2.3.1 Behaviors of quantum fields at high temperatures

The interesting feature about quantum fields is that they can have an energy density similar to a cosmological constant i.e. have a negative pressure. In the following we restrict our study to scalar fields[1] ϕ, a priori complex in the general case. The Lagrangian density[2] $\mathcal{L}$ for a scalar field is of the form

$$\mathcal{L} \equiv \frac{1}{2}\left(\partial_\mu \phi \partial^\mu \phi\right) - V(\phi). \tag{2.12}$$

[1]Although vector fields are relatively well known (e.g. in electromagnetism), scalar fields remain rather unexplored. But the presence, among other things, in most of the current particles theories of an additional scalar field such as the Higgs is expected.

[2]The Lagrangian (spatial integral of the Lagrangian density) of a dynamical system is a function that contains all the information about the dynamics of a system: in classical mechanics, the Lagrangian is defined as the difference between the kinetic energy of a system and its potential energy. Moreover, if the Lagrangian of a system is known, then the equations of motion of the system may be obtained by a direct substitution of the expression for the Lagrangian into the Euler-Lagrange equation.

In addition, Noether theorem[1] gives the energy-momentum tensor:

$$\mathbf{T}^{\mu\nu} = \partial^{\mu}\phi\partial^{\nu}\phi - \mathbf{g}^{\mu\nu}\mathcal{L} \tag{2.13}$$

From Eq. (1.11) and 2.13, we can write the expression for the energy density and pressure:

$$\rho = \frac{1}{2}\dot{\phi}^2 + V(\phi) + \frac{1}{2}(\nabla\phi)^2 \tag{2.14}$$

$$p = \frac{1}{2}\dot{\phi}^2 - V(\phi) + \frac{1}{6}(\nabla\phi)^2 \tag{2.15}$$

If the field ϕ is homogeneous, $\nabla\phi \sim 0$, and constant in time, $\dot{\phi} \sim 0$, we get $p = -\rho$, cf. Eq. (2.5).

2.3.2 Dynamics equation

We can use the conservation of energy[2], i.e. $T^{\mu\nu}_{;\nu} = 0$, to derive the equation of motion for the field[3] ϕ:

$$\ddot{\phi} + 3H\dot{\phi} - \nabla^2\phi + \frac{\partial V}{\partial\phi} = 0. \tag{2.16}$$

Eq. (2.16) is analytically solvable if the spatial inhomogeneities, i.e. $\nabla^2\phi$, can be neglected and if we make the slow-roll assumption, as illustrated in Fig. 2.3: $|\ddot{\phi}|$ is assumed to be negligible compared to $|3H\dot{\phi}|$ and $|\partial V/\partial\phi|$. Thus, the equation of motion can be rewritten as:

$$3H\dot{\phi} = -\frac{\partial V}{\partial\phi} \tag{2.17}$$

The fundamental condition $V \gg \dot{\phi}^2$, needed to obtain the thermodynamic conditions necessary for the inflation, requires that

$$\epsilon \equiv \frac{1}{16\pi G}\left(\frac{\frac{\partial V}{\partial\phi}}{V}\right)^2 \ll 1. \tag{2.18}$$

Derivative of Eq. (2.18) with respect to ϕ gives also $\partial^2 V/\partial\phi^2 \ll \sqrt{G}(\partial V/\partial\phi)$. Combining these last two equations, we obtain the second slow-roll condition, which reads

$$\eta \equiv \frac{1}{8\pi G}\left(\frac{\frac{\partial^2 V}{\partial\phi^2}}{V}\right) \ll 1. \tag{2.19}$$

[1] This theorem states that any differentiable symmetry of the action, $S = \int \mathcal{L} d^4x$, of a physical system has a corresponding conservation law.

[2] The subscript $_{;\nu}$ stands for the covariant derivative.

[3] It is also possible to find this equation starting from the expression of the action $S \equiv \int d^4\mathbf{r}\sqrt{-g}\mathcal{L}$ and then using the Euler-Lagrange equation.

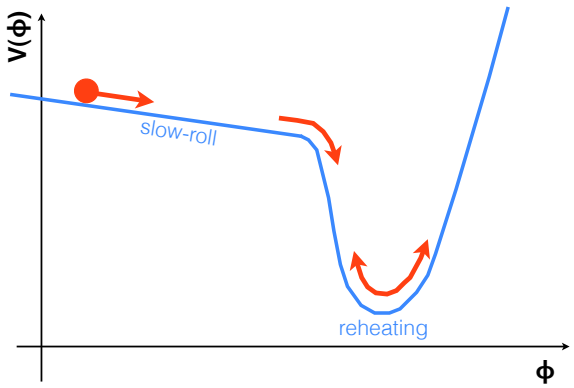

Figure 2.3: Illustration of a possible potential $V(\Phi)$ allowing the field dynamics to verify slow-roll constraints, cf. Eqs. 2.18 and 2.19.

Similar arguments can be constructed for the spatial variables. However, they appear less restrictive, and some terms as

$$\nabla\phi = \frac{1}{a}\nabla_{\text{comoving coord.}}\phi \tag{2.20}$$

increases exponentially during the inflation, which makes spatial perturbations extremely small. This result was one of the most important motivations for the development of inflation theory — it could offer a solution to the problem of monopoles, see Kolb and Turner (73).

2.3.3 End of inflation

Although spatial derivatives of the scalar field are negligible, this is not necessarily true for the time-derivatives. Even if they have a very low value at the beginning, their relative importance increases with ϕ rolling to the minimum of the potential $V(\phi)$. Sooner or later, as depicted in Fig. 2.3, it is possible to obtain the conditions $|\epsilon| \sim 1$ and $|\eta| \sim 1$, which corresponds to the end of the inflationary period. The field does not abruptly stop but rather oscillates around the minimum, and is damped by the $3H\dot{\phi}$ resistance term, cf. Eq. (2.16). As introduced in paragraph 2.2.3, these oscillations cause the reheating phenomenon, during which photons and matter particles are created, and thus maintain an energy density similar to the one initially set for the inflation.

2.4 Inflation models

Contemporary ideas of inflation are actually quite different from the original proposition made by Guth (57). Nowadays, models are usually called inflationary chaotic

models: those are general models in which the field evolves independently from the minimum potential, e.g. Linde (87), and can, among other things, allow for the existence of primordial chaos, where the initial conditions can vary without any important consequences.

2.4.1 Some examples

Parameters of these theories are simply constrained by the desire for an inflationary period, i.e. $p < -\rho/3$, Eq. (2.3): this flexibility allows for a wide variety of models. This is even wider when considering different universes than the de Sitter one: it is sufficient that the cosmos enters a phase of supra-luminous expansion while respecting the equation of state $p < -\rho/3$. In the case of a pure static field, i.e. $p = -\rho$ (the equation of state for the cosmological constant), for a deviation from a de Sitter universe, it is necessary that $\dot{\phi}$ becomes much more important. For example, this could correspond to a much steeper potential — the slope remains determined by the time dependence we want to impose on the scale factor a.

I quote below three typical cases, e.g. Peacock (104):

- the polynomial inflation: if we take $V(\phi) \propto \phi^\alpha$ with $\alpha = 2$ or 4, the scale factor will have an exponential behavior.

- the power-law inflation: if $a(t) \propto t^p$ with $p > 1$, this requires the potential V to be set as
$$V(\phi) \propto \exp\left[\sqrt{\frac{16\pi G}{p}}\phi\right] \tag{2.21}$$

- the so-called intermediate inflation: we set
$$a(t) \propto \exp\left[\left(\frac{t}{t_0}\right)^q\right], \tag{2.22}$$
with $q > 1$. In the slow roll approximation, the potential is $V(\phi) \propto \phi^{-\beta}$ with $\beta \equiv 4(q^{-1} - 1)$.

There are of course many other models, see e.g. Mukhanov (94).

2.4.2 Constraints on the inflation parameters

As written in paragraph 2.2.2, inflation models generally require a number of e-folding $N_e \geq 60$, cf. Eq. (2.11). We can show that, under the slow roll approximation, the number of e-folding N_e between a starting ϕ_i and a final state ϕ_f can be written as
$$N_e = \int H dt = -8\pi G \int_{\phi_i}^{\phi_f} \frac{\partial V/\partial\phi}{V} d\phi. \tag{2.23}$$

Thus, for any reasonable potential, we obtain, in order of magnitude, $N_e \sim \phi_i^2 G$. And the condition for inflation, $N_e \gg 1$, becomes

$$\phi_i \gg \frac{1}{\sqrt{G}}. \tag{2.24}$$

2.5 Generation of perturbations, inflation relics

Until now, I have only considered an idealized universe, homogeneous and isotropic, and in this section, I present deviations from this modeling. In cosmology, these inhomogeneities should have grown with time because of gravity, and this simple fact implies that they should have been much smaller in the past. Consequently, at least in the early universe period, we could treat those as linear perturbations. This assumption stops being valid on small scales in the recent history of the universe but remains quite appropriate to describe the fluctuations of the CMB as seen on the last scattering surface.

In this section, I focus on the perturbations of the inflaton field ϕ and show how the accelerated expansion during inflation converts its initial vacuum quantum fluctuations into classical cosmological perturbations.

2.5.1 Dynamic of a massless scalar field in de Sitter space-time

First, let us remind the de Sitter metric, Eq. (1.2), in the case of an exponential expansion i.e. $a(t) = e^{Ht}$:

$$ds^2 = -dt^2 + e^{Ht} d\mathbf{r}^2. \tag{2.25}$$

To simplify the next equations, it turns out that it is convenient to use, instead of the cosmic time t, the conformal time τ, which is negative and goes from $-\infty$ to 0, defined as

$$\tau \equiv \int \frac{dt}{a(t)}, \tag{2.26}$$

leading in our case to

$$\tau = -\frac{e^{Ht}}{H} = -\frac{1}{aH}, \tag{2.27}$$

so that the scale factor in terms of τ reads

$$a(\tau) = -\frac{1}{H\tau}. \tag{2.28}$$

Using Eq. (2.26), we can write Eq. (2.25) as

$$ds^2 = a^2(\tau) \left[-d\tau^2 + d\mathbf{r}^2\right]. \tag{2.29}$$

Let us have a look at the equation of dynamics satisfied by the perturbations $\delta\phi$ during the inflation. The equation of motion of the inflationary field, cf. Eq. (2.16) reads

$$\ddot{\phi} + 3H\dot{\phi} - \nabla^2\phi + \frac{\partial V}{\partial \phi} = 0, \tag{2.30}$$

and let us assume that $\delta\phi = \delta\phi(k,t)$ can be seen as a plane wave perturbation with a comoving wave number $k \equiv k_{\rm comoving} = a(t)k_{\rm physical}$, and with an amplitude A such that

$$\delta\phi \equiv A\, e^{i\mathbf{k}\cdot\mathbf{x} - \frac{ikt}{a}}. \tag{2.31}$$

Under the slow-roll approximation, we can assume that $\partial V/\partial\phi$ is constant and the perturbation field $\delta\phi$ satisfies the following equation,

$$\ddot{\delta\phi} + 3H\dot{\delta\phi} - \left(\frac{k}{a}\right)^2 \delta\phi = 0. \tag{2.32}$$

By introducing the new variable $v = v(k,t)$ as:

$$v \equiv a\,\delta\phi, \tag{2.33}$$

Eq. (2.32) reads, in Fourier space,

$$\ddot{v}_k + \left(k^2 - \frac{\ddot{a}}{a}\right) v_k = 0. \tag{2.34}$$

This is simply the equation of motion for an oscillator with a time-dependent mass corresponding also to the standard wave equation for a field evolving in an expanding universe, with an effective pulsation ω given by

$$\omega \equiv \sqrt{k^2 - \frac{\ddot{a}}{a}}. \tag{2.35}$$

We can solve this equation to find the quantum fluctuations resulting from the inflationary period. For that purpose, it is usual to quantify this harmonic oscillator: in a flat space of de Sitter type, we can decompose the field on different k modes:

$$v_k(\tau) = u_k(\tau)a_k + u_k^*(\tau)a_k^\dagger \tag{2.36}$$

where the $a_k^\dagger$ and a_k are creation and annihilation operators, satisfying the usual commutation rules

$$a_k\,|0\rangle = 0 \tag{2.37}$$

$$[a_k, a_{k'}] = \left[a_k^\dagger, a_{k'}^\dagger\right] = 0 \tag{2.38}$$

$$\left[a_k, a_{k'}^\dagger\right] = \delta_k{}^{k'}. \tag{2.39}$$

The variance of the field $\delta\phi$ can be written as

$$\begin{aligned}
\left\langle 0 \left| \delta\phi_k^\dagger \delta\phi_k \right| 0 \right\rangle &= \frac{1}{a^2} \left\langle 0 \left| v_k^\dagger v_k \right| 0 \right\rangle \text{ using Eq. (2.33)} \\
&= \frac{1}{a^2} \left\langle 0 \left| \left(a_k^\dagger u_k^* + a_k u_k \right) \left(u_k a_k + u_k^* a_k^\dagger \right) \right| 0 \right\rangle \text{ from Eq. (2.36)} \\
&= \frac{1}{a^2} \left| u_k^2 \right| \left\langle 0 \left| a_k a_k^\dagger \right| 0 \right\rangle \\
&= \frac{|u_k|^2}{a^2}. \qquad (2.40)
\end{aligned}$$

To solve Eq. (2.32), we must find the values of u_k for different expansion regimes, and we will consider the problem in two relevant regimes, above and below horizon, i.e. $k/a \gg H$ and $k/a \ll H$ respectively.

On the one hand, how does the amplitude of a given mode behave when the wavelength crosses the horizon H^{-1}? In the de Sitter case, one can solve explicitly Eq. (2.34) using the fact that $\ddot{a}/a = 2/\tau^2$ and the general solution is given by

$$u_k = \sqrt{\frac{1}{2k}} e^{ik\tau} \left(1 - \frac{i}{k\tau} \right). \qquad (2.41)$$

We can see from Eq. (2.41) that, at early times such that $aH/k \ll 1$, i.e. at the time when the quantum fluctuations dominate, the scale factor a is nearly constant.

On the other hand, if $aH \gg k$, the fluctuations amplitude is frozen and fixed to the value

$$\begin{aligned}
P_{\delta\phi}(k) &\equiv \left\langle 0 \left| \delta\phi_k^\dagger \delta\phi_k \right| 0 \right\rangle \qquad (2.42) \\
&= \frac{|u_k|^2}{a^2} \qquad (2.43) \\
&\approx \frac{1}{2a^2 k^3 \tau^2} \text{ from Eq. (2.41) if aH} \gg \text{k} \qquad (2.44) \\
&= \frac{H^2}{2k^3}. \qquad (2.45)
\end{aligned}$$

A spectrum in which $k^3 P_{\delta\phi}(k)$ is constant with respect to k is an example of a scale-invariant spectrum.

Thus, the initial quantum fluctuations of the vacuum have been turned into classical fluctuations (because exiting the Hubble radius) which should have imprinted the universe on large scales.

2.5.2 Scalar perturbations

Results of the previous paragraph are obtained in the case of a toy model: realistic computation of the perturbations in an expanding universe should be done in a general FLRW universe. In this case, the field ϕ generates the expansion and we should look at the effect of the $\delta\phi$ on the metric. However, by analogy with the simple model detailed in paragraph 2.5.1, we can understand that inflation is a mechanism enlarging quantic perturbations $\delta\phi$ so that they become classical.

One can show that the relation between the scalar perturbations spectra P_S and $P_{\delta\phi}$ are given by, e.g. Langlois (78), Lidsey et al. (86), Stewart and Lyth (129):

$$P_S(k) \equiv \frac{1}{(2\pi)^2} \left(\frac{H^4}{\dot{\phi}^2}\right)\Bigg|_{k=aH}. \tag{2.46}$$

This spectrum can be exactly scale invariant if H and $\dot{\phi}$ are constant in time. We have already seen that the Hubble parameter is nearly constant during the inflationary period. The invariance can be broken by changing $\dot{\phi}$, which is specific to each inflationary model that predicts deviations to the scale invariant spectrum, see Liddle and Lyth (85).

Eq. (2.46), describing the spectrum for cosmological scalar perturbations generated from vacuum fluctuations during a slow-roll inflation phase, is one of the main predictions of inflationary models. Following Lyth and Liddle (88) and Leach et al. (81), deviations from a scale-invariant behavior are modeled as

$$k^3 P_S(k) = A_s k^{n_s - 1} \tag{2.47}$$

with

$$n_s \equiv 1 - \frac{d\log P_S}{d\log k} \tag{2.48}$$

$$\sim 1 - 6\epsilon + 2\eta. \tag{2.49}$$

2.5.3 Gravitational waves

In addition to scalar perturbations, inflationary scenario predicts primordial gravitational waves which are also generated from the vacuum quantum fluctuations.

Any very light particles, follow the spectrum given in Eq. (2.45). When the excited modes of such a field come back into the horizon, they spread like particles: excitations of the de Sitter space eventually become a source of creation of particles, e.g. Kolb and Turner (73). In particular, one of the examples that interests us is the graviton. It corresponds to the mode of propagation associated with the transverse - traceless tensor of the metric perturbations. Gravitons behave like a weakly coupled scalar field with

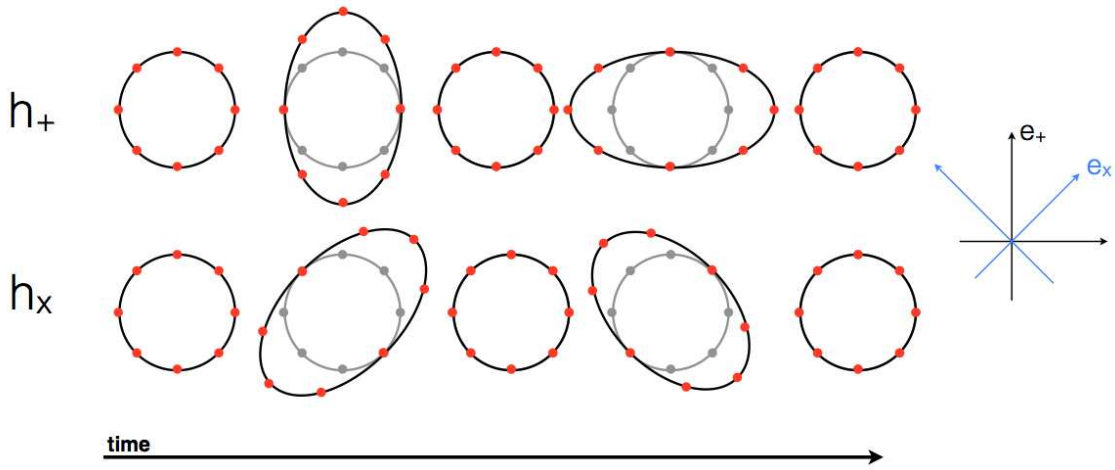

Figure 2.4: Scheme illustrating the effect of a gravitational wave on a circular ring of free particles. The wave direction is assumed to be orthogonal to the plan containing the particles. Upper (lower) part shows the effect of a wave polarized along the $\mathbf{e}_+$ ($\mathbf{e}_\times$) directions, as shown on the right of the figure.

two degrees of freedom: we consider that graviton is formed of two scalar fields ϕ_+ and $\phi_\times$ satisfying

$$h_+ = \sqrt{16\pi G}\phi_+ \tag{2.50}$$
$$h_\times = \sqrt{16\pi G}\phi_\times. \tag{2.51}$$

As illustrated in Fig. 2.4, h_+ and $h_\times$ are related to the dimensionless tensor of the metric perturbation $\mathbf{h}^i{}_j$ defined as

$$\mathbf{h}^i{}_j \equiv h_+\mathbf{e}_+ + h_\times\mathbf{e}_\times, \tag{2.52}$$

where $\mathbf{e}_+$ and $\mathbf{e}_\times$ are the two polarization tensors corresponding to the two modes of the graviton.

The spectrum of gravitational waves $P_T(k)$ can be written as follows

$$P_T(k) = \left(\frac{H}{2\pi}\right)^2\Bigg|_{k=aH} \tag{2.53}$$

Since H is slowly varying, P_T has an approximately scale-invariant behavior. We can choose to model the small dependence of scale by the following power law i.e.

$$k^3 P_T(k) = A_T k^{n_T}. \tag{2.54}$$

Similarly to Eq. (2.49), we set

$$n_T \equiv \frac{d\log P_T}{d\log k} \tag{2.55}$$
$$\sim -2\epsilon. \tag{2.56}$$

On each scale, the amplitudes $h_{+,\times}$ of the primordial gravitational waves remain constant until they approach the horizon. Once they passed it, they begin to evolve. Their oscillations start to decrease progressively after the passage sub-horizon, corresponding to the common redshift phenomenon.

Using the expressions for the amplitudes and spectral indices in terms of the slow roll parameters, we are able to solve for the potential and its first two derivatives and thereby use observations to constrain the form that this potential can take. We have,

$$V \sim \frac{P_T}{G^2} \tag{2.57}$$

$$r \equiv \frac{P_T}{P_S} \sim -16 n_T, \tag{2.58}$$

where we defined r as the tensor-to-scalar ratio, directly related to the energy scale of inflation V through

$$V^{1/4} = 1.06 \times 10^{16} \left(\frac{r}{0.01}\right)^{1/4} \text{ GeV}. \tag{2.59}$$

I explain in the next chapter that tensor perturbations create specific signatures on the CMB, including its polarization, and which can be parametrized with the tensor-to-scalar ratio r. The estimation, through the observation, of the latter is therefore a way to probe the existence of inflation.

Chapter 3

CMB anisotropies and their characterization

The CMB has a remarkably high level of isotropy on the sky, confirming the cosmological principle. The largest temperature anisotropy is a dipole pattern due to the Earth's motion relative to the CMB reference frame. In addition, as explained in the previous chapter, we expect the existence of weak fluctuations of matter, generated by inflation, already present at the time of recombination. Those tiny inhomogeneities, of a relative level of $\sim 10^{-5}$, were filling the universe and be interpreted as the seeds for the formation of galaxies and other large cosmic structures. Those perturbations evolved completely differently before and after recombination. Before recombination (at $z \sim 1100$, see section 1.3), radiation and matter (electrons, protons) were tightly coupled through Compton and Thomson scattering and formed a baryon-photon fluid. After recombination, photons free-streamed from the Last Scattering Surface[1] (LSS) and reach us today.

A few decades ago, cosmologists established that the processes invoked to account for the formation of cosmic structures would indeed lead to the existence of intensity fluctuations in the CMB to a detectable level. In 1989, the COBE satellite was launched to observe the CMB and succeeded in providing the first power spectrum of CMB anisotropies, see Fig. 3.1. Then, the WMAP (2003-2011) and Planck (2009-2012) satellites were launched and observed those small fluctuations with unprecedented sensitivities and accuracy.

In this chapter I briefly review the physics behind the CMB anisotropies, both in intensity (section 3.1) and polarization (section 3.2). In section 3.3, I introduce the statistical tools used to analyze the CMB maps on the sphere and present the

[1] The set of points in space and time where photons began to travel freely is called the last scattering surface.

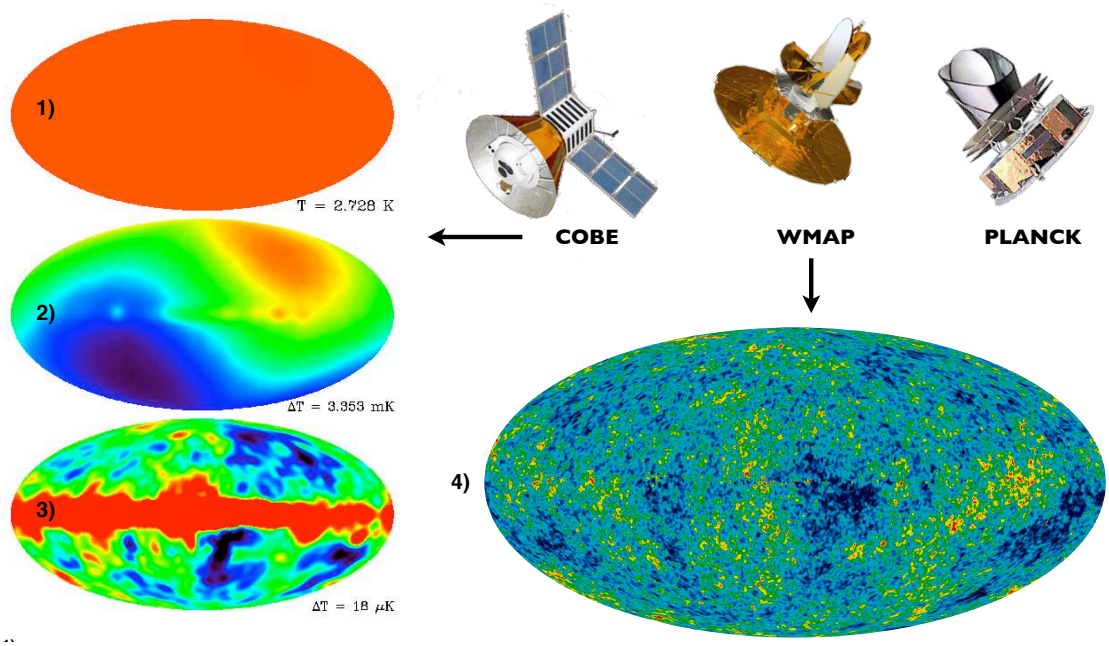

Figure 3.1: Image composed of maps from the COBE experiments (left column) and the 5-year map from WMAP (bottom right) **4)**, in which the signal from our Galaxy was subtracted using the multi-frequency data (this image shows a temperature range of ± 0.2 K). COBE-DMR CMB observation at 53 GHz can be decomposed as a monopole with an amplitude temperature of 2.728 K (**1)**), a dipole across the sky which is the largest anisotropy due to Solar system's motion with respect to the CMB frame (**2)**) and the other modes of fluctuations which are at the 10^{-5} level (**3)**).

quantitative predictions for the anisotropies properties as well as their connection to the cosmological parameters of the commonly accepted ΛCDM model (section 3.4).

3.1 Anisotropies in intensity

Inflation offers an explanation for the CMB anisotropies at the 10^{-5} level and below. In fact, as explained in the previous chapter, inflationary models predict the existence of perturbations with specific scale invariant power spectrum, cd. Eq. (2.45). Quantum fluctuations in the primordial energy field generated spatial mass density variations across space. These perturbations affect the density of the photons-baryons plasma and consequently give specific signatures on the LSS.

It is usual, in observational cosmology, to switch from intensity to antenna temperature, which is the quantity CMB experiments measure. Both quantities are proportional in the Rayleigh-Jeans approximation, valid in the low frequency range of the CMB Planck distribution $B_\nu(T)$:

$$B_\nu(T) \equiv \frac{2h\nu^3/c^2}{e^{\frac{h\nu}{kT}} - 1} \tag{3.1}$$

$$\approx \frac{2h\nu^3}{c^2} \times \frac{kT}{h\nu} \quad \text{for } \nu \ll \frac{kT}{h} \tag{3.2}$$

$$= \frac{2kT\nu^2}{c^2} \tag{3.3}$$

CMB intensity anisotropies are then translated as an "effective temperature", T_{CMB}, imprinted in the CMB map at the recombination time: this it what we call temperature anisotropy. In addition, polarization anisotropies are also imprinted through Thomson scattering, as described in section 3.2.

We usually consider different types of anisotropies of the CMB depending on their amplitude (primary or secondary, respectively paragraphs 3.1.2 and 3.1.2) and the mechanism for generating them (large scale or acoustic fluctuations, respectively paragraphs 3.1.3 and 3.1.4).

3.1.1 Primary anisotropies

As the photons are still coupled to electrons, they keep the footprint of the fluctuations of the matter through both their temperature (Compton scattering) but also their polarization (Thomson scattering). The photons "effective temperature" is lead by three dominant effects, called primordial anisotropies:

- **gravitational perturbations (the so-called Sachs-Wolfe effect)** – when a photon escapes from an under-density (or over-density), it has more (or less)

energy and its wavelength is shifted towards blue (or red). Over-densities (lower densities) of matter correspond to cold (hot) spots in the CMB. For a variation of the gravitational potential $\Delta\Phi$, the relative variation of temperature on the CMB can be written as

$$\frac{\Delta T}{T} \sim \frac{\Delta\Phi}{3}. \tag{3.4}$$

- **intrinsic perturbations (adiabatic)** – quantum fluctuations of the vacuum energy lead to variations in the distribution of matter density ρ_m. The coupling between matter and radiation increases the energy of radiation (i.e. temperature) in the high density regions. Then any density fluctuation is associated to a temperature fluctuation $\frac{\Delta T}{T}$,

$$\frac{\Delta T}{T} = \frac{1}{3}\frac{\Delta\rho}{\rho}. \tag{3.5}$$

- **Doppler** – the primordial plasma velocity causes a Doppler shifting of the CMB photons. This shift is proportional to the velocity v of the fluid motion, i.e.

$$\frac{\Delta T}{T} \propto v. \tag{3.6}$$

  This effect vanishes along the line of sight for scales smaller than the thickness of the LSS. Indeed, at first order, a photon passing through the fluctuation will experience the same shifting in one direction and then while escaping.

3.1.2 Secondary anisotropies

Secondary anisotropies are added to these original primary anisotropies. Generally lower in relative intensity than the primary, they correspond to the rare interactions that the CMB photons can have between the LSS and the detection. These new anisotropies are in part due to the change in the gravitational potential but also to interactions, through Compton scattering with electrons from ionized gas, see Hu and Sugiyama (65).

- **Integrated Sachs-Wolfe effect (ISW)** – it describes the effect of gravitational potential defects integrated along the photon path. Because of the speed of light compared to the characteristic scales of variations of the potential, this effect is limited in amplitude. However, this effect can reach $\Delta T/T \sim 10^{-6}$ at large scales.

- **Gravitational Lensing** – geodesics are bent by over-densities such as large scale structures. Therefore, it induces a distortion of the observed CMB map at all scales (the intensity power spectrum is smoothed at the percent level and reduce the amplitude high order peaks) and also a leakage between E and B polarizations, see section 3.3.2.

- **Rees-Sciama effect** – this effect is due to the fact that potential wells become more important with time: photons going through them gain energy while falling into the well but loose some when climbing out of it. If the well has became deeper during this travel, the energy balance is negative. We expect variations of $\Delta T/T \sim 10^{-7}$, mostly due to the non-linear period of the structures evolution.

- **Sunyaev-Zel'dovich effect (SZ)** – it corresponds to the inverse Compton scattering of CMB photons on electrons from ionized gas of galaxies clusters. The thermal agitation of electrons in the gas modifies locally the CMB photons spectrum (they get hotter): this is called the thermal SZ. If the cluster is in motion, a kinetic phenomenon created by Doppler effect is added to this secondary anisotropy: this is called kinetic SZ. Moreover, diffusion onto the free electrons of the local universe generates a diffuse contamination at high angular scales: those anisotropies could reach the $\Delta T/T \sim 10^{-4}$ level for $\ell > 100$. This corresponds to one of the dominant contaminant of the CMB, as mentioned also in section 9.4.

- **Reionization** – it corresponds to the early period where the universe got ionized a second time after the recombination. During this phase which happened during the first stars formation, the free electrons interact again with the photons through Compton scattering. The effect on CMB photons can be seen at all scales.

Moreover, we will see in chapter 9 that foregrounds are a very important source of diffuse contamination of the CMB map.

3.1.3 Large scale anisotropies, $\Delta\Theta > \Theta_H$

Anisotropies at scales $\Delta\Theta$ larger than the horizon Θ_H are relatively simple to understand because at the time of recombination, the density inhomogeneities are outside the Hubble radius, as illustrated in Fig. 3.2. We can therefore ignore any pressure force of the plasma during the gravitationally-driven evolution of the photon-baryon inhomogeneities. Let us consider a photon emerging from an overdensity $(\Delta\rho/\rho)$ of size R. The term SW, Eq. (3.4), is of order

$$\frac{\Delta T}{T} = \frac{G\Delta M}{R} \sim G\bar{\rho}\left[\frac{\Delta\rho}{\bar{\rho}}\right]_R \frac{4\pi R^3}{3R} \propto \left[\frac{\Delta\rho}{\bar{\rho}}\right]_R R^2. \tag{3.7}$$

And for a matter dominated universe, the last expression is independent of time because

$$\Delta\rho \propto a \tag{3.8}$$

$$R^2 \propto a^2. \tag{3.9}$$

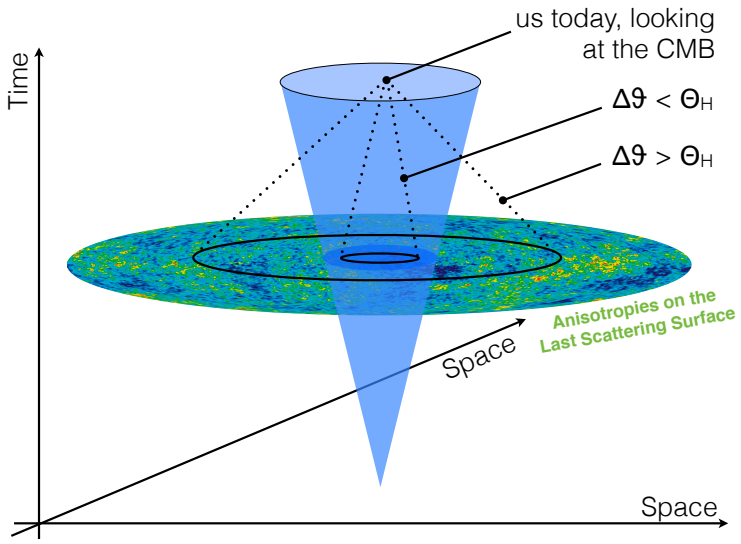

Figure 3.2: Scheme illustrating the geometry of the typical angular scales $\Delta\theta$ above and below the Hubble radius Θ_H.

If fluctuation spectrum is scale-invariant, $\Delta\rho/\rho \propto R^{-2}$, then $\Delta T/T$ is scale independent. Taking $R = d_H$, the hubble radius, we see that the SW anisotropies give directly the density fluctuations, Δ_H, at the entry of the Hubble radius,

$$\frac{\Delta T}{T}(\mathrm{SW}) \sim \Delta_H. \tag{3.10}$$

In addition, the Doppler term could be expressed as

$$\frac{\Delta T}{T}(\mathrm{Doppler}) \sim \Delta_H \frac{\Theta_H}{\Delta\Theta}, \tag{3.11}$$

and the intrinsic temperature fluctuations as

$$\frac{\Delta T}{T}(\mathrm{intrinsic}) \sim \Delta_H \frac{\Theta_H^2}{\Delta\Theta^2}. \tag{3.12}$$

Because of the different values of $\Theta_H/\Delta\Theta$, the SW effect dominates the anisotropies for $\Delta\Theta \gg \Theta_H$. The spectrum is independent of angles if the density inhomogeneities are scale invariant, as predicted by the inflationary models. If this is the case, we expect a flat spectrum at large angles which increases slowly when the scale approaches Θ_H and the Doppler and intrinsic effects become important. As will be illustrated in section 3.4, measurements indicate that this is the case: this is a strong argument showing that the primordial fluctuations are adiabatic and scale invariant.

3.1.4 Acoustic oscillations, $\Delta\Theta < \Theta_H$

At small angular scale, i.e. for $\Delta\Theta < \Theta_H$, distances correspond to sub-Hubble scales and we have to consider the pressure force on the photon-baryon plasma. Indeed, photons and baryons remain tightly coupled as a perfect fluid until recombination. The dynamics equations are somewhat complicated but the resulting phenomenology is well understood, e.g. Hu et al. (66). We have seen that fluctuations in energy density create fluctuations in the local gravitational potential and generate potential wells. At the opposite of a compression of the fluid in the potential wells, there is a rarefaction in the maximum potential. Furthermore, the fluid pressure acts as an opposite force for the gravity, and oscillations start governing the dynamics of the fluid.

Therefore, what we observe is the imprint of these acoustic oscillations contained in the CMB temperature. Compression of a gas increases its temperature and, consequently, the CMB is locally hotter in the regions of compression due to acoustic oscillations and colder in the areas of rarefaction. Initially, the photon-baryon fluid is compressed in the potential wells created by cold dark matter. Compression continues until the fluid pressure resists compression and starts to expand. The expansion then continues until gravitational starts a new compression and so on.

Sound waves stop propagating at recombination when baryons and photons decoupled. Modes that reach the maximum of their oscillations (maximum compression or rarefaction in the potential well) at the recombination correspond to large fluctuations in temperature. The temperature fluctuation in a potential well for a mode with a given wavenumber k will oscillate with the fluid, and it will get compressed and expanded.

Mathematically, the wavenumber of the fundamental mode k_0 is equal to π/sonic horizon. We know that there is a mode with a wavenumber $k_1 = 2 \times k_0$ which has just enough time to compress and expand before recombination. And so on with $k_n = (n+1) \times k_0$, $n \in \mathcal{N}$: these modes represent the first, second, ..., n^{th} acoustic peaks respectively. These latter are harmonics of the fundamental scale (associated to the mode k_0) given by the distance over which sound can travel before recombination. As illustrated in Fig. 3.3, oscillations continue until the time of recombination t_{rec}, when the photons freely escape from the potential wells. The nature of the anisotropies created by a given oscillation mode depends on the oscillation phase, $\phi_{\rm rec}(k)$, at the time of recombination:

$$\phi_{rec}(k) = \int_0^{t_{rec}} \omega_k(t)dt = ka_0 \int_0^{t_{rec}} \frac{c_s(t)dt}{a(t)} \tag{3.13}$$

The phase $\phi_{\rm rec}(k)$, defined for each mode k, determines the relative importance of gravitational redshift, Doppler effect, and effect of intrinsic temperature. We can distinguish three extreme cases:

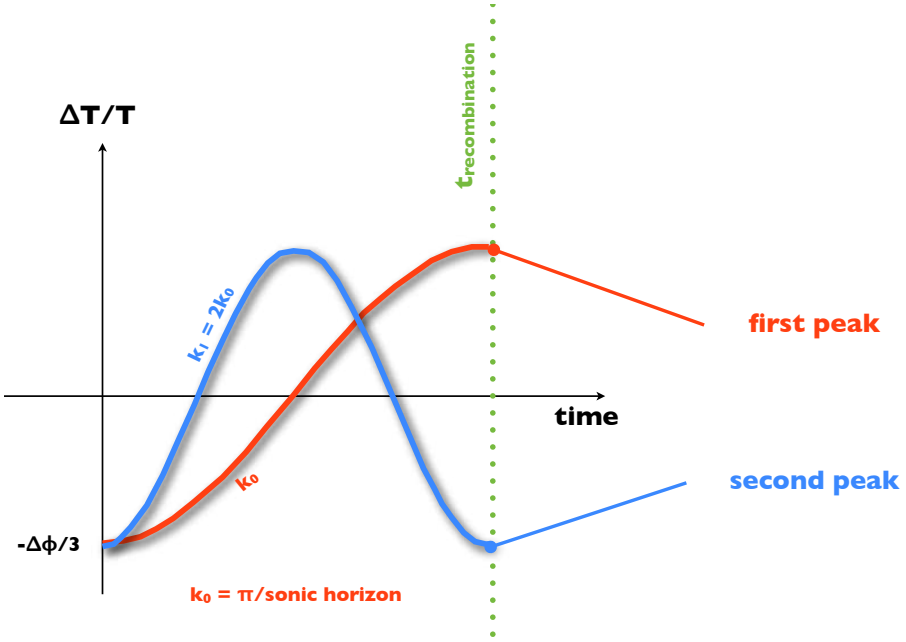

Figure 3.3: Scheme illustrating the evolution of the two first modes $k_0 = \pi$/sonic horizon and $k_1 = 2\,k_0$.

- $\phi_{\rm rec}(k) = n\pi$, for $n = 1, 3, 5,$ ...: the fluid is highly compressed in the potential well. The observed radiation temperature is maximal for photons exiting wells due to the high intrinsic temperature in the wells;

- $\phi_{\rm rec}(k) = n\pi$, for $n = 0, 2, 4,$ ...: the fluid is only moderately compressed in the potential well. The observed photon temperature is minimal for photons exiting wells because of the gravitational redshift;

- $\phi_{\rm rec}(k) = n\frac{\pi}{2}$, for $n = 1, 3, 5,$ ...: effects of intrinsic and gravitational redshift are compensated.

3.2 Polarization anisotropies

Polarization of the CMB photons is due to Thomson scattering with electrons in the primordial plasma[1]. By symmetry, we can show that only the quadrupole anisotropy

[1]In the low-energy limit, the electric field of an incident electric wave accelerates the charged particle, here an electron, causing it to emit radiation at the same frequency as the incident wave, and thus scatter this latter. The particle moves in the direction of the oscillating electric field, resulting in an electromagnetic dipole radiation. The moving particle radiates most strongly in a direction perpendicular to its motion and that radiation will be polarized along the direction of its motion.

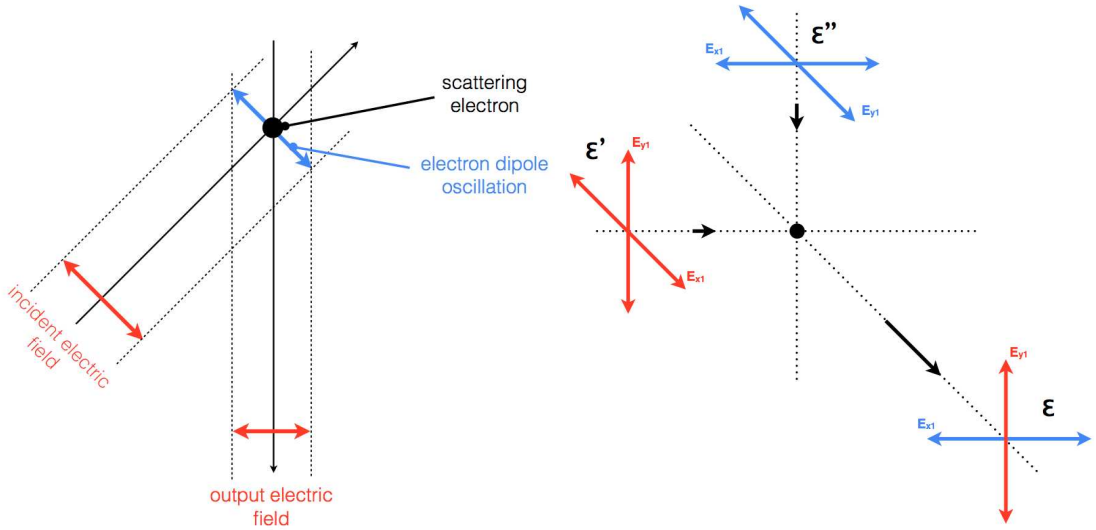

Figure 3.4: Illustration of the Thomson scattering on an electron (black) in the case of a single linearly polarized incident beam (**left panel**) and in the case of two incident beams (**right panel**).

of an incident radiation on an electron can produce polarization. This is illustrated in the left panel of Fig. 3.4 and is explained by the Thomson scattering differential cross section of an electron (assumed at rest) illuminated by an unpolarized photon flux:

$$\frac{d\sigma}{d\Omega} = \frac{3\sigma_T}{8\pi} \left|\epsilon \cdot \epsilon'\right|^2 \tag{3.14}$$

The scalar product $|\epsilon \cdot \epsilon'|$ implies the absorption of the components parallel to the polarization of the incident flux. For instance, as illustrated in the right panel of Fig. 3.4, the observer sees a transmitted polarization corresponding to the vertical part of ϵ' and horizontal of ϵ''. If the flow is less intense in one direction, then the received radiation is linearly polarized. Let us consider the following different cases:

- if the incident radiation is isotropic (i.e. monopole) then the total resulting polarization for the observer is zero;
- if the incident intensity of the incident radiation follows a dipole pattern then each component of the polarization is compensated and there is no resulting polarization;
- if the incident intensity is quadrupolar, then there is no more compensation and a non zero resulting polarization appears.

This reasoning, done in the 2-d case, can be generalized to all directions. So from a non-polarized incident flux but having an quadrupolar anisotropy, a linearly polarized radiation can be generated.

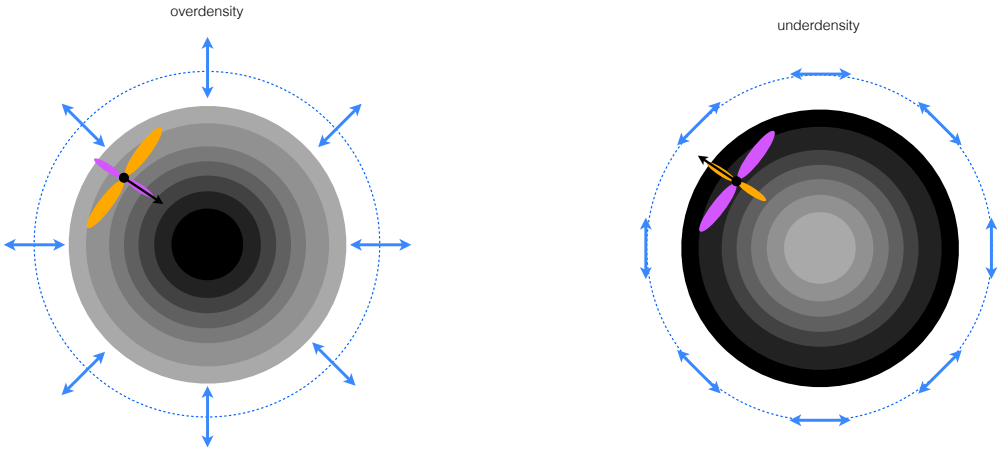

Figure 3.5: Illustration of an electron falling into an over-density (**left panel**) or going away from an under-density (**right panel**). Resulting polarization patterns are shown on the external blue dashed circle. The electron and its speed are depicted in black and the associated quadrupole is depicted in orange (hot direction) and purple (cold one).

There are three types of perturbations, related to three different physical sources, that give rise to quadrupole anisotropies: the scalar (from density fluctuations), the vector (due to vortices) and the tensor anisotropies (related to the passage of gravitational waves):

- **scalar perturbations** – electrons fall into potential wells, corresponding to matter over-densities, illustrated in Fig. 3.5, and do so as more rapidly as they are close the center. Let us consider an electron near an over-density. In its frame, the other plasma particles aligned on the same radius (in the front and in the back of the electron) go away. In contrast, those which belong to the same isocontour of density (left and right sides of the electron) come closer – since isocontours are concentric. The same reasoning applies to matter under-densities. This phenomenon produces quadrupole anisotropies on the LSS.

- **vector perturbations** – movements of vorticies in the primordial plasma can produce quadrupole anisotropies. They are not necessarily related to density fluctuations. However, in most of the inflationary models, vector perturbations are negligible.

- **tensor perturbations** – a gravitational wave passing through a density fluctuation changes the shape of the potential well. Density contours are no longer circular but become elliptical, thus forming quadrupole perturbations and loosing their symmetry properties.

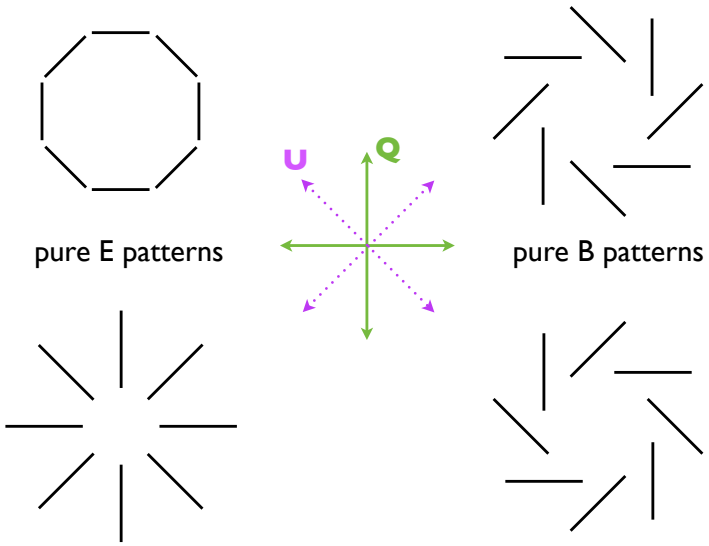

Figure 3.6: Illustration of pure E- (**left**) and B-patterns (**right**) which are a combination of Stokes parameters Q and U. In the middle is the basis for these latter which are introduced in section 3.3.2.

We usually decompose the polarization patterns as seen on the LSS into two geometrical components named E- and B-modes, which are combination of the Stokes parameters Q and U (see section 7.1 for their definition). We will formally introduced the E and B description in section 3.3.2, but one has to notice that this decomposition allows to distinguish physical causes generating those geometrical patterns: in fact, density or scalar perturbations (see Fig. 3.5) generate parallel polarization and therefore generate only E-modes polarization. Contrarily, B-modes can only be generated with gravitational waves (see Fig. 2.4) produced during inflation. These anisotropies, named primordial B-modes, are a smoking gun for inflationary models, see chapter 4.

In addition to these primordial anisotropies, large scale structures between us and the LSS induce a leakage between E- and B-modes. Statistical description and quantitative expectations for this effect are explained in section 3.3.2.

3.3 Statistical analysis of the observed anisotropies

In order to exploit the intensity map of the CMB, $T(\theta, \phi)$, or the polarization information $\{Q(\theta, \phi), U(\theta, \phi)\}$ and compare it with some theoretical predictions, we need statistical tools and their associated formalism.

3.3.1 Intensity

For the purposes of a statistical comparison to the perturbation quantity δ_k^2, the observed CMB temperature distribution on the sky, $T(\theta, \phi)$, is expanded as a series of spherical harmonics Y_ℓ^m, illustrated in Fig. 3.7, with amplitudes $a_{\ell m}$ which are measures of the level of anisotropy present as a function of multipole,

$$T(\theta,\phi) = a_{00} + \sum_{-1\leq m\leq 1} a_{1m}Y_{1m} + \sum_{\ell\geq 2,m} a^T_{\ell m}Y_{\ell m}(\theta,\phi) \tag{3.15}$$

$$= \sum_{\ell=0}^{\infty}\sum_{m=-\ell}^{\ell} a^T_{\ell m}Y^m_\ell(\theta,\phi) \tag{3.16}$$

where θ and ϕ are the usual spherical coordinates and ℓ is the spherical harmonic multipole number. The first term of Eq. (3.15) corresponds to the CMB monopole we described earlier and the second term corresponds to the dipole, which is due to the peculiar velocity of the Earth with respect to the LSS frame. The direction of this velocity gives the preferred direction from which we usually measure the polar angle θ. The temperature is a real quantity, which implies that

$$a^*_{\ell m} = (-1)^m a_{\ell m}. \tag{3.17}$$

The sum over m and $\ell \geq 2$, third term of Eq. (3.15), describes the temperature variations on angular scales $\Delta\Theta$ such as

$$\ell \sim \frac{\pi}{\Delta\Theta}. \tag{3.18}$$

ℓ is called multipole and is the analogue on the sphere of the module of the wave vector $\mathbf{k}$ in an usual 2-d Fourier analysis. In order to describe statistically the anisotropies of the CMB, we usually calculate the angular power spectrum, C_ℓ^{TT}, of the temperature variations. To estimate the this power spectrum, we assume that the distribution of the coefficients $a^T_{\ell m}$ is Gaussian with a variance C_ℓ^{TT}. Therefore the power spectrum contains all the information about temperature anisotropies:

$$\left\langle a^T_{\ell m}\right\rangle = 0 \tag{3.19}$$

$$\left\langle a^T_{\ell m}a^T_{\ell' m'}\right\rangle = C_\ell^{TT}\,\delta_\ell^{\ell'}\,\delta_m^{m'} \tag{3.20}$$

This last equality is obtained thanks to the fact that the universe is isotropic and therefore has no preferred direction (i.e. no dependence on m) for the statistical properties of the anisotropies. Quantitative predictions for the power spectrum are given in section 3.4.

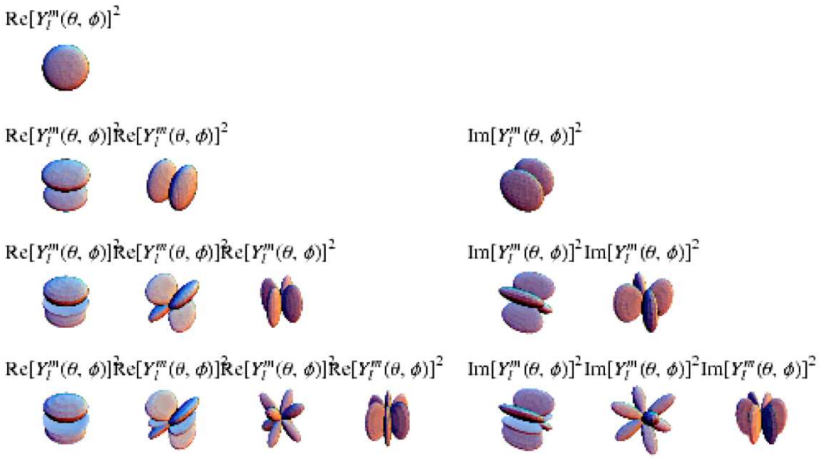

Figure 3.7: Real and imaginary part of some of the first spherical harmonics. From http://mathworld.wolfram.com.

In addition, the correlation function of two temperature fluctuations located in two directions $\mathbf{n_1} = (\theta_1, \phi_1)$ and $\mathbf{n_2} = (\theta_2, \phi_2)$ on the observed sky is given by:

$$C(\mathbf{n_1}, \mathbf{n_2}) \equiv \left\langle \frac{\Delta T}{T}(\mathbf{n_1}) \frac{\Delta T}{T}(\mathbf{n_2}) \right\rangle \tag{3.21}$$

$$= \left\langle \sum_{\ell,m} a^T_{\ell m} a^{T\star}_{\ell' m'} Y_{\ell m}(\theta_1, \phi_1) Y^\star_{\ell' m'}(\theta_2, \phi_2) \right\rangle \tag{3.22}$$

Using the properties of spherical harmonics, we have

$$C(\mathbf{n_1}, \mathbf{n_2}) = \frac{1}{4\pi} \sum_\ell (2\ell + 1) C_\ell P_\ell (\cos\theta) \tag{3.23}$$

$$\sim \frac{1}{2} \int \frac{d\ell}{\ell} \left[\frac{\ell(2\ell+1)C_\ell}{2\pi} \right] P_\ell (\cos\theta), \tag{3.24}$$

where $\theta \equiv \widehat{(\vec{n_1}, \vec{n_2})}$ and P_ℓ is the Legendre polynomials of order ℓ. One should notice that $C(\mathbf{n_1}, \mathbf{n_2}) = C(\theta)$, which results from the sky isotropy, in agreement with the cosmological principle. The quantity $\ell(2\ell+1)C_\ell/2\pi$ gives the contribution of the temperature fluctuations by interval of $\log(\ell)$.

3.3.2 Polarization

As illustrated in Fig. 3.6, CMB polarization distribution is a field of headless vectors, i.e. a spin-2 field. This latter, expressed as $P(\theta, \phi)$ in the following equation and, in a similar way of Eq. (3.16), could be expanded as a series of electric (gradient like) and

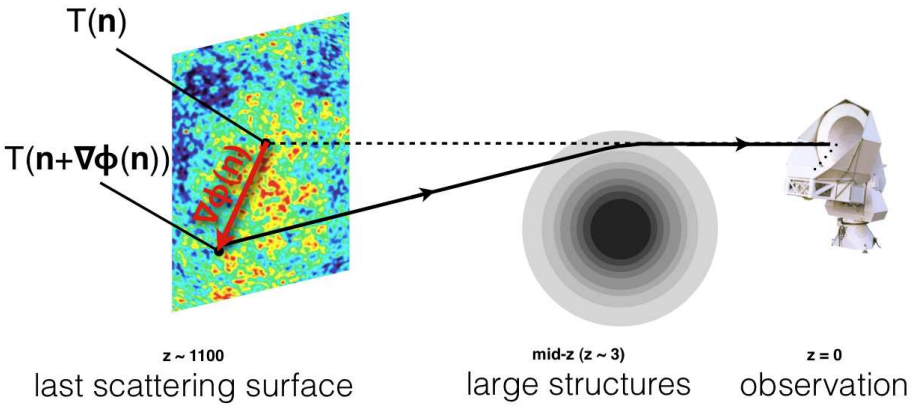

Figure 3.8: Scheme illustrating the geometry of the lensing effect on a CMB photons.

magnetic (curl-like) spherical harmonic modes, see Zaldarriaga and Seljak (151),

$$P(\theta,\phi) = \sum_{\ell=0}^{\infty} \sum_{m=-\ell}^{\ell} a^E_{\ell m} {E_\ell}^m(\theta,\phi) + a^B_{\ell m} {B_\ell}^m(\theta,\phi) \tag{3.25}$$

where ${E_\ell}^m$ and ${B_\ell}^m$ are defined as

$${E_\ell}^m(\theta,\phi) \equiv \frac{1}{2}\left[{}_{+2}Y^m_\ell M_+ + {}_{-2}Y^m_\ell M_-\right] \tag{3.26}$$

$${B_\ell}^m(\theta,\phi) \equiv \frac{1}{2}\left[{}_{+2}Y^m_\ell M_+ - {}_{-2}Y^m_\ell M_-\right] \tag{3.27}$$

in which expressions the matrices $M_\pm \equiv \sigma_3 \mp \sigma 1$ form a spin-2 basis with the Pauli matrices σ_1 and σ_3. Furthermore, the spin-2 spherical harmonics, ${}_{\pm2}Y^m_\ell(\theta,\phi)$, are complex-valued functions on the sphere and are related to the spherical harmonics $Y^m_\ell(\theta,\phi)$ by derivatives operators. Complex numbers allow the phase of each component of the polarization to be represented, allowing for circular polarization.

Lensing

Large scale structures induce deflections in the direction of the CMB photons as they propagate from the LSS to us, as illustrated in Fig. 3.8. The displacement angle can be expressed using the projected gravitational potential Φ along the line-of-sight. The lensing effect on a map $X = T$ or $Q \pm iU$ can be expressed as the following transformation:

$$X(\mathbf{n}) = \tilde{X}(\mathbf{n} + \nabla\mathbf{\Phi}(\mathbf{n})), \tag{3.28}$$

where $\tilde{X}$ is the unlensed field. The deflection angle $\nabla\Phi$ is due to the presence of variations in the gravitational potential Φ, which is defined as

$$\Phi(\mathbf{n}) \equiv -2 \int_{z=0}^{z=z_{rec}} dz\, \Psi\left(z, D(z)\mathbf{n}\right) \frac{D(z_{rec}) - D(z)}{H(z)D(z_{rec})D(z)}, \tag{3.29}$$

where $D(z)$ corresponds to the comoving distance to a redshift z, and Ψ is the zero-shear gravitational potential. One can show that the gravitational potential power spectrum is given by

$$C_\ell^{\Phi\Phi} = \frac{8\pi^2}{\ell^3} \int_{z=0}^{z=z_{rec}} dz\, \frac{D(z)}{H(z)} \left[\frac{D(z_{rec}) - D(z)}{D(z_{rec})D(z)}\right]^2 P_\Psi\left(z, k = \frac{\ell}{D(z)}\right). \tag{3.30}$$

As mentioned earlier, potential ϕ is the reason for a leakage between E- and B-modes. However, because E-modes have a larger amplitude, the effect is significant on the B-modes signal shape and amplitude as it is illustrated in the next section with the lensed B-modes power spectrum curve shown in Fig. 3.9.

Finally, section C.2.1 of Appendix C briefly explains how data analysts are able to reconstruct the lensing potential and therefore "de-lens" the observed polarized CMB maps.

3.4 Power spectrum and cosmological parameters

Power Spectrum

Angular power spectra for CMB temperature anisotropies, as well as for the E- and the expected B-modes anisotropies in polarization, are depicted in Fig. 3.9. These power spectra give different informations depending on the range of multipoles — equivalently the range of angular scales — within which the LSS is observed and analyzed. For instance, the TT power spectrum provides information about the initial conditions (e.g. n_s, A_s, etc.) at low multipoles and the peaks, corresponding to the acoustic oscillations which occurred in the primordial plasma, see paragraph 3.1.4, gives constraints on the spatial curvature of the universe Ω_K, the densities of baryons Ω_b, dark matter Ω_{dm}, etc. Finally the damping tail at high multipoles corresponds to fluctuations which are so close that they are comparable to the distance photons travel during recombination.

In addition, EE and BB angular power spectra are also shown in this figure and their observation will help us to break degeneracies in the estimation of cosmological parameters. Especially, it isolates the recombination and reionization[1] (e.g. Zahn et al. (150) and Zahn et al. (149)) epochs and as well as gravitational wave spectrum. This latter corresponds to the primordial B-modes, is depicted in dark blue in Fig. 3.9.

[1]The TE spectrum, not shown here, gives also strong constraints on the reionization epoch.

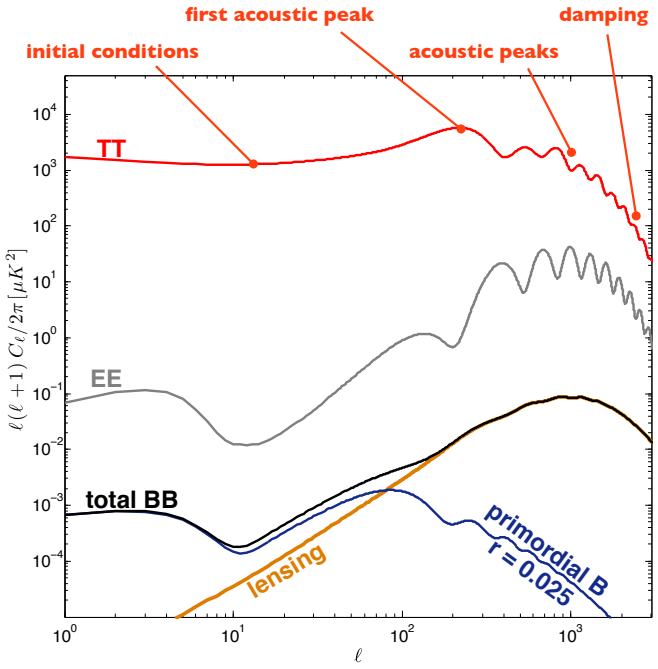

Figure 3.9: Angular power spectra for the temperature anisotropies (TT), the E-modes (EE) and the expected B-modes (BB) which can be decomposed in two parts: the primordial B-modes generated by the inflationary gravitational waves and the ones created by lensing (E-modes leaking into B-modes due to the deflection induced by large scale structures, see section 3.3.2).

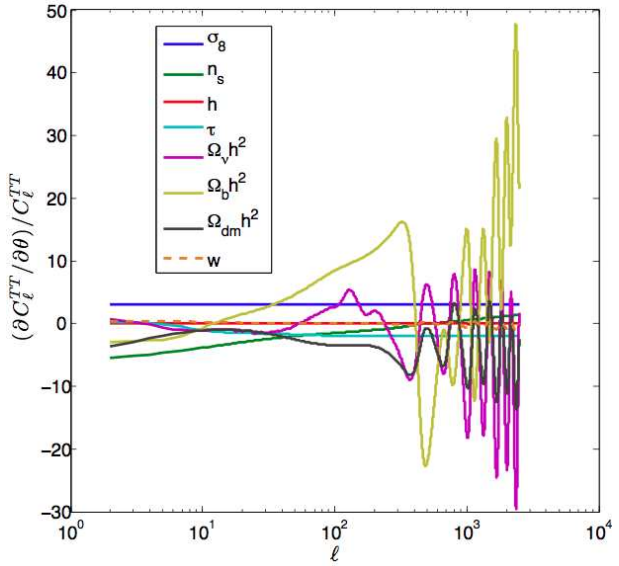

Figure 3.10: Normalized derivatives of C_ℓ^{TT} with respect to some cosmological parameters.

Its amplitude is parametrized by the tensor-to-scalar ratio r, already introduced in Eq. (2.59).

Cosmological Parameters

As illustrated in Fig. 3.10, the shapes of the CMB power spectra are directly linked to the cosmological parameters. I list below a brief description of the effect induced by each parameter on the spectra, while keeping the others constant. It has to be noticed that couple of these parameters are degenerated and those are generally broken using the polarization information and/or other observations such as Ia type supernovae, Cepheides or the abundance of light elements as predicted by the Big Bang Nucleosynthesis.

- H_0 — **Hubble parameter**. It describes the expansion speed of the universe. It is inversely proportional to the distance between us and the last scattering surface. If H_0 is increased, CMB perturbations would appear to the observer with larger characteristic angles. On the power spectrum, this corresponds to a shift of the peaks toward the low multipoles.

- Ω_b — **baryon energy density**. This quantity has a direct impact on the relative amplitudes of the acoustic peaks: the more baryons, the bigger (smaller) will be the first (second) acoustic peak.

- Ω_m — **matter energy density**. This affects both the shape and the amplitude of the peaks. In particular, the ratio Ω_b/Ω_m determines the amplitude of the acoustic peaks (photons are not coupled with dark matter).

- Ω_{tot} — **total energy density**. The total density of the universe is related to its curvature Ω_K, assuming that Ω_Λ and Ω_m are fixed. Thus, increasing Ω_{tot} has the effect of curving space. A fluctuation on the LSS, in a closed (respectively open) universe, would appear with a larger (respectively smaller) angle than for a flat universe. This causes a shift in the angular power spectrum toward smaller (respectively higher) multipoles.

- Ω_Λ — **dark energy energy density**. CMB photons have travelled by following geodesics. But they suffer from the deformations due to the geometry of the universe. Assuming that we know the distance between us and the LSS (equivalent to the expansion parameter H_0), we can constrain the curvature of the Universe Ω_K, which is the sum of the dark energy Ω_Λ and matter densities Ω_m: $1 - \Omega_K = \Omega_m + \Omega_\Lambda$. However, even if CMB provides hard constraints on each of these parameters, these latter are also accessible through the observation of Ia

type supernovae, seen as standard candles at small distances ($z \sim 0.1 - 1$), and provide constraints on the difference $\Omega_m - \Omega_\Lambda$, see Perlmutter et al. (106), Schmidt et al. (118). In addition, the study of gravitational lensing effects can independently constrain the value of Ω_m. The combination of these three observables can therefore constrain both Ω_m and Ω_Λ.

- n_s — **scalar spectral index**. This index parametrizes the power law of primordial perturbations ($\propto k^{n_s}$). Changing n_s results in changing the global slope of the CMB power spectrum. This is how first observations ruled out an important contribution from the topological defaults in favor of the inflation models thanks to the presence of acoustic peaks, e.g. Hanany et al. (61), Lange et al. (77).

- r — **tensor-to-scalar ratio**. It is defined as the ratio of tensor perturbation over scalar ones, and is a direct measurement of the primordial B-modes amplitude, cf. Eq. 2.58.

- $\sum m_\nu$ — **total neutrino mass**. The CMB also allows to constrain the total mass of neutrinos. The effect on the total intensity CMB spectrum is low, but a measure of the lensed B-modes with a combination of other observables (such as gravitational lenses and measurements with the Hubble Space Telescope) can constrain this parameter.

Part II

B-modes: the promises, the road towards their detection and the challenges

First, in chapter 4, I try to convince the reader of the interest of detecting the B-modes: this is mostly an extension of the previous chapter about CMB polarization, but I would like to make a clear statement about our motivations. Second, in chapter 5, I present the current status in the field and what are the forthcoming CMB polarization projects. Finally, in chapter 6, I introduce some of the challenges our community has to face nowadays, from an experimental point of view up to a data analysis one, and explain my contributions in the frame of the projects I have been evolved in, prelude of the detailed Parts III, IV and V.

Chapter 4

Why are we going after B-modes?

CMB polarization is an unique source of informations for observational cosmologists. In particular, its anisotropies help us understanding the physics of the very early universe and the laws governing at the very high energies. Primordial B-modes discovery would correspond to an indirect detection of gravitational waves and would constrain the energy scale of inflation. The observation of lensed B-modes, induced by large scale structures located between us and the LSS, could constrain, among others, the total neutrino mass, the dark energy equation of state w and the helium fraction Y_{He}.

Detected CMB polarization, the E-modes patterns

In chapter 3, I have described the evolution of the hot and dense primordial plasma, before recombination, and in particular that polarization of the CMB was induced by the photons Thompson scattering on electrons. This linear polarization was primarily due to the density perturbations present at that time which also generated the CMB temperature anisotropies. These perturbations force matter to flow along gradient directions, making it rare at the under-densities and getting condensed at the over-densities. This movement created photon intensity quadrupole anisotropies around the charged free particles, as seen in their attached frame. These conditions gave rise to gradient-zero curl polarization patterns on the LSS, the so-called E-modes. Assuming a physics for the baryon-photon plasma and measuring the total intensity T spectrum give constraints on the expected E polarization spectrum. And because temperature and gradient polarization anisotropies share the same physical origins, it implies an expected non-zero cross-correlation between T and E. Measurements of the E-mode power spectrum brings tight constraints on all cosmological parameters, and constrain proposed extensions to current standard cosmology.

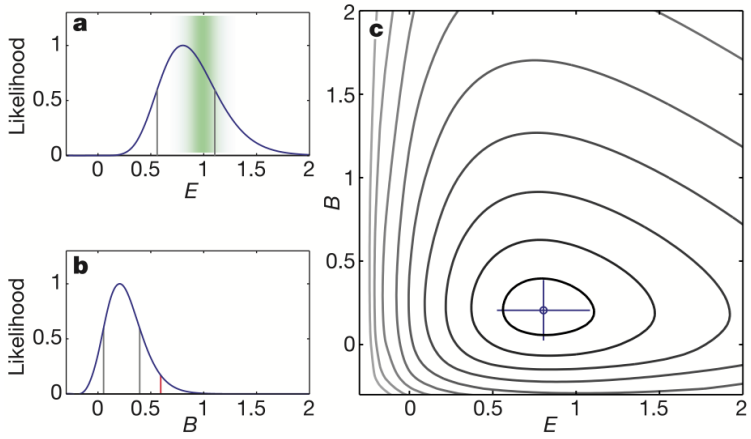

Figure 4.1: Results of the DASI experiment, as published in 2002. The collaboration showed for the first time that CMB has E-modes polarization, but that B-modes were consistent with zero. From Kovac et al. (74).

In 2002, the DASI experiment made the first CMB polarization detection, see Fig. 4.1 and Kovac et al. (74). The estimated amplitude of the E-modes was in agreement with the level predicted by the theory. Since then, other experiments have detected CMB polarized anisotropies among which CAPMAP (Bischoff et al. (13)), CBI (Sievers et al. (124)), QUAD (Brown et al. (20)), BICEP-1 (Chiang et al. (24)), QUIET (Bischoff et al. (14)), WMAP (Gold et al. (54)), MAXIPOL (Wu et al. (148)), and BOOMERANG (Montroy et al. (93)). In Fig. 4.2, published in Chiang et al. (24), one can observe that those observations have given progressively tighter constraints on TT, TE and EE. These results also bring an important consistency test for our understanding of the physics of the primordial plasma but also have provided strong support for the ΛCDM model (best fit model is shown with black solid lines in the figure).

CMB polarization measurements have the potential to confirm that inflation occurred and probe the ultra-high energy physics that drove it.

Given the success of the current model of cosmology in cataloging the contents of the universe, one of the new frontiers in cosmology and fundamental physics is to understand the early stages of the universe. CMB polarization fluctuations provide the extraordinary opportunity to see a signal from the very beginning of the universe, a small fraction of second after the Big Bang. The leading theory for the first instant of the universe is inflation, which is a superluminal expansion of space-time by a factor of $\sim e^{60}$, just after the Big Bang. As described in chapter 2, inflation is a relatively simple concept, but it explains many observational problems, such as why space-time appears

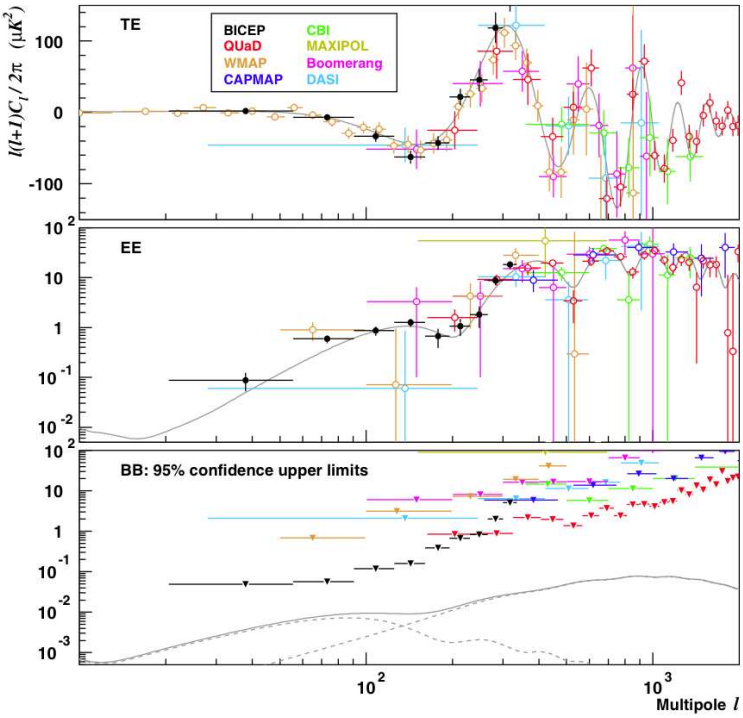

Figure 4.2: Results from the analysis of the BICEP-1 2 years data, as published in 2010. These results are, at the time of writing this thesis, the best constraints on the polarization power spectra leading in particular to the limit $r < 0.72$, obtained without combination with other data sets. From Chiang et al. (24).

to be flat, how the visible universe is not causally connected now but has a homogeneous temperature (this is what we call the horizon problem), and why no magnetic monopoles are observed. The rapid expansion during inflation would have produced gravitational waves that persisted to the time of recombination when the CMB photons last-scattered. The gravitational waves would have induced polarization in the CMB with a B-mode pattern on the LSS, which is gradient-free contrary to the E-modes.

Discovery of the gravitational-wave B-mode signal would demonstrate decisively that inflation occurred in the early universe and rule out some competing models.

As mentioned in chapter 2, inflation is presumed to be driven by vacuum energy associated with an ultra-high energy phase transition. Borrowing the concepts from high-energy physics, the vacuum energy and phase transition are described by a scalar potential and an associated particle, the inflaton. The amplitude of the gravitational wave background and the resulting B-mode signal depend directly on the height of the

inflaton potential and the energy scale of inflation, cf. Eq. (2.59). A measurement of the amplitude of the primordial B-modes would measure the energy scale of inflation.

The upper range of the predictions for the amplitude of the primordial B-modes include the 10^{16} GeV energy scale, which is the GUT scale where the strong, weak, and electromagnetic forces merge, see section 1.3. If we can detect such a signal, it would be really revolutionary. We would have the first probe of physics at an energy twelve orders of magnitude higher than the ones that the Large Hadron Collider (LHC) can achieve. These high energies mean that CMB polarization measurements may allow us to get information of the early physics and dynamics of the universe only 10^{-38} seconds after the Big Bang.

Simple models of inflation (single-field, slow roll) predict a slight tilt to the spectrum of fluctuations measured by the CMB, Eq. (2.47). The WMAP measurements estimated a scalar index $n_s < 1$ as expected in these models. The amplitude of the primordial B-modes is characterized by the tensor-to-scalar ratio, r, Eq. (2.58), and many single-field slow-roll models satisfy the relation $r \sim \mathcal{O}(1-n_s)$ which, given WMAP's n_s estimation, predicts r to be of order of 0.1, well within the reach of next generation experiments, as I describe in the next chapter.

CMB polarization measurements will measure or limit neutrino masses, and thereby determine the neutrino mass hierarchy.

As mentioned in section 3.3.2, we expect a lensing effect, induced by large scale structure between last scattering surface and us, which distorts the initial polarization pattern. This results in converting E- into B-modes to a small extent: the resulting signal is usually called lensed B-modes, and is important at small angular scales. Its measurement could constrain the sum of neutrino masses, as well as the dark energy equation of state w, and potentially reconstruct the projected mass map, e.g. Lewis and Challinor (84).

Measurements of these lensed B-modes have the potential to measure the sum of neutrino masses or set sufficiently strong constraints that can rule out some models for neutrinos. Indeed, these latter contribute today to the total dark matter content of the universe but, unlike normal cold dark matter, on small scales neutrinos do not cluster due to their very high velocity $\sim c$: this effect is called neutrino free-streaming and alters the shape of the perturbations power spectrum. As a direct consequence, neutrinos total mass affects the shape of the deflection field power spectrum, C_ℓ^{dd}, and therefore the shape of the lensed B-modes power spectrum, $C_\ell^{BB-lens}$. This is illustrated in the Fig. 4.3 and discussed in Appendix C.

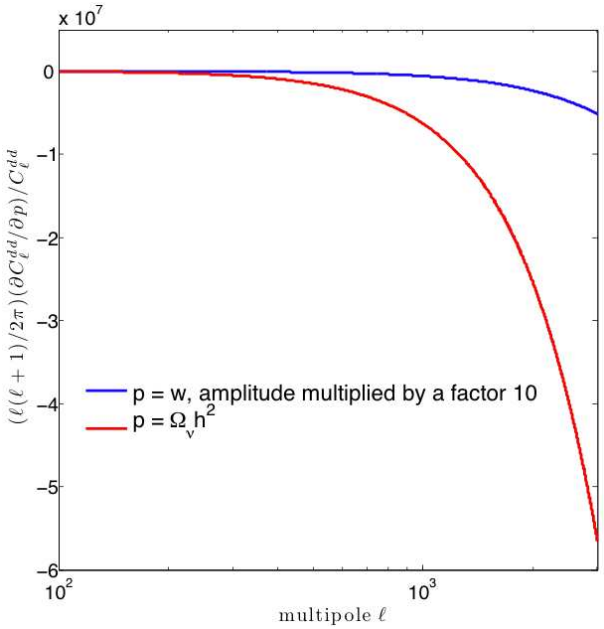

Figure 4.3: Dependence of C_ℓ^{dd} on $\Omega_\nu h^2$ and w. The y-axis is the derivative of C_ℓ^{dd} with respect to these cosmological parameters, and normalized by a fiducial C_ℓ^{dd}.

Therefore, the larger the sum of the mass of the neutrinos, the more structure formation is suppressed and the lower the amplitude of the deflection field and consequently the lensed B-modes. Optical weak lensing is also sensitive to this suppression of large scale structure, but CMB polarization lensing has a fundamental advantage over galaxy lensing measurements: the redshift where the main lensing objects are located is much higher for CMB polarization ($z_{\rm peak} \sim 2$) than for galaxies ($z_{\rm peak} \lesssim 1$), and therefore structure formation is still in the linear regime where theory is more accurate and predictive.

The effect of lensing potential on CMB intensity anisotropies has now been observed by several groups, e.g. Das et al. (30) and van Engelen et al. (141), but lensed B-modes signal is intrinsically more sensitive to the lensing power spectrum, the signal is easier to interpret since it is purely due to lensing, and foreground contamination is significantly less of a problem (e.g. point sources are poorly polarized).

From neutrino oscillation experiments, we know that neutrinos have mass, and we have measurements of the squared differences of the masses of the neutrino species[1]. From these values, we know that the heaviest neutrino has at least a 50 meV mass. The combination of WMAP and large scale structure measurements limit today the sum of neutrino masses to < 700 meV. CMB polarization measurements have the potential to

[1]Current results give $\Delta m^2_{21} = \Delta m^2_{\rm sol} = 7.59^{+0.20}_{-0.21} \times 10^{-5}$ eV^2 and $\|\Delta m^2_{31}\| \sim \|\Delta m^2_{32}\| = \Delta m^2_{\rm atm} = 2.43^{+0.13}_{-0.13} \times 10^{-3}$ eV^2, see e.g. Nakamura and Particle Data Group (97).

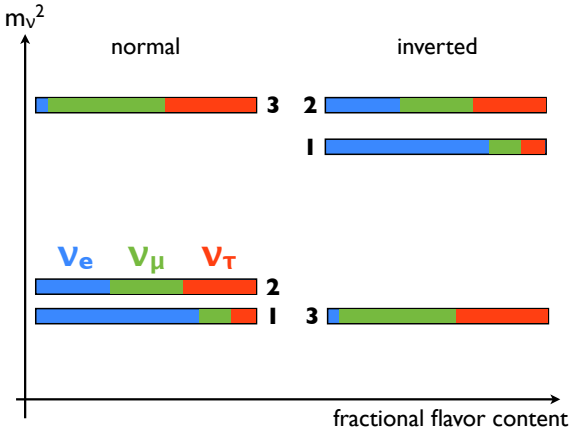

Figure 4.4: The two potential hierarchies for the neutrinos families. Neutrino oscillation experiments can only have access to the squared of the family masses. Cosmology, and especially the observation of lensed B-modes, will constrain the total neutrino mass and then will validate one or the other hierarchy.

give competitive and potentially tighter limits on the sum of neutrino mass in the near future, and they have completely different systematic errors than the laboratory experiments. Theoretically, neutrinos are described as having a hierarchy. The hierarchy determines the order of the masses with respect to the type of neutrino, as illustrated in Fig. 4.4. If neutrinos have an inverted hierarchy, then the differences of the mass squared imply a minimum total mass of 100 meV compared with a minimum of 50 meV for the normal hierarchy.

Last example but not the least, CMB polarization measurements will test the time dependence of dark energy (we often consider constrains on the dark energy equation of state w, as illustrated in Fig. 4.3). CMB lensing measures structures at the highest redshifts possible with gravitational lensing, since the background light is emitted at $z_{rec} \sim 1100$. CMB lensing is therefore sensitive to the early history of dark energy. If this latter had a stronger influence than it would for a cosmological constant model as early as $z \sim 5$, then structure formation is suppressed at this epoch and this can be detected in the B-mode lensing signal. A measurement of the evolution of the dark energy equation of state w could be obtained by comparing the high redshift CMB lensing measurements and lower redshift measurements of large scale structure, such as those from optical weak lensing or galaxy surveys.

Chapter 5

How to get there? Current and future status of the field

CMB experiments can be conducted from the ground, high-altitude atmosphere or space. In this chapter, I will briefly review the requirements that are set for current and future CMB polarization projects, especially those aiming at observing the B-modes, and present their main instrumental specifications such as beam, sensitivity, etc.

First, it is worth emphasizing that CMB observations are more and more complex, using increasingly number of detectors, generating huge data sets more and more difficult to handle. A lot of instrumental options have been explored, as a result of worldwide efforts. However, teams currently designing projects would like to know if there are setups which optimize the detection of the tensor-to-scalar ratio r, or the detection of the lensing potential. Of course, the optimization of a new generation experiment should take into account some requirements, such as the presence of astrophysical foregrounds between us and the LSS, sky coverage constrained by the specific science goals the experiment aims at and finally some mandatory control of instrumental systematics (either hardware or pipeline solutions).

Earth or Space – There is a trade-off to be made in the choice of the experiment one would like to build to detect primordial or lensed B-modes.

On the one hand, it is clear that ground-based and balloon-borne instruments are much cheaper and quicker to deploy. Even if ground-based experiments suffer from atmospheric contamination, they have the advantage of potentially extend the time of their observation, in addition not to having constraints with respect to their focal plane size, allowing for many detectors. And they can be adapted (e.g. experimental setups upgrade, observing strategy optimization) at (almost) any moment.

Balloon-borne, as well as space experiments, have much higher sensitivity for a given type detectors, i.e. a given noise as measured in the lab. But balloons are limited to

Figure 5.1: Ground, balloon and space observatories have different sensitivities, observed sky areas and costs.

rather short time of integration, on the order of couple of weeks at most, because of the flight constraints.

Space observatories are limited to rather short time of integration, on the order of couple of 2-4 years due to the active cryogenic system limitations, especially the finite volume of on-board cryogenic gas. They are also limited in size and weight, because of the launcher limitations: this set constraints on the final number of detectors in the focal plane design, but also on the typical diameters of the optics . Finally, space experiments are the unique setups which can observe nearly the full-sky, but are usually the most expensive option.

To put the trade off arguments between Earth and space – except costs – in a nut-shell, the balance has to be found between a cosmic variance limited experiment (small fraction of the sky) and a noise limited one (either noisy detectors, or too few of them, or too large fraction of the sky, etc.).

Optimum sky coverage – If one aims for an initial detection of CMB B-modes signal, it is most efficient to concentrate all the experiment sensitivity on a as small patch of the sky as possible, being careful with potential problems such as E-B leakage[1]. Now, to have a statistically robust detection of the B-modes, one would not obviously go to bigger patch sizes. This is illustrated in Fig. 5.2 taken from Errard (39). Left panel of this figure depicts the r detectable at the 2-σ level as a function of f_{sky}, in the case of three POLARBEAR experiments which have different sensitivities, as detailed in the caption. Similarly, the right panel shows the evolution of the error on total neutrino mass as a function of the observed fraction of the sky. Quantitatively, these curves are specific to the assumed instrumental setups but can, at least qualitatively, be generalized to other experiments.

[1] As mentioned in section 15.6, analysis of a finite patch size on the sky leads to the correlation of different modes while computing the spherical Fourier transform.

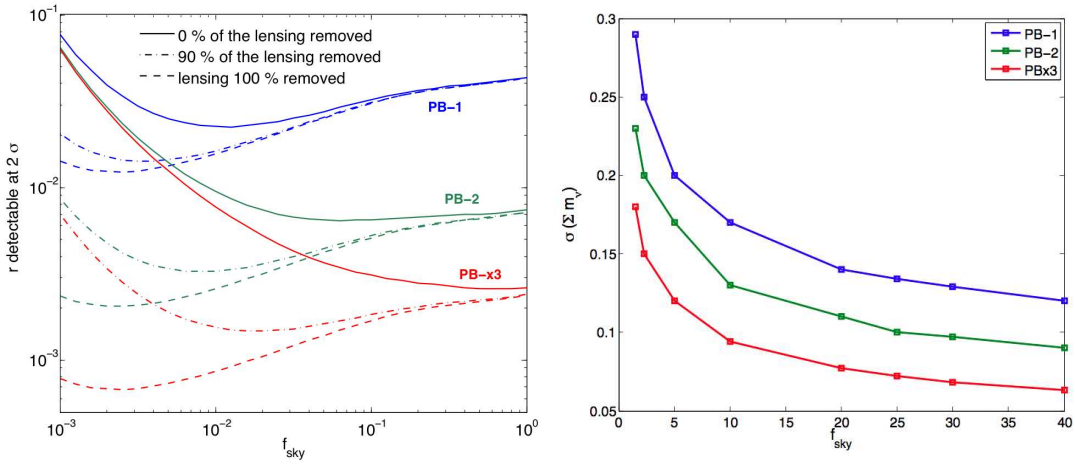

Figure 5.2: POLARBEAR-I, -II and -EXT are assumed to have respectively a 9.0, 5.2 and 2.5 μK·arcmin white noise levels on a 2.5% patch on the sky. Beams are assumed to have a Full Width at Half Maximum (FWHM) of 4 arcmin. **Left panel**: what is the best f_{sky} for these POLARBEAR instruments in order to detect the lowest r? The vertical axis shows the detectable r at the 2-σ level, i.e. the solution of the equation $r = 2\sigma(r)$, where σ is computed with a Fisher approach, considering a total B-modes signal, $C_\ell^{tot} = C_\ell^{prim}(r) + \eta\, C_\ell^{lens}$, and a white homogeneous noise C_ℓ^{noise}, cf. Eq. (5.1). Furthermore, we consider that the noise level satisfies $w^{-1/2} \propto \sqrt{f_{sky}} \sim \sqrt{n_{pix}}$ and depict the result for three different value of η, the fraction of lensing signal: $\eta = \{1.0, 0.1, 0.0\}$. We clearly see an optimal fraction of the sky which should be observed leading to a detection of a minimal r. But these conclusions depend also on the ability of delensing and on the instrumental noise level. **Right panel**: what is the lowest constraint on neutrino mass (expressed in eV)? I still assume the same scaling for the noise level and the y-axis, $\sigma\left(\sum m_\nu\right)$, is computed using a Fisher approach, following Smith et al. (126). I assume $\ell_{max} = 2500$ and a fiducial value of $\Omega_\nu h^2 = 5 \times 10^{-3}$. Contrary to the detection of r, it seems that lensed B-modes detection is optimal for large fraction of the sky, independently of the instrumental sensitivity: this is partially due to the fact that the reconstruction of the lensing potential needs both large and small scales informations, and the considered estimator uses information from all T, E and B. All these results do not take into account any instrumental or sky signal systematic effects.

To obtain these results I consider that, for a given instrumental setup, the quantity $w^{-1/2}/\sqrt{f_{sky}}$ is conserved[1]. This corresponds to the conservation of the total number of hits for a given observation, keeping constant its total time length and the number of detectors, which leads to

$$w^{-1/2} \propto \sqrt{f_{sky}} \propto \sqrt{n_{pix}}. \tag{5.2}$$

This means that, the bigger is the patch, the noisier will be the final map. We can understand the behavior of the curves shown in the left panel of Fig. 5.2: as derived in Appendix C, one can show that the r detectable at 2-σ behaves like

$$r \propto \frac{1+\gamma f_{sky}}{\sqrt{f_{sky}}}, \tag{5.3}$$

where γ is a positive constant which depends on the lensing signal as well as the noise level of the experiment, etc. Therefore, for small (resp. large) observed fraction of the sky, detection of r will be cosmic variance limited (resp. noise limited), i.e.

$$r \,@\, 2\sigma \propto \frac{1}{\sqrt{f_{sky}}} \text{ for small } f_{sky} \tag{5.4}$$

$$\propto \sqrt{f_{sky}} \text{ for large } f_{sky}. \tag{5.5}$$

The $\sigma(r)$ in this estimation of r is computed using a Fisher approach. We consider the signal to be the total B-modes, defined as

$$C_\ell^{tot} \equiv C_\ell^{prim}(r) + \eta\, C_\ell^{lens}, \tag{5.6}$$

and consider a white homogeneous noise $C_\ell^{noise} \propto w^{-1} \propto f_{sky}$, cf. Eqs. (5.1) and (5.2). Between the cosmic variance and noise dominated regimes (Eqs. (5.4) and (5.5)), we clearly see in the left panel of Fig. 5.2 that the detection of the minimal r is reached for an optimal fraction of the sky, around 1% in the case of the POLARBEAR-I instrument. In addition, if we are somehow able to delens the detected B-modes, this will result in a change of the curves' shape at small f_{sky} (depicted as dashed and dot-dashed curves in the figure): delensing is simply studied here by modifying the η parameter and this results in a decrease of the cosmic variance $\propto 1/\sqrt{f_{sky}}$ contribution and therefore decreases the optimal sky coverage. This discussion is detailed in the case of the

[1] $w^{-1/2}$ is an usual notation corresponding to the sensitivity of the instrument, expressed in μK·arcmin. Moreover, the noise power spectrum, N_ℓ, for an instrument with a given Full Width at Half Maximum (FWHM) reads

$$N_\ell = w^{-1} \exp\left[\ell(\ell+1)\frac{(FWHM)^2}{8\log(2)}\right]. \tag{5.1}$$

This assumes a white homogeneous noise across the final map.

POLARBEAR experiment in Appendix C.

The picture changes for an optimization with respect to lensing detection. This is illustrated in the right panel of Fig. 5.2 where we depict the error on neutrino mass, $\sigma\left(\sum m_\nu\right)$, expressed in eV, as a function of the observed sky fraction, f_{sky}. Noise scaling is taken to be the same as before, i.e. $w^{-1/2} \propto \sqrt{f_{sky}}$, and the computation of σ is again based on a Fisher approach, following Smith et al. (126). Contrary to the detection of the lowest tensor-to-scalar ratio r, it turns out that the best constraints on neutrino mass are obtained for an observation of large fraction of the sky, independently on the characteristic noise of the experiment. Even if low f_{sky} leads to a cosmic variance limited estimation of $\sum m_\nu$, large f_{sky} and therefore "noisy" observation keeps bringing information about lensing. This should be partially due to the way the lensing estimator is built, see Hu and Okamoto (64) and section C.2.

Frequency coverage, polarized galactic foregrounds – We expect two important polarized foregrounds, synchrotron and dust, as detailed in chapter 9. The first signal dominates at low frequencies ($\lesssim 80$ GHz) and the second one at high frequencies ($\gtrsim 200$ GHz). CMB dominates between these two regimes, around 100-150 GHz. Different techniques to disentangle CMB from other emissions have been developed, the so-called component separation techniques, and those usually need the information of, at least, three or four distinguished frequency channels, located in the different foregrounds-dominated spectral regions, in addition to obvious CMB dedicated channels.

Optimum experimental design – There is a clear need to have a high enough sensitivity to detect nano Kelvin signals (using big number of detectors, long integration time, large aperture, etc.) but also a good control of the systematic effects. These requirements are usually detailed in the new CMB polarization experiments proposals such as the ones made by The COrE Collaboration (137) or Bock et al. (16). As an example, among those controls, we can cite the modulation of the incoming polarization, using a half wave plate and/or at least sky rotation, which helps a lot to reduce the $1/f$ noise contamination of the cosmological signal. But this mechanism requires to not affect the beam positions and shapes, because if this condition is not satisfied, this could produce dramatic T-B leakage. We introduce a description of similar effects and detail them in chapter 7.

Current and Future Experimental Efforts – Some of the current and future projects are summarized in Table 5.1 with their main properties described. One can find the description of

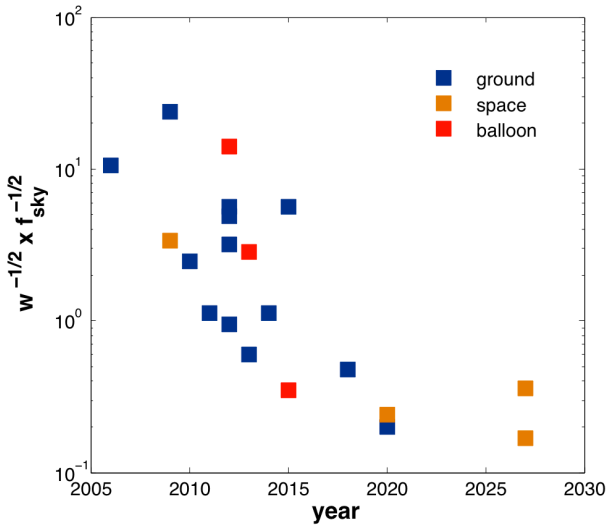

Figure 5.3: Sensitivity of current and future experiments, $w^{-1/2}$, expressed in μK·arcmin, and scaled by a factor $1/\sqrt{f_{sky}}$, shown as a function of the expected year of deployment. One can see that the noise per pixel is decreasing as a function of time and this is mainly due to the use of bigger detector arrays and sometimes longer integration time.

- the frequency channels: those are necessary for components separation. While ground-based and balloon-borne experiments are limited by atmosphere in their choices for the observational frequency bands (see chapter 8), space missions could use many channels, e.g. COrE, CMBpol, LiteBird, etc. Thus, those can bring unique informations about, among others, the astrophysical foregrounds scaling laws, and can give essential knowledge for the small scale experiments.

- the typical angular scale achievable: it constrains the science goals, mainly between primordial and lensed B-modes, as well as other science goals e.g. cluster research (as it is the case in particular for ACTpol and SPTpol).

- the observed fraction of the sky: as mentioned before and illustrated in Fig. 5.2, this quantity is related to the integration depth of the observation, but also set the largest observable scales for the experiment.

- the sensitivity $w^{-1/2}$, expressed in μK·arcmin: one can notice that this quantity increases with time. This is illustrated in Fig. 5.3, where we depict the quantity $w^{-1/2}/\sqrt{f_{sky}}$, corresponding to the integration depth, as a function of the expected year of deployment (and discriminating ground-based, balloon-borne and space experiments). Experiments verify nowadays $w^{-1/2}/\sqrt{f_{sky}} \sim 1{-}5\mu$K·arcmin and will be $\sim 2 \times 10^{-2}\mu$K·arcmin for the potential deployments $\gtrsim$ 2020.

- the detectable r at the 2-σ level and the number of σ for the lensed B-modes signal detection, both computed using a Fisher approach. On one hand, we can notice

that the lowest r detectable is decreasing with time, reaching $\sim 10^{-3}$ around 2020. On the other hand, the lensed B-modes should be well characterized in the next years, likely before $\sim$ 2015.

experiment	type	frequencies [GHz]	beam @ 150 GHz [arcmin]	f_{sky} [%]	sensitivity [μK arcmin]	detectable r 95% c.l.	# of σ for lensed BB detection	ref	deploy. year
BICEP-1	G	100+150+220	36	2	15	0.72	0.7	(135)	2006
Planck	S	30+44+70+100+143+ 217+353+545+857	7	80	30	0.05	3	(136)	2009
BICEP-2	G	100+150+220	36	2	3.5	0.01	8	(22)	2010
KEK-Array	G	100+150+220	36	2	1.6	0.006	18	(23, 122)	2011
SPTpol	G	90+150	1	1.5	6	0.025	14	(15, 91)	2012
POLARBEAR-I	G	150 + 220	3.5	2	8	0.025	12	(5)	2012
ABS	G	145	30	2	4.5	0.015	7	(98)	2012
ACTpol	G	150	1	10 [wide] 0.04 [deep]	20 3	0.03 0.01	7 96	(99)	2012
EBEX	B	150+250+410	8	1	14	0.03	4	(102)	2012
SPIDER	B	90+145+280	30	8	8	0.02	6	(51)	2013
POLAR-1	G	150	6	0.7	0.5	0.01	85	(76)	2013
POLARBEAR-II	G	90+150+220	3.5	40	5	0.01	50	(134)	2014
PIPER	B	200+270+350+600	15	75	~ 3	0.007	140	(27)	2015
POIARBEAR-EXT	G	90+150+220	3.5	60	3	0.001	100	int. com.	2018
POLAR-Array	G	95+150+220	4	1	0.2	0.008	150	(76)	2020
LiteBird	S	100+150+220	30	70	2	2×10^{-3}	110	(63)	2020
COrE	S	45+75+105+135+165 +195+255+285+315+375 +435+555+675+795	8	70	3	$\sim 10^{-3}$	190	(137)	2025-2030?
CMBpol	S	30+45+70+100+150 +220+340+500+850	5.6	80	1.5-3.5	$\sim 10^{-3}$	200	(16)	2025-2030?

Table 5.1: Summary of the specifications of some current and future CMB B-modes experiments, which can be ground-based (G), balloon-borne (B) or spatial (S). r detectable, as well as the # of σ for a lensed BB detection, are computed using a Fisher approach, not including systematics or foregrounds.

Chapter 6

My contribution in the context of the challenges for new generation CMB experiments and their data analysis

This chapter is a transition between the description of the motivations for hunting the B-modes, see chapters 1 to 4, and the details of my research work in the remainder of this thesis, see Parts III, IV and V. The goal of this chapter is to introduce the latter in the context of current challenges for CMB polarization research, both from the experimental and data analysts point of views.

My PhD studies started in September 2009 and I submitted this thesis in July 2012. During those three years, I have focused on data analysis projects, from component separation forecasting for future satellites up to study of some experimental systematic effects. In parallel, I have been involved in the CMB ground-based experiment POLARBEAR. I have especially taken part in the commissioning of the POLARBEAR instrument in February-March 2010, and analyzed its first data during 1) its engineering campaign in May-June 2010 and 2) its first observation runs from Chile in April-May 2012.

Following the discussion of the previous chapter, CMB polarization can be observed from ground or space, and I have had the chance to have an overview of both solutions and work on projects at different stages: from the conception (COrE, a european satellite project, through my work on optimization framework) to the exploitation of real data (as a member of the POLARBEAR collaboration). The projects of this PhD are at the junction between observations, data analysis and new algorithms research.

Section 6.1 summarizes the main current experimental and data analysis challenges. Sections 6.2 and 6.3 introduce the two important parts of my PhD work, precising how they contribute to the B-modes quest.

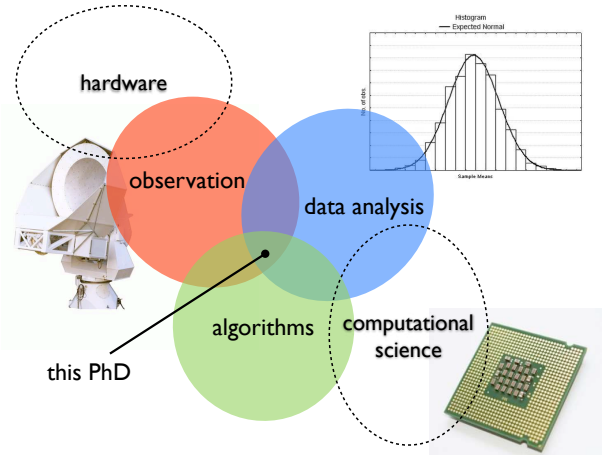

Figure 6.1: My PhD projects are at the junction between observations, data analysis and research for new algorithms. This may be seen as a mid-way point between hardware research and computational science.

6.1 Current challenges

Systematics & sensitivity

New generation CMB experiments are usually based on two pillars: a high sensitivity and a control of the systematic effects. Instrumental sensitivity is improved by using as many photon-noise limited detectors as possible. Currently operating ground-based instruments have on the order of 10^3 detectors, and proposed future satellites will have $\sim 5 \times 10^3$ - 10^4. In addition to this number of observing pixels, experiments need a large enough aperture, i.e. large enough optical throughput, and an as long as possible integration time, on the order of a couple of years. Such criteria allow observatories to achieve sensitivities of $\sim$ 1-10 μK·arcmin in intensity, as detailed in Table 5.1. This level ensures that the experimental setup is sensitive enough to detect tiny CMB signals: for example, lensed B-modes are at the $\sim$ 4-5 μK·arcmin level.

Detecting nano-Kelvin CMB signals, as the B-modes, requires improvements, not only in detectors and optics, but also more generally in systematic error control. For instance, a high sensitivity is only useful if one can disentangle CMB signal from other astrophysical contaminations: consequently, experiments should have, in addition to CMB channels, a sufficient frequency coverage, necessary for the separation of polarized sky components — optimizing the frequency bands of future nearly full-sky experiments is the purpose of Part IV. Fortunately, many of these systematics have been confronted, and in most cases mitigated, by many first-generation CMB polarimeters.

See Table 6.1 for a description of the important expected systematics, with the corresponding solutions to reduce them. Some of these effects are indeed avoidable thanks to the experimental design (e.g. ground shield, baffles, re-imaging lenses, etc.), and some can be corrected during the first stages of the data analysis pipeline (e.g. glitches). Thermal and electrical gain drifts, $1/f$ noise, sidelobes, and pointing errors, are already familiar from previous CMB experiments designed for the observation of total intensity anisotropies. However, for the polarization quest, these effects are becoming more important as the researched signals are relatively weaker. In addition, a new class of potential errors arises from the polarimetric fidelity of the optical system, see chapter 7, which can, among other effects, produce false E- and B-mode polarization signals from much brighter temperature anisotropy or mix polarization states before detection.

error	**definition**	**effect**	**solution**
differential beam size	$\Delta\mu \equiv 2\frac{\sigma_1-\sigma_2}{\sigma_1+\sigma_2}$	$\nabla^2 T \to B$	optics design + calibration + cross linking
differential gain	$\Delta G \equiv \frac{g_1-g_2}{2}$	$T \to B$	design + calibration + cross linking
ellipticity	$\Delta e \equiv \frac{e_1-e_2}{2}$ with $e_i \equiv \frac{\sigma_x-\sigma_y}{\sigma_x+\sigma_y}$	$\nabla^2 T \to B$	design + calibration + cross linking
Beam offsets	$2\frac{\Delta\theta}{\sigma_1+\sigma_2}$	$\Delta T \to B$	design + calibration + cross linking
pointing	Q, U beams offset	$\nabla E \to B$	calibration, pointing specification
cross polarization	rotation of electric field	$E, B \to E, B$	calibration using polarized source
instrumental polarization	creation of polarization from total intensity	$T \to Q, U$	calibration using unpolarized source
far sidelobes	diffraction, scattering	leakage from hot sources e.g. sun, moon, galactic plane	optical baffling and calibration
$1/f$ noise	detector, readout, atmospheric signal drift	striping in map	stabilize detectors and readouts, filter out correlated contamination
bandpass mismatch	variation in filters	differential response to foregrounds	spectral calibration

Table 6.1: Summary of the expected main systematics for a CMB polarization experiment. A differential beam width could occur when two beams are Gaussians, but have different beam widths $\sigma_1 \neq \sigma_2$. A differential gain could occur if two detectors have different gains, i.e. $g_1 \neq g_2$. In such case, differencing the signals associated with each antenna of a pixel pair leads to an apparently polarized signal. If each antenna in a pixel pair produces an elliptically shaped beam, then differential ellipticity could give rise to an effect similar as differential beam width. The effect of differential beam offset is caused when the directions of the two beam patterns on the sky are not identical, and couples gradients in the CMB temperature anisotropy into polarization. Beam systematics induced by differential ellipticity and beamwidth depend on the second gradient of the underlying temperature anisotropy on scales comparable or smaller than the beamwidth. Pointing, cross polarization, instrumental polarization will be discussed in chapters 7 and 15.

Data analysis challenges

Contemporary CMB data analysis requires advanced processing techniques, numerical algorithms and methods, and implementation of these later. There are many reasons for that, see e.g. ANR MIDAS'09 (4).

6. MY CONTRIBUTION IN THE CONTEXT OF THE CHALLENGES FOR NEW GENERATION CMB EXPERIMENTS AND THEIR DATA ANALYSIS

First, CMB data sets generated by observing experiments are in general very heterogenous. This can be due to the complexity of the current superconductor detectors which can have unexpected behavior, or also due to the fact that glitches can occur in the time stream, due to cosmic rays or readout jerk. Data, obtained directly from the instrument, is called time-ordered data (TOD), cf. the typical analysis pipeline shown in Fig 6.2. It contains information about the map of the sky $s(\theta, \phi) \equiv s_p$, where (θ, ϕ) are spherical coordinates and p denotes a given pixel of the sky. Estimating a map from observational data is the first important step in CMB data analysis before disentangling the different sky components, estimating power spectra and constraining cosmological constants, see Fig. 6.2. In fact, as we have seen in section 3.3 and 3.4, for a comparison with theoretical models, e.g. the inflationary models, the major informations are contained in the power spectrum of the CMB signal, which is a spatial frequency domain object. One of the data analysts challenges is to create new tools which can operate in time, spherical and frequency spaces as well as in between these domains.

Second, time domain measurements and sky signals are contaminated by various noise e.g. electronic, atmospheric. Moreover the instrumental noise is typically correlated on long time scales (and correlated between detectors, see section 15.3): this is the so-called $1/f$ noise, giving power to low-frequency modes. This does not allow for a simple parallelization approach, i.e. a "divide and conquer" implementation, for the data analysis since big segments of the data have to be processed simultaneously. Given a rather limited memory per processor anticipated for the forthcoming supercomputers, new generation experiments data analysis requires massive parallelization of the codes. Moreover, noise correlation patterns are unknown ahead of time and has to be determined from the data themselves, see section 15.3. This has to be sufficiently precise to permit the best recover of the sky signals. More generally, the whole TOD processing has to be highly accurate not to affect, bias or remove the informations it encapsulates, i.e. its cosmological contents.

Third, CMB measurements are usually contaminated by a priori unpredictable levels of instrumental and other systematic effects, e.g. ground-pickup or atmospheric fluctuations as described in chapter 8. Those have to be first detected in the presence of dominant noise and later subtracted, again without compromising the cosmological and astrophysical sky signals. In addition, I have previously mentioned that the observed sky is a combination of multiple components, the astrophysical foregrounds. Those "sky systematics" differ from CMB either because they have different frequency behavior, spatial or statistical properties and can be separated from the CMB signal. One can see in Fig. 6.2 the position of the component separation process in a typical CMB data analysis scheme.

Finally, one of the challenges consists in dealing with the hugeness of CMB data sets. The new generation of CMB polarization experiments will observe the sky at least

a few years, using thousands of detectors, each of them sampling the sky as many as hundred times per second. The forthcoming data sets will soon typically contain tens and hundreds of billion of measurements[1] and reach more than a peta byte.

6.2 Study of a future satellite challenge

A part of my PhD consisted in studying the challenges posed by future nearly full sky experiments such as the COrE and CMBpol projects, see The COrE Collaboration (137) and Bock et al. (16). One of these challenges is the optimization of the frequency bands to render the lowest residuals due to component separation, and to allow for a detection of the lowest tensor-to-scalar ratio r possible. This research project consisted in optimizing the focal plane configuration of future nearly full sky experiment, has been published in Errard et al. (41) and is detailed in Part IV.

The proposed framework is based on a maximum parametric likelihood component separation and tries to find the best distribution of detectors among available frequency channels with respect to the detection of primordial B-modes. In addition, we take into account some hardware limitations such as the finite area of the focal plane or the total number of detectors available. To estimate the performance of an experimental configuration, we define three different figures of merit: the lowest r detectable, the level of residuals and the level of noise after the component separation process.

In Errard and Stompor (40), we extend this work and look for potential fundamental limitations on the lowest r detectable due to astrophysical foregrounds residuals. We also generalized the formalism to take into account systematic effects such as calibration errors and spatial variability of the foregrounds.

These two related works have been published in two papers cited above, and in three talks[2].

6.3 Involvement in an operating ground-based experiment: hands-on data analysis

I have taken part in the POLARBEAR project for the last three years, having the chance to work on a working experiment and tackle observational data. Fig. 6.2 shows some of

[1] We expect an amount of data $\sim 10^{13}$ in the case of the POLARBEAR experiment.

[2] PONT conference in Avignon, France, April 2011;
47^{th} Rencontres de Moriond in La Thuile, Italy, March 2012;
Beyond COrE meeting in Paris, France, June 2012.

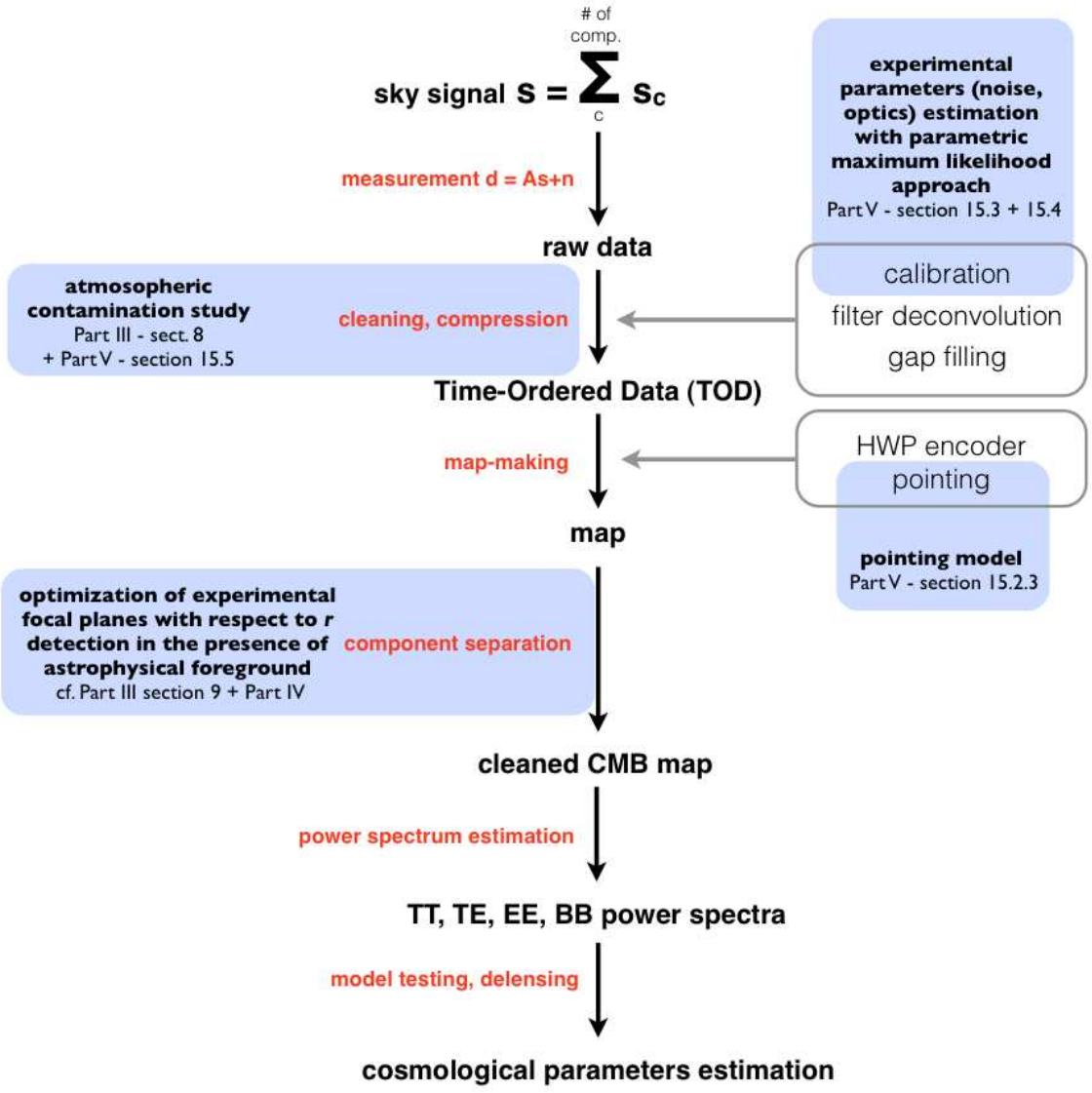

Figure 6.2: Schematic representation of a CMB experiment data analysis pipeline. Blue shaded text correspond to some of my contributions detailed in Part III, IV and V.

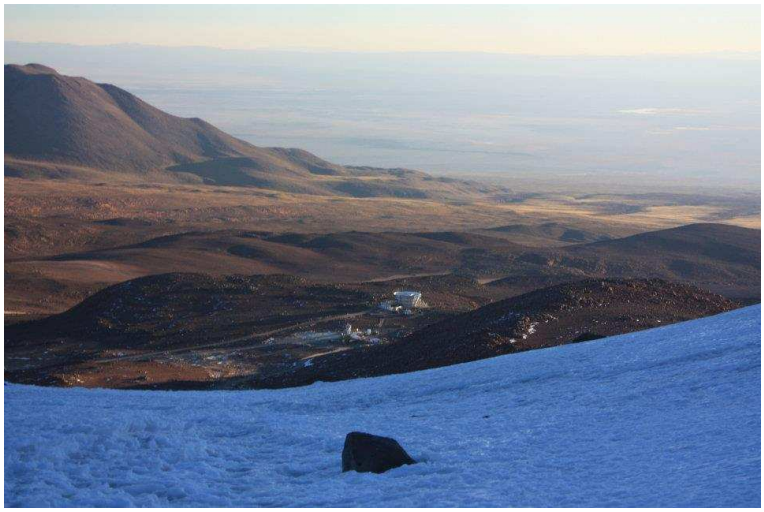

Figure 6.3: The POLARBEAR instrument installed on the Huan Tran Telescope, located at the James Ax Observatory (5200 meters height), Chajnantor plateau, Atacama desert, Chile. Ground-shielded experiment near POLARBEAR is the Atacama Cosmology Telescope.

my contributions shown in blue among the steps of a typical analysis pipeline[1].

Atmospheric contamination studies (September - December 2009) — My first project was about the estimation of the expected atmospheric signal in the case of POLARBEAR. I have developed and implemented a model based on the idea Church (26): results allowed us to have an idea of the expected patterns of contamination across our focal plane, as detailed in chapters 8. One of the current challenging projects for data analysts is now to find an optimal filtering for this contamination, see section 15.5.

Instrument commissioning (February - March 2010) — I developed algorithms based on a parametric maximum likelihood method to study and estimate detectors $1/f$ noise, using lab measurements taken in Berkeley. I also used the lab data from the observation of a non-polarized source to estimate the instrumental polarization due to the cryostat optical system.

[1] One should of course discriminate two different levels of analysis:

- the quick analysis which can be performed directly in the field, necessary to calibrate the instrument, flag the data, and check if the observations are well performed and the data well registered.
- the heavy analysis which has important computational power needs and aims at gather all the informations about the telescope (detectors data, noise characterization, pointing, etc.) and construct the CMB fluctuations maps. On a second step, the power spectra estimation will lead to the estimation of the cosmological parameters.

Even if the POLARBEAR collaboration has been and is currently working on both approaches, I have mainly focused my work on the quick analysis library, see chapter 15.

6. MY CONTRIBUTION IN THE CONTEXT OF THE CHALLENGES FOR NEW GENERATION CMB EXPERIMENTS AND THEIR DATA ANALYSIS

Engineering campaign (May - June 2010) — I was in charge of reconstructing the pointing of the telescope. As written in Table 6.1, pointing errors are one of the main systematic effects one can expect for CMB polarization experiments, and benchmarks for the POLARBEAR telescope were on the order of 10 arcseconds error after reconstruction. This work is detailed in section 15.2. The developed and implemented model gave satisfying results and is currently used for the POLARBEAR data analysis. Results of this project have been included in a successful NSF proposal, submitted in July 2010 (AST-1212230).

Quick analysis development (January 2010 - today) — I also participated to the effort for creating libraries of routines for the quick data analysis. POLARBEAR collaboration first created the Quicklook library (matlab) and then upgraded it for the currently used and developed AnalysisBackend (python) library. This routines allow data analysts to fetch specific observations, and apply to it the first stages of the pipeline depicted in Fig. 6.2, currently up to the map level.

POLARBEAR science forecasting (September - October 2011) — In parallel to the PB-1 deployment and operation, the next POLARBEAR instrument, PB-2, has been developed and will be deployed in 2014. I have been in charge of studying the science forecasts of this new experiment, comparing it with PB-1. Scientific goals were the detection of both primordial (estimation of r) and lensed (neutrino masses, w) B-modes. This work is summarized in Appendix C and results have been published in a successful NSF proposal for PB-2, submitted in October 2011.

Start of the scientific observation campaign (April - May 2012) — I participated to the operation of POLARBEAR, installed in the Atacama desert in Chile, see Fig. 6.3. The main work of the team in the field consists in operating the telescope, especially scheduling the observations and performing maintenance tasks. Spring 2012 corresponded to the beginning of the standard observations, so we had also to find the optimal patches on the sky which could give us a quick access to our scientific goals and which overlap with other experimental observations, such as Herschel-Atlas, for future cross correlation. Furthermore, field team is in charge of analyzing, interpreting and understanding data taken by the instrument, on a daily basis.

Part III

Potential problems on the road to B-modes

I introduce in this Part three different types of systematic effects, among both sky and instrumental ones. First, in chapter 7, I present the Mueller formalism, practical to describe the optics in the case of stationary radiation, as it is the case for CMB observations. This framework is also useful to model some instrumental systematic effects, e.g. cross- or instrumental-polarization. Second, in chapter 8, I describe what a typical ground-based experiment could expect regarding the atmospheric contamination, which is one of the major noises data analysts have to deal with. Third, in chapter 9, I describe the astrophysical polarized foregrounds, which can be called sky systematics in the sense that, even with the best CMB experiment ever, they will always be significant contaminants.

Chapter 7

Description of some instrumental systematic effects

Systematics are errors or contaminants in the measurement which cannot be described as fully-random, or not obviously Gaussian distributed variables. As mentioned in the previous part, they are one of the biggest challenges for the new cosmological observations. Typically, as it is the case for future space- or ground-based experiment, as POLARBEAR, see Part V, observers take a lot of precautions against them, submitting raw data to a wide variety of consistency checks. There are hardware and software solutions for controlling these effects. Experiments can modulate the incoming polarization thanks to quasi-opitcal systems, use ground shield to reduce and control ground pickup, submit detectors to frequent calibration runs. Many of these tests come from common sense and experimental intuition. Data analysts, on their side, can estimate some of the systematic contamination and either correct (e.g. filters) or account for them in the error budget, while extracting science information.

In this chapter I will review the main experimental systematics and introduce the Mueller formalism which gives us a modeling of the telescope optics in the case of a stationary light and an useful parametrization of those effects.

7.1 The Mueller formalism

The Stokes formalism describes polarization and intensity with a 4-vector. Operator acting on this vector, and describing for instance optics, are 4×4 matrices, called the Mueller matrices.

The fully polarized electromagnetic wave at a given time and wavelength can be fully described by the horizontal and vertical amplitudes, E_x and E_y, and the phase difference ϕ between orthogonal components of the electric fields. In addition to these three parameters, we need an extra parameter p to describe the degree of polarization,

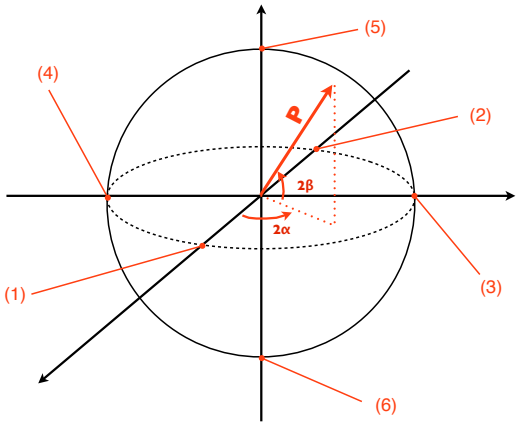

Figure 7.1: Poincaré sphere describing the state of polarization of a light beam. Numbers correspond to specific polarization states depicted in Fig. 7.2. α and β are respectively the polarization angle and the ellipticity, as defined in Eqs. 7.7 and 7.9.

defined as the ratio between the polarized intensity over the total intensity of a given beam of light. As a result, four free parameters can describe the polarized light. These parameters, written I, Q, U and V can be stored in the Stokes 4-vector and defined as

$$\mathbf{S} \equiv \begin{bmatrix} I \\ Q \\ U \\ V \end{bmatrix} \equiv \begin{bmatrix} \langle E_x^2 + E_y^2 \rangle \\ \langle E_x^2 - E_y^2 \rangle \\ \langle 2E_x E_y \cos\phi \rangle \\ \langle 2E_x E_y \sin\phi \rangle \end{bmatrix} \tag{7.1}$$

where brackets $\langle\, . \,\rangle$ indicate that each component is time-averaged assuming that the radiation is in steady state at the time scale of averaging. By introducing two geometrical parameters, the orientation of polarization α and the ellipticity β, the above equation can be rewritten in terms of intensity as

$$\begin{bmatrix} I \\ Q \\ U \\ V \end{bmatrix} = \begin{bmatrix} I_p \\ I_p \cos(2\alpha)\cos(2\beta) \\ I_p \sin(2\alpha)\cos(2\beta) \\ I_p \sin(2\beta) \end{bmatrix} + \begin{bmatrix} I_u \\ 0 \\ 0 \\ 0 \end{bmatrix} \tag{7.2}$$

where I_u and I_p are the polarized and unpolarized intensity, respectively. The first component of the Stokes vector can be normalized to one, and therefore

$$\begin{bmatrix} I \\ Q \\ U \\ V \end{bmatrix} = I \begin{bmatrix} 1 \\ p\cos(2\alpha)\cos(2\beta) \\ p\sin(2\alpha)\cos(2\beta) \\ p\sin(2\beta) \end{bmatrix} \tag{7.3}$$

with

$$p \equiv \frac{\sqrt{Q^2 + U^2 + V^2}}{I} = \frac{I_p}{I_p + I_u} \tag{7.4}$$

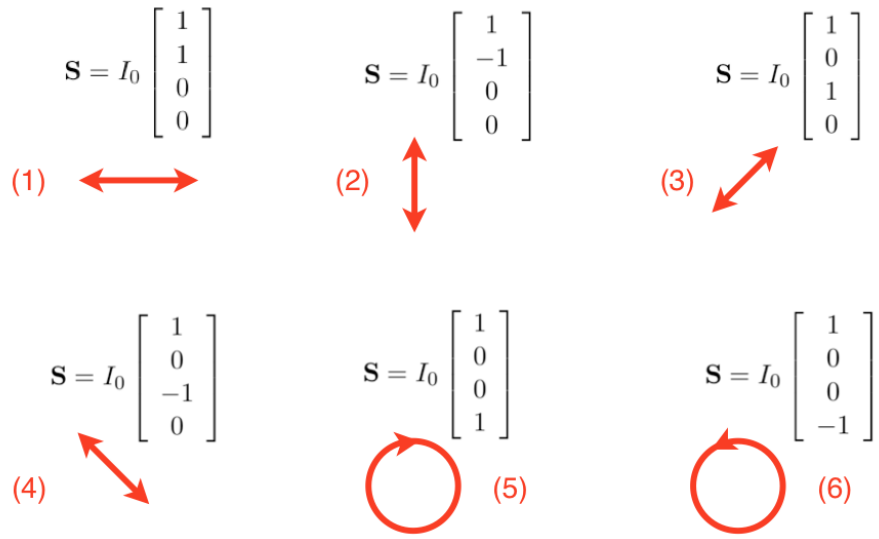

Figure 7.2: Some specific Stokes vectors, with the corresponding polarization patterns drew in red. These six different states can also be seen on the Poincaré sphere, see Fig. 7.1.

p is called the degree of polarization: $p = 1$ is the case of a fully polarized light and $p = 0$ corresponds to an unpolarized one. Therefore we have

$$0 \leq p \leq 1, \tag{7.5}$$

and this translates in the relation between the Stokes parameters

$$I^2 \geq Q^2 + U^2 + V^2, \tag{7.6}$$

where the $=$ and $>$ signs correspond to completely and unpolarized/partially polarized light, respectively.

The angle α is the polarization angle in a coordinate system, defined as

$$\alpha \equiv \frac{1}{2} \arctan\left(\frac{U}{Q}\right) \tag{7.7}$$

and the angle β is the ellipticity, defined as

$$\beta \equiv \arctan\left(\frac{E_y}{E_x}\right) \tag{7.8}$$

$$= \frac{1}{2} \arcsin\left(\frac{V}{I_p}\right) \tag{7.9}$$

Non-zero β indicates that the light is elliptically polarized, and the polarization state leaves the (xOy) plan in Fig. 7.1. In the case of the CMB, the V-component of the Stokes vector is often taken to be zero because the CMB radiation is expected to be linearly polarized, see chapter 3. Some examples of Stokes vectors are illustrated on Fig. 7.2.

7.2 General telescope optics modeling

In general, the polarization state can be changed by modifying the amplitude, the phase or by rotating it. A polarized beam with a given polarization state, while propagating through one or more polarizing elements, may acquire a new polarization state. Input beam is characterized by a Stokes vector $\mathbf{S}_{in}$ and the output beam by a vector $\mathbf{S}_{out}$. The assumption is made that $\mathbf{S}_{in}$ and $\mathbf{S}_{out}$ are linearly related by a 4×4 transformation matrix $\mathbf{M}$, known as the Mueller matrix, which represents the polarizing elements such that

$$\mathbf{S}_{out} = \mathbf{M}\,\mathbf{S}_{in} \tag{7.10}$$

$$\begin{bmatrix} I_{out} \\ Q_{out} \\ U_{out} \\ V_{out} \end{bmatrix} = \begin{bmatrix} m_{II} & m_{IQ} & m_{IU} & m_{IV} \\ m_{QI} & m_{QQ} & m_{QU} & m_{QV} \\ m_{UI} & m_{UQ} & m_{UU} & m_{UV} \\ m_{VI} & m_{VQ} & m_{VU} & m_{VV} \end{bmatrix} \begin{bmatrix} I_{in} \\ Q_{in} \\ U_{in} \\ V_{in} \end{bmatrix} \tag{7.11}$$

Only two polarizing elements are needed to change the three parameters of the polarization state (i.e. Q, U, V or equivalently the orthogonal amplitudes E_x, E_y and phase ϕ). The amplitude can be changed by using a polarizing element, also called a polarizer. Similarly, the phase of a radiation beam can be changed by a retarder, e.g. a wave plate. Finally, the polarization ellipse can be changed by rotation using a component called a rotator.

7.2.1 Typical Mueller matrices describing a new generation CMB experiment

A typical new generation CMB experiment is expected to have, in addition to mirrors and/or lenses, a retarder like a rotating Half-Wave Plate (HWP) and antenna-coupled detectors, equivalent to a grid in front of total power detectors: it filters incoming linearly polarized radiation. This type of optical system is a good description of some current and future CMB B-modes experiments, e.g. POLARBEAR, EBEX, COrE, EPIC, etc.

We can easily determine the Mueller matrix of a single HWP without taking into account the effects due to reflexions and interferences, e.g. Matsumura (90). We use here Mueller matrices to write the output signal detected by a grid detector, in the approximation of normal incidence on the HWP. Let us consider an input Stokes vector $\mathbf{S}_{in}$ of radiation propagating along the $z-$axis, incident on the polarimeter. The output Stokes vector $\mathbf{S}_{out}$ will be given by

$$\mathbf{S}_{out} \equiv \mathbf{H}\,\mathbf{S}_{in} \tag{7.12}$$

$$\equiv \mathbf{G}(p_x, p_y)\,\mathbf{R}(-2\rho)\,\mathbf{\Gamma}(\delta)\,\mathbf{R}(2\rho)\,\mathbf{S}_{in}(\alpha_{in}, \beta_{in}, P_{in}) \tag{7.13}$$

where

- $\mathbf{H}$ is the Mueller matrix describing the global optical system,
- $\mathbf{S}_{in} = \mathbf{S}_{in}(\alpha_{in}, \beta_{in}, P_{in})$ corresponds to the Stokes vector of the incoming light,
- $\mathbf{G}(p_x, p_y)$ describes the detector antenna which is the Mueller matrix of a linear polarizer,
- $\mathbf{R}(2\rho)$ is a rotation matrix — here ρ is the HWP angle,
- $\mathbf{\Gamma}$ describes a retarder, for instance a HWP, and is parametrized by δ.

The rotation matrix is

$$\mathbf{R}(\theta) \equiv \begin{bmatrix} 1 & 0 & 0 & 0 \\ 0 & \cos(\theta) & \sin(\theta) & 0 \\ 0 & -\sin(\theta) & \cos(\theta) & 0 \\ 0 & 0 & 0 & 1 \end{bmatrix}, \tag{7.14}$$

and the Mueller matrix for a linear polarizer is given by

$$\mathbf{G}(p_x, p_y) \equiv \frac{1}{2} \begin{bmatrix} p_x^2 + p_y^2 & p_x^2 - p_y^2 & 0 & 0 \\ p_x^2 - p_y^2 & p_x^2 + p_y^2 & 0 & 0 \\ 0 & 0 & 2p_x p_y & 0 \\ 0 & 0 & 0 & 2p_x p_y \end{bmatrix}, \tag{7.15}$$

where $p_{x,y}$ are the projection of a unitary vector along the antenna (or the grid) on a chosen cartesian coordinate system. The retarder changes the polarization state of a polarized beam by introducing a phase shift between the orthogonal components of the electric field. Wave plates materials include calcite, quartz, sapphire or synthetic retarders. For propagation parallel to the optical axis, the refractive indices are identical and the phases of the beam components are unaffected. However, for beam propagation perpendicular to the optical axis, the phase difference δ, also called the retardance, for a wavelength $\lambda = c/\nu$ and a thickness t is given by

$$\delta \equiv \frac{2\pi\nu}{c} (n_e - n_o)\, t, \tag{7.16}$$

where n_e and n_o are respectively the extraordinary and ordinary refraction indices. When an unpolarized beam propagates through a wave plate, the emerging beam remains unpolarized. This shows that the ordinary- an extraordinary-rays of the unpolarized beam are independent of each other. Wave plates, therefore, can only affect completely or partially polarized light. It can be shown, e.g. Collett (28), that the Mueller matrix of the birefringent optic is defined as

$$\mathbf{\Gamma}(\delta) \equiv \begin{bmatrix} 1 & 0 & 0 & 0 \\ 0 & 1 & 0 & 0 \\ 0 & 0 & \cos(\delta) & -\sin(\delta) \\ 0 & 0 & \sin(\delta) & \cos(\delta) \end{bmatrix}. \tag{7.17}$$

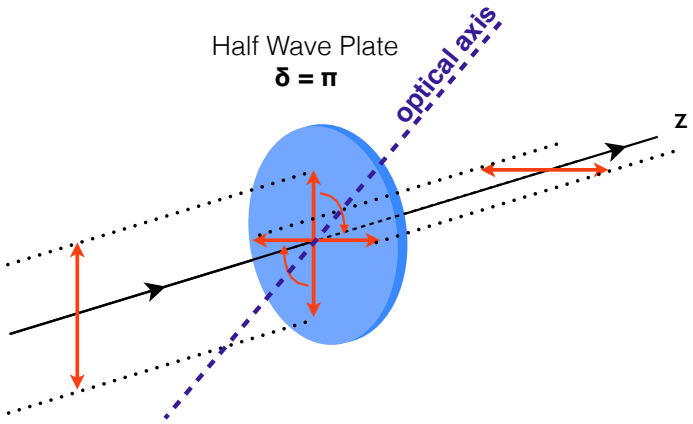

Figure 7.3: Wave plates have the property that along the $x-$axis – called the fast axis – the x component of the field experiences a phase shift of $+\phi/2$ and, similarly, along the $y-$axis – called the slow axis – the y component experiences a phase shift of $-\phi/2$. We see on this illustration the configuration for the wave plate. In the case of a Half-Wave Plate (HWP), we have $\phi = \pi$.

A perfect HWP, illustrated in Fig. 7.3, is obtained for $\delta = \pi$. Therefore, the global Mueller matrix $\mathbf{H}$ for the optical system, Eq. (7.13), containing a rotating half-wave plate and a linear polarizer is given by

$$\mathbf{H} \equiv \mathbf{G}\, \mathbf{M}_{HWP} \tag{7.18}$$

where

$$\begin{aligned} \mathbf{M}_{HWP} &\equiv \mathbf{R}(-2\rho)\, \mathbf{\Gamma}(\delta)\, \mathbf{R}(2\rho) \qquad (7.19)\\ &= \begin{bmatrix} 1 & 0 & 0 & 0 \\ 0 & \cos^2(2\rho) + \cos(\delta)\sin^2(2\rho) & (1-\cos(\delta))\cos(2\rho)\sin(2\rho) & \sin(\delta)\sin(2\rho) \\ 0 & (1-\cos(\delta))\cos(2\rho)\sin(2\rho) & \sin^2(2\rho) + \cos(\delta)\cos^2(2\rho) & -\sin(\delta)\cos(2\rho) \\ 0 & -\sin(\delta)\sin(2\rho) & \sin(\delta)\cos(2\rho) & \cos(\delta) \end{bmatrix}, \end{aligned}$$

which leads to, for a perfect HWP, i.e. $\delta = \pi$ to

$$\mathbf{M}_{HWP} = \begin{bmatrix} 1 & 0 & 0 & 0 \\ 0 & \cos(4\rho) & \sin(4\rho) & 0 \\ 0 & -\sin(4\rho) & \cos(4\rho) & 0 \\ 0 & 0 & 0 & 1 \end{bmatrix}. \tag{7.20}$$

Using the definition of $\mathbf{G}$, cf. Eq. (7.15), Eq. (7.18) reads

$$\mathbf{H} = \frac{1}{2}\begin{bmatrix} p_x^2+p_y^2 & (p_x^2-p_y^2)\cos(4\rho) & (p_x^2-p_y^2)\sin(4\rho) & 0 \\ (p_x^2-p_y^2) & (p_x^2+p_y^2)\cos(4\rho) & (p_x^2+p_y^2)\sin(4\rho) & 0 \\ 0 & 2p_xp_y\sin(4\rho) & -2p_xp_y\cos(4\rho) & 0 \\ 0 & 0 & 0 & -2p_xp_y \end{bmatrix}. \tag{7.21}$$

This matrix models the optical system of a typical CMB polarization experiment: given the incoming Stokes vector into the telescope, e.g. CMB radiation, we can predict the expected light properties at the detectors level.

7.2.2 TOD modeling

Because detectors are usually total power detectors, they only measure the total intensity of $\mathbf{S}_{out}$. Consequently, assuming that the V component is zero, the detector signal is a linear combination of I, Q and U:

$$d_t = \frac{1}{2}\left[(p_x^2+p_y^2)I + (p_x^2-p_y^2)\left(\cos(4\rho)\,Q - \sin(4\rho)\,U\right)\right]. \tag{7.22}$$

As explained in chapter 15, analyzing the detectors data consists in "inverting" Eq. (7.22), that is to say estimating the Stokes parameters I, Q and U for each pixel p on the sky using the only information we have: time stream d_t of each detector. Of course, we have to adapt this model to reality, different from the one given in Eq. (7.22) which only works for idealistic optics. I describe in the next section some of the systematic effects we could expect, giving rise to additional terms in the matrix $\mathbf{H}$.

7.3 Modeling of selected systematics

In this section, I will review and describe, in the frame of the Mueller formalism, the main systematics which can affect the new generation and future CMB polarization experiments. Some of them have been already mentioned in Table 6.1.

7.3.1 Calibration-related systematics

Gain calibration error

Gain miscalibration of the instrument will give rise to a modification of the amplitude of the time stream d_t, which is a combination of I, Q and U, as

$$d_t \equiv d_t(I,Q,U) \rightarrow \mathbf{\Omega}\, d_t, \tag{7.23}$$

where d_t is a vector containing all the detectors data, e.g. I, Q, and U, at a given time t. Ω is a diagonal matrix, which elements ω are equal to 1 in the idealistic case. Miscalibration effect could be translated into the transformation $\mathbf{H} \rightarrow \mathbf{\Omega}\,\mathbf{H}$. Moreover, one

may have to take into account for the data analysis that calibration factors are usually time dependent, because of changes in the observational environment or variations in the detectors electronic system.

Beam systematics

In reality, the I, Q and U describing the incident light beam on the instrument are convolved by the optical beam of the telescope, i.e. $\mathbf{S}_{in} \rightarrow \mathbf{S}_{beam} \equiv \text{beam} * \mathbf{S}_{in}$. Formally, Eq. (7.13) could be written as

$$\mathbf{S}_{out} = \mathbf{H}\,\mathbf{S}_{beam} \tag{7.24}$$

$$= \int_{\mathbf{r}'} d\mathbf{r}'\,\mathbf{H}\,\mathbf{B}(\mathbf{r}-\mathbf{r}')\,\mathbf{S}_{sky}(\mathbf{r}'), \tag{7.25}$$

where $\mathbf{B}(\mathbf{r}-\mathbf{r}')$ encapsulates all the information about the beam shape of the detectors through the telescope optics and $\mathbf{r}$ is a unitary 3-d space-vector.

To understand potential issues posed by beam systematics, let us consider a simple example: while observing over one given pixel on the sky, a polarized-sensitive detector will measure a signal amplitude d_1. In the case of a perfect instrument, because of the sky rotation, when the same detector will come back to this pixel, it will measure a signal amplitude $d_2 = d_1$ if the sky is not polarized (in contrast, if the pixel is polarized then $d_2 \neq d_1$). However, in the case of a not perfect instrument, we can have $d_2 \neq d_1$ for an unpolarized pixel if the beam is not well characterized. The measured signal is the integrated true sky signal over the projected beam on the sky, which can be different at the two different time 1 and 2 if, for instance, the beam has an unmeasured elongation along one specific axis and the sky has been rotated between the two different observations.

To summarize, if the beams are not well characterized, then a difference in the signal amplitude on the same sky pixel would be interpreted, in the analyzing process, as polarization.

Pointing systematics

If the detector does not really point in the direction as characterized by the observers, differences of signal for several attack angles of a sky pixel could be interpreted as a spurious polarization signal. For the ground-based CMB experiments in addition to the potential azimuth and elevation encoder issues, gravity plays a role in affecting the flexure of some parts of the telescope, and leads to errors which are not isotropic on the sky. Paragraph 15.2.3 will describe a pointing reconstruction modeling. This effect can

be included in the pointing matrix, usually written $\mathbf{A}$ which is used in the global data modeling

$$d_t = \mathbf{A}_{tp}\, s_p + n_t, \tag{7.26}$$

where d_t is the data vector in the time domain, s_p is the sky signal of the pixel p (this is what we are usually looking for) and n_t is the noise. The pointing matrix $\mathbf{A}_{tp}$ can be interpreted as a projector between pixel- and time-domains. We will see in section 7.4 how Eq. (7.26) can be generalized to include the Mueller matrices describing optical system and systematics.

7.3.2 Optical-related systematics

I present in this section how one can derive Mueller matrices in order to model systematic effects such as cross-polarization or instrumental polarization.

From Jones to Mueller formalism

In contrast to the Mueller formalism, Jones formalism describes the state of light with only two components, its electric field i.e.

$$\mathbf{E} = \begin{bmatrix} E_x \\ E_y \end{bmatrix}. \tag{7.27}$$

Let us define the $\hat{\mathbf{I}}$, $\hat{\mathbf{Q}}$, $\hat{\mathbf{U}}$ and $\hat{\mathbf{V}}$ operators as

$$\hat{\mathbf{I}} \equiv \begin{bmatrix} 1 & 0 \\ 0 & 1 \end{bmatrix} = \mathbb{1} \tag{7.28}$$

$$\hat{\mathbf{Q}} \equiv \begin{bmatrix} 1 & 0 \\ 0 & -1 \end{bmatrix} = \hat{\sigma}_{\mathbf{3}} \tag{7.29}$$

$$\hat{\mathbf{U}} \equiv \begin{bmatrix} 0 & 1 \\ 1 & 0 \end{bmatrix} = \hat{\sigma}_{\mathbf{1}} \tag{7.30}$$

$$\hat{\mathbf{V}} \equiv \begin{bmatrix} 0 & -i \\ i & 0 \end{bmatrix} = \hat{\sigma}_{\mathbf{2}}, \tag{7.31}$$

where the $\hat{\sigma}_{\mathbf{i}}$ matrices are the Pauli matrices. For any operator $\hat{\mathbf{O}} \in \left\{\hat{\mathbf{I}}, \hat{\mathbf{Q}}, \hat{\mathbf{U}}, \hat{\mathbf{V}}\right\}$ listed above, the corresponding Stokes parameter $O \in \{I, Q, U, V\}$ is given by

$$O = \mathbf{E}^T\, \hat{\mathbf{O}}\, \mathbf{E}. \tag{7.32}$$

This expression therefore relates Jones (based on $\mathbf{E}$) and Mueller formalism (using the four different O).

Cross-polarization

A device that cross-couples one polarization will transform unprimed Jones vectors to primed ones as

$$\mathbf{E}' \equiv \hat{\mathbf{C}}_\mathbf{J}\ \mathbf{E}, \tag{7.33}$$

such that

$$\begin{bmatrix} E'_x \\ E'_y \end{bmatrix} \equiv \begin{bmatrix} \sqrt{1-\epsilon} & -\sqrt{\epsilon}e^{i\psi} \\ \sqrt{\epsilon}e^{-i\psi} & \sqrt{1-\epsilon} \end{bmatrix} \begin{bmatrix} E_x \\ E_y \end{bmatrix}, \tag{7.34}$$

where the particular form of $\hat{\mathbf{C}}_\mathbf{J}$ is chosen to make it unitary. This corresponds to a rotation of the electric field. To calculate the effect of cross-pol on the measurement of a Stokes parameter, described by the operator $\hat{\mathbf{O}}$, the following construction, similar to Eq. (7.32), has to be evaluated

$$O' = \mathbf{E}^T\ \hat{\mathbf{C}}_\mathbf{J}^\dagger\ \hat{\mathbf{O}}\ \hat{\mathbf{C}}_\mathbf{J}\ \mathbf{E}. \tag{7.35}$$

This gives the output Stokes parameter O' obtained from the input Stokes parameter $\hat{\mathbf{O}}$. Using Eq. (7.35) and the definition of $\hat{\mathbf{I}}$, $\hat{\mathbf{Q}}$, $\hat{\mathbf{U}}$ and $\hat{\mathbf{V}}$ in Jones space, we are able to compute the Mueller matrix $\hat{\mathbf{C}}_\mathbf{S}$ modeling the cross-polarization:

$$\hat{\mathbf{C}}_\mathbf{S} = \begin{bmatrix} 1 & 0 & 0 & 0 \\ 0 & 1-2\epsilon & -2\sqrt{(1-\epsilon)\epsilon}\cos(\psi) & -2\sqrt{(1-\epsilon)\epsilon}\sin(\psi) \\ 0 & -2\sqrt{(1-\epsilon)\epsilon}\cos(\psi) & 1-\epsilon(1+cos(2\psi)) & -\epsilon\sin(2\psi) \\ 0 & -2\sqrt{(1-\epsilon)\epsilon}\sin(\psi) & -\epsilon\sin(2\psi) & 1-\epsilon(1-cos(2\psi)) \end{bmatrix}. \tag{7.36}$$

Instrumental-polarization

Instrumental polarization is caused by oblique light reflection on surfaces with finite conductivity. It corresponds to the leakage from I into Q, U and V. Similarly to Eq. (7.34), this effect can be modeled as

$$\begin{bmatrix} E'_x \\ E'_y \end{bmatrix} \equiv \begin{bmatrix} g_1 & 0 \\ 0 & g_2 e^{i\phi} \end{bmatrix} \begin{bmatrix} E_x \\ E_y \end{bmatrix}, \tag{7.37}$$

where g_1, g_2 are two different gains and ϕ is an additive phase. The above Jones matrix has been written in a specific basis such that instrumental polarization axis lies along the axis defined by the matrix basis. Following the same reasoning leading to Eq. (7.36), the Mueller matrix describing instrumental polarization, $\mathbf{I\hat{P}}$, is given by

$$\mathbf{I\hat{P}} \equiv \mathbf{I\hat{P}}(g_1, g_2, \phi) = \begin{bmatrix} \frac{g_1^2+g_2^2}{2} & \frac{g_1^2-g_2^2}{2} & 0 & 0 \\ \frac{g_1^2-g_2^2}{2} & \frac{g_1^2+g_2^2}{2} & 0 & 0 \\ 0 & 0 & g_1 g_2\cos(\phi) & -g_1 g_2\sin(\phi) \\ 0 & 0 & g_1 g_2\sin(\phi) & g_1 g_2\cos(\phi) \end{bmatrix}. \tag{7.38}$$

One interesting thing to note is that Q and U do not mix. This only happens because the axis of the instrumental-polarization were assumed to be along the basis in which Q and U are defined.

De-polarization

Depolarization effect can be seen as the contrary of instrumental polarization: it corresponds to the leakage from $p \equiv \sqrt{Q^2 + U^2 + V^2}$ to the unpolarized intensity I_u, cf. Eq. (7.2), and can be written as an absorption of the polarization signal i.e. $p \to \xi p$, with $\xi \leq 1$.

Thermal quadrupole pattern onto the HWP

Let assume that the Half-Wave Plate is smoothly rotating at a frequency f_{HWP}. Having a quadrupole pattern of temperature onto this plate will give rise to an extra polarization-like signal in the time stream. In fact, one can see in Eq. (7.22) that all the polarization information, i.e. Q and U, is modulated at the frequency $4f_{HWP}$. Having a quadrupole anisotropy in temperature or intensity onto the HWP will create a spurious polarization signal, with an amplitude equal to the one of the temperature quadrupole pattern on the HWP.

7.3.3 Other systematics

Cross-talk

Contrary to the previous effects, this one is not optical. Cross-talk is the consequence of having correlated electronic noises between different detectors/channels. This is mostly due to the fact that usually several detectors use the same or close wires and readout systems.

Scan-Synchronous effects

We define a scan synchronous effect as any signal that does not average down over the duration of the observation and which appears in the TOD as harmonics of the scan frequency. Those signals typically arise from a geometry that is external to the experiment or optics. For instance, far sidelobes response to the Sun, the Moon or the galactic plane will produce a scan fixed pattern. Thus the optical system needs to have a very high degree of off-axis rejection to these sources of emission. Solar heating or ground pickup can also give a scan-synchronous signal.

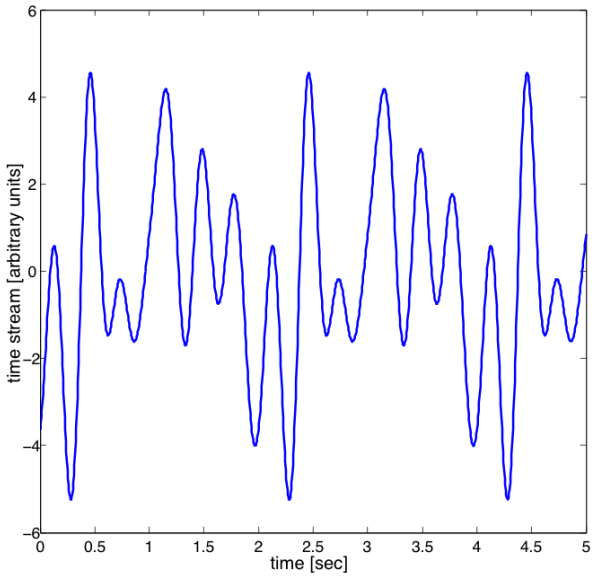

Figure 7.4: A realization of a single antenna time stream ($(p_x, p_y) = (1, 0)$), modeled using Eq. (7.41). I consider a scan frequency $f_{scan} = 0.5$ Hz and other assumptions for the incoming sky signal are given in Eqs. (7.42), (7.43) and (7.44).

Thermal drifts

Temperature drifts in the optics can produce time-varying optical signals on the detectors due to variations in thermal emission. To first order, this largely unpolarized signal is removed by the common-mode rejection of the detector pair difference. But since this filtering is not perfect, the temperature of the emitting optics must be sufficiently stable, thanks to optimized cooling system. Temperature fluctuations of the focal plane also produce false bolometer signals which mimic optical power. These fluctuations could be removed by differencing detectors — to the extent that pairs of detectors are matched.

7.4 Summary: TOD modeling including two important systematics

A bolometer, which is a total power detector, will measure $I_{out} = I_{out}(\mathbf{r}, t, \nu)$, the first component of $\mathbf{S}_{out}$. Given Eq. (7.21), considering only cross- and instrumental-polarization effects, cf. Eqs. (7.36) and (7.38), assuming that $V_{in} = 0$ and a perfect

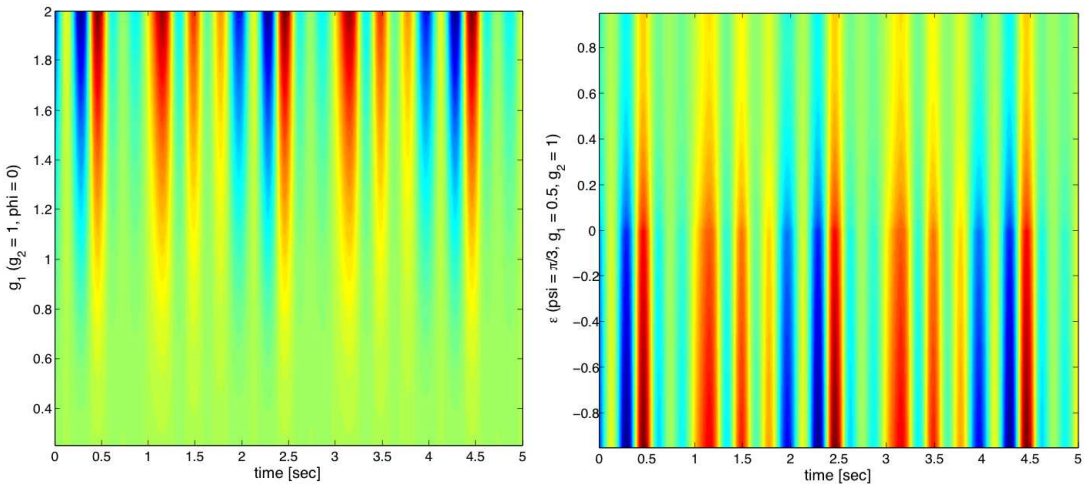

Figure 7.5: **Left panel**: effect of changing g_1 on the time stream of a single antenna with $(p_x, p_y) = (1, 0)$. I use Eq. (7.41) to model the optics of the telescope, and assume that $g_2 = 1$, $\epsilon = \psi = \phi = 0$ (no cross-polarization). Horizontal cut at $g_1 = 1$ corresponds to the time stream shown in Fig. 7.4. **Right panel**: same as left panel but showing variations of the cross-polarization parameter ϵ. I assume that HWP is fixed, $\rho = \pi/3$, that there is a related phase of $\psi = \pi/4$ and some instrumental polarization $g_1 = 0.5$, $g_2 = 1$, $\phi = 0$.

HWP, i.e. $\delta = \pi$, we get

$$
\begin{aligned}
I_{out} &= \sum_i \left(\mathbf{H}_{tot}\right)_{0i} S_{in}^{\ i} && (7.39)\\
&\equiv \sum_i \left(\mathbf{H}\cdot\mathbf{C_p}\cdot\mathbf{I_p}\right)_{0i} S_{in}^{\ i} && (7.40)\\
&= \frac{I_{in}}{2}\left\{(p_x^2+p_y^2)(g_1^2+g_2^2)+\right.\\
&\qquad \left.(p_x^2-p_y^2)(g_1^2-g_2^2)\left[(1-2\epsilon)\cos(4\rho)-2\sqrt{(1-\epsilon)\epsilon}\cos(\psi)\sin(4\rho)\right]\right\}\\
&\quad +\frac{Q_{in}}{4}\left\{(p_x^2+p_y^2)(g_1^2-g_2^2)\right.\\
&\qquad \left.(p_x^2-p_y^2)(g_1^2+g_2^2)\left[(1-2\epsilon)\cos(4\rho)-2\sqrt{(1-\epsilon)\epsilon}\cos(\psi)\sin(4\rho)\right]\right\}\\
&\quad +2g_1g_2\left(p_x^2-p_y^2\right)\frac{U_{in}}{4}\left\{-2\sqrt{(1-\epsilon)\epsilon}\cos(4\rho)\cos(\psi-\phi)\right.\\
&\qquad \left.+\left[1-\epsilon\left(1-\cos(2\psi-\phi)\right)\right]\cos(\phi)\sin(4\rho)\right\}, && (7.41)
\end{aligned}
$$

in which expression, as written in Eq. (7.25), $S_{in}^{\ i}$ are the true sky Stokes parameters convolved with the beam function of the experiment.

To illustrate Eq. (7.41), let us assume that the input Stokes parameters satisfy

$$I_{in}(t) \equiv \sum_{n=1}^{8} A_n^{(I)} \cos\left(2\pi n f_{scan} t + \phi_n^{(I)}\right) \tag{7.42}$$

$$Q_{in}(t) \equiv \sum_{n=1}^{8} A_n^{(Q)} \cos\left(2\pi n f_{scan} t + \phi_n^{(Q)}\right) \tag{7.43}$$

$$U_{in}(t) \equiv \sum_{n=1}^{8} A_n^{(U)} \cos\left(2\pi n f_{scan} t + \phi_n^{(U)}\right), \tag{7.44}$$

where $A_n^{(X)}$ are random amplitudes in arbitrary units, f_{scan} is the scan frequency and $\phi_n^{(X)}$ are random phases. Moreover, I assume that $A_n^{(Q,U)} \sim \mathcal{O}\left(A_n^{(I)}/10\right)$. Fig. 7.4 shows a realization of a time stream for a single antenna ($(p_x, p_y) = (1, 0)$) of the focal plane, assuming no systematics ($g_1 = g_2 = 1$, $\phi = \psi = \epsilon = 0$). This case corresponds to Eq. (7.22), in the case where $\rho = \text{constant} = \pi/3$ (variations of the signal are only due to the telescope scanning). Fig. 7.5 shows the same simulated noiseless time stream, assuming a fixed HWP ($\rho = \pi/3$) and including variations of cross- and instrumental-polarization parameters:

- g_1 variations keeping $g_2 = 1$ and $\epsilon = \psi = \phi = 0$ in the left panel
- ϵ variations keeping $g_1 = 0.5$, $g_2 = 1$, $\psi = \pi/4$ and $\phi = 0$ in the right panel.

Modifications of both cross- and instrumental-polarization parameters in the time streams are not easy to interpret. However, large values of g_1 lead to larger amplitude of the time stream, see left panel of Fig. 7.5: this comes from the fact that p_x is aligned with the assumed direction for g_1, cf. Eq. (7.37). The effect of cross-polarization amplitude, ϵ, is a bit similar to the previous variations, but can also imply small phase shift, depending on the other assumptions about instrumental polarization. In any case, cross- and instrumental-polarization clearly create spurious polarization signal in the time stream, which can potentially contaminate the encapsulated cosmological informations.

We will see in section 15.4 how it is possible to estimate those parameters, i.e. mainly ϵ, g_1 and g_2, from a noisy time stream and using a parametric maximum likelihood approach.

Chapter 8

Atmospheric contamination

Section 8.1 briefly introduces the problems induced by atmosphere. After a succinct description of the atmospheric emission in section 8.2, I describe the turbulence mechanism and its models as assumed in the following computation, see section 8.3. Finally, in section 8.4, I present some of the results as obtained here and their conclusions.

8.1 Introduction

Observation of the CMB temperature and polarization can be performed from the ground using specific frequency bands called "windows", for which atmosphere is almost transparent to electromagnetic waves. However, atmosphere appears to be the warmest body along the line of sight of the ground-based experiments. Water vapor molecules radiate at radio and millimeter wavelengths, see e.g. Fig. 8.1 showing the spectral emissivity of those molecules. These latter are also involved in turbulent processes, driven by complex mechanisms which depend on the properties of the atmosphere above a given observation site. This turbulence results in correlations between detectors both temporal and spatial. Indeed, the atmospheric signal in instantaneous measurements of a ground-based experiment as taken by two different detectors as well as the noise in the measurements of the same detector undertaken at different times are both expected to be correlated, with the correlations in the latter case depending on the scan strategy and the wind. If treated as an additional noise-like component, atmospheric contamination results in an important additional $1/f$ noise in a time stream of any specific detector, but also decreases a number of statistically independent measurements as made by a single focal plane. Alternately, at least under some assumptions, e.g., whenever the scan speed is much larger than the wind speed, atmosphere can lead to the creation of nearly scan synchronous signals. Though atmospheric signal is expected to be largely non-polarized optical systematics such as instrumental polarization or imperfect half-wave plates, see chapter 7, can turn it into polarized signals. Atmosphere can therefore be

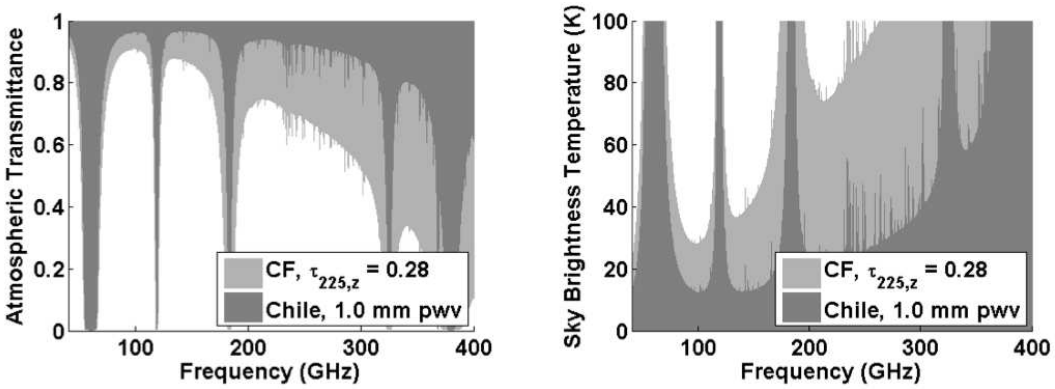

Figure 8.1: **Left panel:** atmospheric transmittance for the Cedar Flat (CF) site, light grey, and for the Chilean site, dark grey. **Right panel:** sky brightness temperature in Kelvins for an elevation of 60 deg. From Arnold (6).

considered as one of the most insidious sources of systematic effect. Nowadays, because of its complexity, its varying and poorly known behavior, atmosphere is removed by data analysts using filters based on effective models such as Lay and Halverson (79).

More precisely, turbulence dissipates energy at unknown scales and have properties depending on e.g. the observation site (dryness, air density, etc.) and on the time of the observation (temperature, pressure, etc.). Moreover, additional wind shears atmospheric structures: all those factors make the modeling arduous. However, in the case of a given experimental setup (focal plane, scan strategy, etc.), some assumptions can be made and a model implemented. In order to obtain some insights into role and properties of the atmospheric signals I have developed a numerical code which aims at simulating the atmospheric contamination, in particular the induced time-dependent correlation between detectors.

8.2 Atmospheric absorption and emission

Atmosphere is a medium absorbing and emitting radiation in the microwave frequency range, especially due to the excitation of rotational modes of water vapor molecules, at 183 GHz, and molecular oxygen, at 117 GHz, see e.g. Spinelli et al. (128). Note that throughout this chapter, I assume that atmosphere only emits unpolarized light – note that this latter can be transformed into linear polarized radiation due to instrumental- or cross-polarization effects[1]. Ground-based and balloon-borne experiments frequency

[1]Hanany and Rosenkranz (60) were the first to point out that the main atmospheric polarized contaminant is the circularly polarized Zeeman emission of molecular oxygen (O_2). I consider that the discussed experiments are not sensitive to V-modes but we could still observe a leak of V into Q, U in the case of a non-perfect experimental setup.

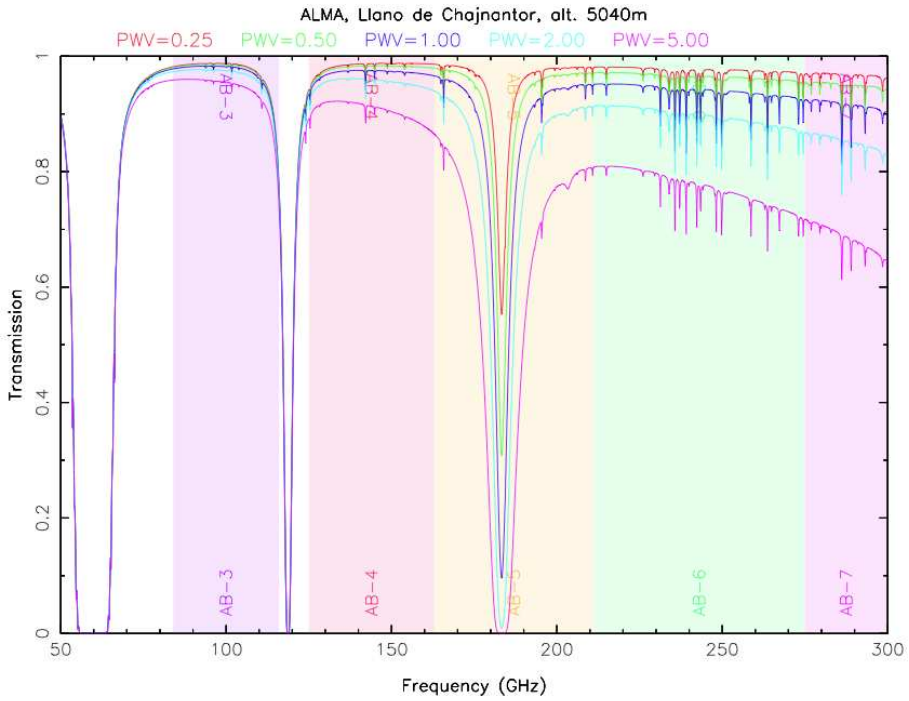

Figure 8.2: Atmospheric transmittance between 50 and 300 GHz, as computed by the online software at almascience.nrao.edu, based on ATM library (100), for different PWV at the Chajnantor plateau.

bands are chosen to avoid those emission lines, but they are still affected by the continuum emission from the combined action of the extended tails of other emission lines at higher frequencies.

It is usual to model the atmosphere as a grey body, such that the atmospheric emission in the Rayleigh-Jeans regime, cf. Eq. (3.3), reads

$$I_{atm} \propto \nu^2 \, T_{atm} \, (1 - \kappa) \tag{8.1}$$

$$\propto \nu^2 \, T_{RJ}, \tag{8.2}$$

where $\kappa \equiv e^{-\tau A}$ is the transmission coefficient, τ - the optical depth, A - the air mass[1] ($A \propto 1/\sin(el)$ for $el \gtrsim 30\,\mathrm{deg}$) and T_{atm} - the atmosphere temperature. The quantity T_{RJ}, defined as

$$T_{RJ} \equiv T_{atm} \left(1 - e^{-\tau A}\right), \tag{8.4}$$

[1]Opacity (or optical depth) τ encodes how the atmosphere attenuates transmitted signals and radiates as a grey body. The specific intensity $I_{in}(\nu)$ of a cosmic signal transmitted through the atmosphere is decreased to $I_{out}(\nu)$ such that

$$I_{out}(\nu) = I_{in}(\nu) e^{-\tau A}. \tag{8.3}$$

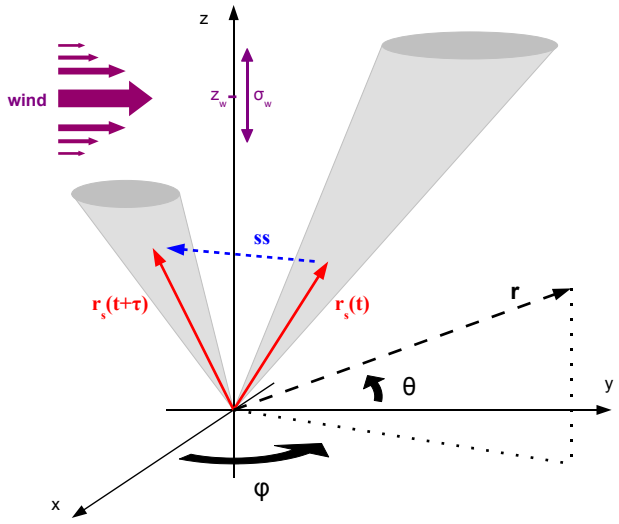

Figure 8.3: A detector of the focal plane observes along a vector $\hat{\mathbf{r}}_\mathbf{s}$ (line of sight), defined in spherical coordinates ϕ and θ (equivalently azimuth and elevation).

is the equivalent Rayleigh-Jeans temperature of the atmosphere.

We define the Precipitable Water Vapor (PWV), expressed in mm, as the amount of water vapor in the atmosphere contained in a vertical column of unit cross-sectional area above a given site extending between two given levels. The PWV can be related to the temperature T_{RJ}, defined in Eq. (8.4), following the ATM software (100),

$$T_{RJ} \sim (6.0 \times \text{ PWV[mm]} + 3.5)\,\text{K}. \tag{8.5}$$

The effect of PWV variations on atmospheric transmission is illustrated in Fig. 8.2, around 150 GHz and as predicted for the ALMA site.

8.3 Atmospheric turbulence, modeling

In addition to its overall intensity I_{atm}, inhomogeneities in the atmosphere emission, due to turbulence along the line of sight, are encoded in the observations when the telescope is scanning across the sky. As mentioned at the beginning of this chapter, those correlations are difficult to model because of their dependence on poorly characterized atmospheric status. In paragraphs 8.3.1 and 8.3.2 are introduced two main models describing the expected atmospheric contamination for current CMB experiments.

8.3.1 Church model

The model described in Church (26) considers the atmosphere as a continuum medium that evolves as one moves up away from the telescope. Turbulence is assumed to be

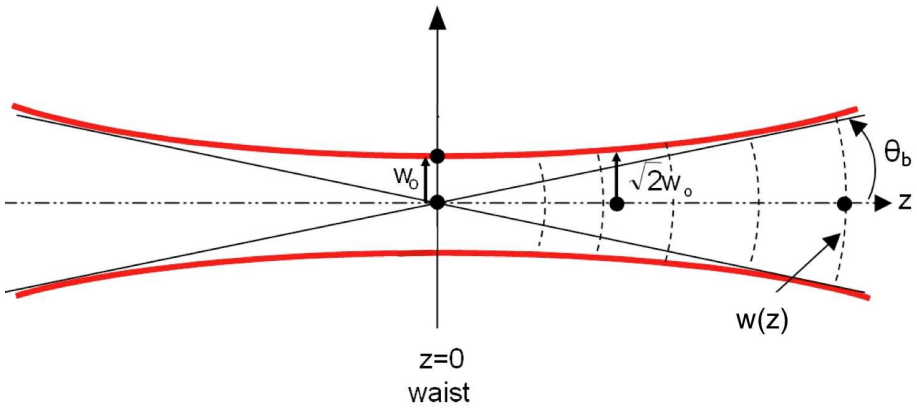

Figure 8.4: Assumed Gaussian beam of a detector, as described by Eqs. 8.10 and 8.11. The waist of the beam, w_0, is defined as the size of the beam for $z = 0$. For large z, $w(z)$ has a slant asymptotic with slope θ_b.

described by a Kolmogorov power law, i.e.

$$P(\|\mathbf{k}\|) \propto \|\mathbf{k}\|^{-\gamma}, \tag{8.6}$$

where $\mathbf{k}$ is the three dimensional wave number. A typical distance L_0 is introduced to describe the typical scale of the turbulence.

In the following descriptions, we use the geometry depicted in Fig. 8.3. Contrary to the formalism used in Church (26), which is expressed in cartesian coordinates, I present the model using spherical coordinates, which are more suitable for scanning experiments.

As detailed in the following paragraph, the atmosphere contribution to the antenna temperature from a given point is proportional to the effective area of the telescope as seen from that point. For the moment, no assumptions are done on the experimental level: a detector of the focal plane simply observes along a vector $\hat{\mathbf{r}}_\mathbf{s}$ (this is the line of sight), defined in spherical coordinates by ϕ and θ, equivalently azimuth and elevation.

8.3.1.1 Water vapor distribution, atmosphere temperature, turbulence

It is usual, in observational cosmology, to switch from intensity (in W.Hz^{-1}.m^{-2}.sr^{-1}) to antenna temperature (in Kelvins): as we have seen in Eq. (8.4), both quantities are proportional in the Rayleigh-Jeans approximation. The experiment we consider in the following is an imager measuring a total intensity in Kelvins. Let us consider that this latter has a beam, related to an effective area B, pointing in a given direction $\hat{\mathbf{r}}_\mathbf{s}$. The contribution dT_{ant} to the antenna temperature, of a small element dV of atmosphere located at $\mathbf{r}$, is given by

$$dT_{ant}(\mathbf{r}) = B(\hat{\mathbf{r}}_\mathbf{s}, \mathbf{r}) \times \alpha(\mathbf{r}) \times T_{phys}(\mathbf{r}) \times \frac{dV}{r^2}, \tag{8.7}$$

where $\alpha(\mathbf{r})$ is the atmospheric absorption or opacity coefficient[1] and $T_{phys}(\mathbf{r})$ is the physical temperature of the given volume of atmosphere. Notice that Eq. (8.7) is not homogeneous and a factor λ^{-2} (λ being the wavelength of observation in meters) should be in front of the r.h.s. term. All the following equations do not include this factor. First, it is convenient to assume that this latter can be written as in the adiabatic case, i.e. the temperature depends linearly on the altitude z,

$$T_{phys}(\mathbf{r}) \equiv T_{phys}(z) = T_0 \left(1 - \frac{z}{z_{atm}}\right), \tag{8.9}$$

with T_0 the temperature in Kelvins at the ground level and z_{atm} a typical height which depends on the observation site.

Second, the effective area of the beam is assumed to be Gaussian such that, for a monochromatic detector,

$$B(\hat{\mathbf{r}}_\mathbf{s}, \mathbf{r}) = \frac{2\lambda^2 |\hat{\mathbf{r}}_\mathbf{s} \cdot \mathbf{r}|^2}{\pi w^2(\hat{\mathbf{r}}_\mathbf{s} \cdot \mathbf{r})} \times \exp\left(-\frac{2(\mathbf{r}^2 - (\hat{\mathbf{r}}_\mathbf{s} \cdot \mathbf{r})^2)}{w^2(\hat{\mathbf{r}}_\mathbf{s} \cdot \mathbf{r})}\right), \tag{8.10}$$

where

$$w(\hat{\mathbf{r}}_\mathbf{s} \cdot \mathbf{r}) = w_0 \sqrt{1 + \left(\frac{\lambda \times \hat{\mathbf{r}}_\mathbf{s} \cdot \mathbf{r}}{\pi w_0^2}\right)^2}, \tag{8.11}$$

with w_0 the beam waist given by $w_0 \equiv \lambda/(\pi \times \theta_b)$. θ_b is the beam opening angle. The geometry of this type of beam is depicted in Fig. 8.4. Note that for large distances from the telescope, i.e. for $|\hat{\mathbf{r}}_\mathbf{s} \cdot \mathbf{r}| \gg 1$, $w(\hat{\mathbf{r}}_\mathbf{s} \cdot \mathbf{r})$ has a slant asymptotic with slope θ_b.

8.3.1.2 Analytical expression for the auto- and cross-correlation between detectors

General expression

Let us assume that the direction $\hat{\mathbf{r}}_\mathbf{s}$ depends on time (telescope line of sight is driven by the scan strategy). Using Eq. (8.7), $T_{ant}(t)$ can be written as

$$T_{ant}(t) \equiv T_{ant}(\hat{\mathbf{r}}_\mathbf{s}(t)) = \int d\mathbf{r}\; B(\hat{\mathbf{r}}_\mathbf{s}(t), \mathbf{r}) \times \alpha(\mathbf{r}) \times T_{phys}(\mathbf{r}). \tag{8.12}$$

[1] We set the opacity τ defined before as

$$\tau = \int_0^R \alpha(r) dr, \tag{8.8}$$

where R is the total path length through the atmosphere.

Assuming the stationarity in time of the atmospheric contamination, the autocorrelation for a single detector between two different times is defined as

$$\begin{aligned} C(\tau) &\equiv \langle T_{ant}(t)T_{ant}(t+\tau)\rangle & (8.13)\\ &\equiv \langle T_{ant}(\hat{\mathbf{r}}_\mathbf{s}(t))T_{ant}(\hat{\mathbf{r}}_\mathbf{s}(t+\tau))\rangle & (8.14)\\ &= \iint d\mathbf{r}d\mathbf{r}' B(\hat{\mathbf{r}}_\mathbf{s}(t),\mathbf{r})B(\hat{\mathbf{r}}_\mathbf{s}(t+\tau),\mathbf{r}')\times A(\mathbf{r},\mathbf{r}')\times T_{phys}(\mathbf{r})T_{phys}(\mathbf{r}') & (8.15)\end{aligned}$$

with $A(\mathbf{r},\mathbf{r}') \equiv \langle\alpha(\mathbf{r})\alpha(\mathbf{r}')\rangle$. More generally, the cross-correlation $C_{ij}(\tau)$ for any τ between two detectors i and j reads

$$\begin{aligned} C_{ij}(\tau) &\equiv \langle T_{ant}^{(i)}(t)T_{ant}^{(j)}(t+\tau)\rangle & (8.16)\\ &\equiv \langle T_{ant}(\hat{\mathbf{r}}_\mathbf{s}^{(\mathbf{i})}(t))T_{ant}(\hat{\mathbf{r}}_\mathbf{s}^{(\mathbf{j})}(t+\tau))\rangle & (8.17)\\ &= \iint d\mathbf{r}d\mathbf{r}' B(\hat{\mathbf{r}}_\mathbf{s}^{(\mathbf{i})}(t),\mathbf{r})B(\hat{\mathbf{r}}_\mathbf{s}^{(\mathbf{j})}(t+\tau),\mathbf{r}')\times A(\mathbf{r},\mathbf{r}')\times T_{phys}(\mathbf{r})T_{phys}(\mathbf{r}'). & (8.18)\end{aligned}$$

It has to be noticed that the only time dependence in Eq. (8.18) is encoded in the scan strategy $\hat{\mathbf{r}}_\mathbf{s}$. This is only true if no wind is assumed. As it will be described in the next paragraph, this latter will affect the correlation term $\langle\alpha(\mathbf{r})\alpha(\mathbf{r}')\rangle$. In addition, quantities in Eq. (8.18) depend on the atmosphere properties, hidden in the $\langle\alpha(\mathbf{r})\alpha(\mathbf{r}')\rangle \times T_{phys}(\mathbf{r})T_{phys}(\mathbf{r}')$ term, and on the experimental design and operation, included in the $B(\hat{\mathbf{r}}_\mathbf{s}^{(\mathbf{i})}(t),\mathbf{r})B(\hat{\mathbf{r}}_\mathbf{s}^{(\mathbf{j})}(t+\tau),\mathbf{r}')$ term.

Correlation induced by atmosphere

In Eq. (8.15), I reduced the correlation $\langle\cdot\rangle$ between two given points $\mathbf{r}$ and $\mathbf{r}'$ in the atmosphere to the $\langle\alpha(\mathbf{r})\alpha(\mathbf{r}')\rangle$ term. Fluctuations in α as the atmosphere drifts through the beam of the telescope cause temporal varying contamination in the observed brightness temperature. We follow Church (26) and assume that

$$\begin{aligned} \langle\alpha(\mathbf{r})\alpha(\mathbf{r}')\rangle &\equiv \chi_{no\,st}(\mathbf{r},\mathbf{r}')\times\chi_{st}(\mathbf{r},\mathbf{r}') & (8.19)\\ &\equiv \chi_{no\,st}(\|\mathbf{r}-\mathbf{r}'\|)\times\chi_{st}(z+z') & (8.20)\end{aligned}$$

First, $\chi_{no\,st}$ is the non-stationary part of the correlation, effective for lengths satisfying $|\mathbf{r}-\mathbf{r}'| \lesssim L_0$ and can be assumed Gaussian, i.e.

$$\chi_{no\,st}(\mathbf{r},\mathbf{r}') \propto \exp\left(-\frac{\|\mathbf{r}-\mathbf{r}'\|^2}{2L_0^2}\right). \quad (8.21)$$

This term is qualified of non-stationary because of the effect of the wind on it, as introduced after. As depicted in Fig. 8.5, one can show that this term is nearly equivalent to Kolmogorov turbulence given by

$$\chi_{no\,st}^{\text{Kolm.}}(\mathbf{r},\mathbf{r}') \propto \int_{\kappa_{min}}^{\kappa_{max}} \kappa^{-11/3}\text{sinc}\left(\kappa\|\mathbf{r}'-\mathbf{r}\|\right)d\kappa, \quad (8.22)$$

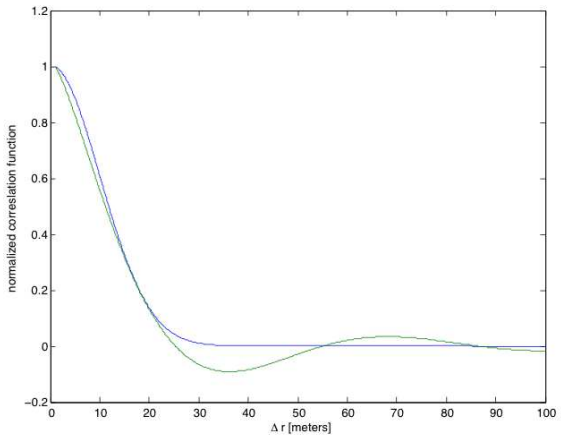

Figure 8.5: Comparison of $\chi_{no\,st}^{\rm Kolm.}$ (green) given by Eq. (8.22) and $\chi_{no\,st}(\Delta r)$ (blue), given in Eq. (8.21). Here I set $L_0 = 10$ m, $\kappa_{min} = L_0^{-1} = 0.1\ m^{-1}$ and $\kappa_{max} = 1000\ m^{-1}$.

where κ_{min} and κ_{max} are proportional to the inverse of atmospheric turbulence typical lengths, respectively outer (incoming energy) and inner (energy dissipation) turbulence scales.

Second, χ_{st} is the stationary part, effective for large scales which depends only on the height, and can be interpreted as the water vapor distribution, here assumed to be a decreasing exponential of the altitude, i.e.

$$\chi_{st}(\mathbf{r},\mathbf{r}') \quad \propto \quad \exp\left(-\frac{z+z'}{2\,z_0}\right). \tag{8.23}$$

Wind

I assume that the wind affects only a horizontal layer of the atmosphere. We expect wind to shear the turbulent structures encoded in the $\langle\alpha(\mathbf{r})\alpha(\mathbf{r}')\rangle$ correlation term. Because it does not mix parts of the atmosphere at two different altitudes, the wind will not affect χ_{st} defined in Eq. (8.23). Therefore, it affects the non-stationary part of the correlation, $\chi_{no\,st}(\mathbf{r},\mathbf{r}')$, and implies this latter to be time dependent, $\chi_{no\,st}(\mathbf{r},\mathbf{r}') \to \chi_{no\,st}(\mathbf{r},\mathbf{r}',\tau)$. The latter will only depend on a time difference $\tau = t - t'$, because we assume the contamination to be stationary in time: wind is assumed to be constant in time, velocity and direction. As shown in Fig. 8.3, it blows in a layer centered at a given altitude z_w^0, following a Gaussian distribution with a width σ_w. Using Eq. (8.21), and switching to cartesian coordinates, $\chi_{no\,st}(\mathbf{r},\mathbf{r}',\tau)$ can be written as

$$\chi_{no\,st}(\mathbf{x},\mathbf{y},\mathbf{z},\mathbf{x}',\mathbf{y}',\mathbf{z}',\tau) = \exp\left(-\frac{1}{2L_0^2}\left[|(x - ws_x(z)\tau) - (x' - ws_{x'}(z')\tau)|^2 \right.\right.$$
$$\left.\left. +|(y - ws_y(z)\tau) - (y' - ws_{y'}(z')\tau)|^2 + |z - z'|^2\right]\right), \tag{8.24}$$

where $ws_x(z)$ and $ws_y(z)$ are the components of the wind speed along, respectively, the x and y directions, at a given altitude z.

8.3.2 Lay & Halverson model

Lay and Halverson (79) modeled the turbulent layer as a frozen screen of thickness Δh — determining the power law of the turbulence —, at height h_{atm}. In comparison with the approach described previously, see paragraph 8.3.1, the condition that defines the observed power law (in the time stream) does not depend on the telescope properties, but only on the physical characteristics of the turbulent layer. Lay and Halverson (79) show that the power spectrum of the atmospheric brightness, $P_{T_{atm}}$, can be expressed as

$$P_{T_{atm}} \equiv \langle T^2(\alpha_x, \alpha_y) \rangle \tag{8.25}$$

$$= \frac{A_{LH}}{\sin\epsilon}\left[\frac{h_{atm}}{\sin\epsilon}\right]^{-5/3} \times \|\alpha\|^{-11/3} \text{ if } \frac{h_{atm}}{2\Delta h \sin\epsilon} \ll \|\alpha\| \ll \alpha_{\text{inner}} \tag{8.26}$$

$$\text{or } \frac{A'_{LH}}{\sin\epsilon}\left[\frac{h_{atm}}{\sin\epsilon}\right]^{-2/3} \times \|\alpha\|^{-8/3} \text{ if } \alpha_{\text{outer}} \ll \|\alpha\| \ll \frac{h_{atm}}{2\Delta h \sin\epsilon}. \tag{8.27}$$

Here $\|\alpha\| \equiv \sqrt{\alpha_x^2 + \alpha_y^2}$ and $\alpha_{x,y}$ denotes the angular wavenumbers defined as

$$\alpha_{x,y} \equiv \frac{k_{x,y}\, h_{atm}}{\sin\epsilon}, \tag{8.28}$$

with $k_{x,y}$ the spatial wavenumbers, following the notations of Fig. 8.6. The constants A_{LH} and A'_{LH} in Eq. (8.27) correpond to the amplitude of the turbulence. Similarly to the κ quantities in Eq. (8.22), α_{inner}, α_{outer} are related to, respectively, inner and outer physical scales of the turbulence. Within these bounds there is a small-scale regime where the three-dimensional conditions of the Kolmogorov model are sustained, Eq. (8.6), and the power spectrum behaves as a power law with an index $\gamma = -11/3$. For scales greater than $2\Delta h$, the two-dimensional regime dominates and the power law index becomes $\gamma = -8/3$.

8.4 Simulations of atmospheric contamination

In this section, I present two different ways of simulating pure-atmospheric time streams. This could give us intuition in order to construct cleaning methods or optimize filters (more details are presented in section 15.5). First, in paragraph 8.4.1, we see what does an assumed turbulence power law imply for the time streams properties and second, in paragraph 8.4.2, I present some results coming from the implementation of Church's approach.

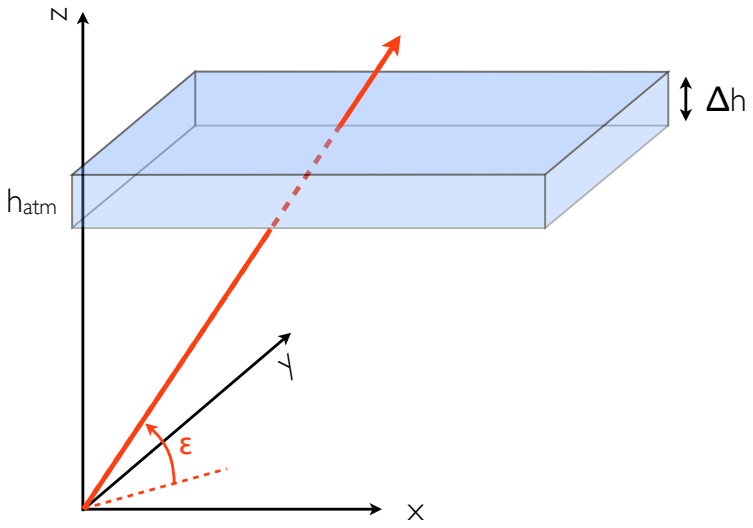

Figure 8.6: Geometry and notations corresponding to the Lay and Halverson (79) approach.

8.4.1 Assuming a power law for the atmospheric turbulence

We consider that atmospheric contamination follows a decreasing power law power spectrum. More precisely, let us consider the brightness temperature of the atmosphere to be a power law in wave number space i.e.

$$T_{atm}(\mathbf{k},t) \equiv A\|\mathbf{k}\|^{\gamma} e^{j\phi(\|\mathbf{k}\|,t)}. \tag{8.29}$$

The time-dependent phase $\phi(\|\mathbf{k}\|,t)$ allows the atmosphere features to change in time. By Fourier transform Eq. (8.29), $T_{atm}(\mathbf{r},t)$ reads

$$T_{atm}(\mathbf{r},t) = A\int d\|\mathbf{k}\|\ \|\mathbf{k}\|^{\gamma}\ e^{j\phi(\|\mathbf{k}\|,t)+2\pi j\|\mathbf{r}\|\ \|\mathbf{k}\|} \tag{8.30}$$

Let us assume that the detector scans across the atmosphere pattern at a given "effective" velocity: this latter would result from the combination of the scan and wind speeds. Then we write $\mathbf{r}(t) \equiv \mathbf{v}t$, where $\mathbf{v} = \mathbf{v}_{scan} + \mathbf{v}_{wind}$ is the effective speed. Injecting this into Eq. (8.30) gives

$$T_{atm}(\mathbf{r},t) = T_{atm}(t) \quad = \quad A\int d\|\mathbf{k}\|\ \|\mathbf{k}\|^{\gamma}\ e^{j\phi(\|\mathbf{k}\|,t)+2\pi j\|\mathbf{v}\|\ \|\mathbf{k}\|t}. \tag{8.31}$$

In frequency domain, this leads to

$$T_{atm}(f) = A\iint dt\, d\|\mathbf{k}\|\ \|\mathbf{k}\|^{\gamma}\ \exp\left[j\phi(\|\mathbf{k}\|,t) + 2\pi j\left(\|\mathbf{v}\|\ \|\mathbf{k}\| - f\right)t\right]. \tag{8.32}$$

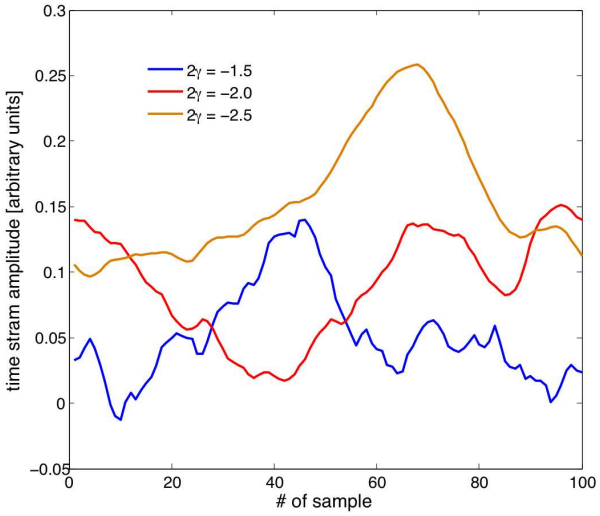

Figure 8.7: Illustration of several simulated time streams having a power-law power spectrum as $P_{atm}(f) \propto f^{2\gamma}$, Eq. (8.36), obtained for different values of γ.

If the phase is independent on time, i.e. $\phi(\|\mathbf{k}\|, t) = \phi(\|\mathbf{k}\|)$, then we have

$$T_{atm}(f) = A \int d\|\mathbf{k}\| \, \|\mathbf{k}\|^{\gamma} \, e^{j\phi(\|\mathbf{k}\|)} \int dt \exp\left[2\pi j \left(\|\mathbf{v}\| \, \|\mathbf{k}\| - f\right) t\right] \tag{8.33}$$

$$= A \int d\|\mathbf{k}\| \, \|\mathbf{k}\|^{\gamma} \, e^{j\phi(\|\mathbf{k}\|)} \delta(\|\mathbf{v}\| \, \|\mathbf{k}\| - f) \tag{8.34}$$

$$= A \left[\frac{f}{\|\mathbf{v}\|}\right]^{\gamma} e^{j\phi(\frac{\mathbf{f}}{\|\mathbf{v}\|})}. \tag{8.35}$$

The power spectrum $P_{atm}(f)$ resulting from the atmospheric turbulence, as seen in the time stream $T_{atm}(f)$, then satisfies

$$P_{atm}(f) \propto f^{2\gamma}. \tag{8.36}$$

Realizations of such time stream are depicted in Fig. 8.7. More generally, we understand from Eq. (8.36) that atmospheric contamination is important at low frequencies. CMB data analysts need efficient and smart high pass filters to remove those signals without taking away cosmological informations also present in the time stream.

8.4.2 Trials for a numerical computation of the Church model

In this section I present some consequences of the implementation of the Church's model, introduced in paragraph 8.3.1, for the correlation in time between detectors of a typical ground-based experiment focal plane, as a function of the wind speed, the field of view as well as the atmosphere properties.

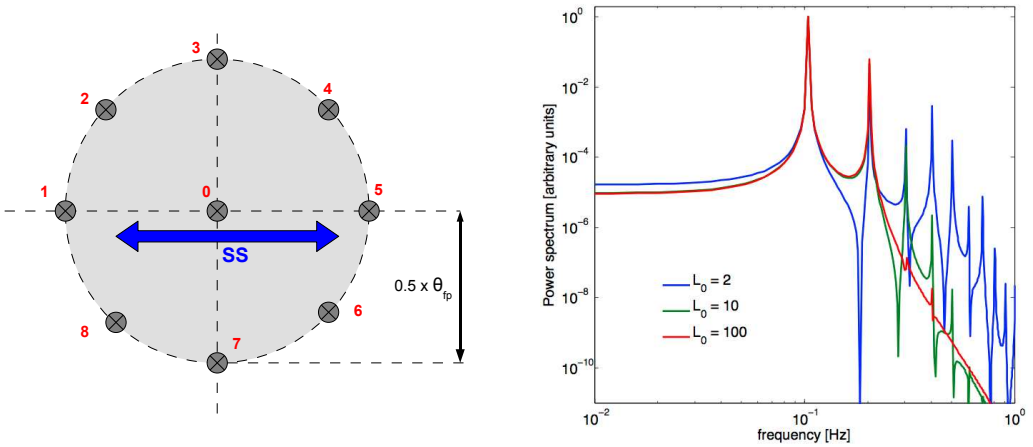

Figure 8.8: **Left panel**: assumptions made about the focal plane layout and the scan strategy (**SS**). The focal plane is composed of 9 detectors, 8 of them are disposed on a circle of radius $\theta_{fp}/2$ and one at the center. The scan strategy direction is assumed to be parallel to the line joining detectors 1, 0 and 5, as modeled in Eq. (8.37). **Right panel**: illustration of the effect of varying the L_0 parameter, the turbulence typical scale, on the atmospheric signal power spectrum. As we could expect, the larger L_0 is, the lower will be the contamination at high frequency.

8.4.2.1 Assumptions : scan strategy, focal plane layout

We set the scan strategy of the telescope, $\hat{\mathbf{r}}_\mathbf{s}(t)$, to be constant in elevation ($\theta_s(t) = \theta_{s,0} = \pi/4$ for the numerical computations) and to move only in azimuth, following a cosine function, such as

$$\phi_s(t) = \phi_{s,0} + \frac{\Delta\phi}{2}\cos\left(2\pi f_{scan} t + \psi\right), \tag{8.37}$$

where we set $\Delta\phi$ to be the angular size of the scan strategy (usually on the order of a couple of degrees for CMB observations) and $f_{\rm scan}$ the scan frequency, defined as

$$f_{\rm scan} \equiv \frac{\text{scan speed}\,[\text{deg}\,.\text{s}^{-1}]}{2\,\Delta\phi}. \tag{8.38}$$

For the following numerical computation, I assume $\Delta\phi = 10$ deg and a scan speed of 2 deg $.s^{-1}$ (as well as $\phi_{s,0} = \psi = 0$), which leads to a scan frequency $f_{scan} = 0.1$ Hz. In addition, I consider the specific focal plane layout depicted in the left panel of Fig. 8.8.

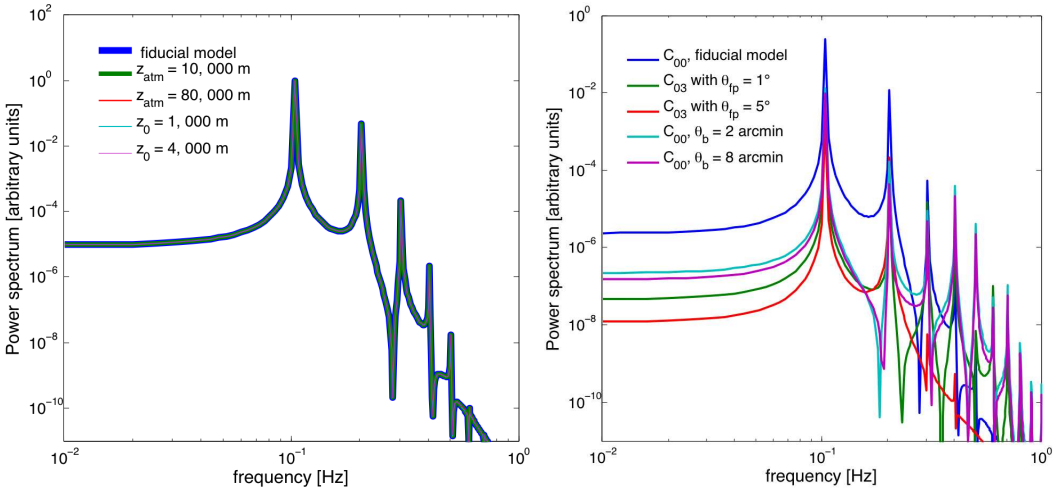

Figure 8.9: **Left panel**: auto power spectrum in the case of z_{atm} and z_0 variations. Differences between the curves are negligible. **Right panel**: effect of changing the focal plane size on the cross-power spectrum between detectors 0 and 3 (called C_{03}) and effect of the beam size. The bigger is the angular distance between the detectors 0 and 3, the lower will be the cross-power spectrum. In addition, increasing the beam size, gives rise to higher power spectrum.

8.4.2.2 Results for the correlation across the focal plane

Implementation

Computation of correlations in time between detectors is not trivial and computationally heavy because it involves, for each time sample, integrations over two three-dimensional spaces. I use a Quasi Monte Carlo method[1], as implemented in MATHEMATICA, to estimate numerically the 6-integrals included in the expression of $C_{ij}(\tau)$, cf. Eq. (8.18). I present below some of the obtained results.

Auto-correlation without wind

The first results are about the correlation in time for a single detector, the 0^{th} of the focal plane, see left panel of Fig. 8.8. Right panel of Fig. 8.8 shows the corresponding power spectra (the Fourier transform of the auto-correlation $C_{00}(\tau)$) for different values of the atmosphere properties, L_0 introduced in Eq. (8.21).

[1]Quasi-Monte Carlo method is similar to the Monte Carlo method but using quasi-random sequences instead of random numbers. The quasi-random sequences, also called low-discrepancy sequences, can permit to improve the performance of Monte Carlo methods, offering shorter computational times and/or higher accuracy.

Parameters describing atmosphere properties are chosen such that

$$L_0 \in \{2; \mathbf{10}; 100 \text{ meters}\}, \tag{8.39}$$

$$z_0 \in \{1,000; \mathbf{2,000}; 4,000 \text{ meters}\}, \tag{8.40}$$

$$z_{atm} \in \{10,000; \mathbf{40,000}; 80,000 \text{ meters}\}, \tag{8.41}$$

in which expressions the bold numbers correspond to the fiducial model.

The main feature of these power spectra is the presence of peaks, harmonics of the scan frequency $f_{scan} = 0.1$ Hz for the specific numerical values chosen here. One should see atmosphere as a medium with structures of specific size L_0 and, as it is the case with the CMB signal, its contamination appears as a scan-synchronous signal. Effect of changing L_0 is depicted in the right panel of Fig. 8.8: smaller turbulent structures result in more power for high frequency harmonics.

Variations of z_{atm} and z_0 are illustrated in the left panel of Fig. 8.9. The auto-power spectrum changes by tiny amounts which are undistinguishable in this figure. This is mainly due to the fact that, in our model, the atmospheric contamination comes mainly from low altitudes, $z \ll z_0$, z_{atm}, where both T_{atm} and χ_{st} terms, cf. Eqs. (8.9) and (8.23), are large:

$$T_{atm} \propto -\frac{z}{z_{atm}} \tag{8.42}$$

$$\chi_{st} \propto e^{-\frac{z}{z_0}}. \tag{8.43}$$

Cross-correlation without wind

The cross-correlation, i.e. the correlation between detectors at different time is an interesting quantity to study variations of the telescope design, especially θ_b and θ_{fp} (fiducial model is obtained for $\theta_b = 4'$ and $\theta_{fp} = 2$ deg). I depict in the right panel of Fig. 8.9 the cross correlation between detectors 0 and 3 (see Fig. 8.8) for two different field of view opening angles, respectively 1 and 5 deg. This latter parameter affects the level of correlation between the two detectors: bigger will be the angle between the detectors lines of sight, lower will be their cross-correlation. Furthermore, variations of the beam θ_b are also depicted in the same figure, which has the consequence of changing the shape of the power spectrum envelop: a small beam allows to have more power at high frequencies and vice versa for a large beam.

Auto-correlation with wind

I depict in the left panel of Fig. 8.10 the result of adding the wind on the auto-power spectrum. These results can be compared to the fiducial model shown in Fig. 8.9.

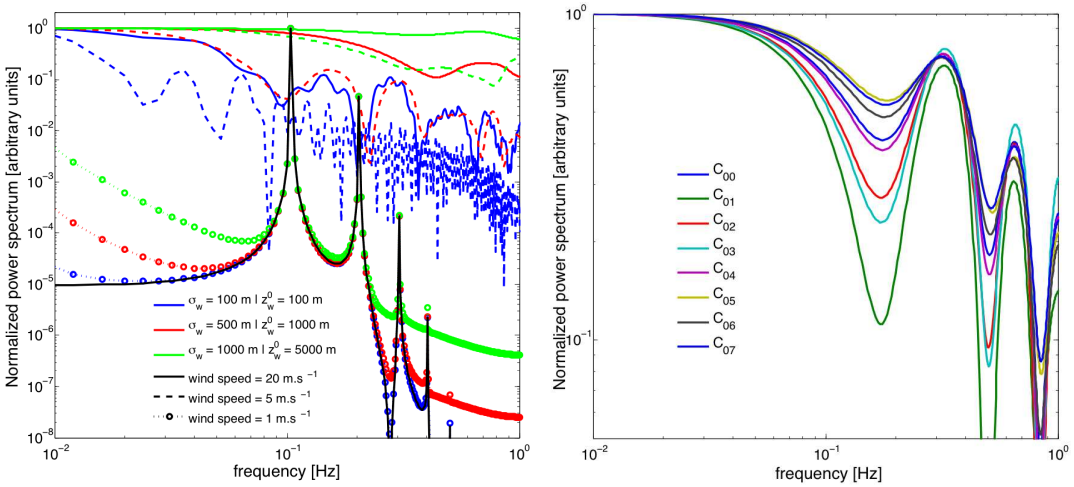

Figure 8.10: **Left panel**: illustration of the effect of varying some wind-related parameters on the atmospheric signal power spectrum. Black solid line is the fiducial model, for reference, i.e. the auto-correlation of the 0^{th} detector. **Right panel**: normalized cross-power spectra between the 0^{th} and the height other detectors, cf. hardware map shown in Fig. 8.8. The wind has the following properties: $z_w^0 = 50\,m$, $\sigma_w = 100\,m$ and $\|\mathbf{w}\| = 5\,m.s^{-1}$. Moreover, projected on the $(x,\,y)$ plane, the wind has the following coordinates $(\|\mathbf{w}\|\cos(\pi/4),\,\|\mathbf{w}\|\sin(\pi/4))$.

Basically, the wind smears out the peaks and the power spectra tend towards a $1/f$-like contamination: it shears the atmospheric structures and therefore "whiten" the features of the power spectrum. Notice that atmospheric contamination in typical ground-based experiment data appears as an additional $1/f$ contribution, with a more or less important f_{knee} depending especially on the observation site, atmosphere stability, etc.

In addition, we can remark that lower wind speed and smaller σ_w lead to power spectra closer to the fiducial one obtained without wind. The largest speed $\|\mathbf{w}\| \sim 20\,m.s^{-1}$ and biggest extension in altitude $\sigma_w \sim 5000\,m$ gives power in all frequencies, and lead to power spectra close to a white noise.

Cross-correlation with wind

Similarly to the right panel of Fig. 8.9, I depict in the right panel of Fig. 8.10 the normalized cross-power spectra between the different detectors of the focal plane, in the case of a non-zero wind: in this chosen case, the wind has the following properties: $z_w^0 = 50\,m$, $\sigma_w = 100\,m$ and $\|\mathbf{w}\| = 5\,m.s^{-1}$. Moreover, projected on the $(x,\,y)$ plane, it is assumed to have the following coordinates: $(\|\mathbf{w}\|\cos(\pi/4),\,\|\mathbf{w}\|\sin(\pi/4))$. One should also remind that the scanning strategy is centered at $\phi_{s,0} = 0$ deg, and staring at a constant elevation $\theta_{s,0} = 45$ deg. I normalized the curves so that their maximum is equal to 1, in order to focus the discussion on the characteristic features: contrary to

the case without wind, the time streams "lose" correlation just because the turbulent structures are sheared and that atmosphere does not give rise to scan-synchronous signals anymore.

A way to understand the cross-correlation behavior between two detectors i and j onto the focal plane is given by the value of the scalar product Θ,

$$\Theta = (\mathbf{w_s} + \mathbf{ss}(t)) \cdot \mathbf{d}_{ij}, \tag{8.44}$$

where $\mathbf{ss}(t) \equiv \dot{\mathbf{r}_s}(t)$ is the scan strategy vector at a given time t, $\mathbf{w_s}$ describes the wind and $\mathbf{d}_{ij}$ is the vector linking detectors i and j. Θ is therefore the projection of the "effective" speed of the telescope across the atmospheric structures onto a line of the focal plane, and brings information about the direction the atmosphere is "effectively" displaced — and could tell us between which detectors onto the focal plane we could expect correlations.

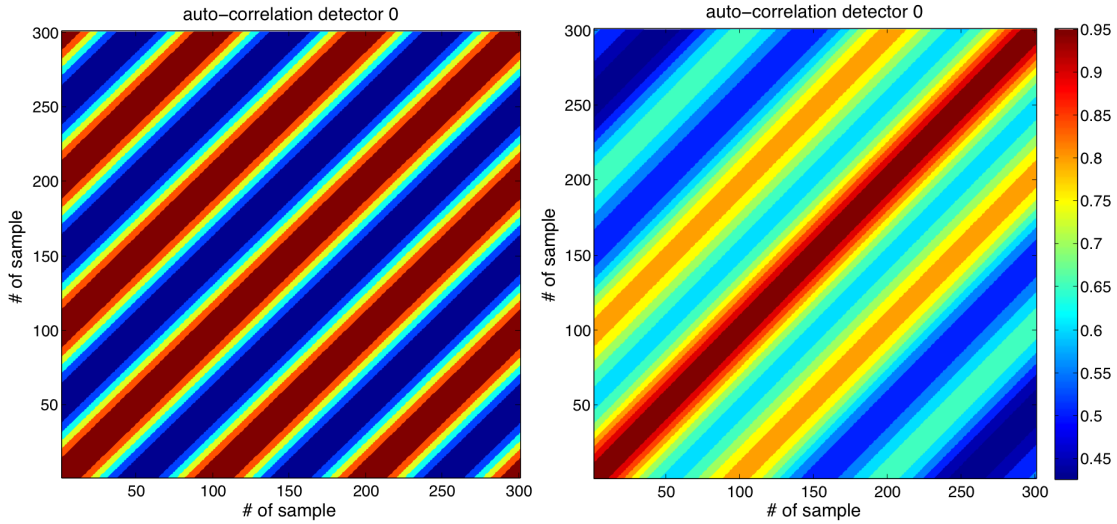

Figure 8.11: **Left panel**: Toeplitz matrix representing the normalized auto-correlation of the 0^{th} detector if there is no wind. In this case, because of the scanning periodicity and non-moving turbulent structures, the atmospheric contamination results in a nearly scan-synchronous signal. **Right panel**: same as left panel but considering non-zero wind speed: structures are sheared between two scans of the telescope and the contamination is no longer appearing at f_{scan}.

I did not explore this reasoning further but, similarly to the reasoning proposed by Bussmann et al. (21) in the case of the Lay & Halverson model, this is definitely something to look at in order to find smart atmosphere rejection algorithms.

8.4.2.3 Atmospheric signal simulation

From the model and its computation, we have access to the quantity $C_{ij}(\tau)$, for given physical atmosphere parameters. Assuming the stationarity in time for the contam-

ination, we can build the 4-dimensional array $\mathbf{C}_{ij\tau\tau'}$ (Toeplitz matrix at given (i,j)) from the 3-dimensional one $\mathbf{C}_{ij\tau}$. I depict in Fig. 8.11 simulated $\mathbf{C}_{00\tau\tau'}$ auto-correlation matrices with and without wind in the atmosphere. We use in the following the notation

$$\beta \equiv \beta(i,\tau) = (n_{det} - 1) \times \tau + i, \tag{8.45}$$

a unique function of indices i and τ, so that we can write $\mathbf{C}_{ij\tau\tau'} \rightarrow \mathbf{C}_{\beta\beta'}$. Considering a random, uncorrelated and normalized vector ξ (i.e. verifying $\langle\, \xi^\dagger \;\xi \,\rangle = 1$), of size $n_{det} \times n_{obs}$, it is possible to simulate a pure atmospheric signal d^{atm}_β given by

$$d^{atm}_\beta \equiv \sqrt{\mathbf{C}_{\beta\beta'}}\, \xi_{\beta'}, \tag{8.46}$$

which, by construction, will verify auto- and cross-correlations seen above. The square-root $\sqrt{\mathbf{C}_{\beta\beta'}}$ is any decomposition verifying

$$\sum_{\beta''} \sqrt{\mathbf{C}_{\beta\beta''}}\, \sqrt{\mathbf{C}_{\beta''\beta'}} = \mathbf{C}_{\beta\beta'}. \tag{8.47}$$

Note that square-root — in particular, Cholesky — factorization of Toeplitz matrices is a classical area of research: among others, the Schur algorithm yields directly the Cholesky factorization of a symmetric Toeplitz matrix. This specific step, i.e. the implementation of Eq. (8.46), could be computationally heavy and makes quite difficult such simulations.

8.5 Conclusion

The different computations of the Church's model presented above are original in several ways. First, instead of the parallel beams considered in Church (26) in the case of an interferometer, I converted the analytic expressions to spherical coordinates so that the optical geometry corresponds to realistic telescope configurations (the beam directions of two detectors of the focal plane are different and separated by a non-zero angle) and the considered scan strategy coincides to the ones usually used by imaging experiments (i.e. a scan in azimuth at a constant elevation, as written in Eq. (8.37)). Second, I derived and studied the expressions for the cross-correlation between detectors for different wind speeds. Finally, I looked at the consequences for the correlations (equivalently the power spectra) of considering different climatic configurations (i.e. different z_{atm}, z_0, wind, etc.), in order to understand the effect of each parameter of the model.

More specifically, we could conclude from these computations that:

- ground-based observations should expect, in realistic climatic conditions, a large $1/f$ contamination due to atmosphere;

- for reasonable opening angles, $\theta_{fp} \sim 1\,\mathrm{deg}$, all the detectors time streams are highly correlated;
- an unpolarized scan-synchronous signal can appear in the time stream if the wind, mainly in the layers close to the ground, is negligible;
- a leak of the atmospheric total intensity into linearly polarized signal could happen through instrumental-polarization (see chapter 7), leading to a potential dramatic systematic effect.

As I mention in section 15.5, this model and resulting simulations could be used to characterize atmospheric contamination, as well as to ultimately find efficient filters, in the frame of new generation ground-based CMB experiments data analysis. In particular, I imagine that, even if it would require very important computational needs, the parametrization of the introduced model could be used for the implementation of a parametric maximum-likelihood cleaning method.

Chapter 9

Polarized foregrounds

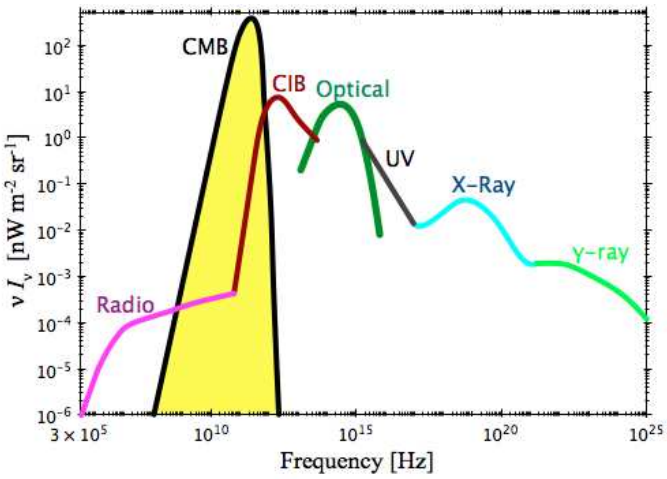

Figure 9.1: Intensity of the background radiation integrated over all sources in the universe, as a function of the frequency. From A. H. Jaffe and H. Dole, www.andrewjaffe.net.

Even if dominant in intensity, CMB is not the only source of photons in the 10-400 GHz band, see Fig. 9.1. Many physical processes involve radio emissions between us and the LSS.

The galactic structure, important at large scales, interferes with the estimation of the lowest multipoles of the CMB in general, and the B-modes in particular, e.g. Fraisse et al. (50). Galaxy contains also smaller scales structures (dust and molecular clouds, supernovae remnants, etc.) which correspond to a significant contamination down to very small angular scales (of the order of $10'$). Mainly because they are far away from us, extragalactic sources are essentially important at small scales, usually below the resolution used to detect the primordial B-modes but could become an issue for the lensing reconstruction, e.g. Smith et al. (126).

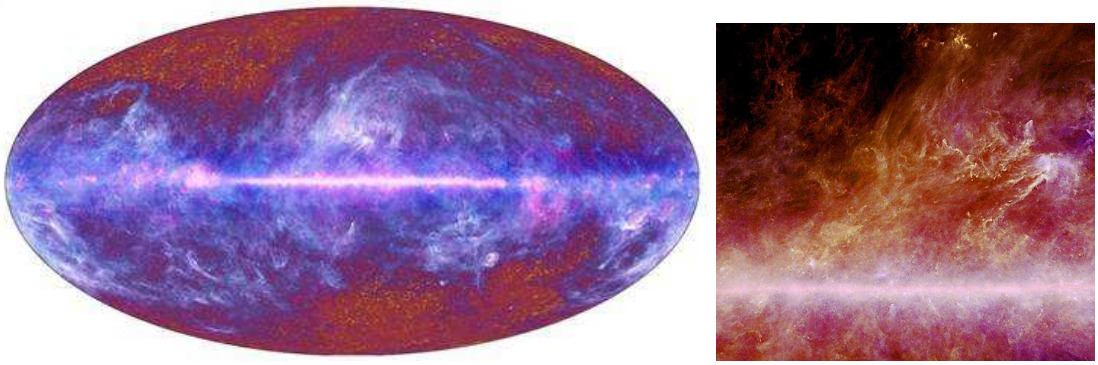

Figure 9.2: One of the first map of the entire sky, as observed by the Planck experiment (nine frequency channels between 30 and 850 GHz), depicted in galactic coordinates, which shows the galactic structures, see Planck Collaboration et al. (108).

This chapter aims at describing the main processes interfering with the measurement of the CMB. First, I will describe InterStellar Medium (ISM) components: dust, synchrotron and extragalactic sources.

As shown on the sky produced by the Planck experiment, Fig. 9.2, one can notice that the most visible structure is the horizontal bar along the equatorial plane corresponding to the Milky Way disk: in this area, the ISM dominates CMB fluctuations. At higher latitudes, even if less dominant, galactic contribution to radiation is non negligible (sections 9.1 and 9.2). Second, I will present several extragalactic contributions which take place over the whole sky (section 9.3).

9.1 Dust

Physical origin

The ISM represents about 10% of the mass of our galaxy, and is composed (by mass) of 70% hydrogen, 28% helium and 2% of heavier atoms, often referred to as metals, e.g. Savage and Mathis (115). This material is mainly a gas but a fraction of it, especially the metals, has also the form of grains, mixed with gas, and represents 1% of the mass of the ISM.

Despite their small contribution to the mass, these grains (or dust) play several major roles and, in particular, they are responsible for most of the infrared and submillimeter emission in the ISM. Supernovae enrich the interstellar medium with heavier elements that allow dust grains to form. Those absorb the visible and ultraviolet light emitted by stars and re-emit in the infrared.

The earliest characterizations of interstellar dust were obtained by measuring the absorption spectrum of stellar light. Attempts in modeling the dust absorption and

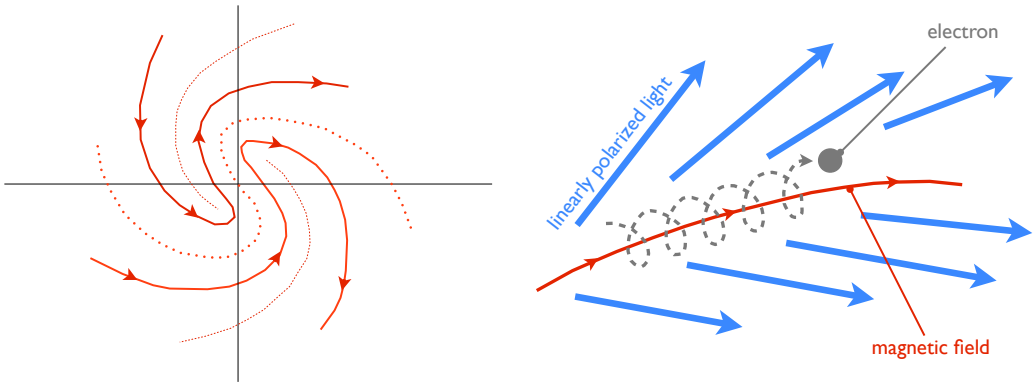

Figure 9.3: **Left panel:** scheme of the large scale structure of the magnetic field of the galaxy Milky Way, in the case of the bisymmetric spiral model. **Right panel:** synchrotron emission by an electron moving in a magnetic field.

emission spectra revealed the need to consider a large variety of grains types, both in terms of size and nature. Nowadays, models generally use three types of grains, e.g. Desert et al. (31), Draine and Li (35):

- large grains — with a size $\gtrsim 10$ nm, they remain in equilibrium with radiation and their emission can be well approximated by a grey body law,
- small grains — out of thermal equilibrium, they mainly emit in the ultraviolet range,
- and PAHs — standing for Polycyclic Aromatic Hydrocarbons, they are large molecules emitting with characteristic vibration modes in the mid-infrared and they have been observed for the first time by the COBE-DMR instrument, see Kogut et al. (72).

Polarization

The existence of a galactic magnetic field with an amplitude $\sim 5\,\mu$G is well established and it manifests itself in several ways. The most important impact for CMB observations is the production of synchrotron radiation, as explain in paragraph 9.2. However it also induces Faraday rotation of the radiation emitted by pulsars (Han et al. (58)) and allows to break, in the emission lines of some clouds, the degeneracy of the angular momentum energy states through Zeeman effect (Myers et al. (96)). Finally the magnetic field imposes the partial alignment of dust grains (Lazarian (80)). In fact, observation of light absorption put in evidence this alignment, causing a partial polarization of the transmitted light (Serkowski et al. (120)). This is the reason why

dust contamination is highly relevant and therefore studied for the analysis of the new generation CMB polarization experiments. In addition, Faraday rotation measurements using pulsars tend to indicate that large scale structure of the galactic magnetic field is consistent with a bisymmetric spiral model (Han et al. (58), Sofue et al. (127)), as depicted in the left panel of Fig. 9.3. In addition to this component which is uniform at small scales, the magnetic field has also a turbulent component.

Emission law

Thermal emission of heated dust grains is the dominant galactic signal for frequencies above 100 GHz. We could explain the dust emission spectrum in the infrared (from 300 GHz to 100 THz) using a combination of contributions coming from a wide range of grain sizes and compositions. At lower frequencies, e.g. $\sim$ 100 GHz, which are of interest for CMB observation, large grains, which are in thermal equilibrium with the interstellar radiation, are expected to be dominant. A measure of this emission over the whole sky was obtained by the IRAS experiment, see Beichman et al. (9).

There is no simple theoretical expression for the emission law of the dust, which is composed of different populations of matter particles. But, in average, an emission law can fit the observational data: it has been shown (Finkbeiner et al. (47)) that the emission of dust, in intensity, is well represented by a mixture of two main components, two populations of grains (silicates and carbon). For these latter, the thermal emission is modeled by a grey body emission law, i.e.

$$I_{\rm dust}(\nu) \sim B(\nu, T)\nu^{\beta_d+1}. \tag{9.1}$$

So far, polarization measurements of the dust were mostly focused on specific regions of the sky, with an exception of the balloon experiment Archeops (Benoît et al. (10)), which mapped $\sim$ 25 % of the sky at 353 GHz, and found a polarization fraction of $\sim$ 4-5%, sometimes up to 10%. These measurements are consistent with some of the predictions made, see e.g. Fosalba et al. (49), Draine and Fraisse (34). Based on IRAS, COBE-FIRAS and Archeops maps, Fauvet et al. (45) proposes a model for the thermal dust emission, i.e. for the three Stokes parameters I, Q and U. In particular, the model is parametrized by the angle between the magnetic field lines and the line-of-sight, as well as the polarization angle.

In addition, as used in Part IV, one can elaborate models for the dust, in which it is assumed a spatially constant frequency scaling (β_d in Eq. (9.1) does not depend on the sky coordinates), as in Model 3 of Finkbeiner et al. (47),

$$I_{\rm dust}(\nu) \sim \frac{\nu^{\beta_d+1}}{\exp\frac{h\nu}{kT_d} - 1}\ , \tag{9.2}$$

where $T_d = 18.0$ K and $\beta_d = 1.65$.

9.2 Synchrotron

Physical origin

Spiraling charged particles in a magnetic field produce a highly polarized synchrotron emission (Rybicki and Lightman (114)), see Fig. 9.3. This radiation is an important source of contamination of the background radiation at low frequencies ($\lesssim$ 80 GHz). In the frequency range of interest for observing the CMB, synchrotron emission has been measured, both in intensity and polarization, by the WMAP team (Gold et al. (53, 54), Page et al. (103)). The intensity of synchrotron radiation depends on the density of charged particles, and also on the magnetic field strength — orthogonal to the line of sight. Its dependence on frequency and polarization fraction depends on the energy distribution of charged particles.

Emission law

For an electron density which follows a power law of index p i.e.

$$n_e(E) \propto E^{-p}, \tag{9.3}$$

synchrotron emission will also follow a power law with an index $\beta_s \equiv -(p+3)/2$, such as

$$I_{\rm sync}(\nu) = I_{\rm sync}(\nu_0) \left(\frac{\nu}{\nu_0}\right)^{\beta_s}, \tag{9.4}$$

where we see that β_s, also called spectral index, is equal to -3 for a typical value of $p = 3$.

Polarization

Moreover, assuming that Eq. (9.3) is still valid, the fraction of polarization for the synchrotron, $f_{\rm sync}$, could be written as:

$$f_{\rm sync} = 3\,\frac{p+1}{3p+7}. \tag{9.5}$$

For $p = 3$, we have $f_{\rm sync} = 0.75$, and, for small changes of p, this value varies only slightly and therefore the fraction of intrinsic polarization of the synchrotron is approximately constant over the sky.

9.3 Extragalactic point sources

Extragalactic objects are generally sufficiently distant to be unresolved by CMB instruments, as far as their brightness is sufficiently small. Their contribution to the observation is the combination of two signals:

- the brightest sources which can be resolved.
- the faintest sources (and the most numerous) which are not individually significant but form a background with fluctuations contributing to the total signal.

On the low frequencies range, radio sources, such as active galactic nuclei (radio galaxies, quasars, blazars), follow a large variety of emission laws. Extrapolation of their flux to CMB wavelengths is therefore difficult. WMAP and Planck experiments have established catalogs of the brightest radio sources at CMB frequencies on the totality of the sky (Planck Collaboration et al. (109), Wright et al. (147)). Polarization measurements are also available for some sources.

On the high frequencies range, IRAS experiment has produced a comprehensive survey of bright sources with frequency between 3 and 25 THz. However, extrapolation of the observed flux from the IRAS bands to the CMB frequencies remains very uncertain.

Finally, the infrared emission of distant galaxies corresponds to a background called the Cosmic Infrared Background (CIB), detected for the first time in the COBE data, see Puget et al. (112), and further studied with the recent Planck data, see Planck Collaboration et al. (110).

9.4 Other foregrounds and secondary anisotropies

9.4.1 Free-free

A significant radiation with a continuous spectrum is emitted by ionized gas regions. Free-free emission comes from the dumping of free electrons in the ions electric fields. This emission is intrinsically unpolarized, even if, in principle, a low level of polarization by Compton effect might exist at the boundaries of ionized regions.

9.4.2 Sunyaev-Zel'dovich (SZ) effect

When CMB photons pass through the hot gas of a galaxy cluster, they interact with energetic electrons of the gas, absorbing some of their energy by inverse Compton scattering. This effect produces a distortion in the CMB spectrum due to

- thermal motion of electrons in the gas (thermal SZ effect),

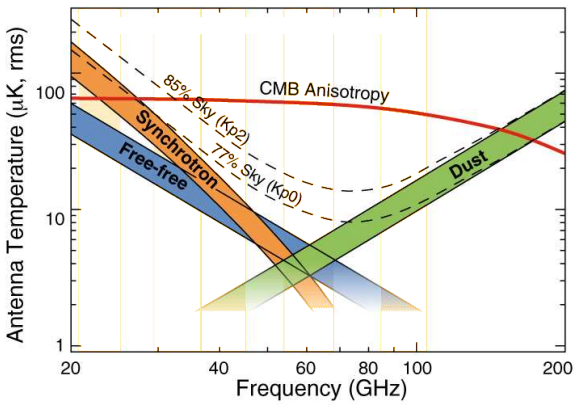

Figure 9.4: Frequency dependence of the CMB anisotropies, red solid curve, and three different astrophysical emissions, in units of antenna temperature. From http://map.gsfc.nasa.gov/mission/observatory_freq.html.

- the overall movement of gas, i.e. the intrinsic speed of the cluster in the comoving frame (kinetic SZ effect).

Both effects produce different spectral signatures, but the thermal effect is clearly predominant.

Polarization

When the incident radiation on the cluster is not isotropic, the Sunyaev-Zel'dovich can become polarized. Several phenomena can cause this effect (Audit and Simmons (7), Sazonov and Sunyaev (116), Seto and Pierpaoli (121)). The two main ones are

- an inherent local quadrupole, i.e. the anisotropy of the incident CMB radiation on the cluster,
- a kinetic quadrupole due to the intrinsic motion of the cluster.

SZ polarization remains small relatively to other polarized contaminants such as dust or synchrotron.

9.5 Summary

Even in ideally circumstances, ground- and space-based experiments will unavoidably suffer due to observing from within the Milky Way: contamination due to galactic materials radiation is an ineluctable effect.

Especially, in the quest of observing polarization of the CMB, two large-scale contamination are important: galactic dust and synchrotron. Spectral behavior of this foregrounds are already characterized in intensity, see Fig. 9.4. However,their polarized fraction remains quite unknown but a good characterization can be expected in the Planck satellite results.

As we will see in chapter 10, data analysts have developed techniques which permit to disentangle the CMB radiation from the other ones. More generally, in the next Part, we optimize experimental focal planes such that this so-called component separation analysis is optimal. We also study if foregrounds can be an ultimate limit for the gravitational B-modes detection.

Part IV

Optimization of a nearly full sky space experiment such as COrE and CMBpol

Figure 9.5: The COrE satellite. From http://www.core-mission.org.

In chapter 10, I introduce the parametric maximum likelihood component separation technique and introduce the work on future experiments focal plane optimization, see Errard et al. (41), chapter 11, as well as its extension, see Errard and Stompor (40), in chapter 12.

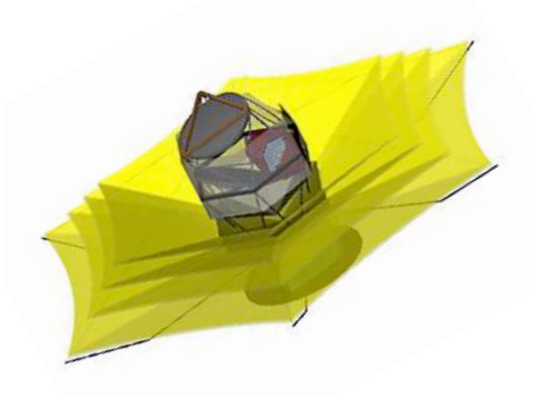

Figure 9.6: The CMBpol design. From Bock et al. (16).

Chapter 10

Parametric maximum likelihood component separation technique

I introduce here the parametric maximum likelihood component separation approach implemented as in Brandt et al. (19), Eriksen et al. (38) and Stompor et al. (133). We thus assume a linear data model, where a signal measured in each pixel p is given by

$$\mathbf{d}_p = \mathbf{A}\,\mathbf{s}_p + \mathbf{n}_p, \tag{10.1}$$

where for each pixel p,

- $\mathbf{d}_p$ is a multifrequency data vector with each entry corresponding to a different frequency channel;
- $\mathbf{s}_p$ is a multicomponent sky signal vector each entry of which corresponds to a different sky component and which is to be estimated from the data;
- $\mathbf{A}$ is a mixing matrix defining how the components need to be combined to give a signal for each of the considered frequency channels; and
- $\mathbf{n}_p$ is a vector containing the instrumental noise and assumed to be Gaussian and uncorrelated with a dispersion given by $\mathbf{N}$.

Here both $\mathbf{A}$ and $\mathbf{N}$ are assumed to be pixel independent for simplicity, but their generalization are straightforward.

In the parametric approach, one assumes that $\mathbf{A}$ is parametrized by a set of spectral parameters, β, which need to be determined together with the sky signal estimates. The noise level per channel, number of frequency channels, etc., are all dependent on instrument properties, which thus will affect the results of the component separation process and could therefore serve as optimization parameters. Some other effects such as beam sizes, and bandwidths are also typically relevant and may need to be included in the modeling. Our work on the impact of calibration errors is presented in chapter 12.

10. PARAMETRIC MAXIMUM LIKELIHOOD COMPONENT SEPARATION TECHNIQUE

Given values of β and defined instrumental parameters we can estimate the sky signal using a standard maximum likelihood solution[1],

$$\bar{\mathbf{s}}_p \equiv \left(\mathbf{A}^t\,\mathbf{N}^{-1}\,\mathbf{A}\right)^{-1}\,\mathbf{A}\,\mathbf{N}^{-1}\,\mathbf{d}_p. \tag{10.7}$$

To estimate the spectral parameters we will use a pseudo (or profile) likelihood, e.g. Stompor et al. (133), given as,

$$-\,2\,\ln\,\mathcal{L} = -\sum_p \left(\mathbf{A}\,\mathbf{N}^{-1}\,\mathbf{d}_p\right)^t\,\left(\mathbf{A}^t\,\mathbf{N}^{-1}\,\mathbf{A}\right)^{-1}\,\mathbf{A}\,\mathbf{N}^{-1}\,\mathbf{d}_p. \tag{10.8}$$

We will refer to this likelihood as the spectral likelihood and will identify its peak value with the best estimate of the spectral indices and the curvature matrix at its peak as the measure of the uncertainties expected for the spectral parameter estimation. These will be used to construct our figures of merit.

[1]Maximum likelihood technique is a statistical method used to estimate the parameters of the probability distribution of a given sample. We call likelihood of the parameters p given the observations $d \equiv \{d_0, d_1, ...d_n\}$, from an independent sample following the distribution law $P(d)$, the quantity $\mathcal{L}$ defined as

$$\begin{aligned}
\mathcal{L} &\equiv \mathcal{L}\,(d_0, d_1, ..., d_n|p) && (10.2)\\
&\equiv P(d_0|p) \times P(d_1|p) \times ...P(d_n|p) && (10.3)\\
&= \prod_{i=0}^{n} P(d_i|p). && (10.4)
\end{aligned}$$

To estimate the parameters, we look for the maximum of this likelihood such that the probabilities of observed realizations are also maximum. Assuming its derivability, this results in the necessary condition

$$\left.\frac{\partial \mathcal{L}\,(d_0, d_1, ..., d_n|p)}{\partial p}\right|_{p_{\rm true}} = 0 \tag{10.5}$$

Moreover, the Bayes' theorem tells us that

$$\forall\; i\;\mathcal{L}\,(d_i|p) = P\,(d_i|p) = \frac{P\,(p|d_i)\,P\,(d_i)}{P\,(p)} \propto P\,(p|d_i)\,. \tag{10.6}$$

The parametric maximum likelihood method is an estimator which has some nice properties such as being

- convergent,
- asymptotically reaching the Cramér-Rao limit, based on Fisher information
- and asymptotically distributed following a normal law.

However, this estimator is not prevented from being biased in the case of a finite sample d.

10.1 Spectral parameter uncertainty

The profile likelihood derivatives with respect to the spectral parameters can be readily computed, the relevant formulas and demonstrations can be found in Appendix A. As our purpose is to gain some insight in the constraining power of different plausible experimental setups rather than analyze any specific data set we will average over the possible noise realization assuming that the noise correlation matrix, $\mathbf{N}$, is known. Using Eq. (A.1) from the Appendix we then arrive at

$$\left\langle \frac{\partial \ln \mathcal{L}}{\partial \beta} \right\rangle_{noise} = \sum_p \left(\mathbf{A}_{,\beta}\, \bar{\mathbf{s}}_p\right)^t \, \mathbf{N}^{-1} \, \left(\hat{\mathbf{A}}\, \hat{\mathbf{s}}_p - \mathbf{A}\, \bar{\mathbf{s}}_p\right) \tag{10.9}$$

for the first derivative. In this equation, as well as everywhere hereafter, we will use a hat over a quantity to mark that we refer to its true, rather than just an estimated, value. $\bar{\mathbf{s}}$ is a sky signal estimate in the case of the noiseless data and it is defined in Eq. (10.7). If the data model in Eq. (10.1) is correct both in terms of assumed scaling laws but also a number of components, the first derivative in Eq. (10.9) vanishes for the true values of the parameters, $\beta \equiv \hat{\beta}$, emphasizing that the estimator is on average unbiased. Indeed in such a case we have $\hat{\mathbf{A}} = \mathbf{A}$ and $\hat{\mathbf{s}} = \bar{\mathbf{s}}$. Under the same assumptions the second order derivatives taken at the true values of the parameters can be then written as, see Eq. (A.7):

$$\begin{aligned} \left\langle \frac{\partial^2 \ln \mathcal{L}}{\partial \beta\, \partial \beta'} \right\rangle_{noise}\Bigg|_{\beta=\hat{\beta}} \;=\; & \mathrm{tr}\, \Big\{ \Big[\mathbf{A}^t_{,\beta}\, \mathbf{N}^{-1}\, \mathbf{A}\, \left(\mathbf{A}^t \mathbf{N}^{-1} \mathbf{A}\right)^{-1}\, \mathbf{A}^t \mathbf{N}^{-1} \mathbf{A}_{,\beta'} \\ & - \mathbf{A}^t_{,\beta}\, \mathbf{N}^{-1}\, \mathbf{A}_{,\beta'} \Big] \sum_p \hat{\mathbf{s}}_p\, \hat{\mathbf{s}}^t_p \Big\}. \end{aligned} \tag{10.10}$$

Hereafter we will use the inverse of this matrix to approximate the error matrix, $\mathbf{\Sigma}$, for the recovered scaling parameters, i.e.,

$$\left[\mathbf{\Sigma}^{-1}\right]_{\beta\beta'} \simeq - \left\langle \frac{\partial^2 \ln \mathcal{L}}{\partial \beta\, \partial \beta'} \right\rangle_{noise}\Bigg|_{\beta=\hat{\beta}}. \tag{10.11}$$

We note that the spatial morphology of the sky components enter the calculation of the errors only in a form of pixel averaged component-component correlations,

$$\hat{\mathbf{F}} \equiv \frac{1}{N_{pix}} \sum_p \hat{\mathbf{s}}_p \hat{\mathbf{s}}^t_p. \tag{10.12}$$

Moreover, only those of the columns and rows of this correlation matrix matter, which correspond to sky components characterized by the scaling laws including some unknown parameters. Mathematically, this just follows from the fact that only columns of the derivatives of the mixing matrix, $\mathbf{A}_{,\beta}$, corresponding to such components do not vanish.

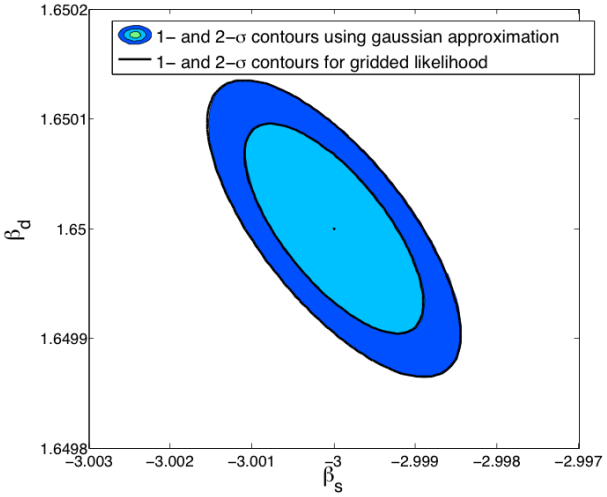

Figure 10.1: 1-σ and 2-σ contours in the β_{dust} - β_{sync} space of the spectral likelihood, $\mathcal{L}$, calculated using Eq. (10.8) for a random realization of the CMB and noise contributions, shaded areas, and compared against the Gaussian approximation with a dispersion as given by Eq. (10.10), solid lines. The former likelihood has been recentered at the true values of the parameters.

Physically, this indicates that the components for which the scaling laws are known unambiguously, e.g., CMB, are subtracted cleanly during the separation process and do not affect the result of spectral indices estimations. This last statement is only true in the absence of systematic effects, e.g. calibration errors or mischaracterization of the bandpasses. An immediate consequence of this is that the resulting expressions are indeed equivalent to those obtained while averaging over an ensemble of realization of noise and CMB signal.

We note that though our conclusion about the impact of different components on the spectral parameter estimation is general, a simple form of the dependence of the latter on the foreground signal morphology is due to our simplifying assumption of a pixel-independent noise level. In general, the relation is more complex, with noise levels selective (de)emphasizing the contributions of some of the pixels on the sky: if the noise is inhomogeneous but changes from a pixel to a pixel in the same fashion in all considered frequency channels, we can write

$$\mathbf{N}_p \equiv \eta_p^{\,p_0}\, \mathbf{N}_{p=p_0}, \tag{10.13}$$

where $\eta_p^{\,p_0}$ is a number specific to a current pixel p and a reference pixel p_0, defining the noise inhomogeneity. The straightforward generalization of Eq. (10.12) is then,

$$\hat{\mathbf{F}} \equiv \frac{1}{\sum_p \eta_p^{\,p_0}} \sum_p \left(\eta_p^{\,p_0}\right)^{-1} \hat{\mathbf{s}}_p \hat{\mathbf{s}}_p^t\,. \tag{10.14}$$

Though this latter case is also idealized as it assumes that all detectors operating at different frequencies observed the sky in a exactly the same manner, it allows to include some basics effects of the scanning strategy in the component separation process. Eq. (10.12) follows from Eq. (10.14) if $\forall\ p$, ${\eta_p}^{p_0} = 1$. Though the formalism developed here is general and can be straightforwardly adopted to a case of arbitrary and correlated noise it can quickly become computationally heavy. Hereafter, in an absence of any specific scanning strategies we use the simplest version of the $\hat{\mathbf{F}}$ matrix.

In Fig. 10.1 we show examples of the contours likelihoods, Eq. (10.8), computed for dust and synchrotron spectral indices for simulated data as described in paragraph 11.5 and for some fiducial nearly full sky experiment. They are compared with a Gaussian approximation based on the variance derived with help of the error matrix, Eq. (10.11). Generally we find a very good agreement. This may breakdown somewhat in cases with very few pixels when the actual spectral likelihoods typically become somewhat skewed (133). Nevertheless, we find that even in those cases though the Gaussian approximation may fail to reproduce properly the tails of the distributions, its overall performance is still rather good. In applications of interest for this work a sufficient number of pixels is always granted.

An interesting question is then how the precision of the spectral parameter estimation depends on the matrix $\hat{\mathbf{F}}$. The short answer is that given the noise levels the higher density contrast of the components, i.e., larger diagonal elements of $\hat{\mathbf{F}}$, the better precision of estimated β, while large cross-correlation terms tend to increase the error.

10.2 Residuals

From the discussion in the previous section it is clear that the precision of the spectral parameters determination though relevant is clearly not a single factor important in quantifying the component separation effects on the B-mode science. This is due to the fact that better precision is usually related to a higher foreground contrast, i.e. higher signal-to-noise. In fact, rescaling the sky components $\hat{\mathbf{s}}_p$ by a contrast factor Φ,

$$\hat{\mathbf{s}}_p \rightarrow \Phi \times \hat{\mathbf{s}}_p, \tag{10.15}$$

we can see that the error on the spectral parameters estimation, given by $\mathbf{\Sigma}$, Eq. (10.11), will verify

$$\mathbf{\Sigma} \ \propto \ \frac{1}{\Phi^2}. \tag{10.16}$$

Eq. (10.16) shows that a better contrast, i.e. $\Phi \geq 1$, will lead to a tighter constraint on β. It is therefore not straightforward to infer an effective foreground contribution left over in the CMB map after the separation process, given just the spectral indices

errors. However, given the estimated value of the spectral parameters, β, we can always calculate the level of the foreground residuals, i.e., a mismatch between the estimated and true sky components. This can be expressed as follows, see Stivoli et al. (130),

$$\mathbf{\Delta} = \mathbf{s} - \hat{\mathbf{s}} = (\mathbf{Z}(\beta) - \mathbf{I})\ \hat{\mathbf{s}}, \tag{10.17}$$

where

$$\mathbf{Z}(\beta) \equiv \left[\mathbf{A}^t(\beta)\ \mathbf{N}^{-1}\ \mathbf{A}(\beta)\right]^{-1}\ \mathbf{A}^t(\beta)\ \mathbf{N}^{-1}\ \mathbf{A}(\hat{\beta}), \tag{10.18}$$

$\mathbf{I}$ is a unit matrix and, as usual a hat over a quantity denotes its true underlying value.

The foreground residuals left in the CMB map are just one component of the vector, $\mathbf{\Delta}$, which for definiteness is assumed to be the zeroth one. We will now restrict ourselves to the CMB component and linearize the problem, assuming that the errors in spectral parameter determination are small. We thus obtain

$$\Delta^{\rm CMB} = \sum_{k,j} \delta\beta_k\, \alpha_k^{0j}\, \hat{\mathbf{s}}^j, \tag{10.19}$$

where

$$\alpha_k^{ij} \equiv \frac{\partial\, \mathbf{Z}_{ij}(\hat{\beta})}{\partial\beta_k}, \tag{10.20}$$

and we assumed that the CMB component is stored as first (i.e., with an index equal to 0) in the component vector, $\mathbf{s}$. We can now characterize the level of the residuals either simply by its *rms* value or, in a more informative way we can estimate the noise average (though noiseless) foreground residual power spectrum, which reads

$$\mathbf{C}_\ell^\Delta \equiv \sum_{k,k'}\sum_{j,j'} \mathbf{\Sigma}_{kk'}\, \alpha_k^{0j}\, \alpha_{k'}^{0j'}\, \hat{\mathbf{C}}_\ell^{jj'}. \tag{10.21}$$

Given that as mentioned before (see also, Stivoli et al. (130)) no CMB signal is left in the CMB map residuals, which combine just the foreground signals, the noise ensemble averages coincide with those made over a full CMB + noise set of realizations. Clearly to compute the residual spectra we need to make assumptions concerning the spatial morphology of the considered foregrounds, i.e., the knowledge beyond the $\hat{\mathbf{F}}$ matrix defined earlier. This is reflected in Eq. (10.21) by the presence of true auto- and cross-spectra for each considered foregrounds, $\hat{\mathbf{C}}^{jj'}$. However, the $\hat{\mathbf{F}}$ matrix provides a sufficient description necessary to calculate the rms value of the residuals. This can be seen noting that

$$\Delta_{rms}^{\rm CMB\,2} = \sum_{k,k'}\sum_{j,j'\neq 0} \mathbf{\Sigma}_{kk'}\, \alpha_k^{0j}\, \alpha_{k'}^{0j'}\, \hat{\mathbf{F}}_{jj'}. \tag{10.22}$$

In the following we will use the C_ℓ^Δ quantity to construct our FOMs making some specific assumptions about the foregrounds spatial properties as described in pargraph 11.5. We point out that the formulas presented above are just a special case of those already studied in Stivoli et al. (130). The important difference is however that the spectral indices uncertainties used in this work are computed effectively as the full CMB + noise, ensemble averages rather than derived in a single, particular study case as in that previous work.

Chapter 11

Optimization of a nearly full-sky CMB B-modes experiment focal plane in the presence of polarized galactic emissions residuals

I will explain in this section the work I have performed in collaboration with drs. F. Stivoli and R. Stompor, summarized in Errard et al. (41).

We propose a general, methodological framework for the experiment optimization and then apply it in specific cases of CMB B-mode observatories. We note that, however sophisticated an adopted optimization procedure may be, it is likely to always come up short in doing justice to all the complexity of an instrument under consideration. The goal of such a procedure, as we pursue here, is therefore not just to find a single best (in some sense) instrumental configuration. Rather, the goal is to provide, on the one hand, a reference against which to judge actual hardware designs and, on the other, guidelines of, first, how to propose, given some science goals, a suitable and viable experimental design and, later, how to modify it to implement inevitable, real-life limitations and constraints in a way which will have a minimal impact on its scientific performance.

Though the discussed formalism lends itself straightforwardly to a number of generalizations, in this work we have demonstrated it in the context of the B-mode detection by multifrequency observatories taking into account the presence of the astrophysical (diffuse) foregrounds, leaving a study of some of the most common instrumental effects to a future work. We note that even in this limited context a result of the instrument optimization problem will depend on a number of factors: scientific goals as set for the experiment in question; models of the physical effects, e.g., foregrounds; specific techniques and assumptions they require, selected to be used for the component sepa-

rations step. This emphasizes the need for using the state-of-the-art physical models of the foregrounds and the separation techniques in this kind of problem, as well as for continuing effort aiming at better, more reliable understanding of the foreground physics.

As the optimization requires a capability to predict the performance of an instrument given its characteristics, it is very closely connected with performance forecasting. In fact, in most of the similar work to date, the problem of selecting the most suitable experimental configurations is typically treated as a performance forecasting problem applied to some predefined, and limited, set of potential candidate experimental setups, the relative merits of which are subsequently evaluated and compared, e.g., Amarie et al. (2), Betoule et al. (12), Dunkley et al. (36), Fantaye et al. (43), Stivoli et al. (130), Verde et al. (142). This is in contrast with this work, which employs an actual optimization procedure. In this respect our approach is most similar to the one by Amblard et al. (3). Here we generalize and extend the latter work on both methodological and implementation levels. We consider broader parameter space and optimization strategies, search for families of acceptable configurations, and by adopting the parametric component separation approach as the component separation technique of the choice, we manage to propagate realistic ensemble-averaged errors to our selected figure of merit indicators in a statistically sound manner.

11.1 Method

Our approach is as follows. We start off from expressing our science goals in terms of acceptable ranges of values of some proposed figures of merit (section 11.2), which are chosen to reflect the physical context of the considered experiment. We then first treat all figures of merit (FOMs) separately and for each of them perform a strict optimization procedure (section 11.3), i.e., minimize or maximize it over a set of considered instrumental parameters. This is usually done in the presence of some external constraints arising for instance due to some hardware requirements but also some other science-driven restrictions, (section 11.3).

As illustrated in Fig. 11.1, this first step aims at determining the best possible instrument performance from the perspective of the considered FOMs and their corresponding configurations. If for any of the FOMs the best performance value does not fulfill our science goals, the procedure halts and either the set of instrumental parameters have to be enlarged or the science goals/FOMs rethought. Otherwise, for each FOM, but one, we select a threshold value, which need to be attained by any acceptable configuration and perform the optimization of the one left-over FOM over the parameter space under additional constraints, requiring that all or some of the remaining FOMs are not worse than their established thresholds. If the optimization fails, we may need

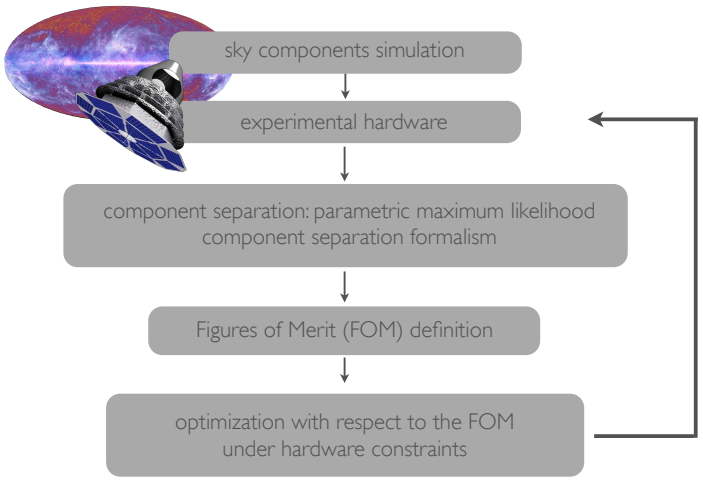

Figure 11.1: Scheme illustrating our methodology for optimizing focal planes with respect to FOMs I define in section 11.2.

to adjust some of the thresholds and repeat the procedure again. This may be also the case if the solution found does not ensure an acceptable value for the FOM, which is used in the optimization. If the tuning of the thresholds succeeds, the solution obtained via the above procedure is used as a starting point for further post-processing and the corresponding set of values of all FOMs used as a reference to compare any other configuration against. The post-optimization processing is used to implement some additional constraints and/or simplifications, which for some reason could not have been imposed on the formal optimization procedure.

Below we present a specific implementation of this general framework in the context of primordial CMB B-mode observations by multifrequency multi-detector observatories in the presence of Galactic foregrounds. In this case our FOMs need to account for some effects arising due to the component separation procedure, which has to be applied to data to recover a genuine CMB signal. We therefore start below by discussing a specific component separation approach, the so-called parametric maximum likelihood technique, and its impact on a CMB B-mode detection.

11.2 Figures of merit

Given the estimates of the foreground residuals provided in the previous Section, we can now define our figures of merit. Hereafter, we will use three FOMs: two referring to the effects of the foreground residuals found in the recovered CMB map as a consequence of the separation process, and the third related to the noise level of that map. As our

scientific goals here are related to the primordial B-mode signal two of the proposed FOMs express the effects of the foreground residuals on a tensor-to-scalar ratio (of the respective CMB spectra), r. The third one is more generic and is just to ensure that the least-noisy map of the sky is produced.

FOM#1: r_{stat} – an r value detectable on 95% confidence level incorporating the component separation uncertainties.

This FOM is computed in two steps. First, we use a generalized Fisher matrix expression to estimate the uncertainty of estimating the tensor-to-scalar ratio, r, for any given assumed r value, and subsequently we determine a value of $r \equiv r_{stat}$, which is detectable on 95% confidence level. This limiting value is defined as

$$r_{stat} \simeq 2\, F_{rr}^{-1/2}\,(r_{stat})\,. \tag{11.1}$$

The Fisher matrix we propose to use here accounts for usual cosmic, sampling, and noise variance, but also for an extra error resulting from the shortcomings of the foreground component separation, which is presumed to be applied to the maps beforehand. We model the separation residuals following the formalism introduced in section 10.2 and which treats the map-level residuals as a linear combination of the foreground templates with Gaussian distributed amplitudes.

The detailed derivation of the Fisher formula is presented in Appendix B. Recalling that C_ℓ^Δ denotes the power spectrum of the residuals, the final expression for the Fisher matrix, F_{rr}, reads then

$$\begin{aligned} F_{rr} \;=\; \sum_{\ell,\ell'}^{\ell_{max}} \frac{\partial C_\ell}{\partial r} \Bigg\{ & \frac{(2\ell+1)\,\delta_{\ell\ell'}}{2\, f_{sky}^{-1}\, C_\ell^2} \;-\; \frac{(2\ell+1)\, C_\ell^{-3} C_\ell^\Delta\, \delta_{\ell\ell'}}{\left(1+\sum_{\ell''}^{\ell_{max}} (2\ell''+1)\,\dfrac{C_{\ell''}^\Delta}{C_{\ell''}}\right)} \\ & + \frac{(2\ell+1)\;(2\ell'+1)\;C_\ell^\Delta\, C_{\ell'}^\Delta}{2 C_\ell^2 C_{\ell'}^2 \left(1+\sum_{\ell''}^{\ell_{max}} (2\ell''+1)\,\dfrac{C_{\ell''}^\Delta}{C_{\ell''}}\right)^2} \Bigg\} \frac{\partial C_{\ell'}}{\partial r} \end{aligned} \tag{11.2}$$

where for shortness we set $C_\ell \equiv C_\ell^{CMB} + C_\ell^{noise}$.

A choice of experimental parameters will in general affect both the white noise level as quantified by C_ℓ^{noise} but also the level of residuals resulting in different r_{stat} values derived for different proposal configurations.

We note that if the level of residuals is very high as a result of the errors on spectral parameters being large then the first order expansion used to obtain Eqs. (10.19) and (10.21) may not be any more sufficient. Likewise, if the foreground contributions are large so their residuals are comparable to the CMB signal, sufficiently precise knowledge of the foregrounds would become necessary to ensure that the above formulas produce reliable results. As one may not be completely comfortable with such a presumption, we will introduce another FOM designed to penalize such configurations.

FOM#2: r_{eff} – an effective r value of the foreground residuals.

We use a proposal of Amblard et al. (3) and we characterize any obtained foreground residuals using its effective value of r defined as

$$s(r_{eff}) \simeq u, \tag{11.3}$$

where

$$\begin{aligned} s\,(r) &\equiv \sum_{\ell}^{\ell_{max}} C_\ell^{cmb}(r) - C_\ell^{cmb}(0), \\ u &\equiv \sum_{\ell}^{\ell_{max}} C_\ell^{\Delta}. \end{aligned}$$

We note that due to a missing factor of $2\ell + 1$ this criterion does not compare power contained in the primordial B spectrum with that of the residuals (up to ℓ_{max}), and in contrast to the latter it gives more weight to low multipoles.

FOM#3: $\sigma_{\rm CMB}^{noise}$ - noise level of the recovered CMB map.

When the true values of the spectral parameters are available the only uncertainty of the recovered component maps, Eq. (10.7), is due to the instrumental noise and reads

$$\mathcal{N} = \left(\mathbf{A}^t\,\mathbf{N}^{-1}\mathbf{A}\right)^{-1}, \tag{11.4}$$

and therefore depends on the number of detectors and frequency channels. With our focus on the CMB we will therefore use the diagonal element of $\mathcal{N}$ corresponding to the CMB component as one of our criteria, which we would like to keep as low as only possible. We thus have

$$\left(\sigma_{\rm CMB}^{noise}\right)^2 \equiv \mathcal{N}_{00}. \tag{11.5}$$

We note that only when $\mathbf{A}$ is a unit matrix the above formulas corresponds to a standard, inverse-noise-coaddition. This in turn can only happen if no sky components are mixed

together, implying no foregrounds. In any other case the final noise of the CMB map is higher than the inverse noise weighting would imply, Bonaldi and Ricciardi (17), and its exact value will depend on the details of the component scalings and experimental set up. We note that unlike two other FOMs implemented here this applies on a map rather than a power spectrum level. Moreover, as the spectral parameters, β, are assumed to be known ahead of the computation, this FOM may lead to configurations in which the estimation of those is not feasible and thus rendering the residuals effectively arbitrary and unknown. Nevertheless, though it needs to be used with a care, it provides a meaningful reference against which to gauge other configurations.

11.3 Optimization procedure

11.3.1 Parameters and optimization approaches

In this work typically we will optimize a number of detectors in each of the pre-defined frequency channels. This is clearly one of the most basic hardware parameters one would like to know designing a B-mode experiment. Though the central frequency of the channels is often constrained from the onset by some hardware constraints, we will also consider more general optimization problems in which a number of frequency channels, their central frequencies, and a number of detectors per channel are all to be optimized with respect to.

In the former case we perform a single global optimization operation. Our numerical codes use a minimization algorithm for constrained nonlinear multivariate function, as implemented in MATLAB, which is based on a line-search algorithm with constraints introduced via a quadratic approximation to the Lagrangian function.

In the second type of the optimization problems we have found that attempts of performing a global optimization are often frustrated by numerical issues and the results are consequently not very reliable. Instead we have devised a multi-step approach which is shown schematically in Fig. 11.2. In the proposed method we start from a configuration consisting of a focal plane overpopulated with a large number of mock channels uniformly covering the requested interval of frequencies. Each of these channels is assigned the same number of detectors or a fraction of the focal plane area, depending on which hardware constraint we use (step 1). We then optimize the number of detectors as in the standard case with the fixed frequency channels with respect to a given FOM (step 2). As the obtained detector distribution is typically rather inhomogeneous (we usually obtain "clusters" in frequency space of non-zero channels) we then merge the channels with close central frequencies, e.g., closer than the expected band-width of the anticipated channels. In the process of merging we replace some subsets of channels by a new channel, centered at the barycenter of the previous frequencies as weighted either by a number of detectors or focal plane assigned to each of the merged channels, and

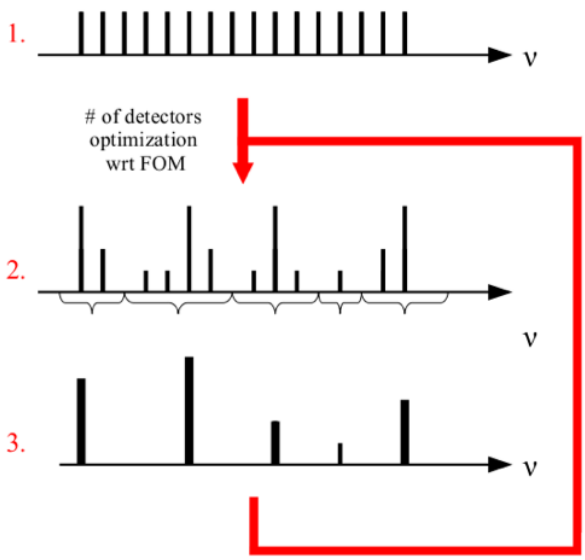

Figure 11.2: Schematic illustration of our optimization procedure in a case of an adjustable number of channels, a number of detectors per channel, and their central frequencies.

assign to it either their detectors or the corresponding focal plane area (step 3). We optimize this new configuration again with respect to numbers of detectors per channel, and go back to step 2 whenever the resulting configuration is found very inhomogeneous. Then we repeat this process again. We find however that usually a single pass over the optimization sequence produces satisfactory results.

11.3.2 Constraints

The constraints can be imposed straightforwardly via Lagrangian multipliers therefore permitting a wide variety of those, which can, and sometimes have to, be introduced.

These include some trivial constraints stemming from the physical interpretation of the optimized parameters, e.g., ensuring non-negative values for detector numbers or focal plane area, which have to be usually included explicitly.

There are also some fundamental constraints without each the convergence could not be reached at all. These typically followed from the hardware restrictions. As an example of the hardware constraint, hereafter we will use either a constraint on a total area of the focal plane or on a total number of detectors, corresponding to cases where we have full freedom to fill in the entire focal plane as densely as only needed or when such freedom is restricted, for instance, by capability of our read-out systems.

Yet another type of constraints invoked in the optimizations studied here includes those driven by the science goals rather than hardware requirements. For instance,

we could require that some specific frequency channel map has a noise level better than some pre-set level in order to make such a map good enough to investigate some sky objects or features of interest. These kinds of constraints are often needed in the post-processing phase described later.

In addition, while considering multiple FOMs simultaneously we will typically use some of them as constraints restricting the optimization to such configurations for which the required values of these FOMs is better than some suitable threshold.

11.3.3 Post-optimization processing

The optimized solution formally determined as described here in most of the cases will require further adjustments and tuning, before it could become a basis for an actual instrument design and later its potential development.

Specific instances of such post-optimization processing, which we consider hereafter include:

- **design simplification** – including either rounding of numbers of detector per channels and/or removing some channels altogether, in particular those assigned a small number of detectors.
- **addition of some ad hoc frequency channels** – for instance, either to improve the overall robustness of the derived configuration with respect to potential surprises concerning physical properties of the foregrounds, or to extend the science goals beyond what is already encoded in the FOMs.

In all these cases a crucial question is how significant modifications from the initial optimized setup are allowed before the science goals, as expressed by the FOMs, are compromised too significantly to be acceptable. Below we outline a general approach devised to answer such questions in some specific cases relevant to the applications considered here, leaving a more detailed description of its practical implementation in our study cases to paragraph 11.6.

11.3.3.1 Detector number rounding

Let us consider only channels for which the optimization procedure has assigned a nonzero number of detectors. Moreover we start from the channels for which we want to decrease a number of detectors, as a result of the rounding procedure, and postpone the treatment of the remaining ones for later. For the time being we also relax all the constraints imposed on the optimization, with an exception of the ones ensuring positivity of a number of detectors or focal plane area. Removing some of the detectors decreases the instrument sensitivity and thus will affect our science goals, unavoidable

rendering the experiment less competitive. For any specific configuration we can always calculate exactly its performance in terms of the adopted FOMs. However, on the experiment designing stage, when many such configurations may need to be considered and often quickly discarded, the need for the case-by-case computation may be a hinderance. In such a context a fast, even if rough and approximate, approach could be therefore a handy substitute permitting one, on the one hand, to zoom quickly on an interesting family of potential solutions, and, on the other, to reject configurations which are clearly of no interest. One way to address such a need could be to construct, for each FOM, a series of hyper-volumes, $\mathcal{V}_k$, $(k = 0, ..., n_{\mathcal{V}} - 1)$, centered on the optimized configuration and such that $\mathcal{V}_0 \subset \mathcal{V}_1 \subset \cdots \subset \mathcal{V}_{n_{\mathcal{V}}-1}$. To each volume, $\mathcal{V}_k$, we can assign uniquely a value, $\tilde{v}_k$, such as,

$$\tilde{v}_k \equiv \min_{\{d_i\} \in \mathcal{V}(v_k)} \Big\{ \mathrm{FOM}\big(\{d_i\}\big) \Big\}, \tag{11.6}$$

i.e., which defines the worst performance plausible within the volume. The values $\tilde{v}_k$ are directly arranged in a descending order given that any volume contains all the previous ones. If now a configuration of our interest belongs to the k-th volume and does not to the $(k-1)$-th one we immediately can infer that its performance, $\tilde{v}$, expressed in terms of the given FOM, is bracketed by the two values corresponding to these two hyper-volumes, i.e., $\tilde{v}_{k-1} \leq \tilde{v} \leq \tilde{v}_k$.

Two features are essential to make such a scheme useful. First, we have to have an easy way to identify whether a given configuration is or is not contained in a given volume. Second, the volumes have to be defined in such a way that the values of $\tilde{v}_k$ assigned to them span a range of interesting values and do so sufficiently densely. Given potential high-dimensionality of the parameter space we consider here, none of these two requirements is straightforward to satisfy. To address the first of them we propose to use as the volumes hyper-ellipsoids defined as

$$\mathcal{V}_k \equiv \Big\{ \{d_i\} \Big| \sum_i \frac{(d_i - d_i^{opt})^2}{{\sigma_i^{(k)}}^2} \leq 1,\, d_i < d_i^{opt} \Big\}, \tag{11.7}$$

where the last condition on the right hand side narrows the volume to the cases of our interest here, as depicted in Fig 11.3. The semiaxes of the ellipsoid, $\sigma_i^{(k)}$, need to reflect the fact that the rate at which the given FOM changes will be in general different in different directions in the parameter space. We therefore determine them for every direction corresponding to varying detector numbers in a single channel separately and we do it for each channel of relevance here, i.e., for which $d_i^{opt} \neq 0$. The procedure here involves two steps. First, we select a grid of values of the considered FOM, v_k, which covers the range of its values of our interest and does that with a sufficient density. This grid is used consistently for all directions and channels. Subsequently,

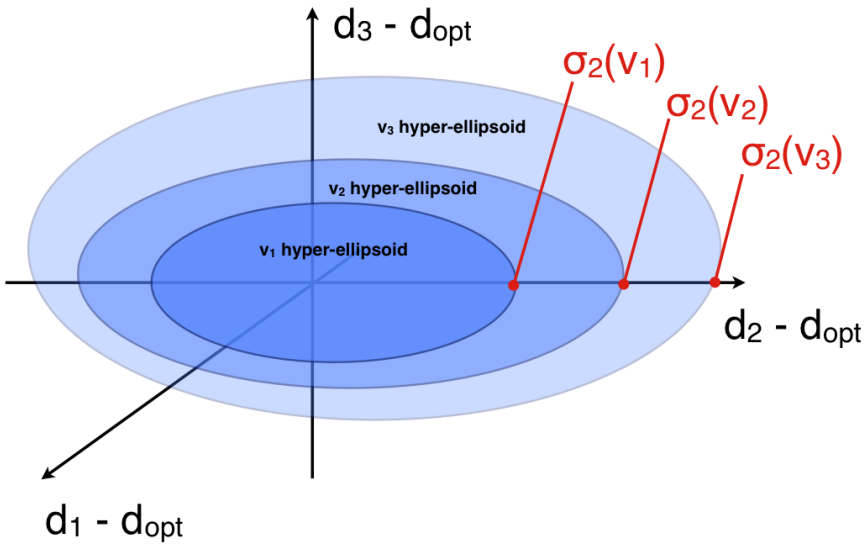

Figure 11.3: Simplified three dimensional schematic illustration of the reasoning we use to probe the acceptable region for the experimental configurations around the optimal one.

for every channel, i, we find numerically a dependence between a value of FOM and a distance from the optimized solution along i-th axis of the parameter space and use this relation to determine $\sigma_i^{(k)}$ so $FOM\left(\sigma_i^{(k)}\right) = v_k$. Typically, the grid point values, v_k, will provide a good approximation to the worst case values, $\tilde{v}_k$, defined earlier. The latter are therefore expected to be automatically well-spaced and to span a sufficient interval of FOM values. In actual applications, we compute more precise estimates of $\tilde{v}_k$ than those provided by v_k. This is done by using Eq. (11.6) and randomly sampling the volume of the corresponding hyperellipsoid.

The proposed construction therefore obeys the two requirements we defined earlier and provides a quick and easy way to find out how far the configuration can be tweaked, without compromising the science goals. The parameters $\sigma_i^{(k)}$ and $\tilde{v}_k$ constitute an additional and important piece of information, which should be determined and provided alongside any optimized configuration to render the optimization process helpful. We demonstrate this in actual applications in paragraph 11.6.5.

So far we have neglected the hardware constraints. Those would require that any subtraction of the detectors from some of the channels needs to be accompanied by adding detectors somewhere else. However, as adding detectors can only improve our FOMs, the procedure outlined above is conservative as the final outcome of the rounding with the constraints fulfilled can be only better than what the procedure implies.

We can now get back to the channels for which we might have wanted to round up the number of channels. This can be done but only by appropriately distributing the detectors we have removed earlier, as the overall hardware constraint has to be fulfilled.

If we do not have however strong preferences regarding their distribution we may try to perform a second round of the optimization to find out how it can be done in an optimized way. This could be done by solving the optimization problem as the initial one but adding extra constraints fixing the number of detectors to their rounded value in all the channels, where the rounding has been applied.

11.3.3.2 Low-populated channels

The formal optimization procedure proposed here may result in configurations, which include a number of channels with a relatively low number of detectors. As extra frequency channels contribute to an overall complexity of the instrument, it could be advantageous to remove those if there is no strong science driver behind them. Removing entire channels is more delicate than a removal of some fraction of the detectors as discussed above. This is because it can render the separation process singular or nearly so with separation errors growing rapidly. The singularities however can be usually avoided by keeping track of a number of channels needed to separate some specific number of components, each described by a well-defined number of parameters. We will therefore assume throughout that this is indeed the case. We then proceed as follows with the underpopulated channels. We remove such a channel or contiguous group of those and either redistribute the extra detectors between the adjacent channels or create a new channel with a central frequency computed as a detector (or focal plane area) weighted average of the frequencies of the channels to be replaced. We then test the change in the FOM values. If either of the options is not satisfactory, we can try to further to improve on it by performing formal optimization but now using only channels which contain a nonzero number of detectors. If that still turns out to be much worse than the optimized values of the FOM, we subsequently need to identify, which of the low-populated channels are crucial from the performance point of view and retain them in our final configuration, while removing or merging the others.

11.3.3.3 Ad hoc extra channels

Clearly our optimized configuration is only as good as the foreground model assumed in the optimization process. The impact of some of the uncertainties in the foreground modeling can be discussed directly within the formalism presented here as, for example, that of details of the foreground correlation matrix and/or shape of their power spectra. It is more difficult however to investigate the role of our assumptions about a number of spectral parameters and/or a number of foreground components. In that respect one may feel more at ease with the configurations, which have the entire frequency range

accessible to the instrument sufficiently populated, as they, at least on the intuitive level, may appear more robust with regard to the unknown.

If the optimization does not lead to a configuration, which satisfies such a condition on its own, one may want to impose it by adding one or more ad hoc frequency channels in the areas they are missing. This can be done straightforwardly by adding a constraint requiring at least some predefined and nonzero number of detectors in those channels. If this number is fixed exactly, it will be obviously not anymore a parameter of the optimization, however the channel will still take part in the optimization process as it will be taken into account in the FOM computation. We use this approach to answer an important question, i.e., how close such a new configuration would perform as compared to the original, optimized one. In other words, should the foreground model used turn out to be correct, would we lose much by trying to make the configuration more robust ? Ideally, the loss of performance will not be significant, permitting us to reach both these goals simultaneously: near optimality whenever our modeling is correct, and ability to meet the surprises. In paragraph 11.6.5 we discuss how the parameters of such ad hoc channels can be proposed in a specific application.

11.4 Design robustness

A problem closely related to the one discussed above is that of the robustness of the final configuration. Given some unavoidable failure rates in a technological process involved in the instrument design and development, a final version of the instrument typically comes short of the actual design target. An important and valid question then is how robust the science goals posed for the experiment are assuming that the target has been defined using the procedure described here. We address this problem in a specific case in which we admit some failure rate for the detector production process, ε. For a set of realistic values of ε we perform a random sampling of the parameter space randomly drawing a number of failed detectors. We then evaluate the full set of FOMs for each of the samples and find what is an average, likely on 95% confidence level impact of the considered failure rates on the FOM values.

11.5 Foreground modelling

As discussed earlier in our formalism there are two key quantities needed to describe completely the effect of foregrounds. These are the auto- and cross-spectra characterizing the spatial distribution of the foreground components and the component correlation matrix, $\hat{\mathbf{F}}$. To calculate these we will rely on a specific model of the Galaxy and since we are interested in the B-modes, we will consider only diffuse foregrounds, synchrotron and dust, with known and non-negligible polarization emission.

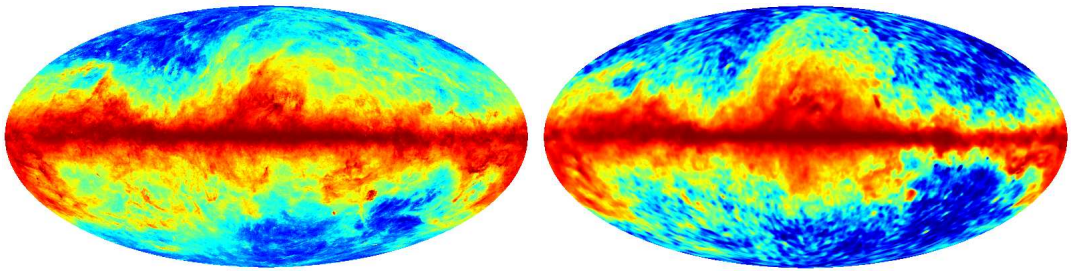

Figure 11.4: **Left panel**: example of a dust map, assuming a beam of $8'$ and $n_{side} = 512$. **Right panel**: same as left panel but for synchrotron emission.

To simulate these emissions in polarization we implement the same recipe as in Stivoli et al. (130), which starts off from deriving reliable total intensity templates from the available data (the Haslam map Haslam et al. (62) for the synchrotron and the combined COBE-DIRBE and IRAS for the dust Schlegel et al. (117)), rescales them using some constant overall polarization efficiency factor, fixed to 10% in order to match the large scale E and B spectra of Page et al. (103), therefore producing polarization intensity templates, as illustrated in Fig. 11.4. The polarization angles on the largest scales are then determined using a combination of the WMAP data and three-dimensional modeling of the Galactic magnetic field as in Page et al. (103), while on the small angular scales ($\lesssim 1^\circ$), by randomly simulating those using their angular power spectra as derived from the data Giardino et al. (52).

We assume spatially constant frequency scalings: a power law with index $\beta_s = -3$ for the synchrotron, i.e.,

$$A_{\rm sync}\left(\nu, \nu_{ref}\right) = \left(\frac{\nu}{\nu_{ref}}\right)^{\beta_s} \tag{11.8}$$

and a uniform greybody scaling law, as in Model 3 of (47),

$$A_{\rm dust}\left(\nu, \nu_{ref}\right) = \left(\frac{\nu}{\nu_{ref}}\right)^{\beta_d+1} \frac{\exp\frac{h\nu_{ref}}{kT_d} - 1}{\exp\frac{h\nu}{kT_d} - 1}\ , \tag{11.9}$$

where $T_d = 18.0$ K and $\beta_d = 1.65$ for the dust.

As pointed out in Stivoli et al. (130), by adopting this model a large amount of correlation is expected between dust and synchrotron both because the Galactic magnetic field is a common ingredient and because of the lack of high resolution data that forces us to extend the correlation to small scales. This is reflected in the fact that the off-diagonal terms of $\hat{\mathbf{F}}$ are of the same order of the diagonal terms. However, as we discuss in paragraph 10.1 large off-diagonal terms inflate the errors on spectral parameters, so from the perspective of foreground residuals the employed model can be considered conservative.

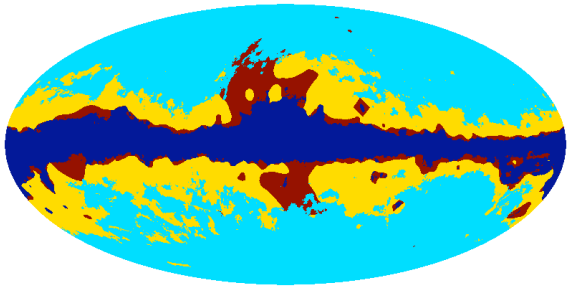

Figure 11.5: Three foreground masks as used in this work. Yellow (largest mask), dark red (large mask round the galactic bulge), and dark blue (narrowest mask around the galactic plane) mark sky areas excluded from the masks: MASK-I, P06, and MASK-II, respectively.

Mask	f_{sky}	$\hat{\mathbf{F}}_{\mathrm{dust-dust}}$	$\hat{\mathbf{F}}_{\mathrm{dust-sync}}$	$\hat{\mathbf{F}}_{\mathrm{sync-sync}}$
P06 mask	0.73	3.20	0.082	0.0025
Mask I	0.82	1.12	0.029	0.00084
Mask II	0.51	1.74	0.053	0.0019

Table 11.1: $\hat{\mathbf{F}}$ matrix elements computed for two foreground components, dust and synchrotron, at the fiducial frequency of 70 GHz for the three masks used in this work and all pixelized using HEALPIX scheme with nside = 128.

To investigate the effects of different foreground contrasts and morphology we consider here three different sky masks. MASK-I and MASK-II are tailored in such a way that they have the possible total polarized foreground contrast (synchrotron plus dust) lower than a predefined threshold equal to 0.86 and 0.36 μK, respectively. We also employ more standard the P06 mask from the WMAP team, which is optimized for the low frequency coverage of WMAP, i.e. it is skewed toward cutting out more the synchrotron than the dust emission. All three masks are shown in Fig. 11.5 and their corresponding foreground (pseudo) power spectra are displayed in Fig. 11.6. In addition, in Table 11.1 we list the elements of the matrix $\hat{\mathbf{F}}$ for each of them.

These masks are thought to be applied a posteriori to the full sky map, assumed to be homogeneously observed by the experiments. This means that the noise level per pixel, described in paragraph 11.6.2, will be the same for each of them and thus the results of the FOM#3 optimization will be the same in all three cases.

11.6 Applications

As an illustration of the method detailed in the previous sections, we will consider the optimization of two different full sky satellite designs: Cosmic Origins Explorer (COrE) proposed in response to the European Space Agency Cosmic Vision 2015-2025 Call (137), and CMBpol (1, 33), proposed as part of the NASA mission concept study. The respective frequency channels and a number of detectors per channel corresponding

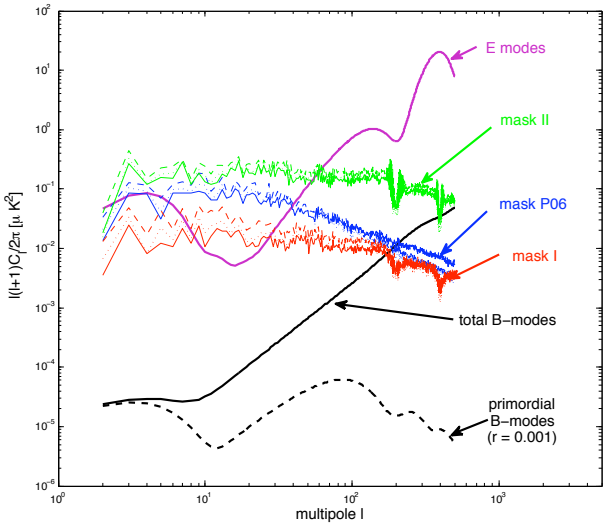

Figure 11.6: Pseudo-power spectra of the foreground templates for the three different masks considered in this work and contrasted with the CMB B-mode power spectrum. For each mask the three lines show dust (solid line), synchrotron (dashed line), and their cross-correlation (dotted line). The foreground signals are computed at the 65 GHz. All the spectra used in this work are computed from HEALPIX-pixelized maps with nside = 512.

Frequency [GHz]	30	45	70	100	150	220	340	500	850
Number of detectors	84	364	1332	196	3048	1296	744	938	1092

Table 11.2: CMBpol distribution of detectors among the different channels, see Bock et al. (16).

to the original designs are summarized in Table 11.2 for CMBpol and in Table 11.3 for COrE.

In our analysis we will assume the same noise levels per detector for each of the experiments, paragraph 11.6.2, and that they scan the sky homogeneously with all the detectors observing simultaneously over the course of 4 years. Everywhere in this section, but in paragraph 11.6.8, we will aim at optimizing a number of detectors per channel, assuming that the latter are fixed and known, and keep either the effective area of the focal plane or total number of detectors constant. The assumed values for the

Frequency [GHz]	45	75	105	135	165	195	225	255
Number of detectors	64	300	400	550	750	1150	1800	575
Frequency [GHz]	285	315	375	435	555	675	795	
Number of detectors	375	100	64	64	64	64	64	

Table 11.3: COrE distribution of detectors among the different channels, see The COrE Collaboration (137).

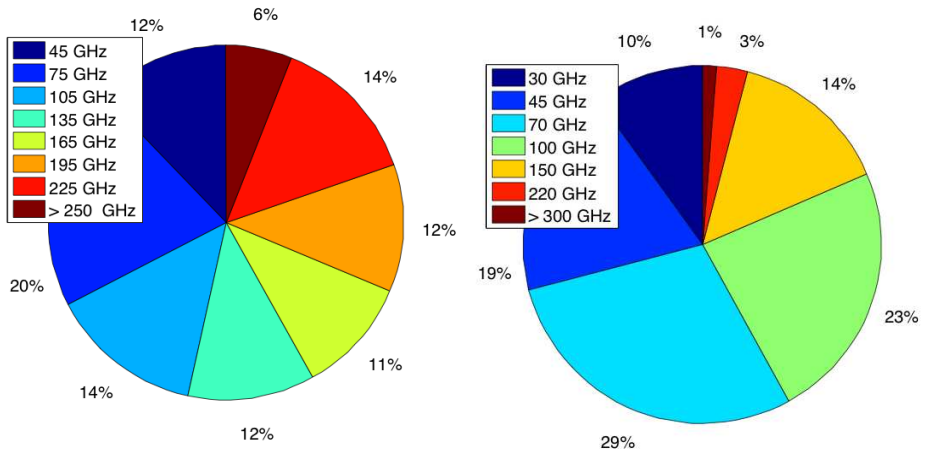

Figure 11.7: Breakdown of the focal plane area between the frequency channels as originally proposed for the COrE, **left**, and CMBpol, **right**, satellites. In the case of COrE all the channels with frequencies larger than 250 GHz represent less than 10% of the total focal plane area.

two constraints are derived given the proposed configurations of COrE (Table 11.3) and CMBpol (Table 11.2). In the case of the focal plane area we assume that an effective area of the focal plane occupied by a single, diffraction-limited detector k operating at frequency, ν_k, can be expressed as

$$\mathcal{A}_{eff}(k) \equiv \left(\frac{c}{\nu_k}\right)^2 = \lambda_k^2, \tag{11.10}$$

where λ_k is the k^{th} observed wavelength. This assumption for the filled area should be modified if the limiting factor is, for instance, driven by the readout system rather than the detector itself. The total focal plane area is then obtained by summing over the contributions coming from all the detectors. We note that this gives at the best some effective area because we do not take into account any kind of filling factor, which is usually driven by technical constraints such as the shape of the detectors, the wiring, etc. Fig. 11.7 shows the fractional area as occupied by each channel in the case of the proposed versions.

Hereafter we neglect the effects of the E-B leakage, e.g., Grain et al. (56), both in the calculations of the foreground spectra as well as the CMB variance. In the former case this is justified given the fact that E and B spectra for foregrounds are on comparable levels and the leakage is usually harmless. For the CMB variance we assume that the effects of such a leakage can be largely removed using one of the methods proposed in the literature. Though corrections of this sort usually lead to some extra precision loss, this is typically only a fraction of the standard cosmic variance and, at least for experiments with a sufficiently large sky coverage, small enough not to change our

results in a significant way. For small-scale observations the effect may not be negligible and should be taken into account, e.g., Grain et al. (56), Stivoli et al. (130).

For some alternative analyses of performance of these two experiments see, e.g., Betoule et al. (12), Bonaldi and Ricciardi (17), Dunkley et al. (36).

11.6.1 Mixing matrix

To define the mixing matrix, Eq. (10.1) relevant for the problem at hand, we will use the component frequency scaling laws as defined in paragraph 11.5. We set the reference frequency, i.e., frequency at which all the component maps are recovered as equal to 150 GHz. We also account for frequency band-shapes. For this we will assume that they are top-hat-like with a width equal to 1/3 of the central value. Therefore, an element, $\mathbf{A}_{ij}$ of the mixing matrix will be given as

$$\mathbf{A}_{ij} \equiv \int d\nu \, \Phi_j \left(\nu, \nu_{ref}\right) W_{TH} \left(\left|\nu - \nu_i\right|, \frac{1}{3}\nu_i \right), \tag{11.11}$$

where ν_i is a frequency of the i-th channel, $\Phi_j \left(\nu, \nu_{ref}\right)$ is a photon flux as measured at frequency ν relatively to ν_{ref}, and $W_{TH}(\cdot, \sigma_{TH})$ is a top hat window centered at 0 and with a width σ_{TH}. As mentioned earlier we assume hereafter that the scaling laws adopted on this stage coincide with the true ones modulo the unknown parameters. Nonetheless we will limit the frequency range of the channels included in our discussion below to between 30 and 400 GHz, to, on the one hand, avoid channels where the CMB is completely swamped by the foregrounds and, on the other, not to stretch the adequacy of the frequency scaling model of the dust over a too broad interval.

11.6.2 Noise levels

We assume sky-noise limited detectors. Their noise level, in antenna units, is taken to be independent on a detectors operating frequency and set to be equal to $\sigma_t \sim 30\,\mu\mathrm{K}\sqrt{s}$, see The COrE Collaboration (137). A single detector noise level per pixel will then be given by an observation total length, T_{obs} and pixel area. The detector noise per channel will also depend on a number of detectors operating at a given frequency. The numbers of detectors for each channel, $\{d_i\}_{(i=0,\ldots,n_f-1)}$, are the parameters we will be most frequently trying to optimize in the reminder of this section. The noise correlation matrix will be then assumed to be diagonal and the diagonal elements will be given by

$$\mathbf{N}_{ii} = \frac{4\,\sigma_t^2\,N_{pix}^{tot}}{T_{obs}\,d_i}. \tag{11.12}$$

Here, N_{pix}^{tot} is a total number of observed pixels (to be distinguished from N_{pix} a number of pixels included in the analysis (N_{pix} will depend on the mask we will consider; see paragraph 11.5).

11.6.3 Resolution

So far we have ignored completely the fact that detectors operating at different frequencies will likely have a different resolution, in particular if they are diffraction-limited. Because the parametric maximum likelihood component separation approach adopted here is pixel-based all the channel maps will have to be however smoothed to some common resolution before the separation can be accomplished. The extra smoothing required here is not generally lossless and may introduce noise correlation between the pixels. Hereafter we will ignore such effects and keep using Eq. (11.12) to compute the noise levels with only the pixel size, and thus a number of pixels, adjusted accordingly. As far as the sky signals are concerned, given that our science goals are mostly constrained by the large angular scales, we will mimic the common resolution by setting a hard limit on the considered value of ℓ to be $\ell_{max} = 500$, as we have found that for the considered noise levels there is no information beyond that range. We note that in a more refined approach one may want to introduce the resolution as an optimization parameter and constraint it by requiring that the gain due to its decrease is larger than some threshold. All the power spectra used in this work have been derived using HEALPIX pixelized maps with the HEALPIX resolution level, nside = 512. This is clearly sufficient given the hard ℓ-space cut off we have adopted here. We stress that this resolution is higher than the one used in paragraph 11.5 for the determination of the matrix $\hat{\mathbf{F}}$. This is because in the latter calculation only pixel-domain quantities are involved, which are overwhelmingly dominated by the large scale fluctuations for which nside = 128 maps are entirely sufficient.

11.6.4 Fixed number of channels with pre-defined, fixed frequencies

In this section, I describe the optimization of the two experiments assuming that the frequency channels are fixed ahead of the procedure. The results are summarized in Tables 11.4 and 11.5 for COrE and CMBpol, respectively, and for each FOM (called there for shortness as F1, F2 or F3), three considered sky masks (P06, Mask I or Mask II), and two hardware constraints (total area or total number of detectors), and are contrasted with results obtained for the original designs of the experiments, as shown in the rightmost columns of the Tables. We note that though the latter configurations are mask-independent, the corresponding FOMs values differ somewhat from mask to mask due to differences of the sky included in the analysis. For each of the optimized configurations the tables show a corresponding total number of detectors, focal plane area, effective noise levels, spectral index determination precision, and values of the three FOMs. A selection of these results is also depicted in Figs. 11.8-11.11, showing, as bars, a number of detectors for each of the considered channels, left panels, and power spectra of the residuals corresponding to each configuration, right panels. The

visualized cases are those based on the P06 mask, however the other cases would look similar. In each Figure the upper left panel shows a corresponding original configuration followed by three panels displaying configurations optimized with respect to each of the three FOMs. Four general observations are in order here.

1. The optimized configurations depend on the FOM used for the optimization.
2. The constraints imposed on the problem affect the results. Constraining the focal plane area gives preference to the high frequency channels with detectors occupying a small area and thus leads to a worse determination of the synchrotron signal, which in turn leads to a higher level of residuals, if these are left unconstrained, i.e. in cases of FOM#1 and FOM#3. Also the overall noise, FOM#3, tends to be higher.
3. The final configurations obtained for each of the three masks are essentially identical, though the actual values of FOMs do differ mostly due to a different number of pixels with MASK-II containing the fewest of those.
4. The optimized configuration contain significantly fewer frequency channels than allowed for in the optimization and therefore fewer than proposed in the original versions of the both these experiments.

Below we comment on some of the result in more detail and leaving a general discussion for the conclusions, paragraph 11.7.

FOM#1 optimization — r_{min}

For all configurations shown in Tables 11.4 and 11.5 for which FOM#1 could be computed, i.e., those containing more than just 3 channels, r_{min} is found to be on the order of 10^{-4} and varying from case to case by no more than a factor of 2. This is also the case for the original designs of the COrE and CMBpol satellites. The values of FOM#1 optimized under the constraint of the total number of detectors tend to be somewhat better (worse) than those derived under the total focal plane area constraint for COrE (CMBpol). The differences are however small across the board and probably irrelevant in practice.

In both the COrE and CMBpol cases, the optimization of FOM#1 leads to configurations for which also FOM#3 is close to the optimum, as the latter is found to be within 5-10% of its best value for the respective hardware constraints. This suggests that this is the variance due to the noise rather than the foreground residual, which contributes to the recovered value of the FOM#1 more significantly (see also Stivoli et al. (130)). Conversely, as a consequence in such cases the level of the foreground residuals is not tightly controlled and therefore the FOM#1-optimized configurations result in values

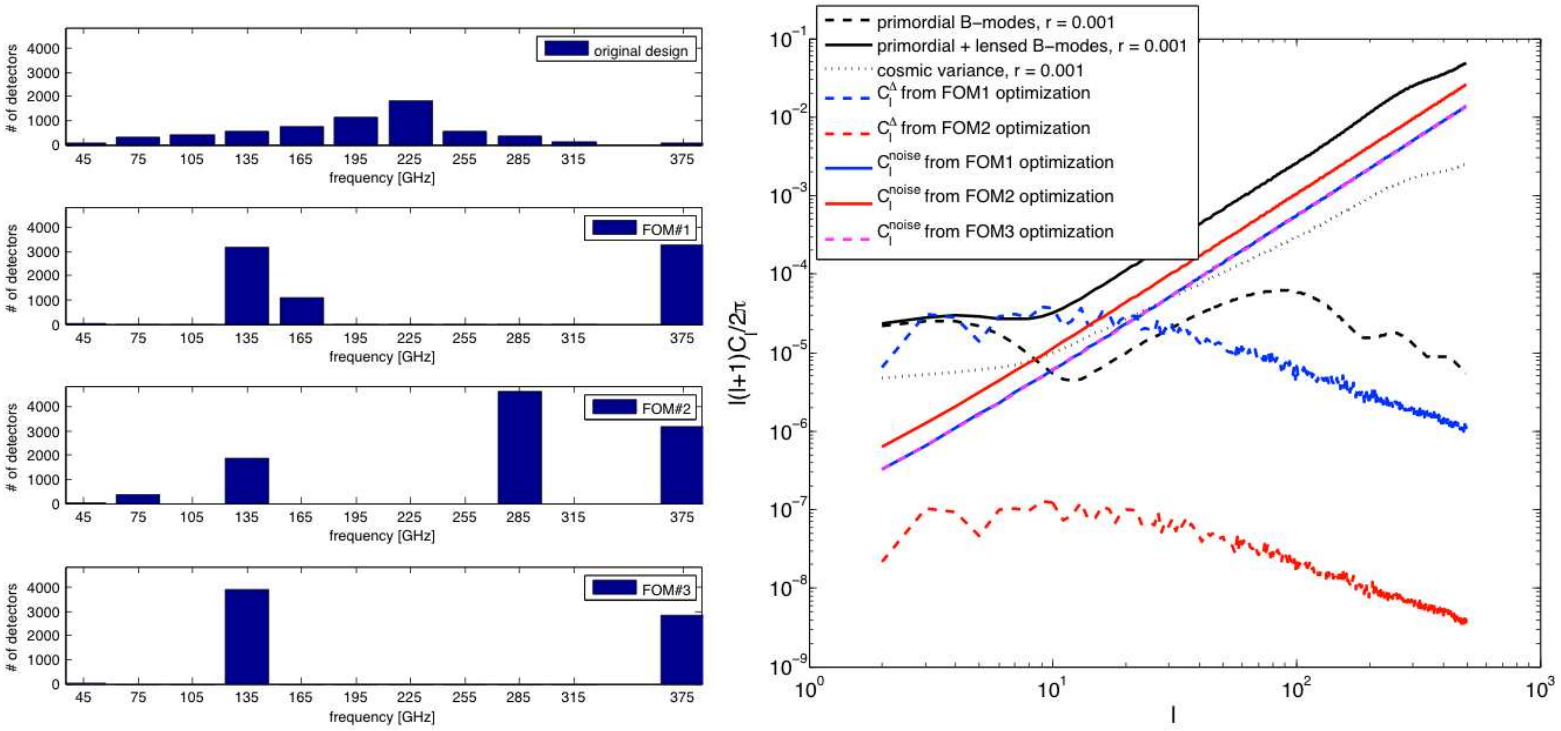

Figure 11.8: **Left panel**: optimized distributions of numbers of detectors per channel derived under the total focal plane area constraint for the COrE satellite, including only channels below 400 GHz. From top to bottom we show first the original distribution followed by the three optimized ones derived using FOM#1 to #3, respectively. **Right panel**: corresponding power spectra of the residuals and the noise computed for the optimized configurations shown on the left and compared against the spectrum of the CMB B-modes with $r = 0.001$.

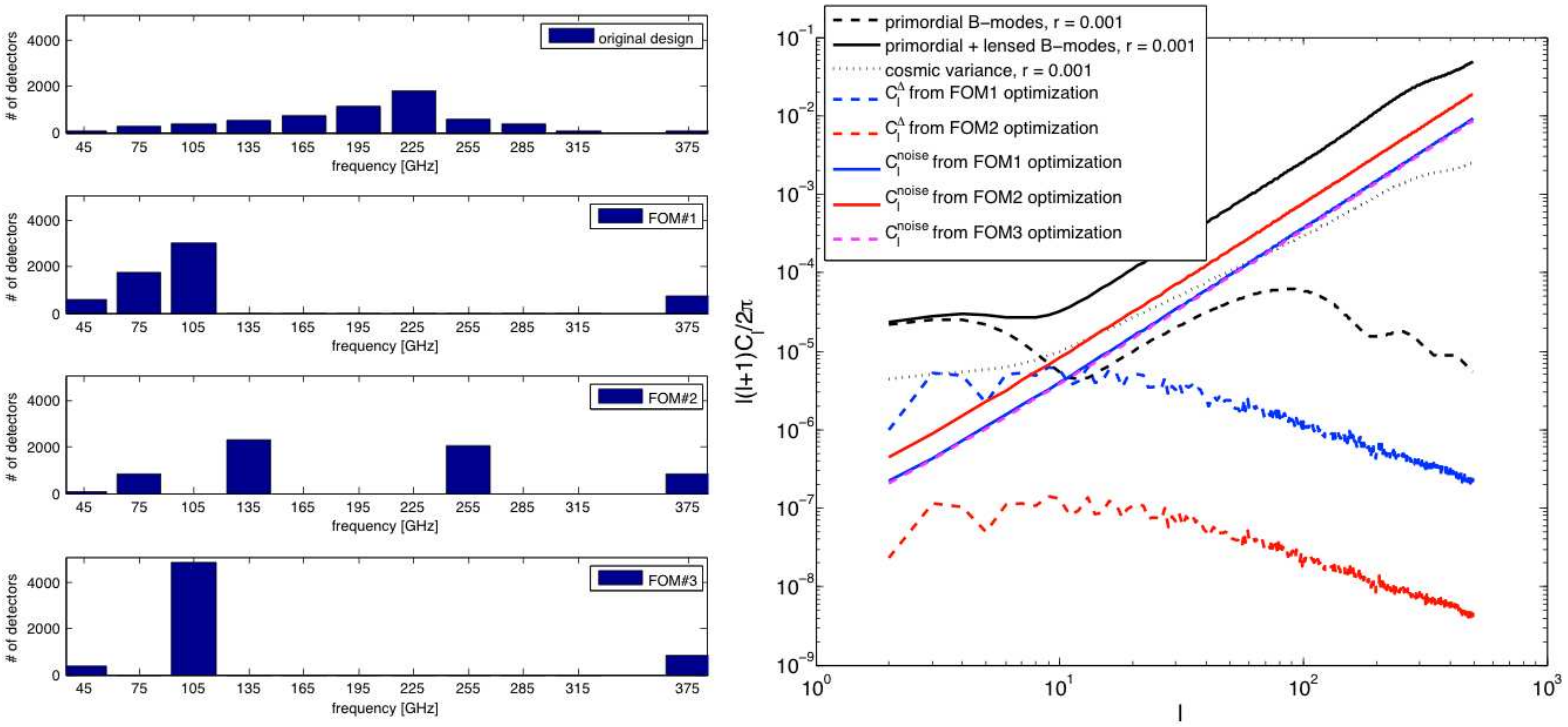

Figure 11.9: As in Fig. 11.8 but imposing the constraint on the total number of detectors.

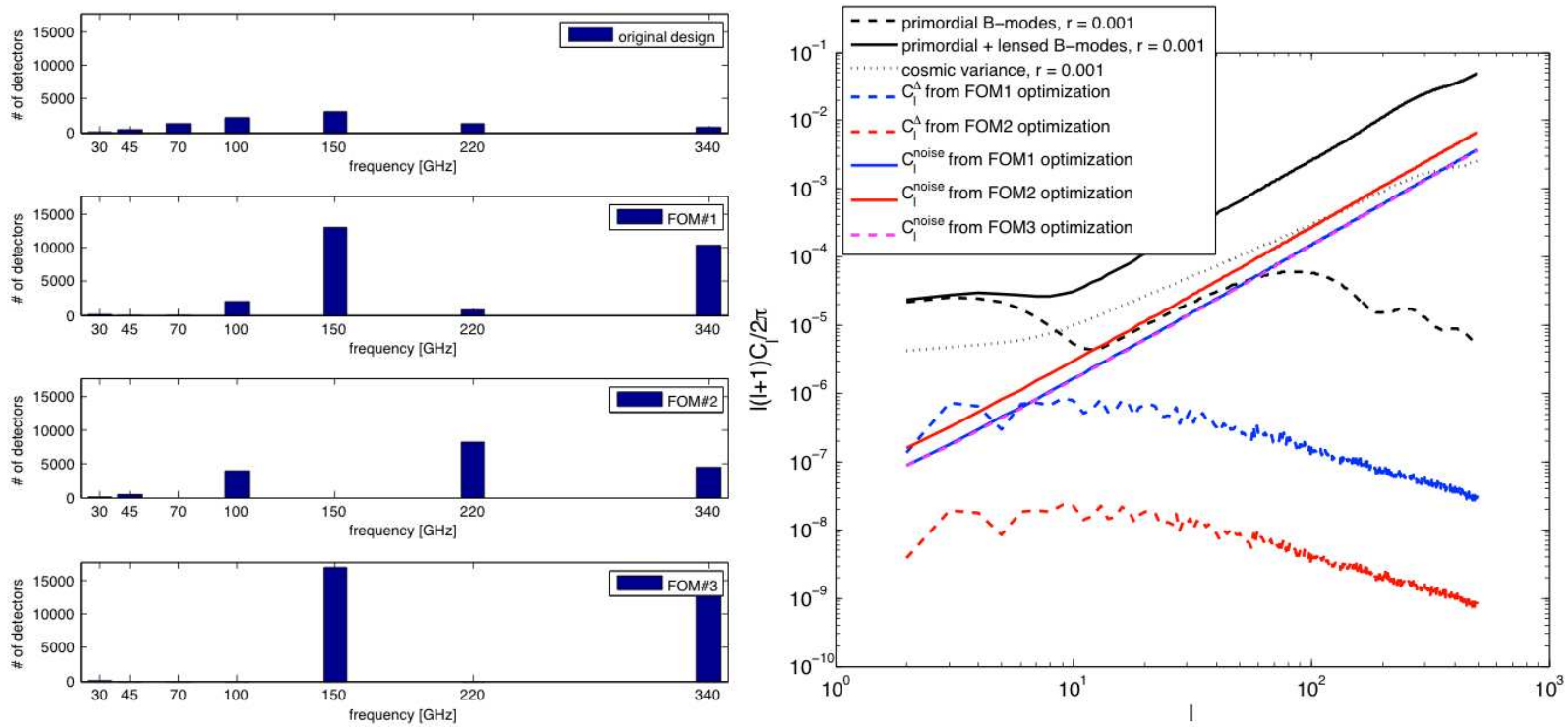

Figure 11.10: As in Fig. 11.8 but for the CMBpol satellite.

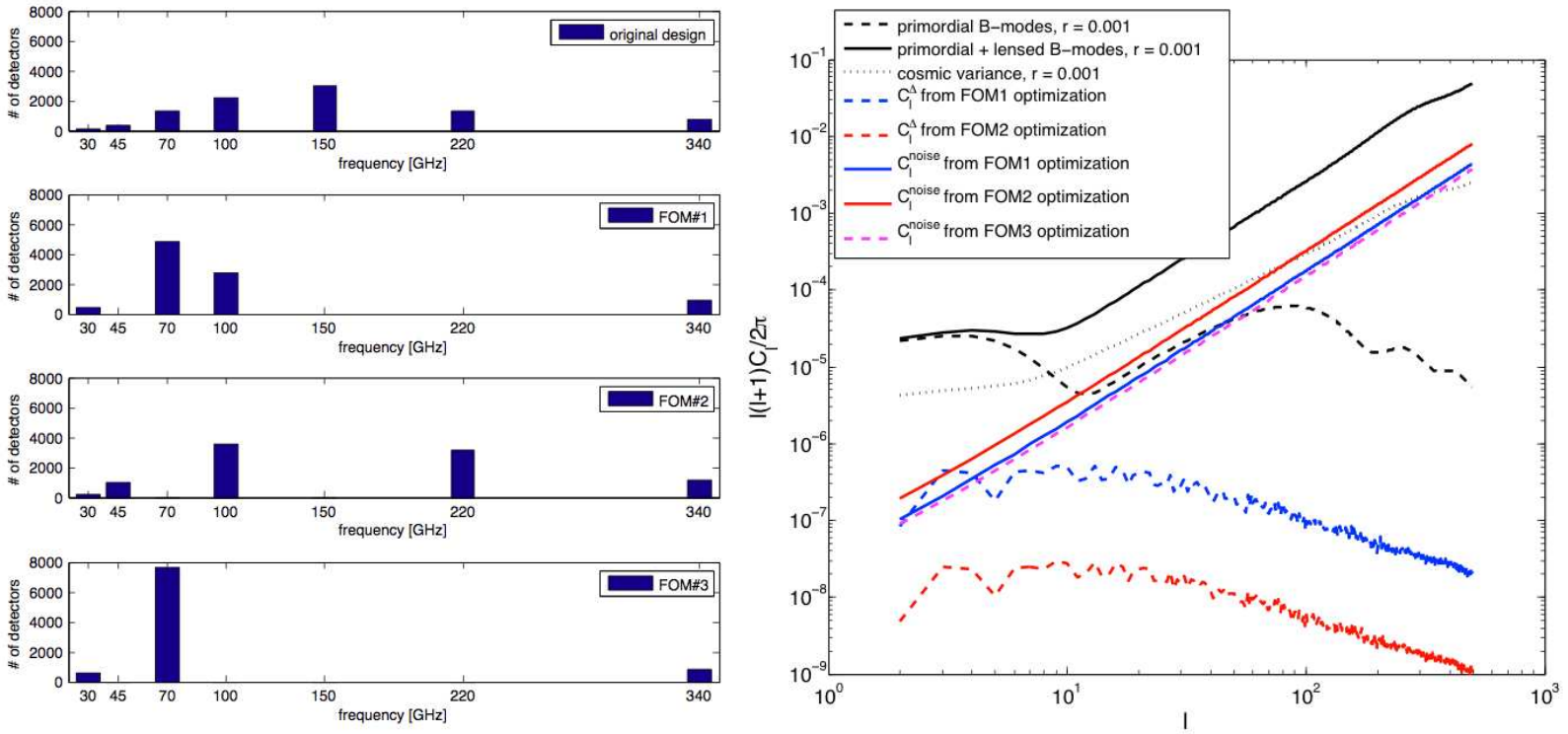

Figure 11.11: As in Fig. 11.9 but for the CMBpol satellite.

Constraint	channels	P06 mask						mask I				mask II				proposed version		
		area			total #			area		total #		area		total #				
	(GHz)	F1	F2	F3	F1	F2	F3	F1	F2	F1	F2	F1	F2	F1	F2	P06 mask	mask I	mask II
Number of detectors	45	45	22	48	610	87	382	45	21	610	72	45	22	607	88	64	-	-
	75	-	370	-	1775	827	-	-	366	1775	778	-	37	1759	832	300	-	-
	105	-	-	-	3027	-	4876	-	-	3026	-	-	-	3042	-	400	-	-
	135	3160	1872	3918	-	2313	-	3161	1886	-	2322	3124	1871	-	2315	550	-	-
	165	1092	-	-	-	-	-	1091	-	-	-	1146	0	-	-	750	-	-
	195	-	-	-	-	-	-	-	-	-	-	-	-	-	-	1150	-	-
	225	-	-	-	-	-	-	-	-	-	-	-	-	-	-	1800	-	-
	255	-	-	-	-	2081	-	-	-	-	2141	-	-	-	2073	575	-	-
	285	-	4623	-	-	-	-	-	4669	-	-	-	4610	-	-	375	-	-
	315	-	-	-	-	-	-	-	-	-	-	-	-	-	-	100	-	-
	375	3281	3186	2859	717	820	870	3281	3156	717	816	3294	3188	719	820	64	-	-
Total area $\sum$ [number of detectors]		0.023	0.023	0.023	0.081	0.032	0.057	0.023	0.023	0.081	0.031	0.023	0.023	0.080	0.032	0.023	-	-
		7579	10073	6824	6128	6128	6128	7577	10099	6128	6128	7608	10062	6128	6128	6128	-	-
Fractional area	45	0.085	0.042	0.091	0.34	0.12	0.30	0.085	0.040	0.34	0.10	0.085	0.042	0.36	0.12	0.12	-	-
	75	-	0.25	-	0.35	0.42	-	-	0.25	0.35	0.41	-	0.25	0.35	0.42	0.21	-	-
	105	-	-	-	0.31	-	0.69	-	-	0.31	-	-	-	0.31	-	0.14	-	-
	135	0.67	0.40	0.83	-	0.36	-	0.67	0.40	-	0.37	0.66	0.40	-	0.36	0.12	-	-
	165	0.15	-	-	-	-	-	0.15	-	-	-	0.16	-	-	-	0.11	-	-
	195	-	-	-	-	-	-	-	-	-	-	-	-	-	-	0.12	-	-
	225	-	-	-	-	-	-	-	-	-	-	-	-	-	-	0.14	-	-
	255	-	-	-	-	0.090	-	-	-	-	0.097	-	-	-	0.090	0.034	-	-
	285	-	0.22	-	-	-	-	-	0.22	-	-	-	0.22	-	-	0.018	-	-
	315	-	-	-	-	-	-	-	-	-	-	-	-	-	-	0.0039	-	-
	375	0.090	0.088	0.079	0.006	0.016	0.010	0.090	0.087	0.0057	0.017	0.090	0.088	0.0057	0.016	0.0018	-	-
Noise per channel $[\mu K_{antenna}]$	45	0.37	0.52	0.35	0.099	0.27	0.13	0.37	0.53	0.099	0.30	0.37	0.52	0.099	0.26	0.31	-	-
	75	-	0.13	-	0.058	0.085	-	-	0.13	0.058	0.088	-	0.13	0.058	0.085	0.14	-	-
	105	-	-	-	0.044	-	0.035	-	-	0.044	-	-	-	0.044	-	0.12	-	-
	135	0.044	0.057	0.039	-	0.051	-	0.044	0.056	-	0.051	0.044	0.036	-	0.051	0.10	-	-
	165	0.074	-	-	-	-	-	0.074	-	-	-	0.072	-	-	-	0.089	-	-
	195	-	-	-	-	-	-	-	-	-	-	-	-	-	-	0.072	-	-
	225	-	-	-	-	-	-	-	-	-	-	-	-	-	-	0.058	-	-
	255	-	-	-	-	0.054	-	-	-	-	0.053	-	-	-	-	0.10	-	-
	285	-	0.036	-	-	-	-	-	0.036	-	-	-	0.036	-	-	0.13	-	-
	315	-	-	-	-	-	-	-	-	-	-	-	-	-	-	0.24	-	-
	375	0.043	0.043	0.046	0.091	0.085	0.083	0.043	0.044	0.091	0.086	0.043	0.043	0.091	0.085	0.31	-	-
$\delta\beta_d\,[10^{-3}]$		0.96	0.12	-	0.95	0.16	-	0.83	0.074	0.82	0.10	1.47	0.19	1.48	0.25	0.28	0.18	0.45
$\delta\beta_s\,[10^{-3}]$		30	2.9	-	4.3	2.2	-	26	1.9	3.7	1.4	38	3.9	5.6	2.9	3.4	2.2	4.5
$\frac{\delta\beta_d\delta\beta_s}{\delta\beta_d\times\delta\beta_s}$		-0.92	-0.44	-	-0.92	-0.57	-	-0.96	-0.46	-0.96	-0.58	-0.91	-0.44	-0.91	-0.57	-0.67	-0.70	-0.67
F1 $[10^{-3}]$		0.22	0.26	-	0.21	0.24	-	0.20	0.23	0.19	0.21	0.31	0.37	0.29	0.34	0.28	0.25	0.40
F2 $[10^{-3}]$		0.95	0.0097	-	0.16	0.011	-	1.1	0.0057	0.18	0.0065	0.79	0.086	0.14	0.0094	0.028	0.018	0.025
F3 [nK_{cmb}]		5.4	10	5.3	3.6	7.4	3.4	5.4	10	3.6	7.7	5.4	10	3.6	7.4	14	14	14

Table 11.4: Summary of the optimization results in the case of COrE considering channels only below 400 GHz. For each of the three masks, we present results for each of the three FOMs optimized under one of the two constraints, either fixing the focal plane area or the total number of detectors. The results for FOM#3 are quoted only once as they do not depend on the choice of the mask.The rightmost columns show the results computed using the original version of COrE as proposed in The COrE Collaboration (137). In the latter case the configuration is always the same, whatever the choice of the mask.

Constraint	channels	P06 mask						mask I				mask II				proposed version		
		area			tot #			area		tot #		area		tot #				
	(GHz)	F1	F2	F3	F1	F2	F3	F1	F2	F1	F2	F1	F2	F1	F2	P06 mask	mask I	mask II
	30	35	62	52	472	185	601	33	61	448	168	56	62	672	187	84	-	-
	45	-	491	-	-	1016	-	-	493	-	975	10	491	1240	1021	364	-	-
Number of	70	-	-	-	4861	-	7646	-	-	4935	-	-	-	3643	-	1332	-	-
detectors	100	1970	4056	-	2776	3546	-	1400	4101	2579	3567	6311	4049	2583	3544	2196	-	-
	150	13159	-	16995	-	-	-	14639	-	-	-	3518	-	-	-	3048	-	-
	220	823	8328	-	-	3164	-	-	8228	-	3207	178	8340	-	3157	1296	-	-
	340	10364	4525	13210	954	1154	817	11586	4259	1102	1148	7988	4566	926	1154	744	-	-
Total area		0.084	0.084	0.084	0.16	0.10	0.20	0.084	0.084	0.16	0.099	0.084	0.084	0.21	0.10	0.084	-	-
$\sum$ [number of detectors]		26352	17462	30258	9064	9064	9064	27658	17143	9064	9064	18061	17508	9064	9064	9064	-	-
	30	0.042	0.074	0.063	0.29	0.18	0.30	0.040	0.073	0.28	0.17	0.068	0.074	0.32	0.18	0.10	-	-
	45	-	0.26	-	-	0.44	-	-	0.26	-	0.44	0.0054	0.26	0.26	0.44	0.19	-	-
Fractional	70	-	-	-	0.55	-	0.70	-	-	0.57	-	-	-	0.31	-	0.29	-	-
area	100	0.21	0.44	-	0.15	0.31	-	0.15	0.44	0.15	0.32	0.68	0.44	0.11	0.31	0.24	-	-
	150	0.63	-	0.81	-	-	-	0.70	-	-	-	0.17	-	-	-	0.15	-	-
	220	0.018	0.19	-	-	0.057	-	-	0.18	-	0.060	0.0040	0.19	-	0.057	0.029	-	-
	340	0.097	0.042	0.12	0.0046	0.0088	0.0032	0.11	0.040	0.0054	0.0090	0.074	0.043	0.0034	0.0087	0.0069	-	-
	30	0.41	0.31	0.34	0.11	0.18	0.010	0.42	0.31	0.12	0.19	0.33	0.31	0.094	0.18	0.27	-	-
	45	-	0.11	-	-	0.077	-	-	0.11	-	0.078	0.77	0.11	0.070	0.077	0.13	-	-
Noise	70	-	-	-	0.035	-	0.028	-	-	0.035	-	-	-	0.041	-	0.067	-	-
per	100	0.055	0.038	-	0.046	0.041	-	0.065	0.038	0.048	0.040	0.031	0.038	0.048	0.041	0.052	-	-
channel	150	0.021	-	0.019	-	-	-	0.020	-	-	-	0.041	-	-	-	0.044	-	-
$[\mu K_{antenna}]$	220	0.085	0.027	-	-	0.044	-	-	0.027	-	0.043	0.18	0.027	-	0.044	0.068	-	-
	340	0.024	0.036	0.021	0.079	0.072	0.086	0.023	0.038	0.074	0.072	0.027	0.036	0.080	0.072	0.090	-	-
$\delta\beta_d\,[10^{-3}]$		0.25	0.086	-	0.71	0.13	-	0.37	0.055	0.62	0.055	0.41	0.14	0.66	0.21	0.16	0.10	0.25
$\delta\beta_s\,[10^{-3}]$		2.39	0.51	-	1.5	0.38	-	3.2	0.33	1.4	0.33	2.7	0.68	0.67	0.50	0.55	0.36	0.73
$\frac{\delta\beta_d\delta\beta_s}{\delta\beta_d\times\delta\beta_s}$		-0.66	-0.46	-	-0.96	-0.48	-	-0.10	-0.48	-0.88	-0.49	-0.88	-0.46	-0.54	-0.48	-0.63	-0.65	-0.62
F1 $[10^{-3}]$		0.19	0.20	-	0.19	0.20	-	0.17	0.18	0.17	0.18	0.27	0.28	0.27	0.29	0.20	0.18	0.29
F2 $[10^{-3}]$		0.024	0.0018	-	0.059	0.0023	-	0.076	0.0011	0.069	0.0014	0.020	0.0016	0.012	0.0020	0.0041	0.0026	0.0036
F3 [$\mathrm{nK_{cmb}}$]		1.5	2.7	1.4	1.6	3.1	1.5	1.4	2.7	1.6	3.2	1.6	2.7	1.7	3.1	3.0	3.0	3.0

Table 11.5: As in Table 11.4 but for CMBpol, see Aguirre et al. (1).

of FOM#2, which are at least 1 order of magnitude above the best achievable r_{eff}, and worse than the values derived for the proposed designs. As we normally would prefer to avoid too high residuals we conclude that FOM#1 is not sufficient as a stand-alone optimization criterion and preferably should be combined with some other indicator, efficient in enforcing the low value of the residuals. We will get back to this issue later on in this Section.

FOM#2 optimization — r_{eff}

From Eqs. (10.19)–(10.21) it follows that a good determination of the spectral parameters β_{dust} and β_{sync} is necessary and sufficient to ensure a low level of the foreground residuals. We therefore expect (see also Amblard et al. (3)) that in the FOM#2-optimized configuration the detectors should populate predominantly low frequency bands, which are dominated by the synchrotron signal, the CMB band, and high frequency bands, dominated by the dust. As we require at least 4 channels in the case at hand to avoid problem singularity and impose the hardware constraint the actual answer is somewhat more complex, nevertheless the overall detector distribution conforms with the above intuition. Indeed the FOM#2-optimized configurations include channels below 50 GHz, around $100 - 130$ GHz, and above 250 GHz. This applies for both the experiments and for every mask. The details of the distribution depend on a type of the constraint. As the high frequency detectors have smaller area we find that the dust is better estimated ($\delta\beta_{dust}$ lower) under the total area constraint case as more high frequency detectors can be had. The opposite can be seen for the synchrotron estimation. The resulting levels of the residuals are however essentially identical in both these cases. More aggressive masking clearly helps, Mask I, but a balance has to be maintained between lowering the overall foreground level and the precision of the spectral index determination. The latter, unlike the former, benefits from a larger number of pixels and higher foregrounds and, otherwise, can therefore start driving the effective residual up, e.g., Mask II.

The FOM#2-optimized configurations usually render good values for FOM#1 (within $10-15\%$ of the best achievable values), but result in the CMB map noise levels (FOM#3) up to twice higher than the best ones. The original versions of the considered experiments also yield the values of r_{eff} close to the best ones.

FOM#3 optimization

For this FOM, and in every considered case, the optimization of the focal plane with respect to the noise in the CMB map ends up with only three nonzero channels:

two at frequencies as extreme as only allowed for, and one at an intermediate one contained in the CMB frequency band. The precise position of the latter is found again to be dependent on a type of the hardware constraint used. For the CMBpol satellite the values of the central frequencies are 70 or 150 GHz for the constraint on the total number of detectors and the area, respectively. For COrE they are 105 and 135 GHz, respectively. We recall that in the case of this FOM all the spectral indices are assumed to be known, otherwise the three channel configurations derived here would be singular and would not permit a determination of the spectral indices. The achieved noise levels are better when the total number of detectors is constrained, and are lower by a factor up to ~ 1.6. The original versions of the satellites result in quite high noise (higher by a factor of $2.5 - 4$) in comparison with the one derived for the optimized configurations.

Consensus configuration

Having postulated three different FOMs we have obtained three different, optimized configurations. Moreover, as we have already mentioned, there is clearly tension between some of the considered FOMs. The issue now is therefore how to find a compromise between them in order to select a single configuration as a result of our procedure. To do so we first recall that in our case the configurations preferred from the point of view of FOM#1 fail to ensure a satisfactory level of the residuals, as quantified by FOM#2, while optimization of the latter yields a rather high level of noise, i.e., FOM#3. Simultaneously however optimizing FOM#1 effectively ensures a near optimization of FOM#3. Therefore we will retain the former as part of the optimization and drop the latter, which from now on will be used only as a benchmark to compare against the obtained configurations. As FOM#1 on its own is not fully satisfactory we will therefore optimize it, while imposing a constraint based on a value of FOM#2. Clearly if more FOMs are used more constraints can be introduced in the same way. What values to choose for the thresholds is a somewhat debatable question, an answer to which will depend on a specific application. In our case, we first note that for the FOM#2-optimized configuration the resulting r_{eff} is an order of magnitude lower than the respective value of r_{min}. The latter is moreover typically 20% higher than its corresponding best value.

From the viewpoint of these two indicators the FOM#2-optimized solution looks therefore quite satisfactory. This is particularly true for the CMBpol case for which this solution can be accepted as indeed the final outcome of the procedure. For COrE the potential remaining problem could be the noise level. In search of the consensus configuration we may therefore want to let the residual grow, in particular, relatively to the value of r_{min} and gain in terms of the noise. Clearly the more we compromise on r_{eff} the more we can gain on σ^2_{CMB}. As for COrE the values of r_{min} are close to 2×10^{-4}

	channels (GHz)	F1-optimized + constraint F2 $\leq 10^{-4}$	no 255GHz channel cases no optimization	no 255GHz channel cases F1-optimized + F2 $\leq 1.5 \times 10^{-4}$	extra channels F1 optimized + F2 $\leq 10^{-4}$	original version (137)
Number of detectors	45	607	607	592	366	64
	75	1771	1771	2112	47	300
	105	3021	3021	2801	4551	400
	135	-	-	**0**	-	550
	165	-	-	**0**	-	750
	195	-	-	**0**	**200**	1150
	225	-	-	**0**	-	1800
	255	17	**0**	**0**	-	575
	285	-	-	**0**	**200**	375
	315	-	-	**0**	-	100
	375	711	711	623	764	64
$\delta\beta_d$ $[10^{-3}]$		0.74	0.95	0.91	0.35	0.28
$\delta\beta_s$ $[10^{-3}]$		3.5	4.3	4.1	8.1	3.4
$\frac{\delta\beta_d\delta\beta_s}{\delta\beta_d\times\delta\beta_s}$		-0.88	-0.92	-0.92	-0.66	-0.67
F1 $[10^{-3}]$		0.21	0.21	0.21	0.21	0.28
F2 $[10^{-3}]$		0.10	0.16	0.15	0.10	0.028
F3 [nK$_{\rm cmb}$]		3.6	3.6	3.6	3.6	14

Table 11.6: Comparison of performance of the variants of the COrE setups considered in paragraph 11.6.5. All the optimization runs have been performed while keeping the total # of detectors constant, used the P06 mask and only the channels below 400GHz. The configurations in the Table include, from left to right, (1) a result of the optimization procedure with respect to FOM#1 with a constraint on FOM#2 of $\leq 10^{-4}$, (2) the same configuration but with the 255GHz channel suppressed, (3) a configuration with the same frequency channels as in (2), but with numbers of detectors re-derived via an optimization with respect to FOM#1 and a constraint FOM#2 $\leq 1.5 \times 10^{-4}$, and (4) a re-optimized configuration with the channels as before plus two extra ones with a fixed number of detectors (= 200 each). The last column shows the original COrE configuration for comparison. Numbers in bold correspond to parameters forced to be at a given value.

and we will allow r_{min} to be as large as 10^{-4}, and reoptimize the problem with respect to FOM#1 with the constraint that $r_{eff} \leq 10^{-4}$. This specific choice is in fact arguably rather high. In fact we find that imposing more strict limits of $r_{eff} \leq 2.5 \times 10^{-5}$ or 5×10^{-5} already can ensure satisfactory noise levels, 4.0 and 3.9 nK$_{CMB}$, respectively, and thus could be preferred for the actual experiment optimization. We will however use hereafter the threshold of 10^{-4} as it is more useful for demonstration purposes.

The resulting configuration is shown in Fig. 11.12 and summarized in Table 11.6, where we show the results obtained for the two hardware constraints. The spectra of the noise and residuals are also displayed in the right panel of the Figure. We conclude that the detector distribution indeed resembles a hybrid between two solutions obtained earlier as a result of the optimization of FOMs: #1 and #2 separately with a respective hardware constraint, Figs. 11.8 and 11.9. As anticipated above the overall level of the foreground residual spectrum is rather high as compared to both the B-mode spectrum and its respective variance due to the noise and the sky. However, as intended, the noise level has been successfully suppressed to the levels close to those computed for FOM#3 optimized configurations.

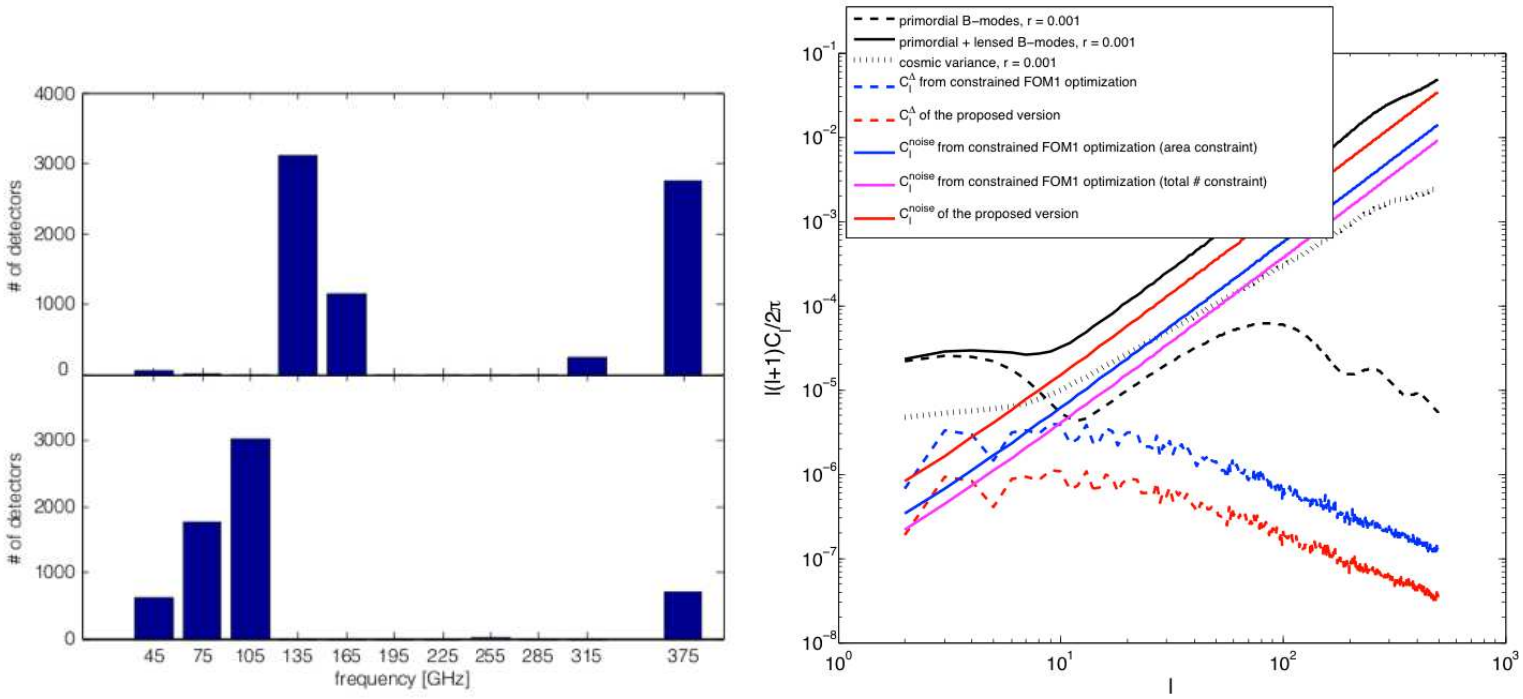

Figure 11.12: **Left panel**: results of the FOM#1-based optimization derived in the case of the COrE experiment with a constraint on FOM#2 ($< 10^{-4}$), and using the P06 mask and channels with frequencies below 400 GHz. Upper (lower) panel is obtained under the total area (total number) constraint. **Right panel**: comparison of the power spectra corresponding to the proposed and optimized versions of the COrE experiment as listed in Table 11.6 and visualized in the left panel. The spectra in blue (mid-level noise spectrum and highest residuals, these latter being depicted with dashed lines) correspond to the cases with the total area constraint. On the other hand, the spectra in magenta (lowest noise level, same residuals as previously) correspond to the cases with the detector number constraint. The foreground residual spectra in both of these cases overlap perfectly in the figure with the magenta curve being invisible.

11.6.5 Post-processing

For definiteness in this Section we focus on a single, specific configuration, and choose for it the optimized COrE setup obtained from the optimization of the FOM#1 value, while constraining the corresponding value of FOM#2 to be no more than 10^{-4} and keeping the total number of detectors fixed, as discussed at the end of the previous Section. The details of this configuration are listed in the fourth column of Table 11.6 together with the respective FOMs values.

The procedure employed in this Section follows the steps outlined in paragraph 11.3.3. In Fig. 11.13 we show an impact of a fractional change of a number of detectors in one channel at the time on the values of the FOMs. The latter are given relative to their optimized values and therefore all the curves shown in the figure are expected to start from the unity for the fractional change equal to zero, as the latter corresponds to the optimized configuration, and then grow typically monotonically with an increasing value of the fractional change. In addition, for reference we also show how the FOMs values would change if numbers of detectors in all the channels are decreased by the same fraction. We note that at least for the two of the FOMs, i.e., FOM#2 and #3, the latter dependence can be straightforwardly predicted using Eqs. (10.10), (10.21), and (11.4) and shown to be inversely proportional to an actual number of detectors in the corresponding configurations and thus inversely proportional to (1−fractional change of detectors). This indeed is adhered to by our numerical results.

The most striking features of some of the results are their apparent flatness extending on occasions to a rather high values of the fractional change. At face value that suggests that one is at liberty to change a number of detectors in some of the channels rather drastically but without noticeably penalizing the performance of the instrument. However, though some freedom indeed exists, it has to be exploited carefully. In particular, significantly changing a number of detectors in one selected channel, will usually have an effect of removing any freedom in adjusting the number of detectors in the remaining channels. Therefore if one's goal is to round-up the optimization results in a way to make them more amenable to an actual implementation that may not be the right way to go. Below we showcase some of these issues in the specific case at hand.

Probably most conspicuous thing about the configuration considered here is the presence of a channel centered at 255 GHz, to which are assigned only 17 detectors, as opposed to a few thousands in some of the other channels. A natural question to ask is therefore whether this channel is needed at all. In fact, the two outermost panels of Fig. 11.13 seem to confirm our feeling that this channel is in practice irrelevant as both the FOMs #1 and #3 effectively do not depend on its being present. This is not so however for the FOM#2 as shown in the middle panel. In this case removing this channel altogether will boost the value of this FOM, and thus the level of the foreground residual by a factor of ~ 1.5. Though not overwhelmingly large it is substantial enough

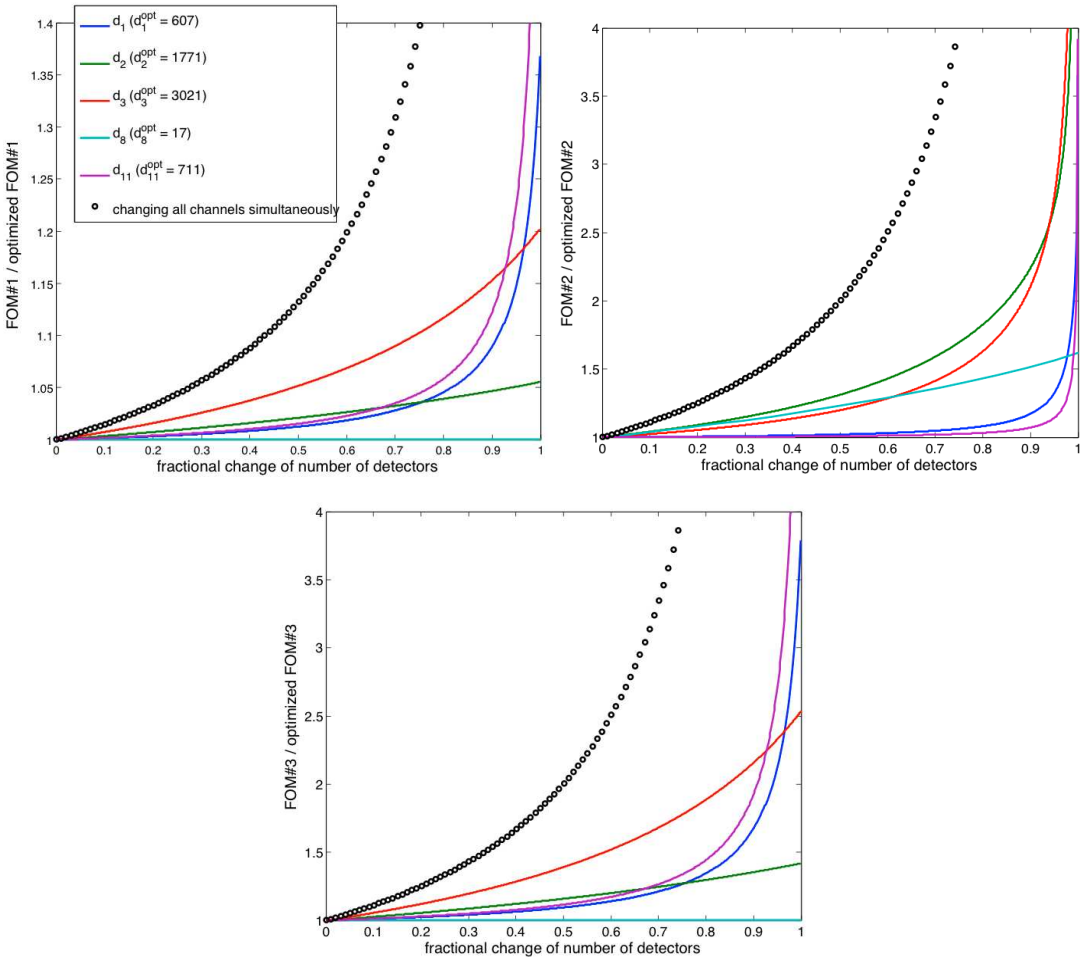

Figure 11.13: Dependence of the values of FOM#1 (top left), FOM#2 (top right), and FOM#3 (bottom), on a fractional change of a number of detectors in the hardware configuration as detailed in the fourth column of Table 11.6. The solid lines show cases with a number of detectors in only one selected channel being gradually decreased (left to right) and all the others being kept fixed at their optimized values. The circles show the case with a number of detectors in all channels decreasing by the same fraction simultaneously. The color schemes for the lines are the same in all the panels and described in the legend.

to justify holding on to this channel (unless of course the hardware cost of having the extra channel tips the balance the other way). These expectations are confirmed by direct calculations, results of which as shown a 5th column in Table 11.6. (We note that an attempt to re-optimize the resulting 4-channel system a posteriori does not bring much improvement either; see Table 11.6, column 6). We note that trying to keep the level of residuals down in this case can be of particular importance given that already in its original, optimized version (Table 11.6) the resulting values of r_{min} and r_{eff} are close enough to each other that this is probably the latter, i.e, the level of residuals, which would drive the actual limit on a detectable r value for this setup, rather than the statistical estimate provided by FOM#1. Letting r_{eff} grow any further would therefore directly affect our science goals. Instead we can therefore try to trim a number of detectors in either 45 or 375 GHz channel. We see that we can potentially reject up to $\sim$ 70% of the detectors in the former or $\sim$ 80% in the latter, without affecting the residuals level (FOM#2) in any appreciable manner. This would have an effect of increasing FOM#1 value by no more than $\sim$ 5% and FOM#3 by no more than $\sim$ 50%, both of which may therefore look perfectly acceptable. Whichever option we opt for, we can then reuse the spare detectors by distributing them to some of the existing channels or creating some additional ones, say at 165 GHz, in order to be better equipped to face some potential surprises (Sect, 11.3.3). However a special care then has to be taken if a number of detectors in some other channels needs to be concurrently decreased. This is because, as illustrated by lines marked with circles in Fig. 11.13, not all directions in the parameter space are similarly flat.

If our aim is to just round-up the detector numbers we can proceed as outlined in paragraph 11.3.3. We first postulate a set of fractional changes from the optimized values. In our case these could be $[v_k] = [1.025, 1.05., 1.1, 1.15]$ for FOM#1 and $[v_k] = [1.05, 1.25., 1.5, 2.0]$ otherwise, and then use Fig. 11.13 to read off the corresponding values of the fractional change for each channel and each FOM. These are values denoted σ in paragraph 11.3.3. In our case for FOM#1 they read

$$\left\{\sigma_j^{(k)}\right\} = \left\{\begin{array}{cccc} 409 & 496 & 555 & 577 \\ 1017 & 1664 & 1771 & \infty \\ 880 & 1477 & 2236 & 2697 \\ \infty & \infty & \infty & \infty \\ 442 & 549 & 624 & 654 \end{array}\right\}, \tag{11.13}$$

where k-th column corresponds to the k-th value of v_k and thus gives values of σ for each of the five channels with nonzero number of detectors in the optimized configuration (see second column of Table 11.6). We can use these values to define, Eq. (11.7), hyperellipsoidal volumes, $\mathcal{V}_k$, in the parameter space centered on the optimized configuration. We note that the infinity sign marks the cases, where the desired value of v_k could not have been reached due to the parameter space boundary. For instance, the

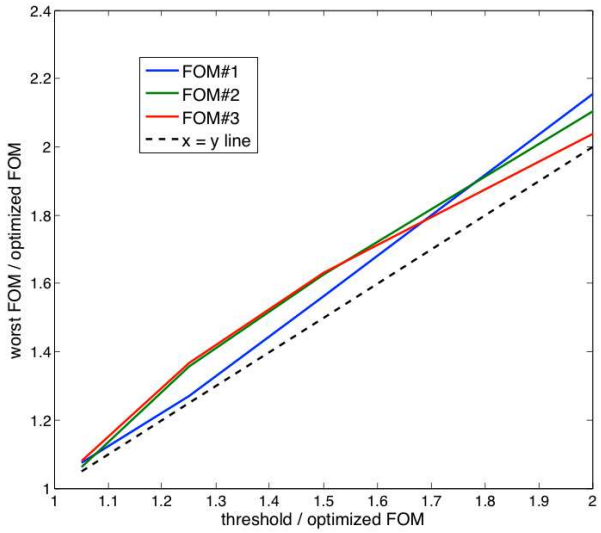

Figure 11.14: The worst values of each FOM, $\tilde{v}$, computed for each of the concentric hyperellipsoids, Eq. (11.7), defined by the threshold values, v, as shown on the horizontal axis. The dotted line shows $\tilde{v} = v$ case. Clearly, $\tilde{v} \simeq v$ in all shown cases, where the latter approximate equality holds to within 10%. The values of $\tilde{v}$ and v given here are relative to the optimized values of the respective FOMs.

values in the fourth row of Eq. (11.13) are all infinite as in the neighborhood of the optimized configuration the value of FOM#1 does not depend on a number of detectors in this channel as can be seen in Fig. 11.13.

To find the worst case value of the FOM for a k-th hyperellipsoid, $\tilde{v}_k$, we use random sampling of first an entire volume of the ellipsoid followed by that of only its surface. The latter requires fewer samples to ensure proper sampling density and is more efficient if we have some expectation of the FOM values monotonically deteriorating away from the optimized configuration. As anticipated in paragraph 11.3.3 the corrected values, $\tilde{v}_k$, and initial ones, v_k, are indeed found to be quite close, typically within 20% of each other as illustrated in Fig. 11.14.

The series of the concentric hyperellipsoids constructed here gives us a quick, though approximate, way to estimate the performance of some proposed configurations derived from the optimized one via small changes of all or some optimization parameters. As an example, consider a configuration with $[d_j] = [600, 1700, 3000, 17, 700]$ detectors in each of the five channels considered here. Given that for FOM#1,

$$\sum_k \frac{\left(d_j - d_j^{opt}\right)^2}{{\sigma_j^{(k)}}^2} \leq 1 \tag{11.14}$$

is fulfilled for any k, we conclude that the respective value of FOM#1 for this case will not be larger than by a factor $\tilde{v}_{k=1} \lesssim 1.025$ than the optimized value. Indeed a direct

calculation renders a value 1.002 times higher than the optimized one in agreement with our quick estimation. Similarly, we can deduce the performance of this configuration as expressed by the two other FOMs. These are more sensitive at least to changes in some of the channels however we find that for this specific configuration we can lose no more than a factor of 1.05 for both of them. These could be compared to the actual values of 1.01 and 1.02, respectively, all relative to the corresponding optimized values.

In this case overall the loss of performance seems rather benign and acceptable. Moreover, as a result of rounding-down the detector numbers we have gained around 100 of those, which we can arbitrarily assign to any of the existing channels or even create a new one to saturate the constraint on the total number of detectors. Whatever decision we make we will not compromise any of the performance figures derived earlier.

To illustrate a process of adding some ad hoc channels at this time we start from a configuration more drastically stripped-down than the one discussed above. Let that be for instance $[d_k] = [500, 1500, 3000, 0, 600]$, where we not only reduced numbers of detectors per channel more substantially but also removed the fourth channel altogether. Using the hyperellipsoid formalism we get quickly a helpful insight into how much we have lost as a result of choosing this configuration. As we already discussed, the biggest loss is found with regard to the value of FOM#2, which is boosted by more than 50% (but less than 100%) with FOM#1 and FOM#3 changing by $\lesssim 1.05$ and ~ 1.1 respectively. (The actual values being $1.01, 1.81$ and 1.09 for FOMs: #1, #2, and #3.) However we have also gained as many as 400 detectors, which can be distributed at our discretion to fill the constraint. Let us do so by introducing two extra channels at 195 and 285 GHz with 200 detectors each. This improves the performance of the considered configuration, an improvement which we can ameliorate even further by performing the optimization with respect to the detector numbers in the four original channels and keeping the detector numbers of the new channels fixed to 200. We indeed find that the new setup performs nearly as well as the initial optimized one (Table 11.6, column 3 vs 7) but possesses a more uniform frequency coverage. If we now want to perform a controlled detector number rounding and analyze its impact on the configuration performance we would need to restart the entire procedure described above.

11.6.6 Robustness tests

As explained in paragraph 11.4, for each FOM, we start from the optimized configurations, as determined earlier and check how the values of the FOMs depend on a random suppression of a number of detectors in each channel by some fraction. Specifically, we assume here that the distribution of the anticipated detector failures is Gaussian with the dispersion equal to ε of which is the same for each of the considered channel and taken to change from 5%, 10%, 25%, and 50 %. We randomly draw some large number

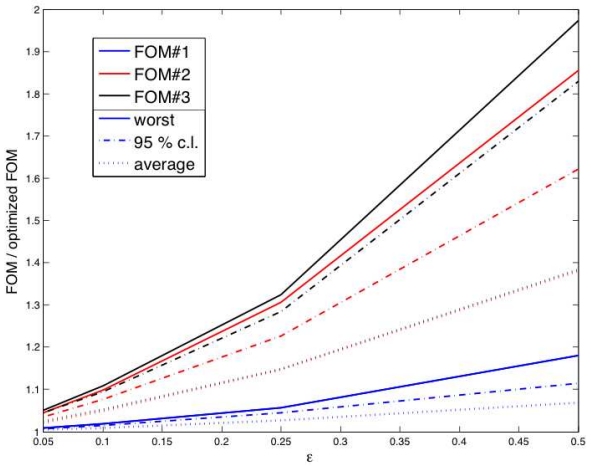

Figure 11.15: Summary of our robustness tests applied to the COrE configuration obtained via the optimization of FOM#1 with constraints of FOM#2 $\leq 10^{-4}$ and a fixed number of detectors. The lines of different colors correspond to different FOMs and different lines show: average (dotted), 95% confidence limit, (dot-dashed), and the worst value (solid).

of samples, here 10^4, and histogram the results for each of the FOMs. We then compute the most likely value of the FOMs, 95%-confidence limit, and the worst drawn value. In the case of the COrE configuration studied in the previous Section we collect the results in Fig. 11.15. We conclude, as probably could have been anticipated from the results of the previous Section, that for a failure rate as large as 30% we will not compromise on the FOM values by more than 50% with respect to the optimized ones, while a failure rate of 10% will result in their 10% increase. These result affirm the practical soundness of the derived configuration.

11.6.7 Robustness with respect to the foreground modeling

Results of the optimization procedures including thus the procedure considered here are usually only as good as the foreground models used in their course. In the specific case studied here we expect that our results are fairly robust as far as foreground morphology is concerned. Our estimates are driven by two compact description of those, the foreground correlation matrix, $\hat{\mathbf{F}}$, and the foreground power spectra, which are not expected to be wildly different than what we have assumed here. We note in particular that an increasing amplitude of the foregrounds leading to an increase of both the elements of the matrix, $\hat{\mathbf{F}}$, and overall normalization of the foreground power spectra would decrease the errors on the spectral parameters, cf. Eq. (10.16), and result in the amplitude of the residuals being virtually unchanged. These expectations are confirmed by the results obtained here for the three different masks.

It is more difficult to assess, though potentially more crucial, the impact of increasing a number of spectral parameters. This could be either due to more complicated spectral dependences of true foreground components, or as a result of a spatial dependence of spectral parameters. The former problem is inherent to all parametric component separation approaches including the one assumed here. In general, a wrong parametrization or frequency scaling laws assumed in such approaches may invalidate separation results. In practice, the effects are more subtle but arising biases can affect an interpretation of the results. It is therefore important that the scaling laws assumed in the optimization continue to be improved, reflecting any relevant, new observational data and more detailed, theoretical models of the foreground physics as they become available. In a case of some doubts, a rather conservative approach can be fruitful, restricting channel frequencies to a range for which the scaling laws are known to provide at least good approximations to the actual ones. This is in fact an approach we used in this work by selecting a parametric model for the dust signal with a single parameter and reduced the frequency range to those lower than 400 GHz.

A spatial dependence of the scaling parameters can be treated more directly. We will implement that by dividing the observed sky into a multiple disjoint regions and introduce one set of parameters for each of those. To abstract from details of the regions shape and position, we assume that they are defined in such a way that the errors on spectral parameters are the same for each of the regions, i.e., that the differences of the overall magnitude of the matrix $\hat{\mathbf{F}}$ are compensated by a respective number of pixels in each area. In general this assumption would imply that more, though smaller by area, regions are defined in high-contrast foreground sky areas. This indeed could well be the case as the high-contrast foreground regions are expected to be more complex and may require more parameters to ensure sufficient accuracy.

For demonstration purposes we assume that we have 10 regions with the corresponding errors on spectral parameters being $\sqrt{10}$ times larger than in the single region case as studied before. We note that cutting the sky into regions will unavoidably affect the foregrounds and thus residual power spectrum on scales larger than a typical size of the region. We will ignore this effect here, motivated by the fact that our earlier results did not find any strong dependence on the shape of the power spectrum. We also neglect here all practical difficulties such as matching the results on the map level coming from the different regions and which will have to be addressed in any actual application of the discussed method. We limit here ourselves to the COrE-like configuration as defined earlier, calculate the FOMs as before, and optimize the configuration following the steps outlined before. As expected we find that the optimal configurations this time are not very different from the ones obtained earlier. This is because FOM#1 and FOM#3 are mostly trying to optimize the overall noise level, which is the same now as before, and though the value of FOM#2 increased by a factor 10 due to increase

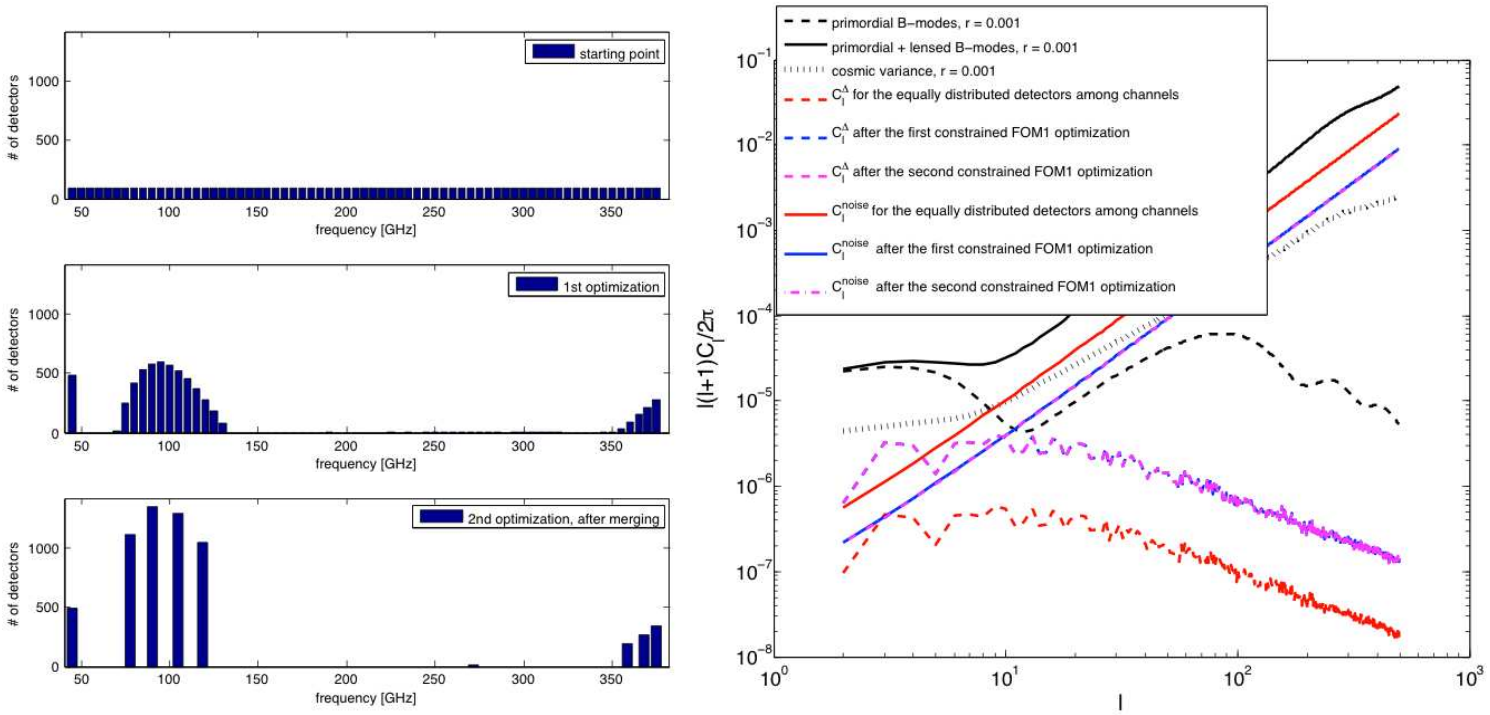

Figure 11.16: Demonstration of the optimization results derived with respect to a variable number of channels, numbers of detectors per channel, and their central frequencies, while constraining the total number of detectors (= 6128 as in the proposed COrE version). **Left panel** shows, from top to bottom, (1) the starting configuration with all the detectors evenly distributed among a fine-grid of channels; (2) a configuration after the first optimization of FOM#1 constrained to ensure that FOM#2 $\leq 10^{-4}$; and (3) the re-optimization of configuration (2) restricted only to channels with a number of detectors larger than five and after adjacent channels merging and re-centering as described in paragraph 11.6.8. **Right panel** shows power spectra corresponding to these configurations contrasted against the expected CMB signals.

of the spectral index errors this is the same configuration, which ensures its minimum. As a consequence the new value of r_{eff} is now higher than that of r_{min}. This clearly does not invalidate results of the optimization procedure as such, however care has to be exercised, while interpreting the obtained values of r_{min}, which may not be taken directly as the performance forecasts for the setup as far as detecting r is concerned.

We could have studied another way of considering spatial variations, according to Stolyarov et al. (131). If dust spectral parameter is spatially varying, this results in a modification of Eq. (10.1) such as

$$d(\nu, \mathbf{r}) \quad = \quad \mathbf{A}\, s + \Delta\beta \left.\frac{\partial \mathbf{A}}{\partial \beta}\right|_{\beta_0} s \tag{11.15}$$

For only three polarized components which are CMB, dust and synchrotron, the mixing matrix $\mathbf{A}$ we consider with this new parametrization would look like

$$\mathbf{A} = \begin{bmatrix} A_{cmb}(f_0) & A_{dust}(f_0) & \left.\frac{\partial \mathbf{A}}{\partial \beta_d}\right|_{\beta_0}(f_0) & A_{sync}(f_0) \\ A_{cmb}(f_1) & A_{dust}(f_1) & \left.\frac{\partial \mathbf{A}}{\partial \beta_d}\right|_{\beta_0}(f_1) & A_{sync}(f_1) \\ \vdots & \vdots & \vdots & \vdots \\ A_{cmb}(f_{\#\text{ of ch}}) & A_{dust}(f_{\#\text{ of ch}}) & \left.\frac{\partial \mathbf{A}}{\partial \beta_d}\right|_{\beta_0}(f_{\#\text{ of ch}}) & A_{sync}(f_{\#\text{ of ch}}) \end{bmatrix}, \tag{11.16}$$

in which I added a column between A_{dust}, Eq. (11.9) and A_{sync}, Eq. (11.8). Consequently, the dimension of $\mathbf{\Sigma}$ increases and the corresponding errors are more important. I will present in section 12.2 a quantitative consequence of such spatial variation for β_d.

11.6.8 Varying the number of channels and their frequencies

We present here some results based on an implementation of the scheme proposed in paragraph 11.3. We start from ~ 70 channels evenly spaced between 45 and 375 GHz every 5 GHz, with ~ 6000 detectors (total number of the COrE proposed version) equally distributed among those, as shown in Fig. 11.16. Then we perform the optimization with respect to FOM#1, while keeping FOM#2 $\leq 10^{-4}$ and the total number of detectors fixed. As a result we obtain a highly clustered distribution of detectors in between the initial channels, with many of these being empty. We therefore combine detectors of neighboring channels and replace them by a new channel with the central frequency set as a weighted, by a number of detectors, mean of the optimized distribution. The new channels are defined to ensure proper spacing between them. Once the new channels are determined we perform a second round of the optimization, this time invoking only the new channels and aiming at optimization of the detector distribution between them. The result is shown in the left bottom panel of Fig. 11.16. We note that

the procedure not only improved the values of the FOMs with respect to the starting (original) configuration, i.e., FOM#1 has been decreased by $\sim 17\%$ ($\sim 25\%$), while the noise by a factor ~ 4 (~ 3), but also, and arguably most importantly, it resulted in a configuration significantly simpler than the initial one with the number of channels reduced from 70 down to 9.

We note that maybe somewhat surprisingly both the configurations derived here, the final one as well as the intermediate one obtained after the first optimization step, show only a minor, $\sim$ few percent, gain over the five-channel configuration we have considered earlier; see, e.g., the first column of Table 11.6. This is due to our setting the threshold for FOM#2 rather high, while the main advantage of the significantly larger set of the initial channels used here is that it permits finding in principle more satisfactory compromises between the three FOMs, characterized by values of FOM#2 lower than what could be achieved with more modest setups discussed earlier.

11.7 Conclusions

In this work done in collaboration with Federico Stivoli and Radek Stompor, we have proposed a general scheme for a performance optimization and forecasting of the CMB B-mode experiments in the presence of astrophysical foregrounds. Our approach is based on a maximum likelihood parametric technique for component separation, for which we have derived Fisher-like error estimates for spectral parameters. We use the latter to calculate the residual level of the foregrounds in cleaned CMB maps given assumed, instrument characteristics and foreground model. We then optimize the former by minimizing a set of proposed figure of merit indicators, which reflect our science goals. Subsequently we have applied this approach to two specific cases of recently proposed CMB B-mode satellites: American CMBpol (Aguirre et al. (1)) and European COrE (The COrE Collaboration (137)). I have discussed in detail the choices and trade-offs inevitable in such an optimization process. I have demonstrated how such a procedure can help to simplify the resulting hardware design, while ensuring the same (or nearly the same) science outcome.

I emphasize that results of such a procedure can be only as reliable as the foreground models that are applied. This underlines the importance of developing better understanding of the polarized foregrounds, in particular, and characteristically of the parametric methods, as far as the functional form of the foreground component scaling laws is concerned. However, our approach is expected to be relatively robust as far as other details of the foreground signals are concerned, such as, spatial distribution or spatial variability of the spectral parameters, with the latter playing a major role in determining the scientific reach of the experiment but not affecting its configuration.

Chapter 12

Is there an ultimate limit due to foregrounds residuals in the detection of r for future experiments?

In this section, following the results summarized in Errard and Stompor (40), we consider experimental setups optimized to ensure the lowest foreground residual level. We still use two component foreground model, including synchrotron and dust, each parametrized with one parameter, referred to as spectral indices. We note that more refined scaling laws with potentially more parameters can be straightforwardly incorporated in the formalism presented below and would affect the conclusions only quantitatively. The foreground templates used here are described in detail in the previous chapter (and also in Errard et al. (41), Stivoli et al. (130)) and we assume nearly full ($\sim 80\%$) sky coverage, corresponding to the choice of MASK-I, see Fig 11.5. Given the optimized setup and its noise we estimate a typical residual and compare it with the total statistical uncertainty. As the latter depends on the tensor-to-scalar ratio, r, for each value of r we determine respective instrumental sensitivity for which the residual is irrelevant given the uncertainties and compare it with the statistical limits due to the noise and the CMB signal only.

12.1 Methodology

12.1.1 Parametric component separation

The fiducial data set we consider hereafter is made of multiple-single frequency maps of Q and U Stokes parameters, with the instrumental noise assumed to be uncorrelated, both between the pixels and channels, pixel-independent, and characterized by

its variance, $\boldsymbol{N}$. The corresponding data model we use hereafter then reads,

$$\boldsymbol{d}_p = \boldsymbol{B}\left(\boldsymbol{\beta}, \boldsymbol{\omega}\right)\, \boldsymbol{s}_p \,+\, \boldsymbol{n}_p \equiv \boldsymbol{\Omega}\left(\boldsymbol{\omega}\right)\, \boldsymbol{A}\left(\boldsymbol{\beta}\right)\, \boldsymbol{s}_p \,+\, \boldsymbol{n}_p, \tag{12.1}$$

where for each pixel p, $\boldsymbol{A}$ is a mixing matrix parametrized by the spectral indices, $\boldsymbol{\beta}$, $\boldsymbol{s}_p$ – a vector of sky signals to be recovered and $\boldsymbol{n}_p$ – instrumental noise. $\boldsymbol{\Omega}$ is a pixel-independent, diagonal matrix with the diagonal elements, $\boldsymbol{\omega}_i \equiv \boldsymbol{\Omega}_{ii}$ corresponding to the calibration factors for each of the channels. I do not consider here any other systematic effects such as imperfect Half-Wave Plate, the presence of cross- or instrumental-polarization which would be described by Mueller matrices, see chapter 7. Moreover, I do not look at imperfect or not well characterized band-passes which will lead to important errors in the foreground scalings estimation. The likelihood function then reads (Stompor et al. (133)),

$$\begin{aligned} -\,2\ln\mathcal{L} = \quad & \sum_p \left(\boldsymbol{d}_p - \boldsymbol{B}\,\boldsymbol{s}_p\right)^t \boldsymbol{N}^{-1}\left(\boldsymbol{d}_p - \boldsymbol{B}\,\boldsymbol{s}_p\right) \\ & + \left[\left(\boldsymbol{\omega} - \bar{\boldsymbol{\omega}}\right)^t \boldsymbol{\Xi}^{-\mathbf{1}}\left(\boldsymbol{\omega} - \bar{\boldsymbol{\omega}}\right)\right], \end{aligned} \tag{12.2}$$

where the last term is simply a prior term constraining the plausible values of the calibration factors, and is the difference with the likelihood expressed in Eq. (10.8). Hereafter we will assume that the true values of the calibration factors are equal to unity, $\bar{\boldsymbol{\omega}}_i = 1$, and that their uncertainty is described by an error matrix, $\boldsymbol{\Xi}$, which for simplicity is assumed to be proportional to a unit matrix, i.e., $\boldsymbol{\Xi}_{ij} \equiv \sigma_\omega^{-2}\,\delta_i^j$, where σ_ω is assumed not to depend directly on the parameters of the considered experiment. Moreover, throughout this section the detector's bandpasses are always taken to be known perfectly and therefore their effects on the mixing matrix, $\boldsymbol{B}$, straightforwardly calculable. The import of the bandpass uncertainties and mismatch will be studied elsewhere. In the cases without calibration uncertainty, $\boldsymbol{B} = \boldsymbol{A}$ and we simply drop the last term. In general, we will estimate both $\boldsymbol{\beta}$ and $\boldsymbol{\omega}$ and maximize this likelihood to perform the component separation.

12.1.2 Residual computation

The computation of the residuals involves two steps. First, we obtain the error of the estimation of the spectral parameters. This is done using a generalization of Eq. (10.11), allowing for the calibration errors (Stompor et al. (133)), and derived again as the Fisher matrix,

$$\boldsymbol{\Sigma}_{ij} \equiv \left\langle \frac{\partial^2 \ln\mathcal{L}}{\partial\gamma_i\,\partial\gamma_j} \right\rangle_{noise}\Bigg|^{-1}_{\hat{\boldsymbol{\gamma}}}, \tag{12.3}$$

of the profile likelihood, $\mathcal{L}$, of the likelihood given in Eq. (12.2), i.e.,

$$\boldsymbol{\Sigma}_{ij}^{-1} = n_{pix}\ \mathrm{tr}\left\{\left[\boldsymbol{B}_{,i}^{t}\,\boldsymbol{N}^{-1}\,\boldsymbol{B}\,\left(\boldsymbol{B}^{t}\boldsymbol{N}^{-1}\boldsymbol{B}\right)^{-1}\boldsymbol{B}^{t}\boldsymbol{N}^{-1}\boldsymbol{B}_{,j} - \boldsymbol{B}_{,i}^{t}\,\boldsymbol{N}^{-1}\boldsymbol{B}_{,j}\right]\hat{\boldsymbol{F}}\right\} + \left[(\boldsymbol{\omega}-\bar{\boldsymbol{\omega}})^{t}\,\boldsymbol{\Xi}^{-1}\,(\boldsymbol{\omega}-\bar{\boldsymbol{\omega}})\right]_{,ij}\Big|_{\hat{\boldsymbol{\gamma}}}, \tag{12.4}$$

which is similar to Eq. (10.10). The last term of the rhs has to be evaluated at the true values of the parameters, $\boldsymbol{\gamma} = \hat{\boldsymbol{\gamma}}$, where $\boldsymbol{\gamma}$ stands for either $\boldsymbol{\beta}$ or $\boldsymbol{\omega}$ and the subscript means $_{,i} \equiv \partial/\partial\gamma_i$. The matrix $\hat{\boldsymbol{F}}$, defined in Eq. (10.12), encapsulates all the information about the sky components needed for the parameter errors estimation. In the following we will be removing the contribution to $\boldsymbol{\Sigma}$ related to the mode

$$\boldsymbol{v}^{t} \propto \begin{bmatrix} 0 \\ \vdots \\ 0 \\ 1 \\ \vdots \\ 1 \end{bmatrix}, \tag{12.5}$$

where the zeros are assigned to the spectral parameters, $\boldsymbol{\beta}$, and ones to the calibration ones, $\boldsymbol{\omega}$, and $\boldsymbol{v}$ is normalized to one. This is done by replacing

$$\boldsymbol{\Sigma} \;\rightarrow\; \boldsymbol{\Sigma} - (\boldsymbol{v}^{t}\,\boldsymbol{\Sigma}\boldsymbol{v})\boldsymbol{v}\boldsymbol{v}^{t}. \tag{12.6}$$

The mode $\boldsymbol{v}$ describes an overall miscalibration of the final CMB map, RMS of which is given by $\sigma_{\boldsymbol{\omega}}$, introducing a similar error in our determination of r. This is typically much smaller than the statistical uncertainty, i.e.

$$\frac{\delta r}{r} \gtrsim 0.01 \gtrsim \sigma_{\omega}^{2} \quad \text{for} \quad r \lesssim 0.1, \tag{12.7}$$

and thus negligible.

We use again the recipe of Stivoli et al. (130), i.e. Eq. (10.21), to calculate the power spectra of the typical noise-free foreground residuals, $\boldsymbol{C}_{\ell}^{\Delta}$, found in the separated maps, i.e.,

$$\boldsymbol{C}_{\ell}^{\Delta} \equiv \sum_{k,k'}\sum_{j,j'} \boldsymbol{\Sigma}_{kk'}\,\boldsymbol{\alpha}_{k}^{0j}\,\boldsymbol{\alpha}_{k'}^{0j'}\,\hat{\boldsymbol{C}}_{\ell}^{jj'}, \tag{12.8}$$

$\hat{\boldsymbol{C}}_{\ell}^{jj'}$ is still a cross-spectrum of components i and j, but this time we define

$$\boldsymbol{\alpha}_{k} \equiv \frac{\partial}{\partial\,\boldsymbol{\gamma}_{k}}\left[\left(\boldsymbol{B}^{t}\,(\boldsymbol{\gamma})\,\boldsymbol{N}^{-1}\boldsymbol{B}\,(\boldsymbol{\gamma})\right)^{-1}\boldsymbol{B}^{t}\,(\boldsymbol{\gamma})\,\boldsymbol{N}^{-1}\boldsymbol{B}(\hat{\boldsymbol{\gamma}})\right]\Big|_{\hat{\boldsymbol{\gamma}}}.$$

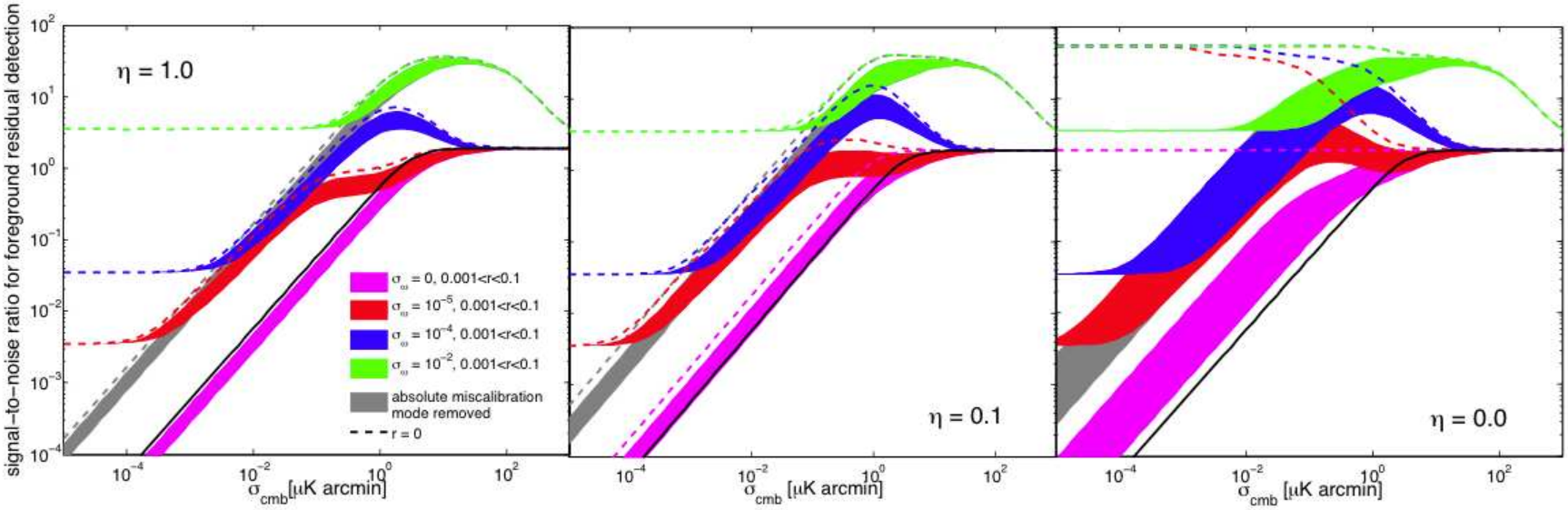

Figure 12.1: The significance of the foreground residuals, σ_α^{-1}, Eq.(12.9), expected in the recovered CMB map covering $\sim 80\%$ of the sky for the cases with no, $\eta = 1.0$, (left panel), partial, $\eta = 0.1$, (middle panel), and complete, $\eta = 0.0$, (right panel), lensing correction, respectively. The color bands correspond to different calibration uncertainties as listed in the left panel with the gray color showing all the cases with $\sigma_\omega \neq 0$ after the removal of the mode $\boldsymbol{v}$. The width of the shaded areas reflects the effect of varying r from 0.001, (upper edge), up to 0.1, (lower), and the dashes show the corresponding $r = 0$ cases. The black solid lines show the case with $\sigma_\omega = 0$, $r = 0$, and $\eta = 1.0$ as a reference.

12.1.3 Residuals significance

We quantify the importance of the residuals as follows:

$$\sigma_\alpha^{-1} = \left[f_{sky} \sum_{\ell}^{\ell_{max}} \frac{(2\ell+1) C_\ell^\Delta}{C_\ell^{\rm prim}(r) + \eta\, C_\ell^{\rm lens} + C_\ell^{\rm noise}} \right]^{\frac{1}{2}}, \tag{12.9}$$

which can be derived as a Fisher error on an overall amplitude, $\alpha(=1)$, of a foreground template, assumed to be known, with the power spectrum given by C_ℓ^Δ. σ_α^{-1} expresses statistical significance with which the template could be detected, had it been known, given the instrumental noise, $C_\ell^{\rm noise}$, and the CMB signal, $C_\ell^{\rm prim}(r) + \eta C_\ell^{\rm lens}$. η (≤ 1) denotes the fraction of the lensing signal left after its removal. We do not perform the delensing of the map per se, but we would like to see how this operation affects the significance, the importance of the residuals in the final map. Whenever σ_α^{-1} is large, the residual can not be neglected in an analysis of the CMB map and may need to be treated by some additional means (Fantaye et al. (44)). Otherwise, the foreground residuals will be irrelevant for the estimation of r.

Note that formally, we could have studied the behavior of FOM#1 introduced earlier. However, as mentioned and illustrated in the last chapter, this figure of merit is quite invariant in the considered parameter space. We derive a more abstract quantity, the significance σ_α, which has the advantage of being much more sensitive to the variations of the experimental setup and gives us a measurement of the relative importance of the residuals with respect to the science signals. As for FOM#2, it is, by construction, independent of any other signal than the residuals: it only provides an absolute measurement of the amplitude of these latter.

12.1.4 Experiment optimization

We use the approach described in the last section, i.e. in Errard et al. (41), to optimize the experimental setups. We assume a fixed, though arbitrary, focal plane area during the optimization and restrict frequencies of the observational channel bands to range from 30 GHz to 400 GHz. The detector noise is assumed to be constant in antenna temperature units. The optimization then tries to minimize FOM#2, the effective r value as proposed in Amblard et al. (3), as defined in Eq. (11.3). The criterion selection reflects the fact that we want to minimize the effects of the foreground residuals and thus keep their expected level as low as possible, irrespective of consequences it may have on, e.g., effective noise of the experimental configuration selected in such a way. The resulting experiment setup includes 5 frequency bands: $\nu = [30, 40, 130, 300, 400]$ GHz occupying, respectively, a fraction $f_{\rm p}(= [9, 21, 36, 25, 9]$ per cent) of the focal plane, as illustrated Fig. 12.2.

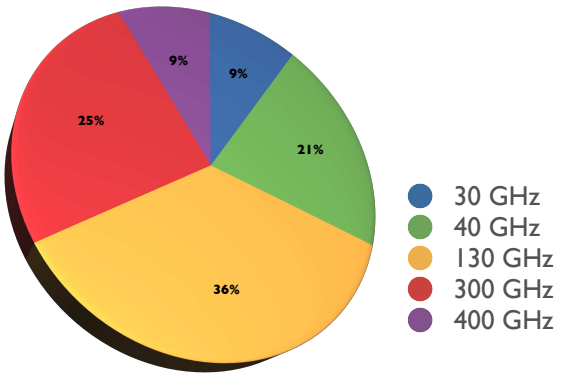

Figure 12.2: Optimal setup with respect to FOM#2, Eq. (11.3), used to illustrate the behavior of the residuals significance as a function of the experimental noise. The pie here shows the fraction of area taken by each channel.

12.2 Results

Hereafter we will use the noise level of the recovered CMB map as a measure of the sensitivity of the considered experimental setups. This is given a generalization of Eq. (11.4),

$$\sigma^2_{\rm CMB} \equiv \left[\left(\boldsymbol{B}\left(\hat{\boldsymbol{\gamma}}\right)^t \, \boldsymbol{N}^{-1} \, \boldsymbol{B}\left(\hat{\boldsymbol{\gamma}}\right) \right)^{-1} \right]_{00}, \tag{12.10}$$

where we still assume that CMB is the zeroth component recovered in the separation procedure. Similarly to Eq. (11.12), the diagonal elements of the correlation matrix, $\boldsymbol{N}$, expressing the noise level of each frequency channel, can be written in antenna temperature units as,

$$\boldsymbol{N}_{ii} = \frac{1}{\Omega_p} \times \frac{4\pi \, f_{\rm sky} \, \sigma^2_{NET}}{A_{\rm fp} \, T_{\rm obs}} \times \frac{A_{\rm d}\left(\nu\left(i\right)\right)}{f_{\rm fp}\left(i\right)} \tag{12.11}$$

where σ_{NET} is a frequency-independent detector of instantaneous noise value (in $\mu{\rm K}_{\rm ant}\sqrt{\rm sec}$), $A_{\rm fp}$, and $A_{\rm d}\left(\nu\left(i\right)\right)$ – total and per detector effective focal plane area, $T_{\rm obs}$ – total observation time, and $\Omega_{\rm p}$ – pixel size in steradians. For the considered experiment we can write numerically,

$$\frac{\sigma_{\rm CMB}}{\mu{\rm K}_{\rm cmb}\,{\rm arcmin}} \simeq 2.6\;10^{-3}\,\frac{\sigma_{NET}}{\mu{\rm K}_{\rm ant}}\sqrt{\frac{f_{\rm sky}}{0.82}\,\frac{1{\rm GHz}^{-2}}{A_{\rm fp}}\,\frac{2{\rm yrs}}{T_{\rm obs}}}. \tag{12.12}$$

The dependence of our measure of the significance of the foreground residuals, σ_α^{-1}, on the noise level, $\sigma_{\rm CMB}$, is illustrated in Fig. 12.1, and its major features can be tracked

back to the behavior of the parameter errors and foreground residuals. In particular in the low-noise regime the value of σ_α^{-1} increases $\propto \sigma^2_{\rm CMB}$ whenever no calibration uncertainty is present or the contribution of the mode $\boldsymbol{v}$ is suppressed. This is due to the fact that the error on all the parameters $\boldsymbol{\gamma}$ is driven by the first term on the right-hand side of Eq. (10.10), resulting in a self-calibrating property of the considered system thanks to the assumed scaling laws spanning the entire range of considered frequency bands. The self-calibration applies only to the relative calibrations fixing the calibration coefficients of the channel maps with precision superseding that given by the assumed priors. The absolute calibration of the final map is in turn always determined by the prior term in Eq. (10.10) and thus independent on the experimental noise, as shown by the flat, low-noise asymptotes of the lines, computed with the mode $\boldsymbol{v}$ included. For higher noise levels the calibration errors have significant impact on the residual level and should be therefore included in any meaningful analysis. Whenever the first term on the right-hand side of Eq. (10.10) is dominant, our results also do not depend, or depend only very weakly, on the foreground amplitude and on the observed sky area (at least as long as the foregrounds are nearly stationary), as the foregrounds amplitudes present in the expressions for $\boldsymbol{\Sigma}$ and C_ℓ^Δ cancel. Physically, this means that higher levels of foreground signals lead to tighter constrains on their parameters, compensating for their higher amplitudes.

The results from the three panels of Fig. 12.1 are translated into limits on $\sigma_{\rm CMB}$, as shown in Fig. 12.3, by solving the relation,

$$\sigma_\alpha^{-1}\left(r, \sigma_{\rm CMB}\right) = \sigma_\alpha^{-1}\big|_{crit}\,. \tag{12.13}$$

Hereafter, we use $\sigma_\alpha^{-1}\big|_{crit} = 1$, corresponding to a "$1\sigma$" detection of the residuals on the map level. In general, this value should be adjusted, and the curves in the figure rescaled by $\propto \sigma_\alpha|_{crit}^{-1/2}$, given a specific application envisaged for the output maps and 1 is used here as an illustration. For each r value, each curve, computed for specific assumptions about the experiment and/or foregrounds, provides an upper limit on the experiments sensitivity so the foreground residuals will be found irrelevant for the analysis of the obtained CMB map. The gray-shaded areas show the statistical uncertainties, corresponding to a different level of gravitational lensing signal cleaning. We note that the foreground residual limits do not prevent detecting arbitrarily low value of r assuming that a sufficiently sensitive observation can be performed. Instead, the lower limit on r can arise due to a residual level of the lensing-induced B-mode signal left over from some cleaning procedure (Kesden et al. (70), Knox and Song (71), Seljak and Hirata (119)). This remains true when the calibration errors are included but also when the spatial variability of the foregrounds is allowed for, and will hold at least as long as no significant deviation from the assumed component scaling laws is observed. To see the effects of the spatial variability of the spectral indices we assume that the sky is

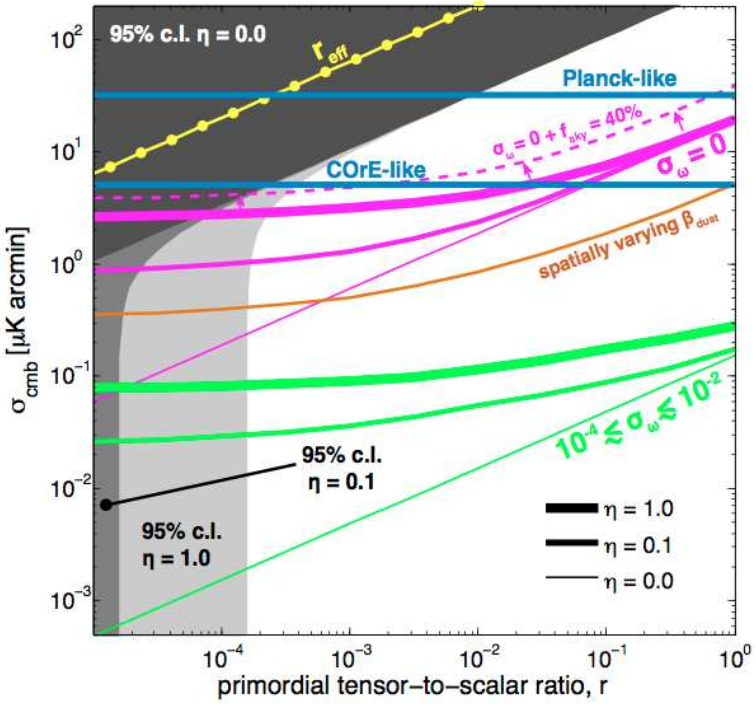

Figure 12.3: Upper limits on the map noise levels, which ensure that the foreground residuals are statistically irrelevant, are shown with solid lines. Each set of three lines corresponds to a different assumptions about the calibration errors as marked in the figure. In each set the lines depict the cases with no (heavy), 90% (medium), and perfect (thin) cleaning efficiency. The thin dashed line shows the change in the derived noise levels incurred as a result of restricting the sky area used to estimate r *after* the component separation step has been already performed. These should be compared to the thick line with $\sigma_\omega = 0$. The thick dots show the analogous noise limits based on an alternative criterion, r_{eff}, Sec. 12.1. The shaded areas depict statistical 2σ limits due to the noise and sky signal for three lensing cleaning efficiencies $\eta = 1.0$, 0.1, and 0.0 (light to dark grey). The noise levels for Planck and COrE-like experiments are also shown as a reference.

subdivided into $n_{\rm p}$ non-overlapping patches, for each of which we assign a different set of spectral parameters. If the patches are of roughly the same size, the resulting errors on the spectral parameters will increase approximately as $\sqrt{n_{\rm p}}$, leading to a tightening of the noise constraints in Fig. 12.3 by the same factor. I depict in Fig. 12.4 the significance of the residuals as a function of the noise level of the experiment, similarly to Fig. 12.1, but in the case of spatial varying dust index β_d. For comparison the (orange) line in Fig. 12.3, labeled "spatially varying β_{dust}", shows a result of implementing the Stolyarov approach (Stolyarov et al. (131)), cf. Eq. (11.15) and an introduction of this approach in section 11.6.8, which also leads to more restrictive noise constraints, but without introducing an ultimate limit on r. This is also shown in Fig. 12.4 where these spatial variations lead to higher a significance of the residuals.

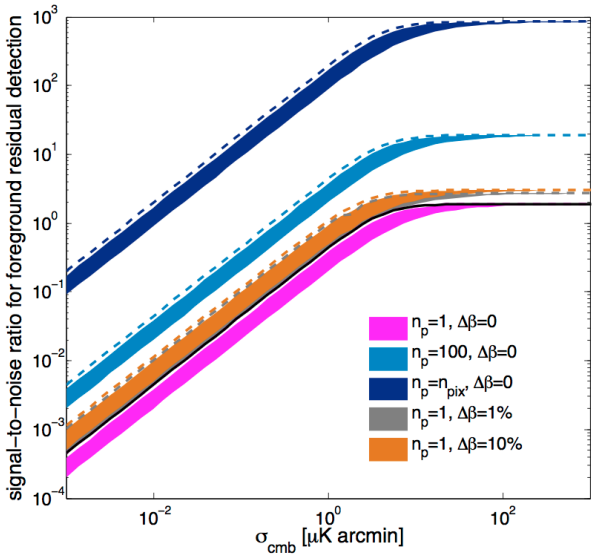

Figure 12.4: Significance of the residuals as a function of the noise in the case of spatial variations for β_d. The pink band and black solid lines are here for reference, they are the same as the one shown in Fig. 12.1, for $\eta = 0.0$. The light and dark blue bands are obtained for respectively 100 and $n_{pix} \sim 2\times10^5$ patches of roughly the same size and having different β_d. As detailed in the text, the curves scale $\propto \sqrt{n_p}$. Besides, the grey and orange bands are obtained with the Stolyarov approach, assuming respectively $\Delta\beta = 1$ % and 10 %.

We also note that by decreasing the statistical uncertainty of the map we increase σ_α^{-1}, as the residual becomes easier to be spotted, and thus the requirements on the noise need to be tighter to ensure that the foreground level is decreased accordingly. This, for instance, explains why any lensing cleaning in Fig. 12.3 renders a tighter limit on the noise. Conversely, re-sorting for the r estimation to a smaller map of the sky, than what has been used for the component separation, will increase the variance and lower σ_α^{-1}, allowing us to tune appropriately the sky area to extend the range of

detectable values of r given a fixed instrumental sensitivity. This will result in lower statistical significance of the detection but will ensure that bias is negligible. This is illustrated in Fig. 12.3 where the (magenta) arrows show a change in the noise upper limit in the perfect calibration case, $\sigma_\omega = 0$, with no lensing cleaning, $\eta = 1.0$, due to using on the second step only half of the area of 80% of the full sky as used for the component separation. This, for a COrE-like experiment, see The COrE Collaboration (137), could extend its capability to detect r reliably down to 8×10^{-4} (2σ), what could be compared to $r \sim 4 \times 10^{-4}$ limit (2σ) potentially achievable, if the foregrounds were absent. We note that the trimming can be made even more efficient if the retained sky is selected to ensure the lowest possible foreground amplitude. If no extra trimming is done, then given our criterion for σ_α^{-1} the COrE-like lower limit on r is found to be $r \sim 3 \times 10^{-2}$, what is at least formally within reach of a suborbital observation with similar sensitivity per pixel but observing $\mathcal{O}(1)$% of the sky (Fantaye et al. (44), Stivoli et al. (130)). The statistical significance of the former limit is $\sim 25\sigma$, (vs. 2σ in the suborbital case) indicating that the experimental sensitivity of such observations should be driven by the foreground separation, not by statistical uncertainties only, but also that a further improvement of the limit on r could be plausible if extra assumptions and processing are included, see Fantaye et al. (44).

The results obtained here demonstrate that in an absence of such post-component separation processing and with calibration uncertainties as typically present in actual experiments the noise levels required for an unambiguous and robust determination of r are on order of $\mathcal{O}(10^{-1})\mu$K arcmin, significantly below the noise levels for the currently considered satellite mission concepts. Moreover, if the lensing contribution left over after its cleaning is higher than ~ 10% of its initial value, the dependence of the noise levels on the targeted value of r is rather weak. This emphasizes that once the sufficient noise level is indeed attained the measurable values of r would be limited only by the statistical uncertainties. On the contrary, a failure to reach such a noise level may render the experiment incapable of setting any constraints on r of current interest. If the lensing could be cleaned nearly perfectly, $\eta \lesssim 10$%, lower noise levels lead to a progressively lower limit on the detectable r.

12.3 Conclusion

Summarizing, we have studied the importance of the foreground residuals left over from the maximum likelihood parametric component separation procedure on the detection of the primordial tensor-to-scalar ratio coefficient, r, by nearly full-sky CMB B-mode experiments. We have found that though the foreground residuals are likely to be a major driver in defining the sensitivity requirements for such experiments, they do not

on their own lead to any fundamental lower limits on detectable r, at least as long as sufficiently precise frequency scaling models are available. These will be rather set by the uncertainty due to the lensing signal present in the maps after its cleaning. We note that the latter may also in turn depend on the presence of foregrounds and instrumental noise (Hu and Okamoto (64), Smith et al. (126)).

Chapter 13

Discussion

Component separation is a crucial step for any new generation B-modes experiment. I described the parametric maximum-likelihood component separation which is a method based on the assumption that the spectral scaling laws of the foregrounds are well characterized. In addition, we built three figures of merit (FOM) describing the performances with respect to our science goals, in the case of COrE or CMBpol, future nearly full sky experiments. I implemented routines which optimize the distribution of detectors among frequency channels regarding the FOMs, while keeping the total area of the focal plane or the total number of detectors constant. We showed that optimal setups have usually $\sim$ 4 filled channels to ensure that the experiment alone could recover the two unknown spectral parameters β_d and β_s. We explored the scientific performances of our setups while moving away from the optimal configuration, proposed and applied some robustness tests such as the study of the consequence of losing couple detectors, a whole frequency channel, etc.

First, we can note that the presented optimization framework could be extended to any component separation method. It only requires the estimation of the mixing matrix, in a parametric or nonparametric way, and being capable of producing estimates for the errors of the spectral parameters for any hardware configuration. One could, and ideally would, therefore use the formalism proposed in chapter 11 to define configurations, which would ensure that many of the available component separation methods perform well. Though the component separation methods usually conform with the first requirement about the mixing matrix, the second about the residuals computation is more demanding and typically can be done only via computationally-heavy Monte Carlo simulations. Those may be often impractical for the optimization purposes, making an implementation of such a program difficult. A related, but simpler to address, problem is whether the configurations optimized with one method will work for satisfactorily with the others.

Second, the FOMs defined for the optimization procedure are also suitable for the performance forecasting. This also clearly applies to the FOMs proposed here and in particular FOM#1 and FOM#2 seem relevant to the primordial signal detection producing values of r_{min} and r_{eff} on order of $\mathcal{O}\left(10^{-4}\right)$ for the considered optimized configurations. However, given that each of these two FOMs reflects a somewhat different aspect of the problem, a statistical uncertainty in former case versus a systematic one in the latter, care has to be taken while interpreting these values. Nevertheless, our results seem to support at least the contentions made elsewhere suggesting that $r \simeq 10^{-3}$ is a realistic goal for the future nearly full sky experiments.

Third, it has to be pointed out that the science goals we have posed for the considered CMB experiments are clearly more modest than those targeted by the original CMBpol and COrE designs. This is responsible, at least in part, for the more complex and advanced instrumental configurations as proposed in the original proposal. Galactic science, SZ clusters study, lensing, etc. are all exciting science goals which should be looked at, modeled and maybe encoded as new FOMs: more diverse science goals can, and should, be studied in the presented framework.

Finally, in chapter 12, we considered an experimental setup optimized with respect to FOM#2. We derived a quantity, the so-called significance of the residuals, σ_α, which measures the potential impact of the residuals at the map level. We computed the residuals and their corresponding significance for various noise levels, from current levels ~ 10 μK·arcmin down to $\sim 10^{-3}$ μK·arcmin — which is close to science fiction nowadays, cf. Table 5.1. We also looked at cases with non-zero calibration errors and complete or partial delensing. The main result is that there is no fundamental lower limit on detectable tensor-to-scalar ratio as long as we know the scaling laws of the polarized foregrounds. Limitations may rise from the uncertainty due to delensing residuals, which will depend on the presence of instrumental systematics, astrophysical foregrounds, instrumental noise, etc. Besides, we studied the case of spatially varying spectral parameter for the dust, and an interesting extension could be to include the developed formalism to the previous optimization framework.

It is worth mentioning that Tucci et al. (139) realized a similar study, about the limits on the detectability of r imposed by foregrounds. Among other results, they show that, in the ideal limit of an instrumental noise-free experiment, a full-sky coverage with a resolution of 1 deg lead to a detection of $r \sim 10^{-4}$. Fig. 13.1 is taken from this work and depicts one of their results for future space missions i.e. how the detectability limit on r improves when reducing the instrumental noise. In the upper line of the figure, they assume that foregrounds are subtracted using a method in which the spectral parameter β is assumed to be pixel independent (the so-called average spectral index method), and the lower curve is obtained with a method assuming a pixel-dependent spectral index.

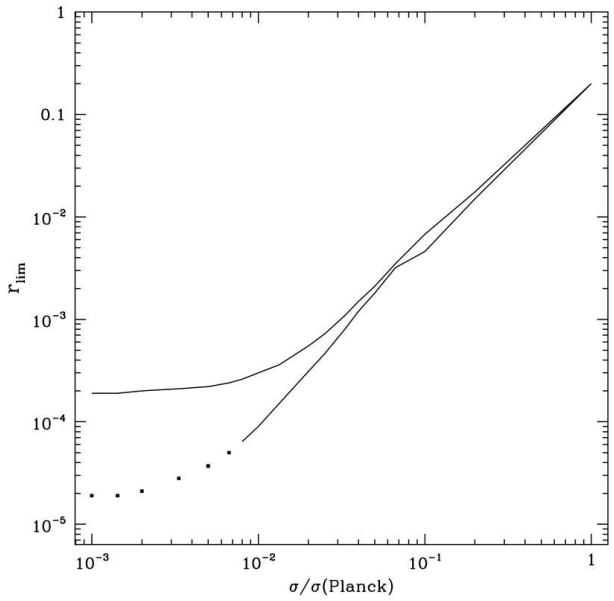

Figure 13.1: The value of the lowest r detectable for an experiment like Planck, but with sensitivity improved by a factor σ/σ_{Pl}. The upper line depict the case for which foregrounds are subtracted following a pixel independent spectral behavior, and for which extragalactic foregrounds are partially removed. For the lower curve, the components separation is done following a pixel dependent method, and extragalactic foregrounds are completely removed. From Tucci et al. (139).

The separation technique we used in the previous chapter, assuming also a pixel independent β, lead to the result depicted in Fig. 12.3: we showed that, in the case of a perfectly calibrated experiment ($\sigma_\omega = 0$) and for sufficiently low noise ($\lesssim 1$ μK·arcmin), the detection of r would be limited by the cosmic variance corresponding to $r \sim 1 - 2 \times 10^{-4}$. This result is in agreement with the plateau of the upper curve of Fig. 13.1, in the very low noise limit. Furthermore, similarly to what I mention above about delensing, they also studied the effects of radio sources and gravitational lensing on the r sensitivity, and showed that, after the subtraction of the galactic foregrounds, they become the major contaminant on large scales.

Part V

Down-to-Earth: the new generation experiment POLARBEAR

I present in this part the new generation CMB B-modes ground-based experiment, POLARBEAR. This project is an international collaboration between the US, Japan, Canada, Great Britain and France, see institutes shown in Fig. 13.2. Thought in the early 2000s, it started its scientific observations at the beginning of 2012, from the Atacama desert in Chile.

Figure 13.2: Institutes involved in the POLARBEAR project.

In chapter 14, I briefly describe the instrument, from a technical point of view up to its latest results and performances, as well as its future upgrades, POLARBEAR-II and POLARBEA-extended. In chapter 15, I introduce some analysis and calibration tools the POLARBEAR collaboration has developed and how they are integrated in the analysis pipeline. I also show the implementation of selected algorithms, based on the parametric maximum likelihood approach, which aim at controlling systematic effects and ultimately removing them.

Figure 13.3: POLARBEAR instrument installed on the Huan Tran Telescope, at 5200m, Cerro Toco, Chile. Picture taken by A. T. Lee, PI of the experiment.

Chapter 14

Description of the POLARBEAR experiment

As I mentioned in Part II, in order to characterize the small CMB polarization fluctuations, and in particular to be able to detect the primordial and lensed B-modes, POLARBEAR must have 1) an unprecedented sensitivity on the angular scales of interest, for multipoles $\ell \in \{25 - 2500\}$ in our case, and 2) a precise control of systematic instrumental effects. This chapter describes how the overall design of the instrument, with the main experimental properties are summarized in Table 14.1, addresses these goals.

frequency bands	150 GHz (+220 GHz)*
# of detectors	1274
sensitivity	21 μK$\sqrt{s}$ for the whole array
bandwidth	38 GHz
resolution (FWHM)	$3.5'$
field of view	2.3 deg
sampling frequency	190.73 Hz

Table 14.1: Summary of the main POLARBEAR-I properties. $\star$ The 220 GHz detectors are not currently observing but will replace some of the 150 GHz ones after couple of months of observations.

14.1 Frequencies of observation

The CMB blackbody intensity spectrum, $B_\nu(T)$, peaks at ~ 160 GHz. To optimize the measurement of temperature variation around the average of 2.725 K, we would like our experiment to observe at frequencies where $|\partial B_\nu / \partial T|$ is the biggest. This is the case around 220 GHz.

As I have explained in chapter 9 and Part IV, astrophysical foregrounds also play a major role in defining the optimal region of the spectrum for measuring CMB anisotropies.

Two polarized components are dominant over the spectral range of interest: polarized dust and synchrotron. Parametric component separation techniques requires at least four channels to estimate the spectral scaling laws and therefore disentangle those emissions, see Part IV . The signal from dust (synchrotron) emission is increasing (decreasing) as a function of frequency, as depicted in Fig. 9.4. Because the spatial distribution of the two signals is different, the frequency of minimum foreground signal changes as a function of spatial scale and position on the sky, but is around 100 GHz.

Moreover, for a CMB experiment observing from the ground, the atmosphere is one unavoidable source of both CMB signal attenuation and emission of optical power that contaminates the measurement, see chapter 8. To minimize this contamination, ground-based CMB experiments observe in spectral bands where the atmospheric attenuation is law, between molecular absorption frequency bands, the so-called atmospheric windows. The goal of POLARBEAR detectors is to optimally fill these windows so that the received photons will be mainly coming from space.

The spectral bands for the POLARBEAR experiment are defined by filters located within each focal plane pixel, and POLARBEAR-I is designed to exploit the atmospheric window centered at 150 GHz, between 120 and 180 GHz.

14.2 The dedicated Huan Tran Telescope (HTT)

As mentioned in chapter 3, primordial and lensed B-mode power spectra peak respectively at large scales, $\ell \sim 100$, and at small scales, $\ell \sim 1000$, i.e. ~ 0.1 deg. Therefore, designing a telescope equipped with an imaging experiment requires a large enough primary aperture with a diffraction limited resolution $\theta_{\rm resolution}$ below 0.1 deg. Moreover, the angular resolution of an imaging telescope is given by

$$\theta_{\rm resolution} = \frac{K\lambda}{D}, \tag{14.1}$$

where λ is the wavelength of observation and D is the diameter of the telescope. The constant K, usually close to unity, depends on how the primary aperture is illuminated by the detectors, see Goldsmith (55). Arnold (6) explains that, in the case of POLARBEAR, requiring $\theta_{\rm resolution} = 0.05$ deg results in $D \sim 2$ meters.

The need for a high experimental sensitivity sets a requirement on the optical throughput, also called étendue, given by

$$\sigma_{\rm étendue} \equiv A\Omega, \tag{14.2}$$

where A is the effective area of the primary aperture and Ω is the integral over the angular Field Of View (FOV) of the experiment. For a given primary aperture size, a wider FOV optical system, meaning larger Ω, will result in a larger electromagnetic

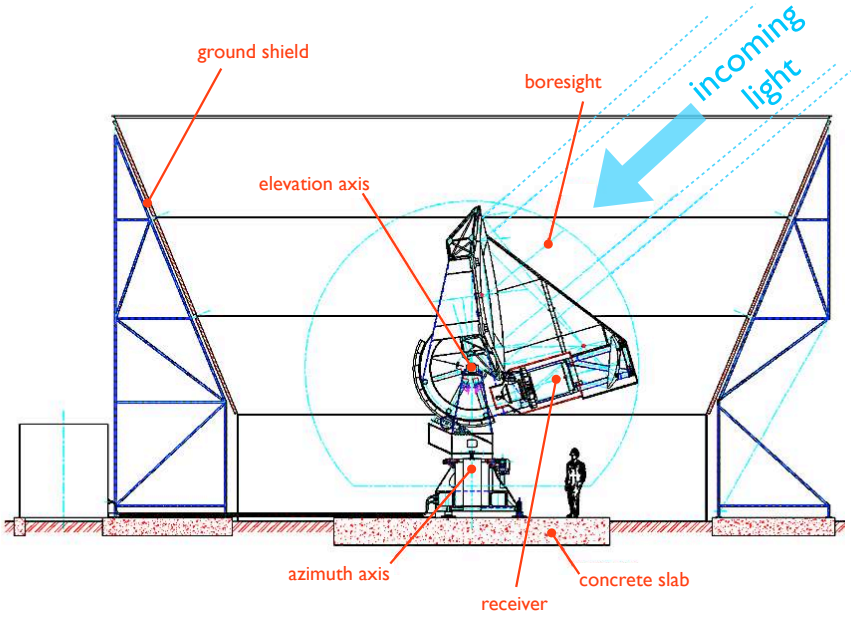

Figure 14.1: Schematic cross-section of the POLARBEAR experiment installed on the Huan Tran Telescope (HTT) at the James Ax Observatory.

throughput $A\Omega$. The sensitivity is therefore dictated by the global throughput given all the optical system of the telescope.

The Huan Tran[1] Telescope (HTT), shown in Fig. 14.1, has a primary aperture of 2.5 meters, so that it provides an angular resolution of $\sim 4'$ at 150 GHz. HTT optical system has been designed to have a large étendue $\sigma_{\text{étendue}}$, necessary to obtain a high sensitivity, while minimizing the instrumental- and cross-polarization as well as reducing the sidelobe response, i.e. the response outside the diffracted-limited main beam. Hanany and Marrone (59), Tran (138) did an analysis of crossed-Dragone (on-axis) and Gregorian-Dragone (off-axis) telescope designs for this application. They showed that although the crossed-Dragone offers smaller systematic polarization effects and a larger diffraction-limited FOV, the Gregorian-Dragone, illustrated in Fig. 14.2, provides acceptable performance while allowing more complete baffling of the optical elements to reduce sidelobe response.

[1]In December 2009, the POLARBEAR project manager Huan Tran died in a tragic domestic accident while on a trip to work on the telescope. He was deeply involved in the design of the experiment. The telescope has now been renamed the Huan Tran Telescope (HTT) in his honor.

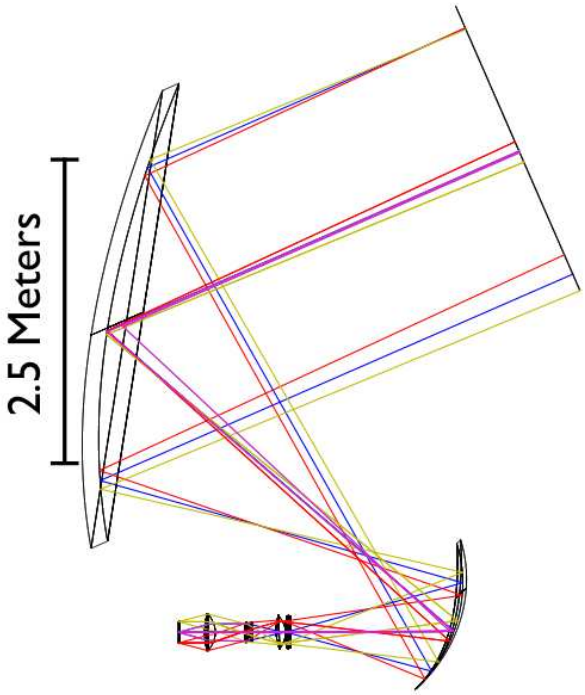

Figure 14.2: A ray-tracing schematic of the telescope optics. The focus created by the primary and secondary are re-imaged using the cold re-imaging optics to the flat, tele-centric focal plane.

14.3 Experiment location

As mentioned in chapter 5, space, balloon-borne and ground-based CMB experiments all have strengths and weaknesses. For a ground-based experiment, the most important weakness is the atmospheric contamination, obviously less important for stratospheric balloons. Besides, science goals of POLARBEAR are the detection of both primordial and lensed B-modes so we need to have access to a large fraction of the sky, which is possible from a balloon, although imposing a short integration time. Indeed, given the noise level of the experiment, we prefer to look during couple of months on a small patch of the sky. As explained in chapter 8, within the frequency range of interest, atmospheric absorption and emission are dominated by O_2 and H_2O transitions. So any ground-based experiment gains in being located in a high-altitude desert where the atmosphere is thin and dry. The POLARBEAR location is a solution to these requirements with a quite dry region (Atacama desert) and an important elevation (5200 m).

An other interesting location for millimeter observations is the South Pole, which has a 6-months winter night with a stable atmosphere. Moreover, astronomers have the ability to observe the same patch of sky at a given elevation angle: the patch appears to rotate around the zenith. From a mid-latitude site such as Atacama desert ($\sim$ 23 deg South), the orientation of the patch of sky with respect to the ground changes over its

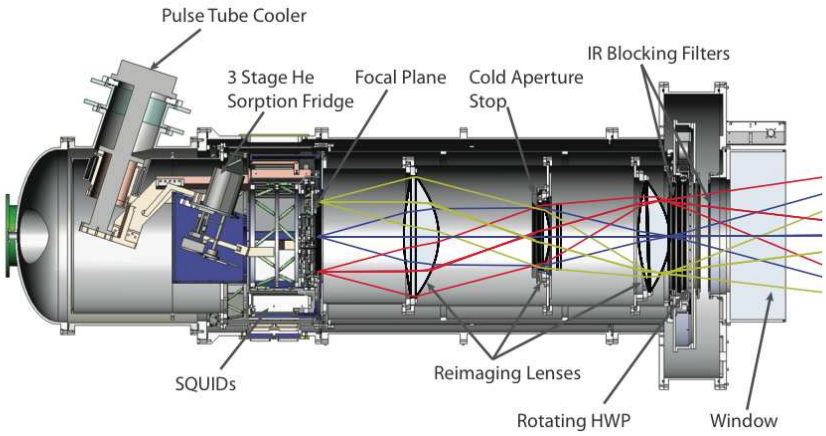

Figure 14.3: Mechanical and optical design of the POLARBEAR 2-meter long cryogenic receiver. The focal plane is cooled to 260 mK.

course of the day and the year. As explained in sections 6.1 and 15.4, sky rotation can be crucial in mitigating systematic effects, because it implies a natural modulation of the polarization in the Time-Ordered Data (TOD).

14.4 Receiver

Cryogenic bolometers are the most sensitive detectors of electromagnetic radiation in the frequency range optimized for CMB experiments: individual cryogenic bolometers can be sufficiently sensitive that their noise properties are limited by the intrinsic statistical noise of the radiative signal being detected, called the photon noise. To achieve that sensitivity, the bolometric detectors must be sufficiently cooled down so that the detector noise, mostly thermal noise, becomes smaller than the photon noise. This requires temperatures around ~ 250 mK.

As illustrated in Fig. 14.3, POLARBEAR achieves this cooling using a pulse-tube cooler and a 3-stage helium sorption refrigerator. To maintain this temperature, the detectors must be shielded using thermal filtering, integrated into the POLARBEAR cryogenic receiver.

14.5 Detectors

The Berkeley group has successfully created an Antenna-Coupled, TES bolometer which can measure polarized radiation with a very high sensitivity. This was an important technological success for the POLARBEAR project, and was the first step in producing the large arrays that are required for the next generation of CMB experiments.

14.5.1 Antenna

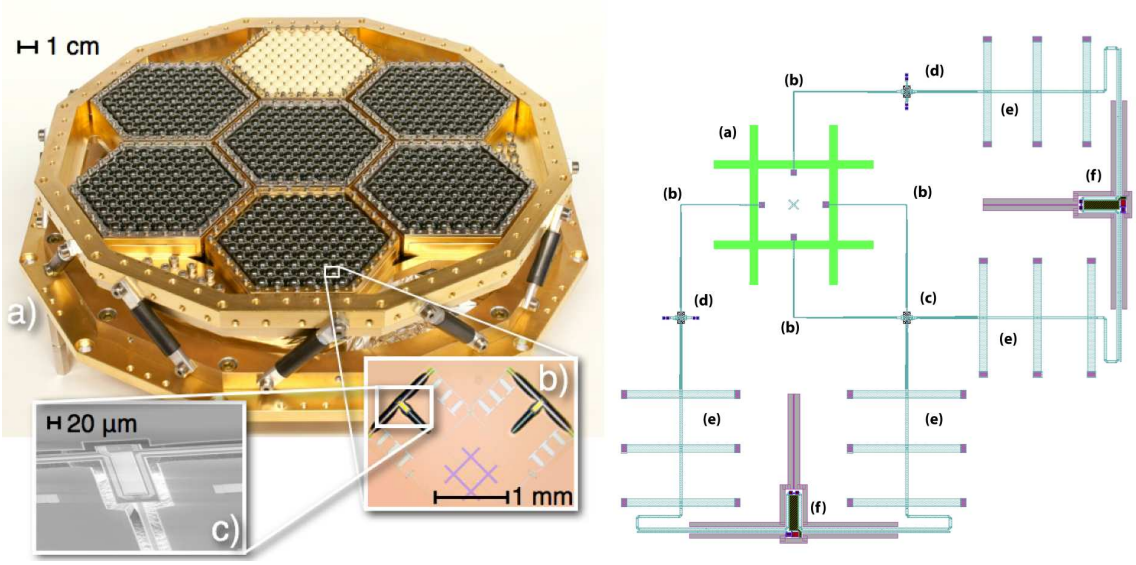

Figure 14.4: **Left panel:** a photograph, **a**, of the POLARBEAR focal plane. For scale, the outer frame is 25 cm in diameter. Six of the hexagonal sub-arrays have single crystal silicon lenslets; the single array of white lenslets are made of alumina, which is similar in performance. A photograph, **b**, of a single-detector pixel with a dual-polarization crossed double-slot dipole antenna, microstrip transmission lines, band-defining filters, and suspended Transition Edge Sensor (TES) bolometers. A scanning electron micrograph of the bolometer, **c**, showing its thermally isolating silicon nitride suspension. **Right panel:** a design scheme of the structure of a POLARBEAR pixel. One can see crossed double-slot dipole **(a)**, microstrip transformer **(b)**, microstrip cross-under **(c)**, cross-under balancing structures **(d)**, microstrip filters **(e)** and bolometers **(f)**.

The antenna used in our detector is a double slot dipole, see Arnold (6), Myers et al. (95), directly sensitive to the polarization of the incident light. As one can see in Fig. 14.4, a silicon hemispherical lens is placed onto the antenna. The detector chip sits directly on the lens. This antenna/lens combination has been used extensively at these frequencies and have been proven to couple efficiently to typical telescope optics.

14.5.2 Superconducting microstrip

The antenna is connected to a transmission line, which is used to bring the incoming optical power to the detector, the bolometer. Commonly used materials would cause high power loss at our frequencies ($\sim$ 150 GHz), which is unsuitable if we want to detect extremely weak signals. POLARBEAR uses a superconducting micro-strip which is a very low loss transmission line. Moreover, niobium is a convenient choice of materials, thanks to the fact that it has the highest superconducting temperature of all the elements.

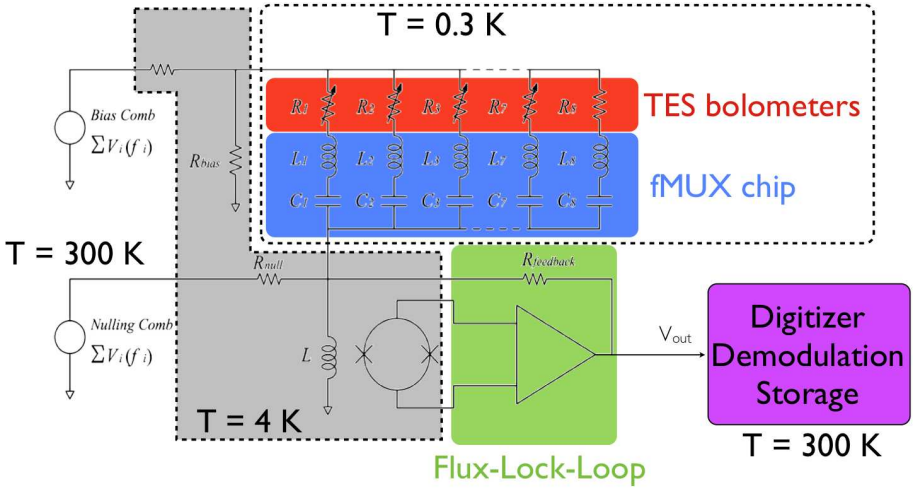

Figure 14.5: Scheme of the POLARBEAR multiplexer system.

14.5.3 Band defining microstrip filters

One of the advantages of using a micro-strip to connect the antenna to the bolometer is that band defining micro-strip filters can be integrated into the transmission line, see Fig. 14.4 and e.g. Myers et al. (95). In a typical millimeter wave receiver, band defining filters are metal mesh off-chip optical filters. If several bands are required, several of these off-chip filters must be used. In our detectors, the filters are integrated on the chip and different pixels can easily have different frequency sensitivities.

14.5.4 Bolometers

Bolometers are composed of a terminating resistor and a superconducting Transition Edge Sensor (TES), located on a leg that is isolated from the substrate. The incoming power on the superconducting micro-strip is dissipated in the load resistor as heat, and the change in temperature is measured by the TES. In order to reach the sensitivity we aim at, the bolometer must be thermally isolated from the silicon nitride legs and the bath temperature must be below 300 mK. This reduces the detector noise to below the photon noise mentioned earlier. TESs have many advantages over conventional semiconducting bolometers, see e.g. Essinger-Hileman et al. (42), Kuo et al. (75).

14.5.5 Detector electrical/ digital interface

The most important advantage in our application is that the TES readout electronics can be multiplexed, e.g. Dobbs et al. (32), so that the signal from several pixels can be brought out on an unique wire: as the number of bolometer arrays grows, this benefit becomes increasingly important. In fact, large arrays of bolometric detectors require

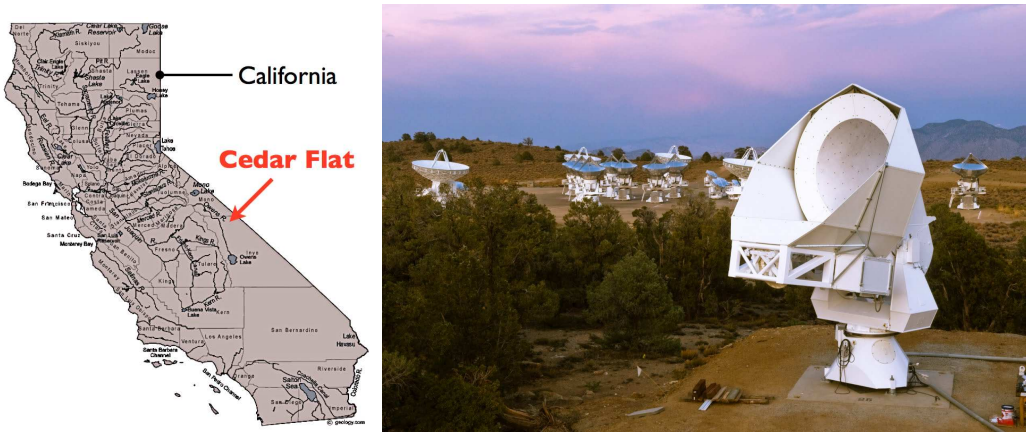

Figure 14.6: Picture of POLARBEAR installed on the Huan Tran Telescope at Cedar Flat, California, as in summer 2010.

sophisticated readout schemes. Even if a potential source of cross-correlations between detectors, this technique reduces thermal loading onto the coldest stages of POLARBEAR and reduces also the complexity of instrumenting large arrays. Each sensor is biased with a sinusoidal voltage at a unique frequency. The sensor signals are thus separated in frequency domain and can by summed before being readout by Superconducting QUantum Interference Devices (SQUID). This is illustrated in Fig. 14.5, where one can see that each sensor R_i is placed in series with a tuned filter consisting of an inductor and a capacitor with values chosen to give center frequencies from 300 kHz to 1 MHz.

14.6 Engineering campaign results

HTT and POLARBEAR receiver were assembled for an end-to-end engineering run during the summer of 2010 at Cedar Flat, California, the site of the Combined Array for Research in Millimeter-wave Astronomy (CARMA[1]) interferometer (see Fig. 14.6). Three of the seven detector sub-arrays were installed in the receiver.

The collaboration tested the telescope, the bolometers, the readout, the cryogenics, the data acquisition, the Quick Analysis software, etc. We performed calibration of the beams (beam maps using in particular Jupiter and Saturn), the telescope pointing (see section 15.2.3), the gains of the detectors, etc. We found a beam size of 3.8 arcmin (FWHM) which was consistent with optics simulations. We also estimated differential beam systematics, and it turned out that these latter were satisfactorily low for $r \sim 0.025$ required sensitivities, see Miller et al. (92), Shimon et al. (123), as summarized in Table 14.2. Small beam ellipticity, $\sim 3\%$, comes from the telescope design combined with the re-imaging lenses. But this effect, common to both polarizations,

[1]For more information: http://www.mmarray.org/

effect	estimated systematic error	requirement
Differential Beam Size	0.4 %	1.5 %
Differential Pointing	0.41"	1.1"
Differential Ellipticity	0.5 %	2.9 %

Table 14.2: Constraints on some systematics parameters from the POLARBEAR engineering run in California, summer 2010.

and if well characterized, does not introduce a beam-sourced systematic error. In addition, for differential polarization measurements, it is important that the beams for the two polarizations in one pixel are well matched. The two beams should have the same shape, size, and center position on the sky. As mentioned in section 7.3.1, a difference in shape between the two polarized beams allows leakage from intensity to polarization when the two beams are subtracted.

Another result from the engineering campaign is illustrated in Fig. 14.7, which shows polarization and intensity maps of the TauA supernova remnant. Measurements of the fractional polarization of the source and the average polarization angle are consistent with the estimation at 90GHz using the IRAM 30-meter telescope, see Aumont et al. (8).

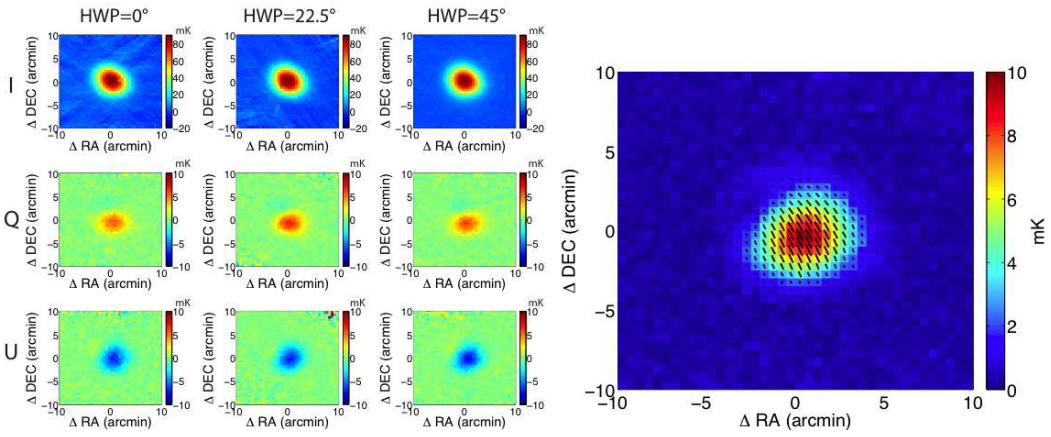

Figure 14.7: POLARBEAR maps of Tau A, a polarized supernova remnant, from data taken during its engineering run. TauA is barely resolved, so the map is effectively a polarized beam map, although the small amount of ellipticity seen in the Q maps is consistent with that expected from other maps of TauA. **Left pannel**: I, Q, and U maps of Tau A with a range of half-wave plate angles. The data is consistent between wave-plate angles. **Right panel**: map of Tau A with all half-wave plate angles combined. Polarized intensity $p \equiv \sqrt{Q^2 + U^2}$ is shown in color and polarization angle as lines.

Left panel of Fig. 14.10 shows the power spectrum of the sum and difference of two bolometers in a pixel demonstrating high common-mode rejection of atmospheric fluctuations. The $1/f$ f_{knee} in the sum is 8 Hz and 100 mHz in the difference. The reduction in amplitude of atmospheric fluctuations is a factor of 100 at 100 mHz.

Figure 14.8: A picture of the POLARBEAR experiment mounted on the Huan Tran Telescope, in the Atacama desert, as it was in May 2012.

The atmospheric fluctuations at the 2200 meters site during the summer 2010 were an order of magnitude higher in amplitude than we observe now from our Chilean site, and the photon-noise limited detector NET was roughly a factor 2 higher than in Chile, as detailed in the following section.

14.7 Current status of POLARBEAR — Spring 2012

The successful engineering run led to the final development of the receiver and focal plane. In late September of 2011, James Ax Observatory was built at an altitude of 5200 m on Cerro Toco in the Atacama desert of Chile, cf. Fig. 14.8. During the next months the Huan Tran Telescope was assembled at the site and the POLARBEAR receiver integrated. First light with the fully integrated experiment was achieved on January 10th, 2012 with an observation of Jupiter. Since then, the POLARBEAR collaboration performed several tests and studies and below are some preliminary results on the instrument performance.

- **beam maps** — Maps of planets such as Jupiter and Saturn are important calibration sources and bring a lot of information about the instrument response. Their solid angle are much smaller than the POLARBEAR beams and are quite bright within the radio wavelengths, hence constitute an efficient way of probing, understanding and characterizing the structures of the detectors beam. In particular, this allows the designed beam-size and ellipticity to be estimated for every detector. The difference between the location of each pixel on the sky and

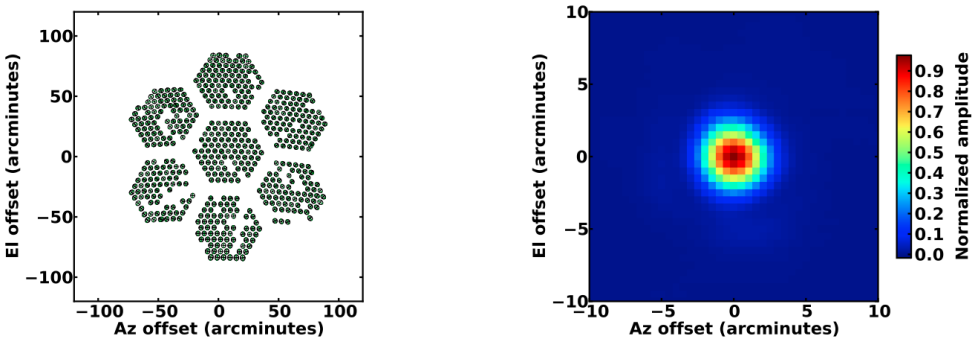

Figure 14.9: **Left panel**: Gaussian fit for all the observing detectors among the POLARBEAR focal plane. **Right panel**: the resulting co-added instrument beam from all detectors in five separated observations of Saturn.

the centered telescope pointing, known as the pixel offset, can also be measured from these maps. This will be detailed in section 15.2.3 as I was in charge of the pointing reconstruction during the POLARBEAR engineering run, which is a key step in the data analysis pipeline. Moreover, one can calibrate the gain of the two detectors of a single pixel via either the response to atmospheric signal or using the beam map itself normalized to a known source temperature. The point sources maps can also be used to probe the differential beam properties of each pixel by differencing the two orthogonal antennas signals. Beam maps also bring information about the detector NET. The left panel of Fig. 14.9 shows the fit beam parameters for the focal plane resulting from several observations of Saturn from Chile. The right panel depicts the result of coadding the maps from all detectors from five separate observations of Saturn. This gives us a high fidelity map of the overall instrument beam. All the results about beam analysis is consistent with expectations from simulations of the optical properties across the field of view.

- **pixel differencing and atmospheric rejection** — Differential beam properties were investigated by differencing the orthogonal polarization beam maps. For POLARBEAR, the dominant contribution to the differential beams arrises from the differential pointing, cf. chapter 6. This systematic effect across the array was found to be 4.6 ± 3.0 arcseconds. Taking into account this relative calibration and computing the difference between the two polarization of a pixel allows us to see how well the unpolarized atmosphere is suppressed at low frequencies. The f_{knee} of this $1/f$ noise contaminates our polarization signals measurement at large angular scale. The sum and difference amplitude spectral densities for an observation of one of the POLARBEAR CMB patches gives similar results to the ones depicted in Fig. 14.10.

- **fractional throughput and noise** — On the one hand, measurements of the product $\eta\Delta\nu$ of the fractional throughput η and the integrated bandwidth $\Delta\nu$, can be made from the beam maps presented above, as well as from lab measurements and from elevation-nods[1] of the telescope. η is a measure of the fraction of the power seen by a detector from a source next to the input of the receiver compared to the expected theoretical signal, i.e. what would be seen if the detector had perfect efficiency to that same source. On the other hand, measurements of the detector NETs can be made similarly by using beam maps or elevation-nods for an absolute detector temperature gain and making a comparison to the measured noise. The design bolometer noise equivalent temperatures (NET) are about $500\mu\mathrm{K}\sqrt{s}$ due to bolometer saturation powers and atmospheric conditions, cf. Arnold (6). Preliminary measurements from both beam maps with planets and elevation nods show a peak in the NET distribution at $550\mu\mathrm{K}\sqrt{s}$, and a total array NET of $\sim 21\mu\mathrm{K}\sqrt{s}$, cf. Kermish et al. (69).

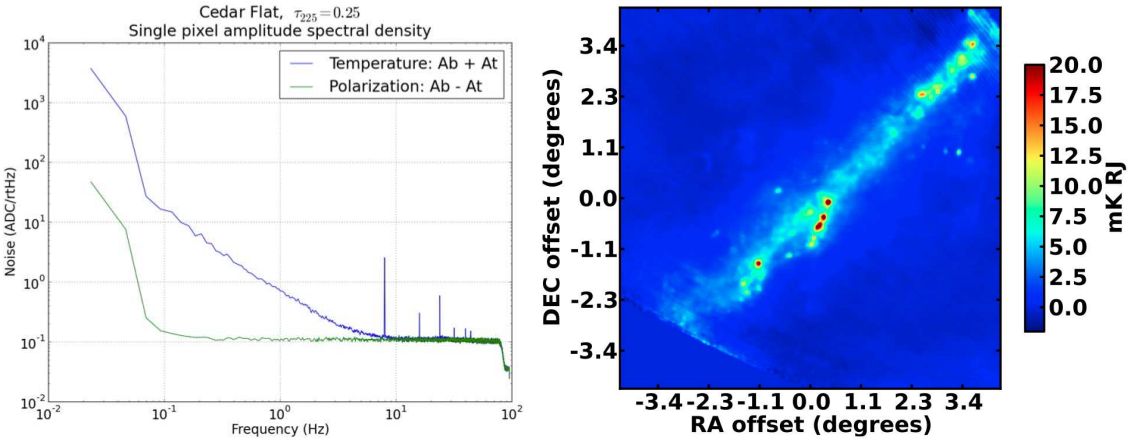

Figure 14.10: **Left panel**: sum and difference of bolometers in a pixel demonstrating common-mode removal of atmospheric fluctuations. The knee at 100 mHz in the difference data is likely an upper limit due to length of data stream. **Right panel**: a map of a bright region of the galaxy, as observed during few hours by the POLARBEAR experiment. From Kermish et al. (69).

- **polarized maps of Tau A** — POLARBEAR collaboration produced maps of Tau A, a supernova remnant in the middle of the Crab nebula. Tau A is polarized by synchrotron emission and the experiment uses it as a polarized astrophysical calibrator, especially for the characterization of detector polarization angles. As illustrated in Fig. 14.7, observations of Tau A are made at several HWP rotation angles to both characterize systematic errors and verify the detector polarization angles on the sky.

[1] Elevation-nods are specific scans in elevation (constant azimuth) which are used to calibrate the relative gain of the detectors (based on the assumptions of parallel atmospheric layers).

- **scientific observations** — The instrument is able to performe routine observations since late April of 2012, and I had the chance to participate to the transition period, as I explained in chapter 6. The telescope runs on a 36 hour cycle[1]: ~ 20 hours are used for the observation of CMB patches, 4.5 hours to cycle our milliKelvin fridge, and the remaining 11.5 hours currently dedicated to calibration and instrument characterization measurements (point sources, galaxy, tau A, etc.). I depict in Fig. 14.10 a preliminary temperature map of patch of the galaxy with bright compact sources (from Kermish et al. (69)). This map demonstrates the functionality of the instrument and several key analysis tasks, involved in the map-making. Relative calibration of all detectors is performed using the POLARBEAR stimulator[2], done for every Constant Elevation Scan (CES). A pointing model generated from many observations of point sources is applied, cf. section 15.2.3. Beam centers are estimated using observations of Saturn and are used to construct the pointing matrix, i.e. to offset and co-add the observing individual detectors. Clear features in the map such as the bright compact sources in the galaxy shows the achievement of the early analyses done by the collaboration from the $3.5'$ resolution POLARBEAR instrument.

14.8 Future: POLARBEAR-II and POLARBEAR-EXT

14.8.1 POLARBEAR-II

POLARBEAR-II is an upgrade of the POLARBEAR cryostat, depicted in Fig. 14.11, which will use more detectors (7,588 bolometers) with larger multiplexed SQUID readout, all dichroic detectors ($150+220$ or $90+150$ GHz), cf. Suzuki et al. (134). The observation over a fraction of the sky of 40% will give a final sensitivity of $\sim 21\ \mu\mathrm{K}\sqrt{s}$ in intensity. This could lead to a detection of $r = 0.01$ at the 2-σ level and a constraint on the total neutrino mass of 90 meV if POLARBEAR-II is analyzed alone and $\lesssim$ 50 meV (below the inverted hierarchy configuration) if it is combined with Planck, cf. Appendix C.

14.8.2 Long-term development: towards POLARBEAR-EXT

In the longer term, the POLARBEAR design is scalable to multiple telescopes in order to increase overall mapping speed. A set of 3-6 telescopes could approach the full potential of ground-based CMB polarization measurements.

Limiting the elevation range to greater than 30 degrees, 80% of the entire sky is visible from the Chilean POLARBEAR site. Because of galactic contamination, applying

[1] The cryostat, as any fridge, need to regularly cycle its cryogenic fluids.
[2] a small chopped source feed through a waveguide opening in the secondary mirror

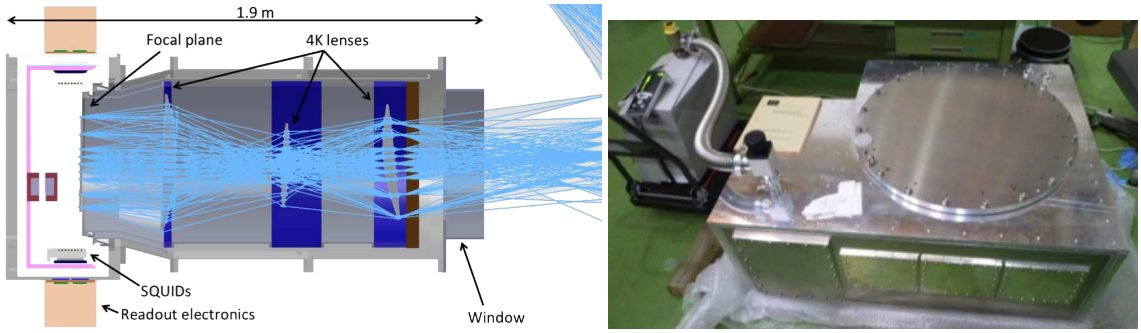

Figure 14.11: **Left panel:** cross section views of the POLARBEAR-II receiver. The design and the POLARBEAR-I one, as shown in Fig. 14.3, have many common points in cryogenics, wiring layout, and optics. The optics for POLARBEAR-II are larger in size and throughput. The largest lenses in POLARBEAR-I and POLARBEAR-II are 34 cm and 56 cm in diameter. The lenses in POLARBEAR-I are polyethylene and the lenses in POLARBEAR-II are alumina (sintered sapphire). **Right panel:** photograph of POLARBEAR-II cryostat back section at the KEK lab. This section will house the focal plane, sub-kelvin cooler, and cold readout electronics.

the WMAP polarization sky cut leads to 60% of the sky available. Lensing measurements of the sum of neutrino mass and dynamics of the dark energy equation of state will be improved as roughly the square root of the sky area for sufficiently low-noise observations, cf. Appendix C. The clean sky available from Chile is a large fraction of those available from space, and this set of ground-based experiments may almost reach the limit of sensitivity achievable by space instruments.

Chapter 15

Description of POLARBEAR data analysis

The aim of CMB polarization experiments is to produce high quality polarized maps in order to compute power spectra and estimate cosmological parameters. However, the first step, the map-making process, is already non trivial mainly because of the huge volume of data to analyze and because of the noise correlations, e.g. Stompor et al. (132). Similarly to the component separation process, Eq. (12.1), the idea is to invert the following data modeling equation

$$\mathbf{d} = \mathbf{A}\,\mathbf{s} + \mathbf{n} \tag{15.1}$$

so that we can estimate the unknown sky signal $\mathbf{s}$, having access to the data $\mathbf{d}$ and some informations about the statistical properties of the noise $\mathbf{n}$. In the case of POLARBEAR, typical size for $\mathbf{d}$ is $\sim 10^{12}$. As I mentioned in chapter 6, predominantly due to unavoidable noise correlations, this problem cannot be solved with a simple bin by bin approach.

Section 15.1 summarizes the two basic levels of analysis we should consider to solve the problem set above. To illustrate these two levels, I introduce in section 15.2 some example of quick analysis, crucial in understanding the instrument. In sections 15.3 and 15.4, I present ways of estimating the statistical properties of the noise as well as some parameters modeling systematic effects from the time stream. Section 15.5 introduce different potential filtering of the atmospheric contamination. Finally, even if this has not been personal projects, I explain in section 15.6 the power spectra and cosmological parameters estimations.

15.1 Overview: in-the-field and future analysis

I first briefly describe the steps of the pipeline illustrated in Fig. 6.2. This chain of analysis is not performed once but some parts can be done on a daily basis for moni-

toring the instrument performance, e.g. from flagging and data filtering to quick noise estimation and simple map-making. It is usual to discriminate two different levels of analysis:

- the quick analysis which can be performed directly in the field, necessary to calibrate the instrument, flag the data, and check if the observations are well performed and the data well registered. The POLARBEAR collaboration has developed the Analysis Backend library (AB) in order to achieve these goals.
- the more sophisticated analysis which has important computational power needs and aims at gather all the informations about the telescope (detectors data, noise characterization, pointing, etc.) and construct the CMB fluctuations maps. On a second step, the power spectra estimation will lead to the estimation of the cosmological parameters.

For the first level of analysis, besides developing some quick analysis routines, I contributed to the application of a pipeline software, Pipelet[1], to the AB library. This latter provides a frame to pipe routines and keep track in time of all the input/output products, in particular with an user friendly web interface. This may help the in-the-field researchers to run quick analysis and monitor in almost real time the quality of the data, of the calibration runs, of the noise properties, etc.

For the second level of analysis, in addition to study algorithm based on parametric maximum likelihood technique, I participated to the ANR MIDAS'09 (4), project lead by R. Stompor which aims at finding new algorithms in order to solve the computational problems due to the immensity of data sets involved in the map-making process.

15.2 Description of selected quick analysis

As I mentioned in Part II, reaching a very high sensitivity is necessary to achieve our science goals. But understanding and characterizing the instrument is an essential piece of information to discern and mitigate systematic effects.

15.2.1 Flagging the glitches

Glitches are (almost instantaneous) spurious signals corresponding to the passage of a particle in the detector (it can be also generalized to any contamination which makes the time stream unusable). The particle leaves energy in the instrument and heats one or more bolometers. A glitch results in a brutal increase of the signal amplitude followed by a gradual decrease in temperature corresponding to the thermalization of the detector.

[1]Python-based software developed by M. Betoule (LPNHE) and M. Le Jeune (APC). Further informations can be found at http://supernovae.in2p3.fr/∼betoule/pipelet/

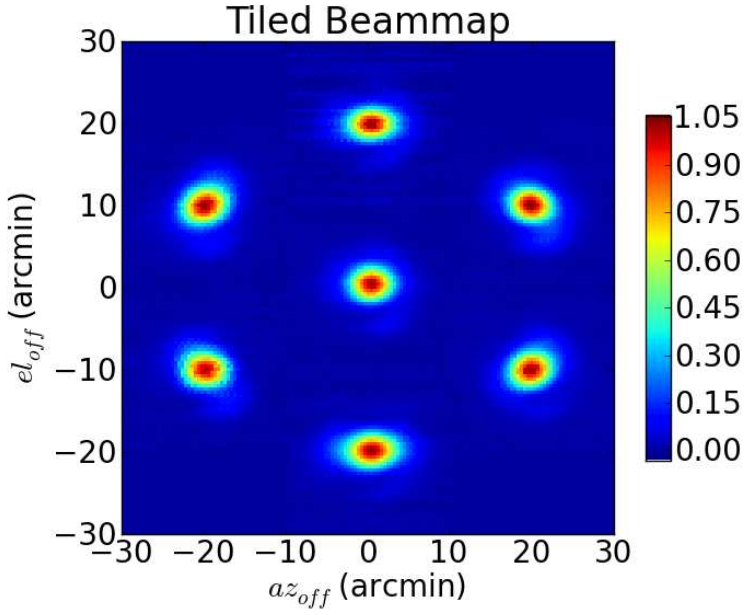

Figure 15.1: POLARBEAR beams coadded per wafer.

During those few short periods, this contamination, more or less important (up to several orders of magnitude higher than noise amplitude), is added to the "usual" sky signal. Glitches and instrument response study is essential for filtering these contaminants. However, it has to be noticed that they can also be used to characterize the detectors response and in particular estimate the detectors time constants.

In order to detect these events, flag and clean them, the first step is to detect peaks in the TOD. The procedure can be described in three points:

- we can estimate locally the standard deviation of the TOD by computing the dispersion with respect to the median after convolution with e.g. a top hat window, in order to avoid glitches in the noise estimation.
- all points above a threshold of detection, e.g. with a $4 - 10$ σ amplitude, are interpreted as glitches.
- these events (time, detectors id, etc.) are stored together and a list of potential glitches is created: this is the flagging.

15.2.2 Beam calibration

Beams represent the optical transfer function of the detectors. They characterize the resolution of the instrument, and perfect optics result in circular Gaussian beams. In practice, asymmetry of the beam shape have to be well characterized because it can

become an important source of systematic error for CMB polarization experiments, see chapter 7. Often characterized with ellipsoids, see previous chapter and Fig. 15.1 depicting results obtained with POLARBEAR, they can sometimes present more complex shapes with several maxima. In addition, beams can have spatially distant structures (up to a few degrees) called sidelobes. POLARBEAR optics are designed so that the instrument is not sensitive to sidelobes, and this can be measured using very bright sources (Moon, Jupiter, etc.).

As illustrated in section 14.7, to determine the actual shape of the main lobe of the beam, POLARBEAR uses point sources which are, by definition, much smaller than the resolution of the instrument. The experience observes selected planets of the Solar System to characterize the beam ($\sim 3.5 - 4$ arcmin), in particular Jupiter (angular size of ~ 43 arcsec) and Saturn (~ 18 arcsec).

In addition, to model the beams, the POLARBEAR collaboration can use complete bases such as

- a Gauss-Hermite (GH) polynomial expansion (as used by Planck and QUIET collaborations), based on a series of Hermite polynomials H_n illustrated in the left panel of Fig. 15.2,

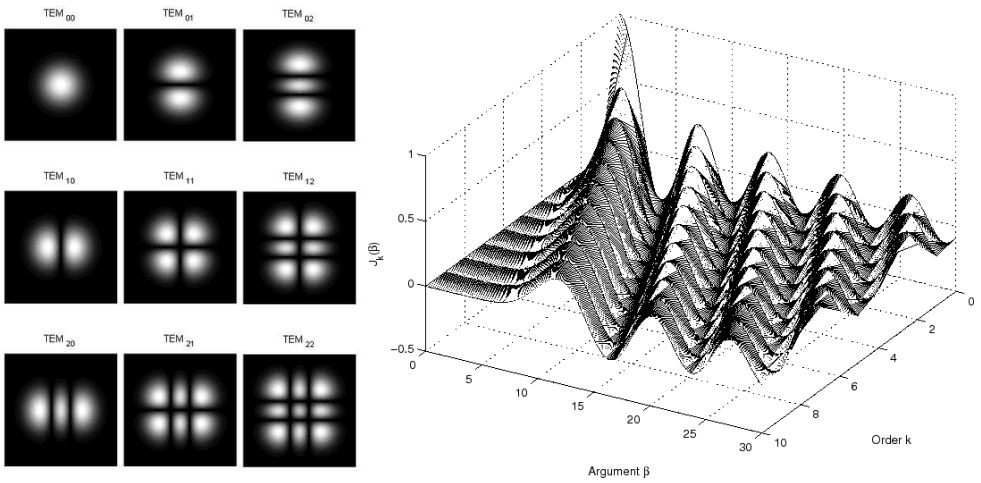

Figure 15.2: **Left panel**: the first nine Gauss-Hermite modes. **Right panel**: a selection of Bessel harmonic functions $J_k(\beta)$, related to the spherical Bessel function through Eq. (15.2).

- or a Bessel Harmonic expansion (BH) — i.e. plane-wave expansion, which is simply the flat-sky limit of the spherical harmonic Y_ℓ^m expansion — based on a series of Bessel polynomials j_n, see right panel of Fig. 15.2, which are related to the Bessel polynomials J_n by the relation

$$j_n(x) = \sqrt{\frac{\pi}{2x}} J_{n+1/2}(x). \tag{15.2}$$

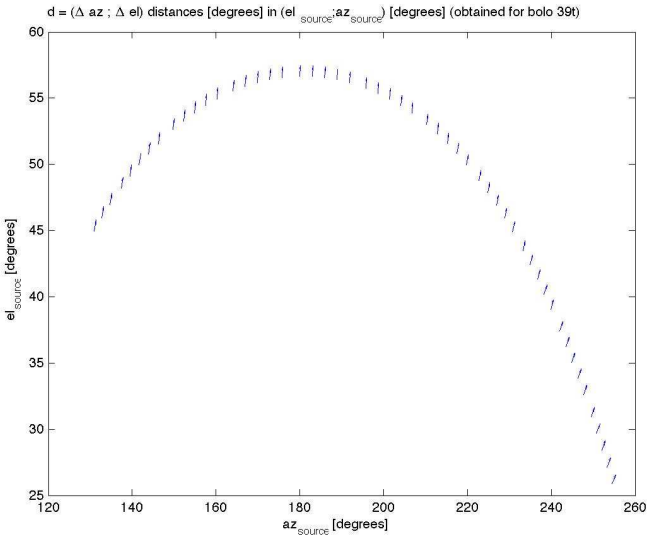

Figure 15.3: (Δaz, Δel) vectors located at different ($\mathrm{az}_{\mathrm{source}}$, $\mathrm{el}_{\mathrm{source}}$), as estimated for a single bolometer observing Saturn in June 2010.

15.2.3 Pointing calibration

I have been in charge of reconstructing the POLARBEAR telescope pointing during its engineering run in California, see section 14.6. A working pointing model for the telescope was one of the requirements imposed by the POLARBEAR funding agency, the National Science Foundation, essential for the deployment of the experiment in Chile. In this section, I describe this method which is still part of the current AB library.

15.2.3.1 Data

Data comes from multiple raster scans of bright planets like Jupiter, Saturn, etc.. Each raster corresponds to $\sim$ 20 minutes of observation. Because of the short time scales, I assume that the planet is fixed in (RA, Dec) coordinates during the time of the observation. In addition, I do not take into account the specific position of the studied pixel onto the focal plane, which have to be accounted for as offsets using the hardware map of the detectors.

I define the pointing errors as follow:

$$\mathbf{d} \equiv \begin{pmatrix} \Delta\mathrm{az} \\ \Delta\mathrm{el} \end{pmatrix} \tag{15.3}$$

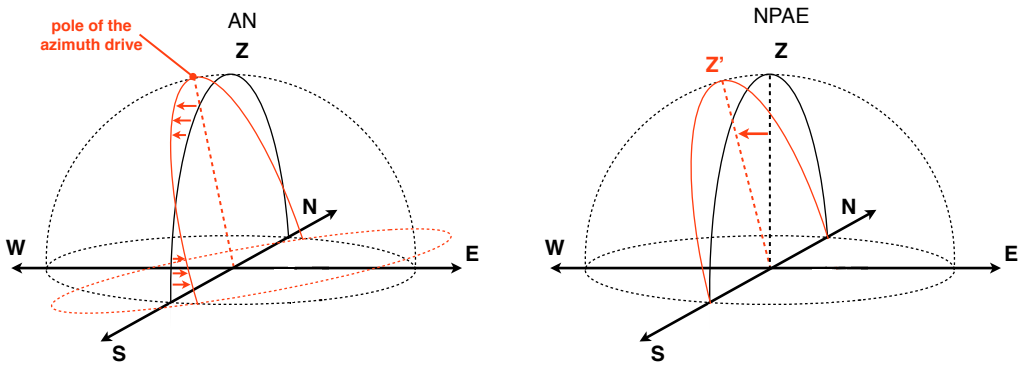

Figure 15.4: **Left panel**: scheme showing the effect of the main azimuth drive being West of the vertical. This corresponds to the AN parameter in Eqs. (15.6) and (15.7). The AW parameter would be the equivalent but for the East-West axis. **Right panel**: consequence of a non-zero $NPAE$, i.e. the amount by which the azimuth and elevation drives are non-perpendicular.

with

$$\Delta\mathrm{az} \equiv (\mathrm{az}_{\,\mathrm{estimated}} - \mathrm{az}_{\,\mathrm{source}}) \times \cos(\mathrm{el}_{\,\mathrm{source}}) \equiv \mathrm{az}_{\,\mathrm{offset}} \times \cos(\mathrm{el}_{\,\mathrm{source}}) \quad (15.4)$$

$$\Delta\mathrm{el} \equiv \mathrm{el}_{\,\mathrm{estimated}} - \mathrm{el}_{\,\mathrm{source}} \equiv \mathrm{el}_{\,\mathrm{offset}}. \quad (15.5)$$

$(\mathrm{az}_{\,\mathrm{estimated}}, \mathrm{el}_{\,\mathrm{estimated}})$ is the estimated position of the planet and $(\mathrm{az}_{\,\mathrm{source}}, \mathrm{el}_{\,\mathrm{source}})$ is the expected one. The coordinates $(\mathrm{az}_{\,\mathrm{estimated}}, \mathrm{el}_{\,\mathrm{estimated}})$ are obtained after doing the map from the few detectors which have observed the source. Second, these maps are fitted with a 2d-Gaussian, reasonable approximation of the main lobe shape. For each selected map (e.g. with a good source coverage) obtained by one bolometer at constant elevation, $\mathrm{az}_{\,\mathrm{estimated}}$ and $\mathrm{el}_{\,\mathrm{estimated}}$ are set to be the center of the fitted 2d-Gaussian. Another way of estimating the center of the source is to take the maximum intensity peak in the TOD but this change turns out to be not significant for the pointing analysis. Finally, $(\mathrm{az}_{\,\mathrm{source}}, \mathrm{el}_{\,\mathrm{source}})$ is given by the ephemeris and for each raster we can therefore determine a pointing error $(\Delta\mathrm{az}, \Delta\mathrm{el})$. I show in Fig. 15.3 the components $(\Delta\mathrm{az}, \Delta\mathrm{el})$, illustrated as arrows, as a function of $(\mathrm{az}_{\,\mathrm{source}}, \mathrm{el}_{\,\mathrm{source}})$. It corresponds to the compilation of several observations during the course of Saturn, i.e. couple of hours.

15.2.3.2 Model

I present the model used to fit the data introduced above and allow us to reconstruct the pointing of the telescope. The dependence of the pointing errors $(\Delta\mathrm{az}, \Delta\mathrm{el})$ on the mechanical parameters of the telescope are described by Wallace (145). This model

assumes that it exists seven parameters $(AN, AW, NPAE, CA, IA, IE, TF)$ such that

$$\begin{aligned}\Delta\mathrm{az}(\mathrm{az_s}, \mathrm{el_s}) &= -AN\ \sin(\mathrm{az_s})\ \sin(\mathrm{el_s}) - AW\ \cos(\mathrm{az_s})\ \sin(\mathrm{el_s}) \\ &\quad +NPAE\ \sin(\mathrm{el_s}) - CA + IA\ \cos(\mathrm{el_s}) \quad (15.6)\\ \Delta\mathrm{el}(\mathrm{az_s}, \mathrm{el_s}) &= AN\ \cos(\mathrm{az_s}) - AW\ \sin(\mathrm{el_s}) - IE + TF\ \cos(\mathrm{el_s}), \quad (15.7)\end{aligned}$$

where for shortness az_s, $el_s = az_{\mathrm{source}}$, el_{source}. This parametrization corresponds to specific sources of error, some of them being depicted in Fig. 15.4,

- AN: azimuth axis offset/misalignment North-South
- AW: azimuth axis offset/misalignment East-West
- $NPAE$: elevation axis not perpendicular to the mount azimuth axis
- CA: telescope beam not perpendicular to elevation axis (collimation error of the electromagnetic axis)
- IA: azimuth encoder zero-point
- IE: elevation encoder zero-point
- TF: telescope flexure

One should consider adding the total encoder corrections in both azimuth and elevation, respectively in Eqs. (15.6) and (15.7). I depict this pointing model in Fig. 15.5, where I show the potential contribution of each of the parameters listed above.

Models taking into account the refraction induced by atmosphere have been also studied. In particular, I studied the Ulich model, leading to the following transformation of Eq. (15.7):

$$\Delta\mathrm{el} \rightarrow \Delta\mathrm{el} + R_0(\mathrm{pressure},\ \mathrm{temperature},\ \mathrm{humidity}) \times f(\mathrm{el_s}), \quad (15.8)$$

where R_0 is a function of atmospheric quantities, and can be modeled following Ulich (140). $f(\mathrm{el_s})$ is a geometric function depending only on the elevation angle of the observation. Furthermore, the ABC model, also named IRAM/JCMT model transforms Eq. (15.7) as

$$\Delta\mathrm{el} \rightarrow \Delta\mathrm{el} + A\cot(\mathrm{el_s}) + B\cot^3(\mathrm{el_s}) + C\cot^5(\mathrm{el_s}), \quad (15.9)$$

where the constants A, B and C have to be determined from the data, similarly to the other seven parameters used in the model, Eqs. (15.6) and (15.7).

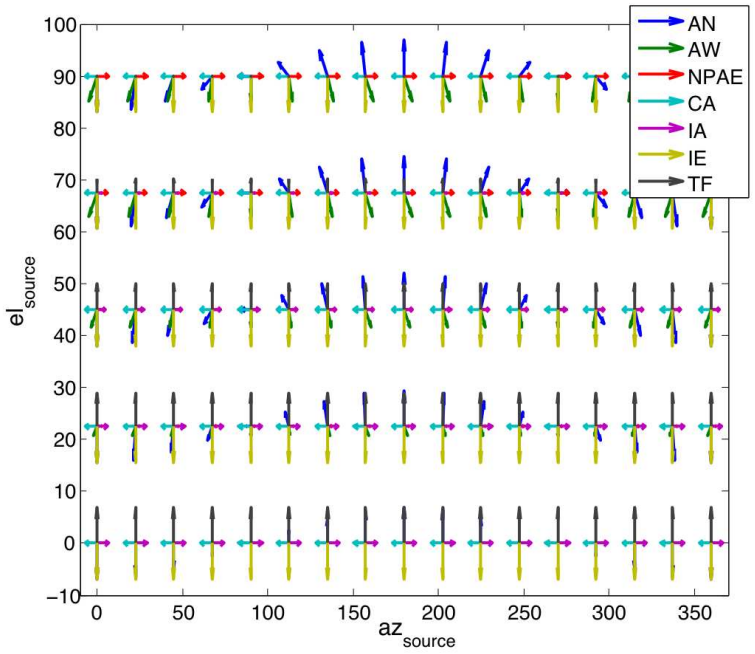

Figure 15.5: (Δaz, Δel) vectors as a function of (az_s, el_s) as predicted from the pointing model given by Eqs. (15.6) and (15.7). All the parameters AN, AW, etc. are taken to be equal to 10^{-5}. In reality, one has to understand that some parameters, such as the telescope flexure TF, will be negative in order to agree with its mechanical description.

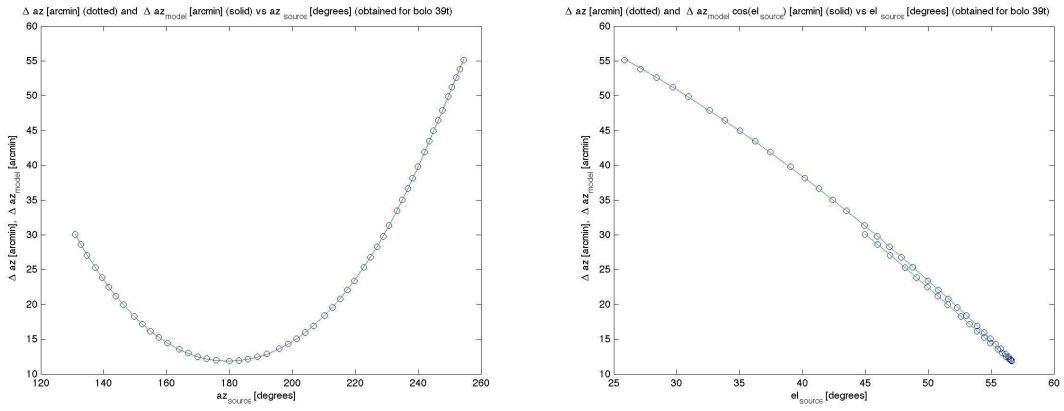

Figure 15.6: Δaz as a function of az_s (**left**) and el_s (**right**), read from the telescope encoder. Blue circles are estimated from the data and green solid lines are the fitted curves based on the proposed model, cf. Eqs. (15.6) and (15.7).

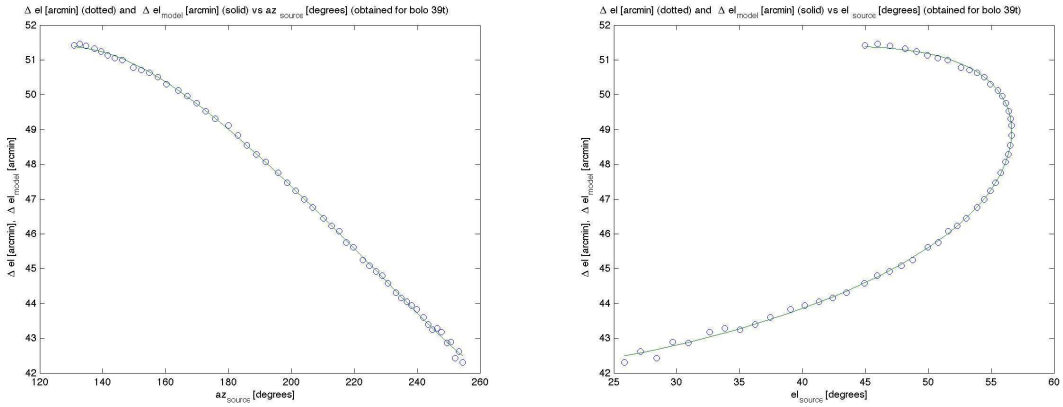

Figure 15.7: Same as Fig. 15.6 but showing Δel as a function of az_s and el_s.

15.2.3.3 Parameters estimation

I briefly explain the method used to estimate the parameters from the two quantities Δaz and Δel, which are both $1 \times N$ vectors, with N the number of observations (i.e. the number of (az_s, el_s) couples). Using a similar formalism as the one used in Part IV, in a different context, we set the data modeling **d** as

$$\mathbf{d} \equiv \begin{pmatrix} \Delta\text{az} \\ \Delta\text{el} \end{pmatrix} \equiv \mathbf{A}\ \mathbf{s} + n \tag{15.10}$$

where the pointing matrix **A** can be set as

$$\mathbf{A}^T \equiv \begin{bmatrix} -\sin(az_s(p_0))\sin(el_s(p_0)) & \dots & -\sin(az_s(p_{N-1}))\sin(el_s(p_{N-1})) & \cos(az_s(p_0)) & \dots & \cos(az_s(p_{N-1})) \\ -\cos(az_s(p_0))\sin(el_s(p_0)) & \dots & -\cos(az_s(p_{N-1}))\sin(el_s(p_{N-1})) & -\sin(az_s(p_0)) & \dots & -\sin(az_s(p_{N-1})) \\ \sin(el_s(p_0)) & \dots & \sin(el_s(p_{N-1})) & 0 & \dots & 0 \\ -1 & \dots & -1 & 0 & \dots & 0 \\ \cos(el_s(p_0)) & \dots & \cos(el_s(p_{N-1})) & 0 & \dots & 0 \\ 0 & \dots & 0 & -1 & \dots & -1 \\ 0 & \dots & 0 & \cos(el_s(p_0)) & \dots & \cos(el_s(p_{N-1})) \end{bmatrix}$$

where p_i is a parameter denoting the i^{th} observation. **A** is therefore a $2N \times 7$ matrix. In addition, the vector s we would like to estimate, is stored as

$$s^T \equiv [AN,\ AW,\ NPAE,\ CA,\ IA,\ AN,\ AW,\ IE,\ TF]\,. \tag{15.11}$$

The noise term n in Eq. (15.10) is not taken into account in this analysis. It could have been the misestimation of the source center in the map or a consequence of the assumption that the point source does not move in (RA, Dec). Consequently the $2N \times 2N$ noise covariance matrix,

$$\mathbf{N} \equiv \langle n^t\ n \rangle, \tag{15.12}$$

is taken to be the identity matrix. Finally, the vector $\mathbf{s}$ is estimated using the usual map-making equation, Eq. (10.7):

$$\mathbf{s} = \left(\mathbf{A}^T\mathbf{N}^{-1}\mathbf{A}\right)^{-1}\ \mathbf{A}^T\mathbf{N}^{-1}\,\mathbf{d} \tag{15.13}$$

$$= \left(\mathbf{A}^T\mathbf{A}\right)^{-1}\ \mathbf{A}^T\,\mathbf{d} \ \text{ under the assumption } \mathbf{N} = \mathbf{I_d}. \tag{15.14}$$

The potential degeneracies of the modeling can be studied by looking at the correlations between the different parameters. Eigen values and corresponding eigen vectors of the $\left(\mathbf{A}^T\mathbf{A}\right)$ matrix give us the necessary informations. Degeneracies or poor conditioning of specific combination of parameters (i.e. directions in the parameter space) result in singular modes of this matrix. In addition, the square roots of the diagonal terms of $(\mathbf{A}^T\mathbf{A})^{-1}$ give us a measurement of the errors made on the estimation of the parameters.

15.2.3.4 Star camera

In addition to the radio data, POLARBEAR is equipped with an optical camera, fixed on the boom of the telescope: following the same recipe explained above (but using optical data), this allows the collaboration to calibrate and cross-check the estimated pointing parameters.

The presented pointing reconstruction method, applied to real POLARBEAR data, gives satisfactory results and allows the collaboration to currently have errors $\lesssim 10$ arcsec after reconstruction.

15.3 Noise estimation

The estimation of the noise statistical properties is essential to reconstruct the maps. We usually expect a $1/f$ power spectrum for the noise contamination of the time stream, with a typical frequency $f_{knee} \sim 0.1 - 2$ Hz being driven by the atmospheric properties (stability of the water vapor column, wind, etc.).

I depict in Fig. 15.8 the reasoning I will follow in this section. I first simulate a TOD corresponding to a time stream which has the form given in Eq. (7.22), forgetting about the total intensity term. Second, after introducing a model for the noise, I estimate the noise parameters using a parametric maximum likelihood approach, similarly to the original idea of Ferreira and Jaffe (46). Finally, I reconstruct the TOD using this noise estimation.

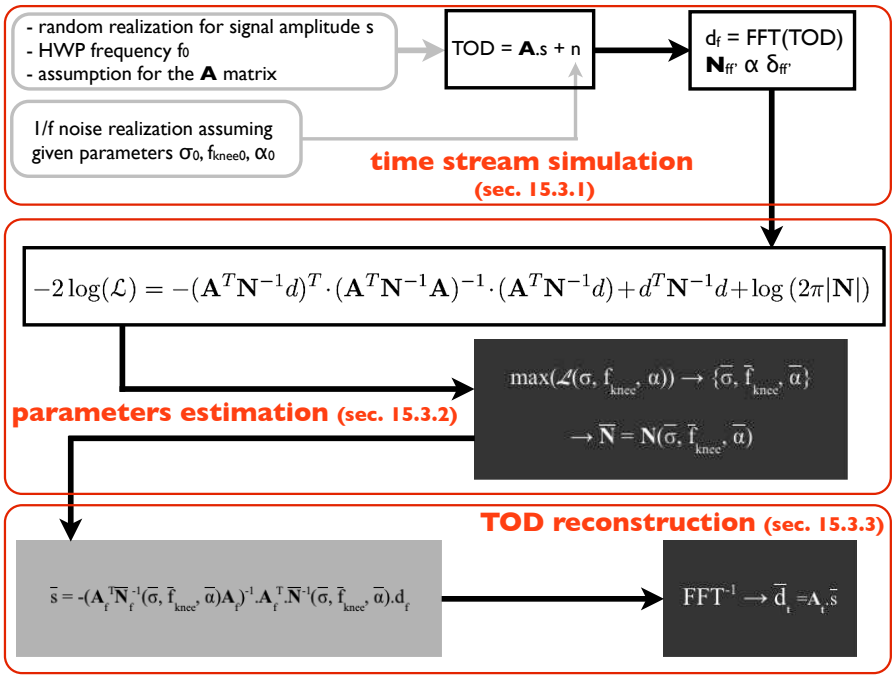

Figure 15.8: Scheme depicting the reasoning followed in section 15.3.

15.3.1 Simulation of a TOD

Following the results from the MAXIPOL experiment which had a smoothly rotating HWP, see Johnson et al. (68), I assume that the TOD can be written as a sum of height harmonics of the HWP frequency, say f_0, such that we can write

$$TOD(t) = \sum_{n=1}^{8} A_n cos(2n\pi f_0 t) + B_n sin(2n\pi f_0 t) + n(t), \tag{15.15}$$

where I drop the constant term, not modulated by the HWP, i.e. the total unpolarized intensity. The form of Eq. (15.15) does not correspond to the one we expect for POLARBEAR, in which case the HWP is stepped i.e. the cos and sin becomes function of the discrete HWP and sky angles. However, the presented method is generalizable to any parametrization of the TOD. Similarly to Eq. (15.10), we consider that the linear operation $\{A_n, B_n\} \mapsto TOD$ can be written using the operator $\mathbf{A}$ as

$$TOD = \mathbf{A}\ s + n, \tag{15.16}$$

where, following the specific parametrization of Eq. (15.15), we set the mixing matrix **A** as

$$\mathbf{A}^T \equiv \begin{bmatrix} cos(2\pi f_0 t_0) & \dots & cos(2\pi f_0 t_N) \\ sin(2\pi f_0 t_0) & \dots & sin(2\pi f_0 t_N) \\ cos(4\pi f_0 t_0) & \dots & cos(4\pi f_0 t_N) \\ \vdots & & \vdots \\ sin(16\pi f_0 t_0) & \dots & sin(16\pi f_0 t_N) \end{bmatrix}, \tag{15.17}$$

and the sky signal s as

$$s \equiv \begin{bmatrix} A_1 \\ B_1 \\ A_2 \\ \vdots \\ B_8 \end{bmatrix}. \tag{15.18}$$

In the simulation of the TOD, s is a random vector computed using some given arbitrary seeds[1]. In order to estimate the noise properties, we have to assume a model for this latter, simulate and add it to the time stream. Let us compute a $1/f$ noise realization in the frequency domain. The assumed power spectrum as a function of the white noise amplitude σ, the characteristic frequency f_{knee}, and the associated power law α is given by

$$P(\sigma, f_{knee}, \alpha, f) \equiv \sigma^2 \left(1 + \left(\frac{f_{knee}}{f}\right)^{\alpha}\right). \tag{15.19}$$

The considereded noise n_f is a random realization having the power spectrum written in Eq. (15.19). Writting

$$\mathbf{N}_{ff'} \equiv \langle n_f^T \, n_{f'} \rangle \tag{15.20}$$

$$= P(\sigma, f_{knee}, \alpha, f) \delta_f^{\ f'} \tag{15.21}$$

and considering a random vector $\xi_f \in \mathbb{C}$, normalized such that $\sum_f \xi_f^\dagger \, \xi_f = 1$, the simulated noise in frequency domain reads

$$\begin{aligned} n_f &= \sqrt{\mathbf{N}_{ff'}} \, \xi_{f'} \\ &= \sqrt{P(\sigma, f_{knee}, \alpha, f)} \times \xi_f. \end{aligned} \tag{15.22}$$

Finally, the simulated signal d_f computed in the frequency domain is given by

$$d_f = \sum_i \mathbf{A}_{fi} \, s_i + n_f \tag{15.23}$$

[1] I assumed a Gaussian probability law: the mean and standard deviation values are chosen so that the obtained signal is similar to what have been observed during the MAXIPOL flight, Johnson et al. (68).

where $\mathbf{A}_{fi}$ is the Fourier transform of the $\mathbf{A}$ matrix defined in Eq. (15.17). I depict in Fig. 15.9 a realization of d_t, i.e. the inverse Fourier transform of d_f coming from Eq. (15.23).

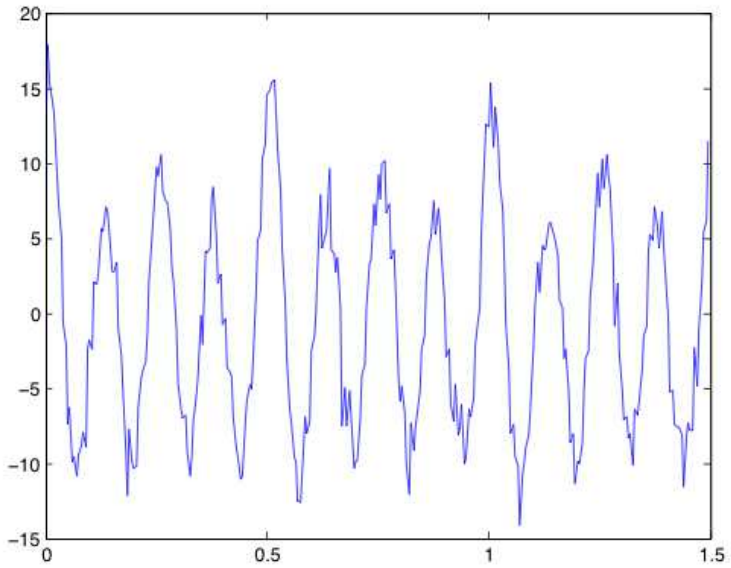

Figure 15.9: Example of a noisy TOD realization, assuming a signal (i.e. A_n and B_n in Eq. (15.15)) to noise (i.e. σ in Eq. (15.19)) ratio of 10. The y-axis shows the amplitude (arbitrary units) and the x-axis shows time (seconds).

15.3.2 Likelihood formalism for parameters estimation

Now, given a time stream d_t, we would like to estimate the noise parameters σ, f_{knee} and α. In order to do that, we compute the following likelihood (46)

$$-2\log(\mathcal{L}) = -(\mathbf{A}^T\mathbf{N}^{-1}d)^T\ (\mathbf{A}^T\mathbf{N}^{-1}\mathbf{A})^{-1}\ (\mathbf{A}^T\mathbf{N}^{-1}d) + d^T\mathbf{N}^{-1}d + \log\left(2\pi|\mathbf{N}|\right) \quad (15.24)$$

which is similar to Eq. (10.8), but, contrary to what we used to estimate the foregrounds scaling laws, I keep here the second and third terms in the r.h.s. which depend on $\mathbf{N}$ (and therefore on the studied parameters). In particular, $|\mathbf{N}|$ is the determinant of the matrix $\mathbf{N}$ and the $\log\left(2\pi|\mathbf{N}|\right)$ term comes from the normalization of $\mathcal{L}$. This latter contribution essential to have a non monotonic likelihood in the $\{\sigma, f_{knee}, \alpha\}$ space. Furthermore, in the time domain the noise covariance matrix would be Toeplitz if we assume the noise to be stationary. In fact, a stationarity in time domain implies a diagonal form in Fourier space, as it has been used in Eq. (15.21). Finally, $\mathcal{L}$ is a scalar and $\mathcal{L} \equiv \mathcal{L}(\sigma, f_{knee}, \alpha)$ because $\mathbf{N} \equiv \mathbf{N}(\sigma, f_{knee}, \alpha)$ (there is an implicit sum over time

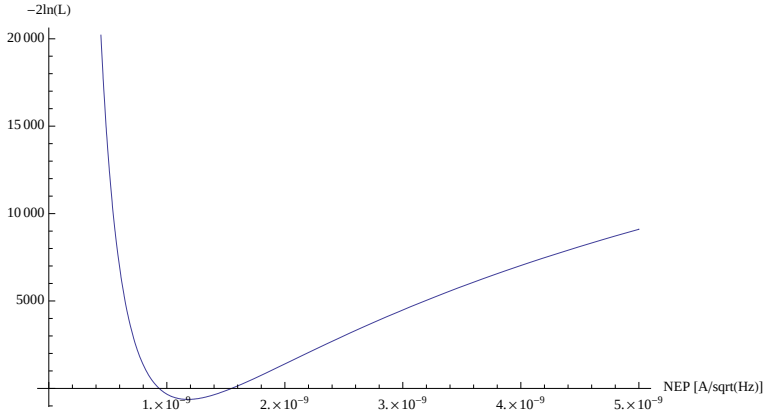

Figure 15.10: $-2\log(\mathcal{L})(\sigma)$ behavior for fixed values of the other parameters f_{knee} and α.

in Eq. (15.24)).

I depict in Fig. 15.10 the quantity $-2\log(\mathcal{L}(\sigma))$ for a given couple $(f_{knee},\ \alpha)$. The log term in the r.h.s. of Eq. (15.24) contributes at high σ and the $d^T\mathbf{N}^{-1}d$ term behaves as $\propto 1/\sigma^2$. This computation is made in frequency domain, such that the matrix $\mathbf{N}$ is diagonal, cf. Eq. (15.21). In the following, I will consider the full space of parameters, simulating the time stream d with chosen parameters $p_0 \equiv \{\sigma_0, f_{knee_0}, \alpha_0\}$. I show that the likelihood $\mathcal{L}(\sigma, f_{knee}, \alpha)$ reaches its maximum at the p_0 point. I use a combination of a Nelder-Mead and a BFGS quasi-newton algorithms, as implemented in MATHEMATICA, such that the routine estimates the extremum coordinates $\bar{p}$ as well as the Hessian matrix computed at this point. This latter, corresponding to the curvature of the likelihood at its maximum is used to compute likelihood contours, as shown in Fig. 15.11.

From this result, we can build an estimated noise correlation matrix $\bar{\mathbf{N}} \equiv \mathbf{N}(\bar{p})$, which will be used in the reconstructing process, as explained in the next paragraph.

15.3.3 Reconstructing the HWPSS

From the estimated noise correlation matrix $\bar{\mathbf{N}}$, we can get an estimation of the sky signal $\bar{s}$. Similarly to Eq. (10.7), the maximum likelihood for s is reached for

$$\bar{s} = (\mathbf{A}^T\bar{\mathbf{N}}^{-1}\mathbf{A})^{-1}\ \mathbf{A}^T\ \bar{\mathbf{N}}^{-1}d, \tag{15.25}$$

where I assume that the mixing/pointing matrix $\mathbf{A}$, expressed in Eq. (15.17), is perfectly known. $\bar{s}$ given by Eq. (15.25) corresponds to the best estimation of the unknown

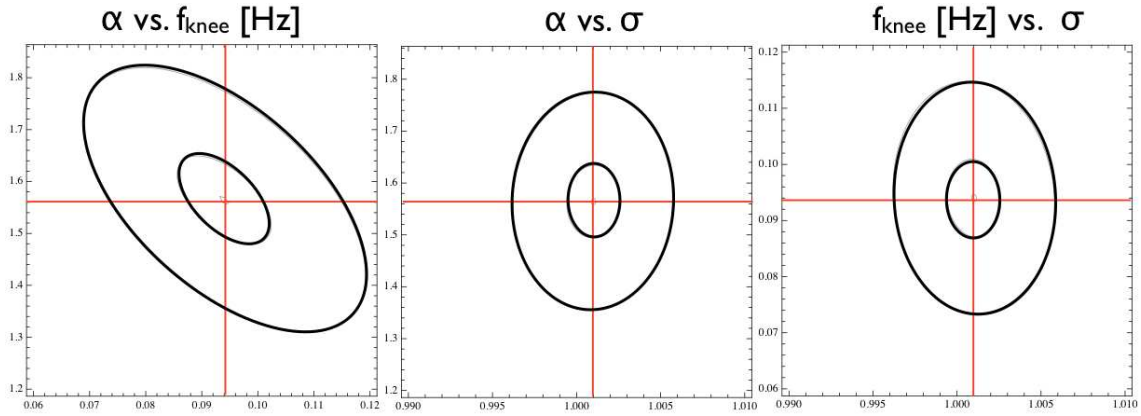

Figure 15.11: Typical contours (0.1σ, 1σ and 3σ) for the likelihood $\mathcal{L}(\sigma, f_{knee}, \alpha)$ for 3 different couples of parameters (and marginalized over the last parameter in each case): $\{\alpha, f_{knee}\}$ (**left panel**), $\{\alpha, \sigma\}$ (**middle panel**) and $\{f_{knee}, \sigma\}$ (**right panel**). In this particular case, the signal to noise ratio is 10 and the integration time is $T = 2^{11}$ sec ~ 30 min. The true values correspond to the red lines.

parameters we can get. I depict in the left panel of Fig. 15.12 an example of a reconstructed signal, compared to the simulated one. Corresponding power spectra are plotted in the right panel.

15.4 Optical systematics estimation

From the modeling of the time stream given in Eq. (7.41), it is possible to estimate some systematic amplitude through the estimation of parameters modeling, for instance, cross- and instrumental-polarization effects.

Let us write the raw time stream of a detector as

$$d \equiv \sum_i (\mathbf{H}_{tot})_{0i} S^i_{in} \tag{15.26}$$

$$\equiv \sum_i (\mathbf{H}\ \mathbf{C_p}\ \mathbf{I_p})_{0i} S^i_{in} \tag{15.27}$$

where $\mathbf{H_{tot}} \equiv \mathbf{H}\ \mathbf{C_p}\ \mathbf{I_p}$ is the full Mueller matrix, ideally describing all the optics, s is the true sky signal i.e. following the notation of chapter 7, $s = S_{in}(t) \equiv [I_{in}, Q_{in}, U_{in}, 0]^T$, and n is the noise. The term $(\mathbf{H_{tot}}\ s)_0$ is detailed in Eq. (7.41) and the index 0 stands for the fact that the considered detectors only measure a total power I: the full optical system "projects" the three Stokes parameters of the sky onto the unique Stokes parameter, the 0^{th} one in our formalism, measured by the detectors.

As it was the case for the noise estimation, section 15.3, we can optimize the likelihood $\mathcal{L}$ to estimate these parameters,

$$-\log(\mathcal{L}) = (d - \mathbf{A}\ s)^T \mathbf{N}^{-1} (d - \mathbf{A}\ s) \tag{15.28}$$

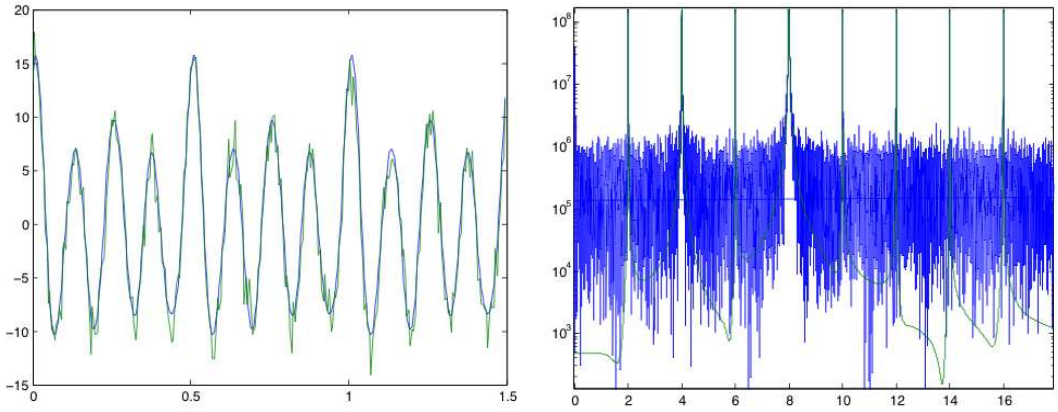

Figure 15.12: **Left panel**: example of a reconstructed signal (blue curve) from a simulated, noisy one (green curve). The units are amplitude [arbitrary units] vs time [sec]. The integration time is $T = 2^{11}\, sec \sim 30$ minutes and the signal to noise ratio is 10. **Right panel**: power spectra of the simulated signal (blue) and the reconstructed one (green). Units are power [arbitrary units] vs. frequency [Hz]. Here the first harmonic (HWP frequency) is set to be $f_0 = 2$ Hz.

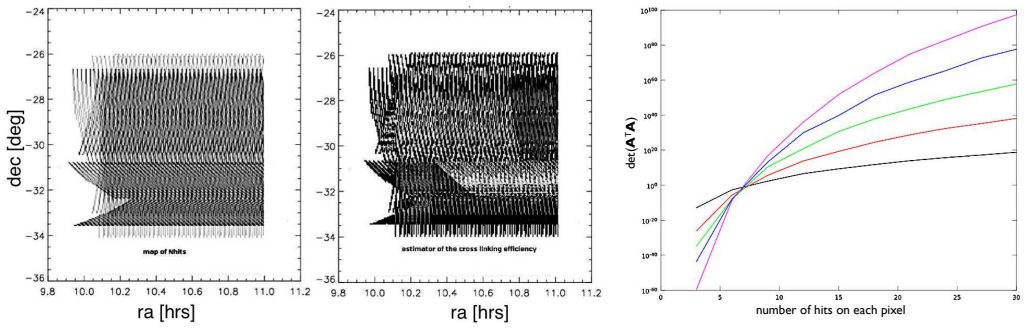

Figure 15.13: **Left panel**: number of hits per pixel obtained after 10 hours of a POLARBEAR-like simulated scan where we switch the position of the center of the scan each hour. **Middle panel**: Cross-linking efficiency, as measured by the figure of merit Λ defined in Eq. (15.31). White correspond to $\Lambda = 0$ and black to $\Lambda = 1$. **Right panel**: value of $\det\left(\mathbf{A}^T\,\mathbf{A}\right)$, as a function of the number of hits per pixel of the sky.

where $\mathbf{N} \equiv \langle n\ n^T \rangle$ is the noise covariance matrix and $\mathbf{A}\ s \equiv (\mathbf{H_{tot}}\ s)_0$ where the pointing matrix $\mathbf{A}$ could be written as

$$\mathbf{A} \equiv \begin{bmatrix} a & b & c & 0 & \dots & \dots & \dots & \dots & 0 \\ 0 & 0 & 0 & a' & b' & c' & 0 & \dots & \vdots \\ \vdots & \vdots & \vdots & \ddots & \ddots & \ddots & \ddots & 0 & 0 \\ 0 & \dots & \dots & \dots & 0 & \dots & a'' & b'' & c'' \end{bmatrix} \tag{15.29}$$

which goes from a time domain sky signal $s(t) = [I(t), Q(t), U(t)]$ to a time domain time stream $d(t)$. The blocks $[a, b, c]$ and $[a', b', c']$ differs mainly due to sky or HWP rotation. In the specific model we consider, cf. Eq. (7.41), we have

$$\begin{aligned} a &\equiv \frac{1}{2}\left\{(p_x^2 + p_y^2)(g_1^2 + g_2^2) + \right. \\ &\qquad \left. (p_x^2 - p_y^2)(g_1^2 - g_2^2)\left[(1-2\epsilon)\cos(4\rho) - 2\sqrt{(1-\epsilon)\epsilon}\cos(\psi)\sin(4\rho)\right]\right\} \\ b &\equiv \frac{1}{4}\left\{(p_x^2 + p_y^2)(g_1^2 - g_2^2) \right. \\ &\qquad \left. (p_x^2 - p_y^2)(g_1^2 + g_2^2)\left[(1-2\epsilon)\cos(4\rho) - 2\sqrt{(1-\epsilon)\epsilon}\cos(\psi)\sin(4\rho)\right]\right\} \\ c &\equiv 2g_1 g_2 \left(p_x^2 - p_y^2\right)\frac{1}{4}\left\{-2\sqrt{(1-\epsilon)\epsilon}\cos(4\rho)\cos(\psi - \phi)\right. \\ &\qquad \left. + \left[1 - \epsilon\left(1 - \cos(2\psi - \phi)\right)\right]\cos(\phi)\sin(4\rho)\right\} \end{aligned} \tag{15.30}$$

In collaboration with C. Pelletier, master student, we simulated POLARBEAR-like time streams $d(t)$ and implemented routines to estimate the systematic effects parameters hidden in $\mathbf{A}$.

One should notice that $\left(\mathbf{A}^T\mathbf{A}\right)$ has singular modes if the telescope do not pass at least three times on the same sky pixel with three different attack angles i.e. if the first block in Eq. (15.29) does not have at least three other different blocks below. This simply means that we should have at least three informations for one pixel of the sky to recover its Stokes parameters I, Q and U. Moreover, the better will be the number of attack angles, also called cross-linking, the better the problem will be conditioned, i.e. the more regular will be the eigen modes of $\left(\mathbf{A}^T\mathbf{A}\right)$. Ponthieu (111) introduced a figure of merit for the cross-linking given by

$$\Lambda_p \equiv \langle \cos(2\alpha_p) \rangle^2 + \langle \sin(2\alpha_p) \rangle^2 \tag{15.31}$$

where α_p is the attack angle on the pixel p. $\langle\ \rangle$ are the average over all the observations of the given pixel p and a perfect scan strategy would lead to $\Lambda_p = 0$ for every pixel of the map. However, having a small Λ is necessary but not sufficient: in fact, one should look rather at the conditioning of the full $\left(\mathbf{A}^T\mathbf{A}\right)$ matrix. I depict in Fig. 15.13 an illustration of a typical N_{hits} and Λ maps as obtained by a POLARBEAR-like experiment

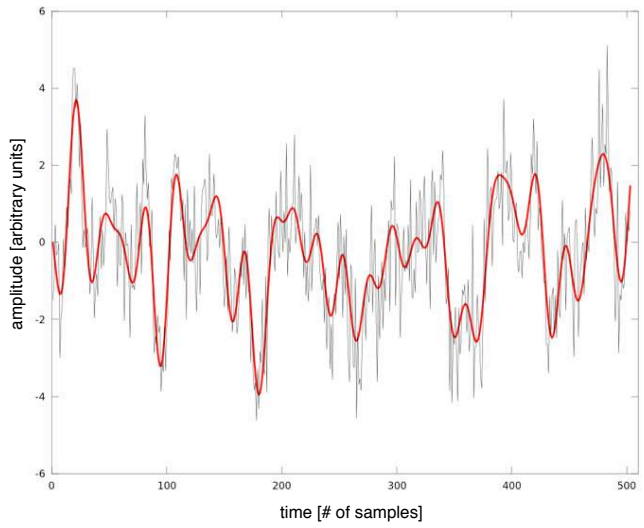

Figure 15.14: Simulated time stream without noise (red) and with a $1/f$ noise contamination (grey), assuming a signal-to-noise ratio of 1, $\alpha = 1.5$ and a $f_{knee} = 1$ Hz.

after a 10 hours scan. In the right panel of this figure is also shown how the quantity $\det\left(\mathbf{A}^T\ \mathbf{A}\right)$ behaves as a function of the number of scans over the whole patch of sky: this gives a rough idea of the conditioning of the matrix $\mathbf{A}^T\ \mathbf{A}$ as a function of the number of observations we have per pixel.

As a first approach of the problem, I assume that the sky signal is perfectly known and simulate it as

$$s^{(i)}(t) \equiv \sum_{j=1}^{8} A_n^{(i)} \cos\left(2\pi n f^{(i)} t + \phi_n^{(i)}\right) \tag{15.32}$$

where $s^{(i)}$ is one of the three Stokes parameters. $A_n^{(i)}$, $f^{(i)}$ and $\phi_n^{(i)}$ are random constants, but we ensure that the Q/U amplitudes are ~ 10 times lower than I, as it is roughly the case for CMB observations. In addition, we assume that the time stream is contaminated by a $1/f$ noise, cf. Eq. (15.19). I depict in Fig. 15.14 a simulated time stream, based on the Eqs. (15.30) and (15.32).

To illustrate the results of the method, I depict in Fig. 15.15 the likelihood curves defined in Eq. (15.28) for two varying parameters, fixing the others to their "true" values, i.e. the ones we use for the simulation. The left panel represents the likelihood surface in the parameters space describing the instrumental-polarization. The likelihood is almost Gaussian, and this can be analytically checked using Eq. (15.30). The right panel shows the likelihood in the parameters space modeling the cross-polarization. This time, the

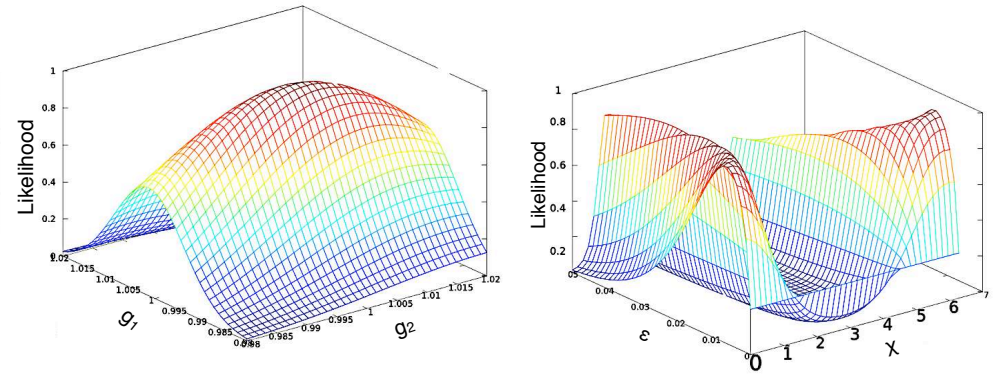

Figure 15.15: **Left panel**: likelihood surface defined in Eq. (15.28) for one detector (assuming $p_y = 1$ and $p_x = 0$) as a function of the two parameters modeling the instrumental parameters g_1 and g_2 ($\phi = 0$ here). Other parameters are fixed to their true values, i.e. the ones we used to simulate the time stream. The maximum of the surface is reached for the true (g_1, g_2) couple. **Right panel**: same as left panel but for the two parameters modeling the cross-polarization, ϵ and χ. We see the periodicity of the surface along the χ direction: this is due to the fact that only periodic functions of χ are involved in $\mathbf{A}$.

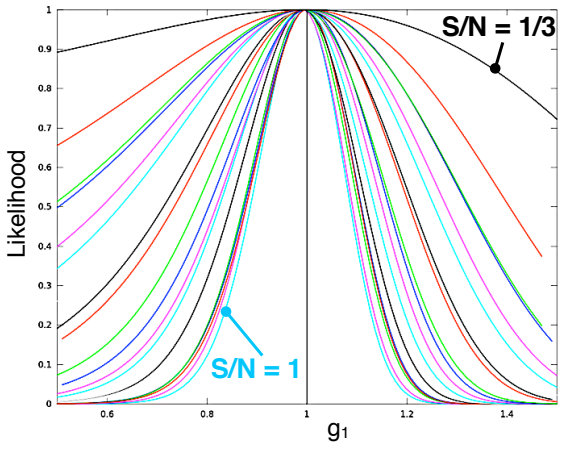

Figure 15.16: Effect of the noise levels on the shape of the likelihood along g_1 (all the other parameters being fixed to their true value). We assume here a $1/f$ noise with $\alpha = 1.5$ and $f_{knee} = 1$ Hz. The inner curve is obtained for a signal-to-noise ratio of 1 and the outer curve for a ratio of 1/3. We clearly see that a larger noise amplitude result in a more relax constraint on the parameters estimation.

surface is more complex and this is partially due to the involvement of $\sqrt{\epsilon}$ and periodic functions of χ in Eqs. (15.30). In addition, an increase of the noise results in a decrease of the estimation accuracy: this statement is illustrated in Fig. 15.16 where the likelihood as a function of g_1 is depicted for various noise levels.

Of course, in reality, we will not know the sky signal $s(t)$ and we should rather consider the likelihood given in Eq. (15.24) which is marginalized over the sky signal, see Stompor et al. (133). In our case,

$$-\log(\mathcal{L}) \propto (\mathbf{A}^T\mathbf{N}^{-1}d)^T\ (\mathbf{A}^T\mathbf{N}^{-1}\mathbf{A})^{-1}\ (\mathbf{A}^T\mathbf{N}^{-1}d) \tag{15.33}$$

could have important computational needs, especially for the inversion of $(\mathbf{A}^T\mathbf{N}^{-1}\mathbf{A})^{-1}$. This work was still in progress in July 2012.

15.5 Filtering atmosphere

As described in chapter 8, atmospheric contamination dominates ground-based CMB experiments measurements. Data analysts have to find optimal filters in order to remove this contamination without taking away the cosmological informations encoded in the time streams.

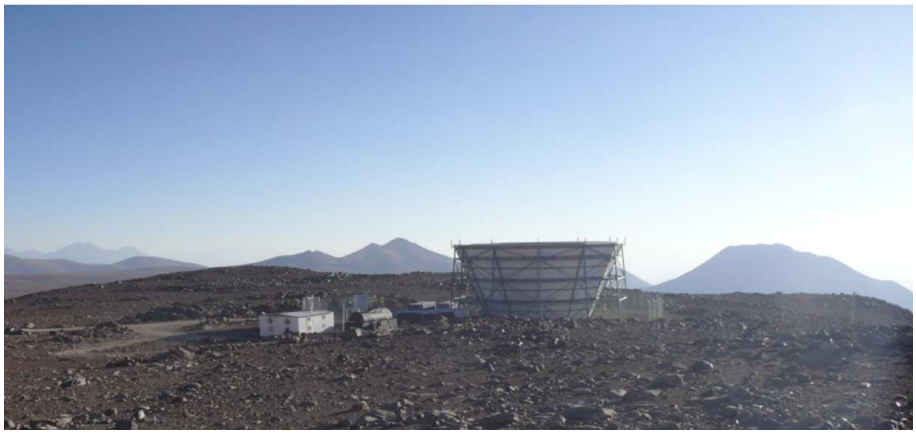

Figure 15.17: Picture of the Atacama Cosmology Telescope, located at the Chajnantor plateau, 100 meters away from the POLARBEAR site. From ophelia.princeton.edu.

First, I present in paragraph 15.5.1 the filtering technique adopted by the team of the Atacama Cosmology Telescope (ACT), a CMB experiment located ~ 100 meters away from the POLARBEAR site and therefore suffering from the same type of atmosphere. Second, in paragraph 15.5.2, I explore another approach and formulation to remove atmospheric contamination, which would have to be tested on the coming POLARBEAR data.

15.5.1 Large low-frequency modes subtraction

As presented in Das et al. (29), the ACT collaboration (Fig. 15.17) considered the following data modeling

$$d = \mathbf{A}\, s + \mathbf{P}\, c + n \tag{15.34}$$

where $\mathbf{A}$ is the pointing matrix, s the sky signal, $\mathbf{P}$ are (assumed constant) patterns of correlation across the array and c are the time streams associated with each pattern in $\mathbf{A}$. The ACT collaboration found that taking the array patterns $\mathbf{A}$ to be the eigenvectors corresponding to the 10 largest eigenvalues of the data covariance matrix for each 15−minutes chunk of TOD worked well for correlated noise rejection.

For the 218 GHz data, Das et al. (29) claims that substantial atmospheric power remains with the previous technique so that they adapt the removal for this specific channel: first, for each TOD they take the band-limited data between 0.25 and 4 Hz, find the eigenvalues and eigenvectors of the corresponding data covariance matrix, and keep all modes with eigenvalues larger than ~ 12 times the median eigenvalue: they typically find between 30 and 50 modes. Then, they create the covariance matrix from the data high-passed above 4 Hz, project out the modes already found in the 0.25-4 Hz band, and keep all remaining modes with eigenvalue larger than ~ 6 times the median. They typically find 1 or 2 additional modes in this step. Of the several different mode removal schemes they tried, they found that this fairly aggressive one gave the best signal-to-noise on intermediate and small angular scales, where the 218 GHz data are most valuable, at the price of worse signal-to-noise and slower convergence of the mapper on large scales, see section C.2.3. Since the method estimates both the correlated modes and the map of the sky simultaneously, mode removal does not bias the maps, although it makes some sky map modes noisier.

The atmospheric contamination in the case of POLARBEAR, is well illustrated in the left panel of Fig. 15.18, a screen shot of the waferview software[1] showing in real time the rms of the time streams for each detector across the focal plane. We clearly see an atmospheric structure moving across the field of view of the telescope, giving rise to large correlations in time (between samples t and t') and space (between detectors i and j). Therefore, another idea to filter the atmospheric contamination could be to

[1] Python-based code developed by the POLARBEAR collaboration.

consider the full data covariance matrix defined as

$$\mathbf{D} \equiv \mathbf{D}_{tt'}^{ij} \equiv \mathbf{D}_{\lambda\lambda'} \quad \text{where } \lambda \text{ is a unique combination of i and t} \tag{15.35}$$

$$\equiv \langle d_t^i d_{t'}^{j\,\dagger} \rangle \tag{15.36}$$

$$= \begin{bmatrix}
\langle d_0^0 d_0^{0\,\dagger}\rangle & \langle d_0^0 d_0^{1\,\dagger}\rangle & \dots & \langle d_0^0 d_0^{n_{dets}\,\dagger}\rangle & \dots & \langle d_0^0 d_{t'}^{j\,\dagger}\rangle & \dots & \langle d_0^0 d_{n_{samples}}^{n_{dets}\,\dagger}\rangle \\
\langle d_0^1 d_0^{0\,\dagger}\rangle & \ddots & & \vdots & & \vdots & & \vdots \\
\vdots & & \ddots & \vdots & & \vdots & & \vdots \\
\langle d_0^{n_{dets}} d_0^{0\,\dagger}\rangle & \dots & \dots & \langle d_0^{n_{dets}} d_0^{n_{dets}\,\dagger}\rangle & & \vdots & & \vdots \\
\langle d_1^0 d_0^{0\,\dagger}\rangle & & & & & \vdots & & \vdots \\
\langle d_1^1 d_0^{0\,\dagger}\rangle & & & & & \vdots & & \vdots \\
\vdots & & & & & \vdots & & \vdots \\
\vdots & & & & & \vdots & & \vdots \\
\langle d_t^i d_0^{0\,\dagger}\rangle & \dots & \dots & \dots & \dots & \langle d_t^i d_{t'}^{j\,\dagger}\rangle & & \vdots \\
\vdots & & & & & & \ddots & \vdots \\
\langle d_{n_{samples}}^{n_{dets}} d_0^{0\,\dagger}\rangle & \dots & \dots & \dots & \dots & \dots & \dots & \langle d_{n_{samples}}^{n_{dets}} d_{n_{samples}}^{n_{dets}\,\dagger}\rangle
\end{bmatrix}$$

where the number of samples, $n_{samples} \sim 10^5$ for a 15 minutes TOD and $n_{dets} \sim 10^3$ in the case of the POLARBEAR experiment. A schematic representation of this matrix is depicted in the right panel of Fig. 15.18. In order to remove the biggest modes affecting the data at low frequencies we could consider only the data covariance in Fourier space and diagonalize it for frequencies verifying $f, f' < 5 - 10$ Hz, which "reduces" the problem to a matrix of size $\sim 10^9 \times 10^9$. The implementation of this approach is obviously computationally challenging.

15.5.2 Exploration of the analytical expressions describing atmospheric patterns across the focal plane

We model the time stream by

$$d_\beta = \mathbf{A}_{\beta p}\, s_p + \mathbf{B}_{\beta a}\, o_a + n_\beta \tag{15.37}$$

where

- d_β corresponds to the time stream, β being the index such that

$$\beta \equiv \beta(\#det, sample) = (n_{det} - 1) \times sample + \#det, \tag{15.38}$$

  of length $n_{obs}\, n_{det}$

- s_p is the sky (e.g. CMB) signal vector of length n_{pix},

- $\mathbf{A}_{\beta p}$ is the pointing matrix which projects from the sky pixels s_p to the time domain. It is of size $n_{obs}\, n_{det} \times n_{pix}$,

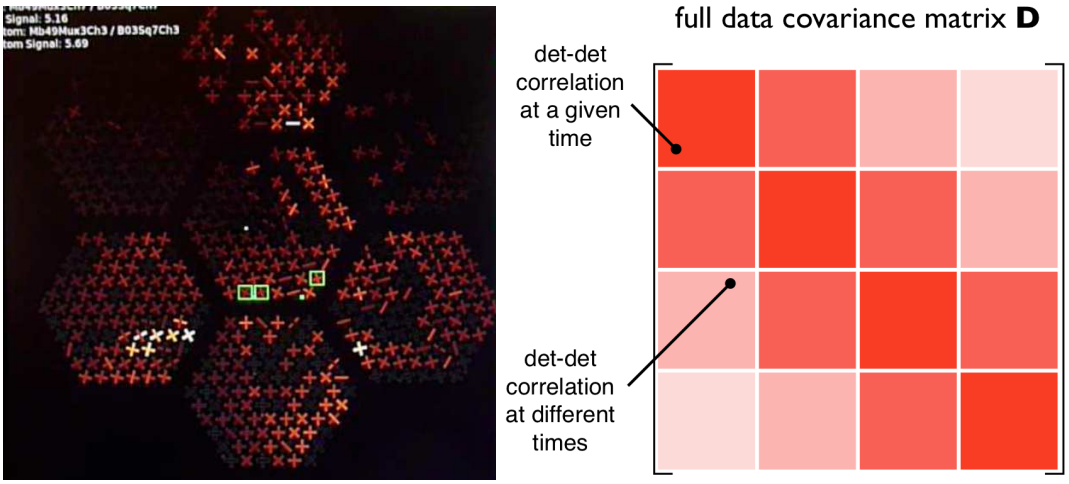

Figure 15.18: **Left panel**: screenshot of our POLARBEAR software called "waferview" which allows the field team to monitor the time streams of the bolometers in real time. Here we see, in red scale, the rms value of the time streams across the array: we clearly see atmospheric fluctuations going through the detectors. **Right panel**: schematic representation of the full data covariance matrix given in Eq. (15.36). Correlations between detectors due to atmosphere are high for a given sample (i.e. given block) and decrease as a function of time.

- o_a is the 'offset' vector of length n_{atm}. This latter quantity is the assumed number of atmosphere realizations i.e. if we assume that the atmosphere is a constant signal for all the detectors during a period Δt (homogeneous with a number of samples), we have

$$n_{atm} \equiv \frac{n_{obs}}{\Delta t} \tag{15.39}$$

- $\mathbf{B}_{\beta a}$ is the matrix which projects from the atmosphere contamination amplitude o_a to the time domain. It is of size $n_{obs}\ n_{det}\ \times\ n_{atm}$,
- n is the noise vector of size $n_{obs}\ n_{det}$

By writing Eq. (15.37) as

$$d_\beta = [\mathbf{A}_{\beta p}\ ,\ \mathbf{B}_{\beta a}] \begin{bmatrix} s_p \\ o_a \end{bmatrix} + n_\beta \tag{15.40}$$

$$\equiv \mathbf{\Lambda}_{\beta i}\, r_i + n_\beta \tag{15.41}$$

If we set $\mathbf{N} \equiv \langle n\ n^T \rangle$, one can write

$$(\mathbf{\Lambda}^T \mathbf{N}^{-1} \mathbf{\Lambda}) = \begin{bmatrix} \mathbf{A}^T\mathbf{N}^{-1}\mathbf{A} & \mathbf{A}^T\mathbf{N}^{-1}\mathbf{B} \\ \mathbf{B}^T\mathbf{N}^{-1}\mathbf{A} & \mathbf{B}^T\mathbf{N}^{-1}\mathbf{B} \end{bmatrix} \tag{15.42}$$

$$\equiv \begin{bmatrix} (\mathbf{\Lambda}^T\mathbf{N}^{-1}\mathbf{\Lambda})_{ss} & (\mathbf{\Lambda}^T\mathbf{N}^{-1}\mathbf{\Lambda})_{so} \\ (\mathbf{\Lambda}^T\mathbf{N}^{-1}\mathbf{\Lambda})_{os} & (\mathbf{\Lambda}^T\mathbf{N}^{-1}\mathbf{\Lambda})_{oo} \end{bmatrix}. \tag{15.43}$$

A simple computation of $\log(\mathcal{L})$ gives us the best estimations $\tilde{s}$ and $\tilde{o}$, respectively for s and o, which read

$$\begin{cases} \tilde{s} &= \left(\mathbf{A}^T\mathbf{N}^{-1}\mathbf{A} - \mathbf{A}^T\mathbf{N}^{-1}\mathbf{B}\ \left(\mathbf{B}^T\mathbf{N}^{-1}\mathbf{B}\right)^{-1}\ \mathbf{B}^T\mathbf{N}^{-1}\mathbf{A}\right)^{-1} \\ & \qquad\qquad \left(-\mathbf{A}^T\mathbf{N}^{-1}\mathbf{B}\ \left(\mathbf{B}^T\mathbf{N}^{-1}\mathbf{B}\right)^{-1}\ \mathbf{B}^T\mathbf{N}^{-1}\ d + \mathbf{A}\mathbf{N}^{-1}\ d\right) \\ \tilde{o} &= \left(\mathbf{B}^T\mathbf{N}^{-1}\mathbf{B}\right)^{-1}\ \left(\mathbf{B}^T\mathbf{N}^{-1}\ d - \left(\mathbf{B}^T\mathbf{N}^{-1}\mathbf{A}\right)\ \tilde{s}\right) \end{cases}$$

Considering one year of observation with a sampling rate ~ 200 Hz, with an assumed $\Delta t \ \sim \ 10 \sim 10^3$ samples sec, cf. Eq. (15.39), we typically have

$$n_{pix} \ \sim \ 10^4 \tag{15.44}$$
$$n_{obs} \ \sim \ 10^9 \tag{15.45}$$
$$n_{det} \ \sim \ 10^3 \tag{15.46}$$
$$n_{atm} \ \sim \ 10^6, \tag{15.47}$$

so that the sizes of the main matrices are

$$\text{size}\,(d_\beta) \ \sim \ 10^{12} \tag{15.48}$$
$$\text{size}\,(\mathbf{A}) \ \sim \ 10^{12} \tag{15.49}$$
$$\text{size}\,(\mathbf{B}) \ \sim \ 10^{12} \tag{15.50}$$

Computation $\mathbf{A}^T\mathbf{N}^{-1}\mathbf{A}$

Following the definitions, $\mathbf{A}^T\mathbf{N}^{-1}\mathbf{A}$ is a $(n_{pix} \times n_{pix})$ matrix and the non-zero terms are given by

$$\left(\mathbf{A}^T\mathbf{N}^{-1}\mathbf{A}\right)_{pp'} = \sum_{k\in K_p} \sum_{l\in L_{p'}} \mathbf{N}^{-1}_{kl} \tag{15.51}$$

where K_p ($L_{p'}$) is the collection of t (t') indices corresponding to the observation of the p (p') pixel.

Computation $\mathbf{B}^T\mathbf{N}^{-1}\mathbf{B}$

$\mathbf{B}^T\mathbf{N}^{-1}\mathbf{B}$ is a $(n_{atm} \times n_{atm})$ matrix and the non-zero terms are given by

$$\left(\mathbf{B}^T\mathbf{N}^{-1}\mathbf{B}\right)_{aa'} = \sum_{k=a\ \Delta t\ n_{det}}^{(a+1)\ \Delta t\ n_{det}} \ \sum_{l=a'\ \Delta t\ n_{det}}^{(a'+1)\ \Delta t\ n_{det}} \mathbf{N}^{-1}_{kl} \tag{15.52}$$

Computation $\mathbf{A}^T\mathbf{N}^{-1}\mathbf{B}$

$\mathbf{A}^T\mathbf{N}^{-1}\mathbf{B}$ is a $(n_{pix} \times n_{atm})$ matrix and the non-zero terms are given by

$$\left(\mathbf{A}^T\mathbf{N}^{-1}\mathbf{B}\right)_{pa'} = \sum_{k \in K_p} \sum_{l=a'\ \Delta t\ n_{det}}^{(a'+1)\ \Delta t\ n_{det}} \mathbf{N}_{kl}^{-1} \tag{15.53}$$

Computation $\mathbf{B}^T\mathbf{N}^{-1}\mathbf{A}$

$\mathbf{B}^T\mathbf{N}^{-1}\mathbf{A}$ is a $(n_{atm} \times n_{pix})$ matrix and the non-zero terms are given by

$$\left(\mathbf{B}^T\mathbf{N}^{-1}\mathbf{A}\right)_{ap'} = \sum_{l=a\ \Delta t\ n_{det}}^{(a+1)\ \Delta t\ n_{det}} \sum_{l \in L_p} \mathbf{N}_{kl}^{-1} \tag{15.54}$$

Noise covariance matrix computation

I assume an effective $1/f$ noise such that, in frequency domain,

$$\begin{aligned} \mathbf{N}_{ff'} &\equiv \mathbf{N}_{ff'}(\sigma, f_{knee}, \alpha) & (15.55)\\ &= \sigma^2 \left(1 + \left(\frac{f}{f_{knee}}\right)^{\alpha}\right) \delta_f^{f'}. & (15.56) \end{aligned}$$

I introduce the "Fourier" operator $\mathbf{F}$ such that

$$\mathbf{N}_{tt'} \equiv \sum_{ff'} \mathbf{F}^{\dagger}{}_t^{\ f}\ \mathbf{N}_{ff'}\ \mathbf{F}_{t'}^{\ f'}. \tag{15.57}$$

Moreover, $\mathbf{F}$ can be explicitly written down as, for all the frequencies f and times t

$$\mathbf{F}_{tf} \equiv e^{2i\pi ft}. \tag{15.58}$$

Working in frequency domain is useful for the implementation of such problem, because it reduces computational power needs: the stationarity in time of the noise result in a Toeplitz $\mathbf{N}_{tt'}$ matrix, which lead to a diagonal $\mathbf{N}_{ff'}$, i.e.

$$\begin{aligned} \mathbf{N}_{ff'} &= \sum_{tt'} \mathbf{F}^{\dagger}{}_f^{\ t}\ \mathbf{N}_{tt'}\ \mathbf{F}_{f'}^{\ t'} & (15.59)\\ &\propto \delta_{ff'}. & (15.60) \end{aligned}$$

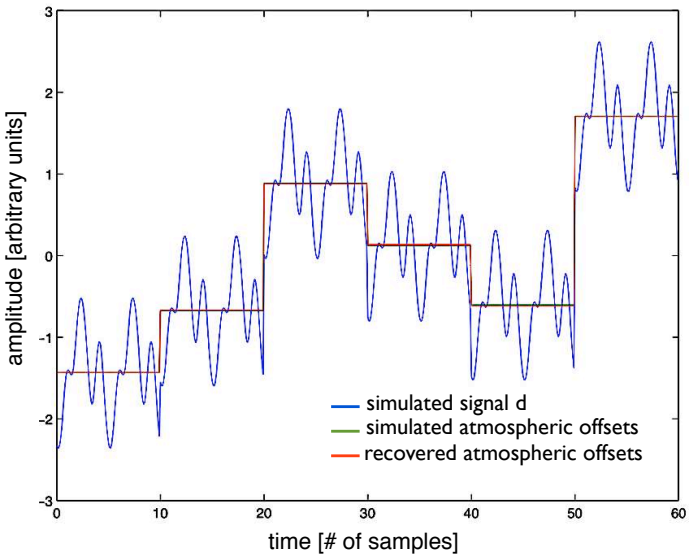

Figure 15.19: Illustration of a data realization d, following Eq. (15.61), including the simulated and recovered atmospheric signals, respectively o and $\tilde{o}$, in a case without noise.

Noise-free case

In this case, Eq. (15.37) becomes

$$d_\beta = \mathbf{A}_{\beta p}\, s_p + \mathbf{B}_{\beta a}\, o_a. \tag{15.61}$$

The noise covariance matrix is therefore the identity matrix, meaning that the equations we have to solve for $\tilde{s}$ and $\tilde{o}$ read

$$\begin{cases} \tilde{s} &= \left(\mathbf{A}^T\mathbf{A} - \mathbf{A}^T\mathbf{B}\ \left(\mathbf{B}^T\mathbf{B}\right)^1\ \mathbf{B}^T\mathbf{A}\right)^{-1}\ \left(-\mathbf{A}^T\mathbf{B}\ \left(\mathbf{B}^T\mathbf{B}\right)^{-1}\ \mathbf{B}^T\, d + \mathbf{A}\, d\right) \\ \tilde{o} &= \left(\mathbf{B}^T\mathbf{B}\right)^{-1}\ \left(\mathbf{B}^T\, d - \left(\mathbf{B}^T\mathbf{A}\right)\ \tilde{s}\right) \end{cases}$$

where d is given by equation 15.61.

I depict in Fig. 15.19 an illustration of a simulated time stream d as well as the simulated and recovered atmospheric offsets, respectively o and $\tilde{o}$. Residuals, denote Δ_X, between the estimated sky (offset) signal and the true sky (offset) signal, i.e.

$$\Delta_s \equiv \tilde{s} - s - \langle s \rangle \tag{15.62}$$

$$\Delta_o \equiv \tilde{o} - o \tag{15.63}$$

are depicted in the two panels of Fig. 15.20. These results simply illustrate that the algebra we derived in previous equations is working.

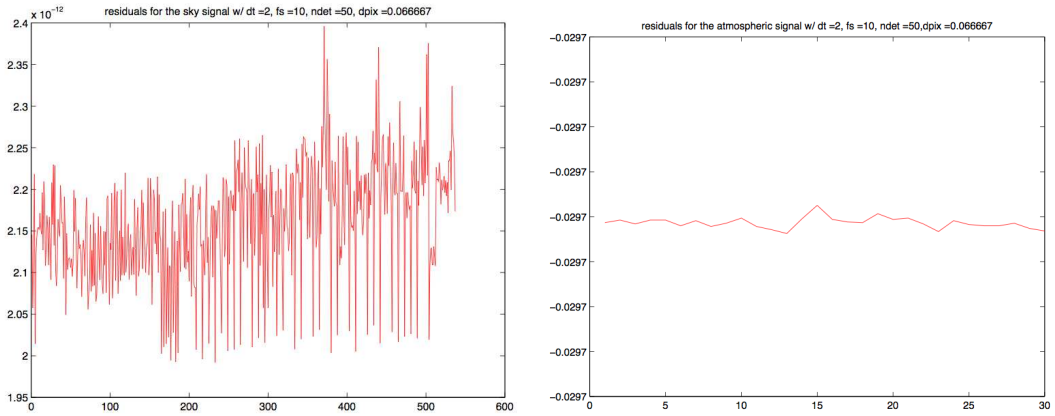

Figure 15.20: **Left panel**: residuals Δ_s, defined in Eq. (15.62), as a function of the sky pixel number i.e. the index p in Eq. (15.61). rms of the signal is $\sim 10^{-12}$. **Right panel**: residuals Δ_o, defined in Eq. (15.63), as a function of the "atmosphere" number i.e. the index a in Eq. (15.61). The mean value of the atmospheric residuals corresponds to the sky signal offset.

15.5.3 Perspectives

I presented in this section the filtering technique adopted by the team of the Atacama Cosmology Telescope (ACT), and explored another approach and formulation to remove atmospheric contamination, which would have to be tested on the coming POLARBEAR data. Although the first method have shown convincing results, e.g. Das et al. (29), the other formulations have only been demonstrated on non-realistic toy data. At the time of writing this thesis, the POLARBEAR collaboration filters out atmosphere contamination using polynomials, fitted to the time stream, on each subscan (i.e. left- or right-only motion of the telescope).

I imagine several perspectives for the work presented in chapter 8 and section 15.5. First, a quantity of interest which could be studied in the near future is the full data covariance matrix, written $\mathbf{D}$ in Eq. (15.35), so that we have access to the level of correlation across the focal plane and are able to check if the simulations presented in chapter 8 are reasonable. Second, the implementation of a parametric maximum-likelihood method, in which the parametrization follows the new formulation of the Church's model, could also be an approach for filtering atmospheric emission. Finally, the destriping-like method, as described in paragraph 15.5.2, has to be tested on real data and we should evaluate its performances as compared to other techniques.

15.6 Power spectra and cosmological parameters estimations

This section has not been a part of my PhD work, but I think it is worth mentioning the final steps of the pipeline to access to the main goals of the CMB experiments such as POLARBEAR, that is to say the extraction of cosmological informations from the CMB maps.

Given a CMB map, s_p, and its pixel-pixel noise correlations $\mathbf{N}_{pp'}$, the likelihood $\mathcal{L}$ of the data given the corresponding angular power spectra C_ℓ (under the assumption of a Gaussian, azimuthally symmetric CMB and a uniform Bayesian prior) can be expressed, see Borrill (18), as

$$-2\log(\mathcal{L}) = s^T\mathbf{D}^{-1}s + \mathrm{tr}\left[\log\mathbf{D}\right] \tag{15.64}$$

where $\mathbf{D}$ is the data correlation matrix,

$$\begin{aligned}\mathbf{D} &\equiv \langle d\, d^T\rangle &(15.65)\\ &= \langle s\, s^T\rangle + \langle n\, n^T\rangle &(15.66)\\ &\equiv \mathbf{S}+\mathbf{N}, &(15.67)\end{aligned}$$

which is the sum of the signal and noise correlations, respectively $\mathbf{S}$ and $\mathbf{N}$. Since there is no analytical solution which could be implemented for the spectral coefficients maximizing this function, iterative search techniques such as Newton-Raphson algorithms could be use. In order to calculate the quadratic correction to the current estimate of C_ℓ given by

$$\delta C_\ell = -\left(\frac{\partial^2\log\mathcal{L}}{\partial {C_\ell}^2}\right)^{-1}\frac{\partial\log\mathcal{L}}{\partial C_\ell}, \tag{15.68}$$

we need to evaluate the first two derivatives of $\log(\mathcal{L})$ with respect to C_ℓ

$$\begin{aligned}\frac{\partial\mathcal{L}}{\partial C_\ell} &= \frac{1}{2}\left(d^T\mathbf{D}^{-1}\frac{\partial\mathbf{S}}{\partial C_\ell}\mathbf{D}^{-1}d - \mathrm{tr}\left[\mathbf{D}^{-1}\frac{\partial\mathbf{S}}{\partial C_\ell}\right]\right) &(15.69)\\ \left\langle\frac{\partial^2\mathcal{L}}{\partial C_\ell\partial C'_\ell}\right\rangle_{\text{ensemble average}} &\equiv \mathbf{F} = \mathrm{tr}\left[\mathbf{D}^{-1}\frac{\partial\mathbf{S}}{\partial C_\ell}\mathbf{D}^{-1}\frac{\partial\mathbf{S}}{\partial C'_\ell}\right]. &(15.70)\end{aligned}$$

Solving this system is quite CPU-time consuming and maximum-likelihood power spectrum estimation can only be used for up to $\mathcal{O}(10^5)$ pixels. Larger data sets are restricted to the analysis of reduced resolution maps (in particular critical for low ℓ spectral analysis) or small patches with full resolution (for example chosen for their low foreground contamination).

If maximum-likelihood analysis is intractable, Monte Carlo pseudo-spectral methods may be used. In this case we assume that the signal and noise pseudo-spectra, respectively $\hat{C}_\ell^S$ and $\hat{C}_\ell^N$, are independent and that the pseudo-spectra are related to the real spectra C_ℓ by an invertible linear transformation

$$\hat{C}_\ell^d = \hat{C}_\ell^S + \hat{C}_\ell^N \quad (15.71)$$

$$\hat{C}_\ell = \mathbf{T}_{\ell\ell'} C_{\ell'} \quad (15.72)$$

at which point Monte Carlo realizations of simulated signal with noise and noise only (with the same properties as the observational data) observations can be used to reconstruct the transfer matrix $\mathbf{T}_{\ell\ell'}$ and hence obtain the real spectra.

In addition, one potential source of systematics has to be taken into account at this level: to compute CMB power spectra on small fraction of the sky, as it is the case for POLARBEAR, it has been long recognized that a straightforward application of the pseudo-spectrum technique leads to the so-called E-to-B leakage, or power aliasing. This implies that the cosmological information encoded in the CMB B-modes is overwhelmed by the statistical uncertainty of the (much larger) E-modes. Two main techniques solving the problem have been proposed: one correcting the leakage on the correlation function level, e.g. Chon et al. (25), and the other one doing so directly at the map level, e.g. Smith (125). Grain et al. (56) built a code called X^2pure which is based on this latter approach and includes the optimization of apodization windows at the map level.

Cosmological parameters estimation

As mentioned in section 3.4, from the angular power spectra, we want to constrain cosmological models. To do that, we should adjust the value of cosmological parameters to obtain a set of spectra that best fits the data. Couple of methods can be used to perform this estimation:

- a grid of all the desired cosmological parameters. Power spectra are estimated for each associated node of the grid and are compared to the spectra coming from the data.
- COSMOMC, see Lewis and Bridle (83), which involves Markov chains to reduce the number of estimated power spectra. It uses a convergence criterion for movement in space of cosmological parameters.

Conclusions

This thesis is an attempt to summarize the work, which I have performed during the course of three years of my PhD studies at Université Paris VII - Denis Diderot and Laboratoire AstroParticule & Cosmologie and its results, while at the same time placing it within a broader context in order to explain why we do that, why we find it exciting, and why we think it is important.

Part I provides a brief introduction to the standard cosmology extended to include the theory of inflation as well as its observable signatures encoded in the CMB anisotropies. In this part the reasons why cosmologists consider an inflationary period during the early universe are given. Those include the resolution of the classical problems like that of the horizon, which were unexplained in the standard framework. Most interestingly, it is a process, which generates classical perturbations from quantum ones, which can then further serve as the seeds of the current large scale structures we observe today. Notable missing evidence in favor of this theory is the observation of the CMB B-modes, specific anisotropies in polarization and unique signature of the primordial gravitational waves generated during inflation.

Part II is a transition between the introduction and a presentation of my PhD work. There I detail the interests of observing the B-modes and the status of CMB polarization observations today and expectations for the near future. I also introduce my research projects, as seen from the contemporary experimental and data analysis challenges.

Part III presents some systematic effects affecting new generation of CMB polarization experiments with an emphasis on optical systematics as well as atmospheric and polarized astrophysical contaminations. I introduce there some data models and techniques, which could be used to suppress or at least control contaminants. Given their high sensitivity, understanding the instruments and the sky properties is essential for the success of the current and future CMB polarization experiments.

Part IV was a summary of the work I have performed in collaboration with drs. F. Stivoli and R. Stompor and concerning focal plane optimization for future nearly full-sky CMB experiments (e.g. COrE and CMBpol), in the presence of astrophysical foregrounds. I consider there three specific Figures Of Merit (FOM) quantifying performance of a given experimental design given the pre-defined science goals, and second find and test optimal configurations with respect to those FOM. The adopted component separation technique is based on the parametric maximum likelihood approach. We devise a global framework for this optimization process, including various robustness tests, e.g. how does the FOM vary in the case of a lost of detectors, channels? We also introduced a special quantity, the so-called significance of the residuals, which quantify the importance of the residuals at the map level and study its behavior for different experimental noise levels. We show that, ultimately, in the limit of very low noise levels, foregrounds will not be a fundamental limit (at least as long as sufficiently

precise scaling laws are available), i.e., will not prevent us from reaching arbitrarily low values of tensor-to-scalar ratio, r.

Finally, in Part V, I presented the POLARBEAR instrument, mounted on the Huan Tran Telescope at Chajnantor plateau, 5200 m, Chile and which has begun its observations in January 2012. The main goal of the experiment is a high quality characterization of the CMB polarization, and the detection of the B-modes, both lensed and primordial. In this part I describe some of the analysis I have developed and/or tested as a member of the international POLARBEAR collaboration. I introduce some of the projects I have worked on, in particular the pointing reconstruction, the noise estimation, parameters of selected systematic effects estimation and potential atmosphere filtering.

In the introduction, I formulated the global problematic of this thesis as "how to describe and control systematic effects at the data analysis level?". Of course, because there are as many such effects as there are instrumental designs and observational strategies, I could not, within the three years of the French PhD, study in detail every potential contamination of the CMB polarization observation. I rather formalized selected systematics, from their instrumental impact (relative to optics, using the Mueller formalism, chapter 7) to their sky sources (atmospheric contamination, chapter 8 as well as polarized foregrounds, chapter 9). After the formulation and modeling of the latter effects, the main goal of these different research projects was to find, study and exploit solutions for suppressing or at least controlling contamination. For instance, I showed in the last chapter how to estimate instrumental systematics parameters based on a parametric maximum likelihood approach. A component separation solution is also detailed and tested for various purposes in Part IV, mainly focused on the optimization of future CMB polarization observations. Finally, I have developed a framework, which could become a starting point for a better approach to deal with the atmospheric contaminations.

Afterwords

I have learned a lot from each of these research projects. First, this thesis has allowed me to get acquainted with nearly all the stages of a development, commissioning, observations, and data analysis of a new CMB polarization experiment, POLARBEAR. I have had also the opportunity to visit Berkeley and San Pedro de Atacama to work on this project: at the junction between the experiment and the data analysis, enriched by many exchanges, those travels constitute a great experience. In particular, to participate in the observational campaigns (in California, 2010 and in Chile, 2012) allowed me to access real data as well as acquire useful knowledge of the instrumental issues. For instance, it would have been very difficult to reconstruct the pointing of the telescope while staying in Paris. I am also part of the POLARBEAR-II collaboration which will deploy its instrument around 2014. My contribution to this future experiment has been so far mainly focused on the science forecast, relative to the detection of the primordial B-modes as well as the constraints on large scale structures one can derive after reconstructing the gravitational lensing potential. This latter project gave me the opportunity to study the lensing reconstruction methods, in collaboration with G. Fabbian.

Second, the project about the optimization of the distribution of detectors among frequency channels gave me the opportunity to study the parametric component separation technique and the related algebra based on the parametric maximum likelihood approach. Besides, it allowed me to learn basics about the physics of astrophysical contaminants such as dust and synchrotron. Thanks to the expertise and pedagogical efforts of my collaborators, this work has been fruitful and resulted in the publication of two papers. This project has been undertaken in a period of reflection for the European CMB community, corresponding to the writing of a proposal for a future ESA satellite project, COrE.

Third, the starting project of this thesis was related to the study of the atmospheric contamination and the impact of optical systematics in the time stream, as expected in the particular case of the POLARBEAR experiment. During an internship at Berkeley in 2008 with H. T. Tran and A. T. Lee, I learnt the basics of the Mueller formalism: I used this latter here in order to construct a modeling for the cross- and instrumental-polarization effects on a POLARBEAR-like time stream. In Spring 2012, I advised the internship of a master student, C. Pelletier, who worked with me on the simulated estimation of these instrumental parameters from raw data, in the frame of the parametric maximum likelihood formalism.

Finally, even if rarely mentioned in a PhD-related context, I have learned a lot from my teaching experience at the University. Students were not always ready and motivated to listen to physics lectures, but they have taught me the basic know-how of the teaching. This experience has been very valuable for me, and I hope it has been

reciprocal for my students. This exercise has been enriched by my participation to different general public events, and I really think that presenting his or her own research to people who do not know anything about the subject helps a lot.

This PhD work is not the end but rather the starting point of a larger project which aims at contributing to a full analysis pipeline. Because of a quite competitive environment for CMB observations nowadays, time scales for POLARBEAR are quite short and I am delighted to pursue my research as a member of this collaboration, aiming at the extraction of cosmological results from the data. I will continue working on the analysis of the POLARBEAR data, taking part in the research effort lead by J. Borrill at Lawrence Berkeley National Lab in Berkeley.

Last, there are of course possibilities to improve the work undertaken during this PhD. I see several potential extensions for the project on component separation: first, we could think of an implementation of a web interface so that people from various projects could test their preferred hardware configurations with respect to the figures of merit we introduced. Besides, they would be able to optimize the distribution of detectors among available frequency channels under some hardware constraints they would have chosen. Second, we could enlarge the science case to, for instance, the lensed B-modes science e.g. constraints on total neutrino mass, dark energy equation of state, etc.

About systematics control or suppression, the main goal is going to be the implementation and large scale tests (on real data) of the several simple algorithms I previously presented, from the component separation to the estimation of instrumental parameters. For example, the collaboration as other ground-based experiments have to find efficient and smart filters to reject atmospheric contamination. A possibility could be to use the model summarized in paragraph 8.4.2 and build a method based on the maximum parametric likelihood approach, with the parameters being the turbulence's typical scales, the wind speed and direction, etc. However, because of its computational power needs, this idea would require a non-trivial implementation. However, because of its computational complexity, this idea requires a non-trivial implementation and therefore has been left for the future.

Appendices

Appendix A

Spectral likelihood derivatives.

I present here some details of the derivation of Eqs. (10.9) and (10.10). First ,from Eq. (10.8) we have

$$\frac{\partial \ln \mathcal{L}}{\partial \beta} \;=\; \sum_p \left(\mathbf{A}_{,\beta}\,\mathbf{s}_p\right)^t\,\mathbf{N}^{-1}\,\left(\mathbf{d}_p - \mathbf{A}\,\mathbf{s}_p\right) \tag{A.1}$$

from which the second derivatives of the spectral likelihood follow as

$$\frac{\partial^2 \ln \mathcal{L}}{\partial \beta\,\partial \beta'} \;=\; \sum_p \left\{ \left(\mathbf{A}_{,\beta\beta'}\,\mathbf{s}_p + \mathbf{A}_{,\beta}\,\mathbf{s}_{p,\beta'}\right)^t\,\mathbf{N}^{-1}\,\left(\mathbf{d}_p - \mathbf{A}\,\mathbf{s}_p\right) \;-\; \left(\mathbf{A}_{,\beta}\,\mathbf{s}_p\right)^t\,\mathbf{N}^{-1}\,\left(\mathbf{A}_{,\beta'}\,\mathbf{s}_p + \mathbf{A}\,\mathbf{s}_{p,\beta'}\right) \right\}.$$

And the noise ensemble average reads,

$$\begin{aligned}\left\langle \frac{\partial^2 \ln \mathcal{L}}{\partial \beta\,\partial \beta'} \right\rangle_{noise} \;=\; \sum_p \Big\{ & \mathrm{tr}\left[\mathbf{A}^t_{,\beta\beta'}\,\mathbf{N}^{-1}\,\left\langle \left(\mathbf{d} - \mathbf{A}\,\mathbf{s}_p\right)\,\mathbf{s}_p^t \right\rangle_{noise}\right] \;-\; \mathrm{tr}\left[\mathbf{A}^t_{,\beta}\,\mathbf{N}^{-1}\,\mathbf{A}_{,\beta'}\,\left\langle \mathbf{s}_p\,\mathbf{s}_p^t \right\rangle_{noise}\right] \\ + \quad & \mathrm{tr}\left[\mathbf{A}^t_{,\beta}\,\mathbf{N}^{-1}\,\langle \left(\mathbf{d}_p - \mathbf{A}\,\mathbf{s}_p\right)\,\mathbf{s}^t_{p,\beta'} \rangle_{noise}\right] \;-\; \mathrm{tr}\left[\mathbf{A}^t_{,\beta}\,\mathbf{N}^{-1}\,\mathbf{A}\,\langle \mathbf{s}_{p,\beta'}\mathbf{s}_p^t \rangle_{noise}\right] \Big\}.\end{aligned}$$

From Eqs. (10.1) and (10.7) we now have

$$\left\langle \mathbf{s}_p\,\mathbf{s}_p^t \right\rangle_{noise} \;=\; \bar{\mathbf{s}}_p\,\bar{\mathbf{s}}_p^t \;+\; \left(\mathbf{A}^t\,\mathbf{N}^{-1}\,\mathbf{A}\right)^{-1}, \tag{A.2}$$

$$\begin{aligned}\left\langle \mathbf{s}_p\,\mathbf{s}^t_{p,\beta'} \right\rangle_{noise} \;=\; & -\,\bar{\mathbf{s}}_{\mathbf{p}}\,\bar{\mathbf{s}}^t_{\mathbf{p}}\,\left(\mathbf{A}^t_{,\beta'}\mathbf{N}^{-1}\mathbf{A} + \mathbf{A}^t\mathbf{N}^{-1}\mathbf{A}_{,\beta'}\right)\,\left(\mathbf{A}^t\mathbf{N}^{-1}\mathbf{A}\right)^{-1} \;+\; \bar{\mathbf{s}}_p\,\bar{\mathbf{q}}^t_{p\,(\beta')} \\ & -\,\left(\mathbf{A}^t\mathbf{N}^{-1}\mathbf{A}\right)^{-1}\,\left(\mathbf{A}^t_{,\beta'}\mathbf{N}^{-1}\mathbf{A}\right)\,\left(\mathbf{A}^t\mathbf{N}^{-1}\mathbf{A}\right)^{-1}\end{aligned} \tag{A.3}$$

$$\begin{aligned}\langle \left(\mathbf{d}_p - \mathbf{A}\,\mathbf{s}_p\right)\,\mathbf{s}_p^t \rangle_{noise} \;=\; & \left(\hat{\mathbf{A}}\,\hat{\mathbf{s}} \;-\; \mathbf{A}\bar{\mathbf{s}}_{\mathbf{p}}\right)\,\bar{\mathbf{s}}^t_{\mathbf{p}} \\ \langle \left(\mathbf{d}_p - \mathbf{A}\,\mathbf{s}_p\right)\,\mathbf{s}^t_{p,\beta'} \rangle_{noise} \;=\; & -\,\left(\hat{\mathbf{A}}\,\hat{\mathbf{s}} \;-\; \mathbf{A}\bar{\mathbf{s}}_{\mathbf{p}}\right)\,\bar{\mathbf{s}}^t_{\mathbf{p}}\,\left(\mathbf{A}^t_{,\beta'}\mathbf{N}^{-1}\mathbf{A} + \mathbf{A}^t\mathbf{N}^{-1}\mathbf{A}_{,\beta'}\right)\,\left(\mathbf{A}^t\mathbf{N}^{-1}\mathbf{A}\right)^{-1} \\ & +\,\left(\hat{\mathbf{A}}\,\hat{\mathbf{s}} \;-\; \mathbf{A}\bar{\mathbf{s}}_{\mathbf{p}}\right)\,\bar{\mathbf{q}}^t_{\mathbf{p}\,(\beta')} \;+\; \mathbf{A}_{,\beta'}\,\left(\mathbf{A}^t\mathbf{N}^{-1}\mathbf{A}\right)^{-1} \\ & +\mathbf{A}\,\left(\mathbf{A}^t\mathbf{N}^{-1}\mathbf{A}\right)^{-1}\,\left(\mathbf{A}^t\mathbf{N}^{-1}\mathbf{A}_{,\beta'}\right)\,\left(\mathbf{A}^t\mathbf{N}^{-1}\mathbf{A}\right)^{-1},\end{aligned} \tag{A.4}$$

where $\hat{\mathbf{A}}$ and $\hat{\mathbf{s}}$ are respectively the true mixing matrix and sky components. $\bar{\mathbf{s}}$ is a component estimate in a case of noiseless experiment, given by

$$\bar{\mathbf{s}}_p \equiv \left(\mathbf{A}^t\,\mathbf{N}^{-1}\,\mathbf{A}\right)^{-1}\,\mathbf{A}^t\,\mathbf{N}^{-1}\,\hat{\mathbf{A}}\,\hat{\mathbf{s}}_p. \tag{A.5}$$

Besides, $\bar{\mathbf{q}}_{(\beta)}$, which appears in Eq. (A.4), is defined as,

$$\bar{\mathbf{q}}_{p\,(\beta')} \equiv \left(\mathbf{A}^t\,\mathbf{N}^{-1}\,\mathbf{A}\right)^{-1}\,\mathbf{A}^t_{,\beta'}\,\mathbf{N}^{-1}\,\hat{\mathbf{A}}\,\hat{\mathbf{s}}_p. \tag{A.6}$$

Hence,

$$\begin{aligned}
\left\langle \frac{\partial^2 \ln\mathcal{L}}{\partial\beta\,\partial\beta'} \right\rangle_{noise} = & - \sum_p \Big\{ \left(\mathbf{A}_{,\beta\beta'}\,\bar{\mathbf{s}}_p\right)^t\,\mathbf{N}^{-1}\,\left(\mathbf{A}\,\bar{\mathbf{s}}_p - \hat{\mathbf{A}}\,\hat{\mathbf{s}}_p\right) + \left(\mathbf{A}_{,\beta}\,\bar{\mathbf{s}}_p\right)^t\,\mathbf{N}^{-1}\,\left(\mathbf{A}_{,\beta'}\,\bar{\mathbf{s}}_p\right) \\
& + \mathrm{tr}\left[\mathbf{A}^t_{,\beta}\,\mathbf{N}^{-1}\,\left(\hat{\mathbf{A}}\,\hat{\mathbf{s}}_p - \mathbf{A}\,\bar{\mathbf{s}}_p\right)\,\bar{\mathbf{s}}^t_p\,\left(\mathbf{A}^t_{,\beta'}\mathbf{N}^{-1}\mathbf{A} + \mathbf{A}^t\mathbf{N}^{-1}\mathbf{A}_{,\beta'}\right)\,\left(\mathbf{A}^t\mathbf{N}^{-1}\mathbf{A}\right)^{-1}\right] \\
& - \mathrm{tr}\left[\left(\mathbf{A}_{,\beta}\,\bar{\mathbf{q}}_{p,(\beta')}\right)^t\,\mathbf{N}^{-1}\,\left(\hat{\mathbf{A}}\,\hat{\mathbf{s}}_p - \mathbf{A}\,\bar{\mathbf{s}}_p\right)\right] \\
& - \mathrm{tr}\left[\mathbf{A}^t_{,\beta}\,\mathbf{N}^{-1}\,\mathbf{A}\,\left(\mathbf{A}^t\mathbf{N}^{-1}\mathbf{A}\right)^{-1}\,\left(\mathbf{A}^t_{,\beta'}\mathbf{N}^{-1}\mathbf{A} + \mathbf{A}^t\mathbf{N}^{-1}\mathbf{A}_{,\beta'}\right)\,\bar{\mathbf{s}}_{\mathbf{p}}\,\bar{\mathbf{s}}^t_{\mathbf{p}}\right] \\
& + \mathrm{tr}\left[\mathbf{A}^t_{,\beta}\,\mathbf{N}^{-1}\,\mathbf{A}\,\bar{\mathbf{q}}_{p\,(\beta')}\,\bar{\mathbf{s}}^t_p\right]\Big\}\,.
\end{aligned} \tag{A.7}$$

Moreover assuming now the true values of the spectral indices, i.e., $\beta = \hat{\beta}$,

$$\begin{aligned}
\left\langle \frac{\partial^2 \ln\mathcal{L}_{profile}}{\partial\beta\,\partial\beta'} \right\rangle_{noise}\Bigg|_{\beta=\hat{\beta}} = & - \mathrm{tr}\left[\mathbf{A}^t_{,\beta}\,\mathbf{N}^{-1}\,\mathbf{A}_{,\beta'}\,\sum_p \hat{\mathbf{s}}_p\,\hat{\mathbf{s}}^t_p\right] \\
& + \mathrm{tr}\left[\mathbf{A}^t_{,\beta}\,\mathbf{N}^{-1}\,\mathbf{A}\,\left(\mathbf{A}^t\mathbf{N}^{-1}\mathbf{A}\right)^{-1}\,\left(\mathbf{A}^t_{,\beta'}\mathbf{N}^{-1}\mathbf{A} + \mathbf{A}^t\mathbf{N}^{-1}\mathbf{A}_{,\beta'}\right)\,\sum_p \hat{\mathbf{s}}_p\,\hat{\mathbf{s}}^t_p\right] \\
& - \mathrm{tr}\left[\mathbf{A}^t_{,\beta}\,\mathbf{N}^{-1}\,\mathbf{A}\,\left(\mathbf{A}^t\,\mathbf{N}^{-1}\,\mathbf{A}\right)^{-1}\,\mathbf{A}^t_{,\beta'}\,\mathbf{N}^{-1}\,\mathbf{A}\,\sum_p \hat{\mathbf{s}}_p\,\hat{\mathbf{s}}^t_p\right] \\
= & \mathrm{tr}\left\{\left[\mathbf{A}^t_{,\beta}\,\mathbf{N}^{-1}\,\mathbf{A}\,\left(\mathbf{A}^t\mathbf{N}^{-1}\mathbf{A}\right)^{-1}\,\mathbf{A}^t\mathbf{N}^{-1}\mathbf{A}_{,\beta'} - \mathbf{A}^t_{,\beta}\,\mathbf{N}^{-1}\,\mathbf{A}_{,\beta'}\right]\,\sum_p \hat{\mathbf{s}}_p\,\hat{\mathbf{s}}^t_p\right\},
\end{aligned} \tag{A.8}$$

from which Eq. (10.10) follows.

Generalization in the case where $\mathbf{A}$ is replaced by $\mathbf{B} \equiv \boldsymbol{\Omega}\cdot\mathbf{A}$ is easy. Because, we consider calibration errors this time, derivatives can be taken with respect to β and ω, the calibration parameters.

$$\begin{aligned}
\boldsymbol{\Sigma}^{-1}_{ij} = & \; n_{pix}\;\mathrm{tr}\left\{\left[\boldsymbol{B}^t_{,i}\,\boldsymbol{N}^{-1}\,\boldsymbol{B}\,\left(\boldsymbol{B}^t\boldsymbol{N}^{-1}\boldsymbol{B}\right)^{-1}\,\boldsymbol{B}^t\boldsymbol{N}^{-1}\boldsymbol{B}_{,j} - \boldsymbol{B}^t_{,i}\,\boldsymbol{N}^{-1}\boldsymbol{B}_{,j}\right]\,\hat{\boldsymbol{F}}\right\} \\
& + \left[(\boldsymbol{\omega}-\bar{\boldsymbol{\omega}})^t\,\boldsymbol{\Xi}^{-\mathbf{1}}\,(\boldsymbol{\omega}-\bar{\boldsymbol{\omega}})\right]_{,ij}\Big|_{\hat{\boldsymbol{\gamma}}},
\end{aligned} \tag{A.9}$$

in which expression we let the explicit derivative of the second term in the r.h.s. This latter will only be non-zero in the calibration-calibration block of the $\boldsymbol{\Sigma}$ matrix.

Appendix B

Fisher matrix algebra.

The Fisher matrix can be expressed as (144),

$$F_{\alpha\beta} \equiv \left\langle \frac{\partial^2 ln\mathcal{L}}{\partial\lambda_\alpha \partial\lambda_\beta} \right\rangle = \frac{1}{2}\mathrm{tr}\left[\mathbf{C}_{,\alpha}\mathbf{C}^{-1}\mathbf{C}_{,\beta}\mathbf{C}^{-1}\right] \tag{B.1}$$

where $\mathbf{C}$ is the covariance matrix and λ is some parameter.

In our case, $\lambda_\alpha = \lambda_\beta = r$, the tensor-to-scalar ratio, while the covariance matrix in a harmonic space, $\mathbf{C}$, is given by,

$$\mathbf{C} \equiv \mathbf{C}_{jj'} \equiv \langle a_{\ell m} a^\dagger_{\ell' m'} \rangle, \tag{B.2}$$

where,

$$\begin{aligned} j &= \ell^2 + \ell + m, \\ \ell &= \mathrm{round}[(-1+\sqrt{1+4j})/2], \\ m &= j - \ell\,(\ell+2)\,, \end{aligned} \tag{B.3}$$

and thus j goes from 0 to $(\ell_{max}+1)^2 - 1$. The function "round" in Eqs. (B.3) rounds a real number to a closest integer. The Fisher matrix expression can be now written as,

$$F_{rr} = \frac{1}{2}\sum_{j,j'} \frac{\partial C_\ell}{\partial r}\,\left[\mathbf{C}^{-1}\right]^2_{jj'}\,\frac{\partial C_{\ell'}}{\partial r}. \tag{B.4}$$

where j (j') is related to ℓ (ℓ') as in Eqs. (B.3).

Because there are three uncorrelated contributions to the overall signal, which are CMB, noise, and foreground residuals, we can write,

$$\begin{aligned} \mathbf{C}_{jj'} &= \langle a^{CMB}_{lm} a^{CMB,\dagger}_{l'm'}\rangle + \langle a^{noise}_{lm} a^{noise,\dagger}_{l'm'}\rangle + \langle a^{\Delta}_{lm} a^{\Delta,\dagger}_{l'm'}\rangle \\ &= C_l^{CMB}\delta_{jj'} + C_l^{noise}\delta_{jj'} + f_j\, f^\dagger_{j'} \\ &\equiv D_{jj'} + f_j\, f^\dagger_{j'} \end{aligned} \tag{B.5}$$

where f_j stands for a vector of $a^{\Delta}_{\ell m}$ coefficients arranged according to the j index.

To compute the $\mathbf{C}^{-1}$ matrix used in Eq. (B.1), we can use the Sherman-Morrison formula which gives

$$\mathbf{C}^{-1} = \mathbf{D}^{-1} - \mathbf{D}^{-1} f (1 + f^{\dagger}\mathbf{D}^{-1} f)^{-1} f^{\dagger}\mathbf{D}^{-1}. \tag{B.6}$$

In this equation $(1 + f^{\dagger}\mathbf{D}^{-1} f)^{-1}$ is a number and, hence,

$$\mathbf{C}^{-1} = \mathbf{D}^{-1} - \frac{\mathbf{D}^{-1} f f^{\dagger}\mathbf{D}^{-1}}{\left(1 + f^{\dagger}\mathbf{D}^{-1} f\right)}, \tag{B.7}$$

which, given that $[D^{-1}]_{jj'} = (1/C_\ell)\delta_{jj'}$, becomes

$$\left[\mathbf{C}^{-1}\right]_{jj'} = \frac{\delta_{jj'}}{C_\ell} - \frac{C_\ell^{-1}\, C_{\ell'}^{-1}\, f_j f_{j'}^{\dagger}}{1 + \sum_{\ell''=0}^{\ell_{max}} (2\ell''+1)\, \dfrac{C^{\Delta}_{\ell''}}{C_{\ell''}}}, \tag{B.8}$$

where C^{Δ}_{ℓ} is a residuals power spectrum, Eq. (10.21), defined here as

$$C^{\Delta}_{\ell} \equiv \frac{1}{2\ell+1} \sum_{m=\ell^2}^{\ell^2+2\ell} |f_m|^2. \tag{B.9}$$

So now we have finally

$$\left[\mathbf{C}^{-1}\right]^2_{jj'} = \frac{\delta_{jj'}}{C_\ell^2} - \frac{2\, f_j f_j^{\dagger}}{C_\ell^3 \left(1 + \sum_{\ell''=0}^{\ell_{max}} (2\ell''+1)\, \dfrac{C^{\Delta}_{\ell''}}{C_{\ell''}}\right)} \delta_{jj'} + \frac{f_j^2 {f_{j'}^{\dagger}}^2}{C_\ell^2\, C_{\ell'}^2 \left(1 + \sum_{\ell''=0}^{\ell_{max}} (2\ell''+1)\, \dfrac{C^{\Delta}_{\ell''}}{C_{\ell''}}\right)^2}, \tag{B.10}$$

which inserted into Eq. (B.4) gives Eq. (11.2).

Appendix C

Quantitative discussion about optimum observation: the case of POLARBEAR

POLARBEAR experiment has mainly three science goals:

- better characterization of the E-modes signal: this, combined with informations on the total intensity, can break degeneracies in the estimation of cosmological parameters;
- detection of the lensed B-modes: this signal corresponds to the leakage from the E- into the B-modes induced by large scale structures, see section C.2;
- detection of the primordial B-modes down to $r = 0.025$ with 95 % c.l., see section C.1: it is maybe the most exciting goal because it corresponds to the last observational pillar of the inflation theory, cf. Parts I and II.

I present in this appendix the forecast of the POLARBEAR experiments with respect to these science goals — mostly corresponding to the work I have performed and presented in October, 2012 at Berkeley in the frame of a POLARBEAR-II meeting. In particular, I present how one can optimize the patch size on the sky for such observations.

In the following reasonings, for sensitivity calculations, we assume a conservative overall observational efficiency of 18% which assumes 12 hours per day (patches are available for 15 hours), 9 months per year, 70% array yield (the measured fabrication yield is 93%), and 5 days of maintenance per month. For reference, QUIET (14) achieved 30% overall efficiency. With all observation time focused on the three CMB patches chosen for deep POLARBEAR observations with a total area of $700\,\mathrm{deg}^2$, we find a noise level of $8\,\mu$K.arcmin for polarization and $5.7\,\mu$K.arcmin for intensity. Corresponding forecast at the power spectrum level is shown in Fig. C.1.

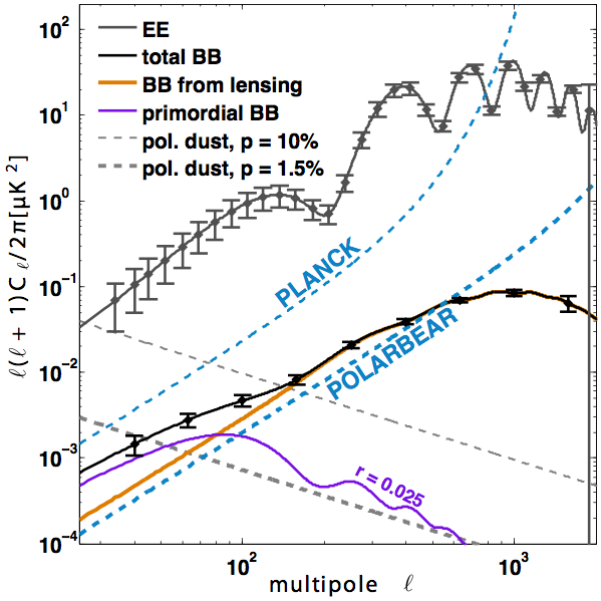

Figure C.1: Projected CMB polarization power constraints for POLARBEAR-I. Inflationary signal (purple solid curve) is plotted for $r = 0.025$. The blue dashed lines show noise levels for Planck and POLARBEAR-I experiment with a $\Delta\ell = 30$ binning. Polarized dust levels have been estimated for the planned observation patches and bracket the likely range of dust fractional polarization (1.5 and 10 %).

C.1 Optimizing for primordial gravitational waves detection

C.1.1 Signature of inflation theories

Current spectral index measurements give some hints that a simple slow-roll single-field model of inflation is correct. If so, the inflationary gravitational wave signal could be in a range that is detectable by POLARBEAR. Current limits are $r < 0.17$ from the WMAP+SPT+BAO+H_0 data, well within POLARBEAR's reach of $r = 0.025$ at the 2-σ level. POLARBEAR's constraint would rule out a large volume of presently allowed inflationary models.

I have computed the $r = 0.025$ constraint using a Fisher approach, assuming the experimental sensitivity and the sky area without consideration of foregrounds, cf. chapter 9, or E-B mixing, cf. section 15.6. The error on r is given by:

$$\sigma_r \approx \frac{1}{\sqrt{F_{rr}}} \tag{C.1}$$

where

$$F_{rr} \equiv \sum_{\ell,\ell'} \frac{\partial C_\ell}{\partial r} \mathbf{C}^{-2}_{\ell\ell'} \frac{\partial C_\ell}{\partial r} \tag{C.2}$$

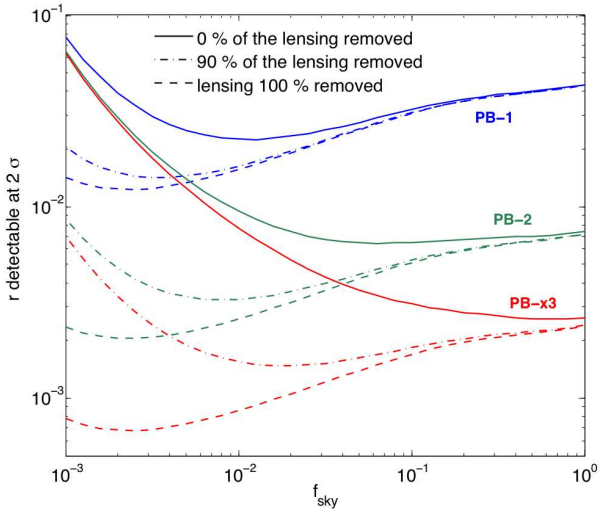

Figure C.2: What is the best f_{sky} for POLARBEAR in order to detect the lowest r?

and

$$\mathbf{C}_{\ell\ell'}^{-2} \equiv \frac{(2\ell+1) f_{sky} \delta_\ell^{\ell'}}{2\left(C_\ell^{prim}(r) + \eta C_\ell^{lens} + C_\ell^{noise}\right)^2} \tag{C.3}$$

Notice that I derived another expression for this Fisher error, cf. Eq. (11.2), which takes into account the presence of astrophysical foregrounds residuals. The η parameter tunes the fraction of lensing signal which we consider, allowing us to "artificially" study the impact of delensing. The $r = 0.025$ value has been obtained assuming no delensing, i.e. $\eta = 1$.

C.1.2 Optimizing the observation of POLARBEAR with respect to r

I briefly explain in this paragraph the way of optimizing the observed fraction of the sky, f_{sky}, with respect to the detection of r for a given experimental setup. First, what I call the detectable r at the 2-σ level is the solution of

$$r = 2 \times \sigma_r, \tag{C.4}$$

where σ_r is given in Eq. C.1. Eq. C.4 leads, as a function of f_{sky}, to

$$r \propto \frac{1 + \gamma f_{sky}}{\sqrt{f_{sky}}} \tag{C.5}$$

where γ is a positive constant which depends on the lensing signal (and therefore on η) as well as the noise level of the experiment, etc. I depict in Fig. C.2 the r detectable at the 2-σ level as a function of f_{sky} and η, in the case of three different experiments:

POLARBEAR-I (8.1 μK.arcmin for $f_{sky} = 1.5\%$), POLARBEAR-II (3.3 μK.arcmin for the same f_{sky}) and POLARBEAR-EXT (1.9 μK.arcmin for the same f_{sky}).

At low f_{sky}, the $1/\sqrt{f_{sky}}$ factor in Eq. C.5 dominates, and corresponds to the impact of the cosmic variance. At high f_{sky}, noise term, i.e. the numerator of Eq. C.5, dominates. As shown on the figure, the lowest r is reached between these two regimes: this is the optimal r one would like the observation to target. However, changing the level of lensed B-modes (i.e. changing η for 1.0, 0.1 and 0.0 in Fig. C.2) shifts left- and down-wards the solid curves: this is because the cosmic variance goes like η. Assuming that we are somehow able to delens the data[1], this means that the optimal point for the detection of primordial B-modes would be at lower f_{sky}, $\lesssim 1\%$ in the particular case of POLARBEAR.

On the grounds of all the science goals of the experiment, POLARBEAR-I collaboration chose to target 3 CMB-patches which will cover a fraction $f_{sky} \sim 2.3$ % of the entire sky.

C.2 Lensed B-modes detection?

The other science goal of the POLARBEAR experiment is the detection of the lensed B-modes. This signal may certainly be the third detection after the intensity and E-modes signals. Lensing results from the leakage of E- into B-modes induced by large structures located in the mid-z universe which deflect the light and break the symmetry associated to the E-modes. Because of its physical origin, CMB lensing reconstruction allows us to add an additional source of information to the usual CMB temperature and polarization fields — namely, the lens reconstructed deflection field, d_ℓ^m — and contains information about late time geometry and structures in the universe and helps to break the angular diameter distance degeneracy in the CMB.

Physics causing lensing is briefly explained in chapter 3 and I describe in section C.2.1 the technique I have used to estimate the precision of POLARBEAR with respect to the total neutrinos mass and w, the dark energy equation of state. Those two parameters, related to the properties of the large scale structures, can be derived from the detection of lensed B-modes.

[1] Being able to delense depends on the noise of the observation but also at the angular scales which can be reach by the observation, e.g. Hu and Okamoto (64).

C.2.1 Lensing reconstruction

The basic idea for extracting the gravitational lensing signal from the CMB observation is to invert Eq. 3.28, in a statistical way: this is possible because the B-modes generated by gravitational lensing are highly correlated to the E-modes, and the correlation is due to the convolution of the unlensed CMB with the lens potential Φ. For a given realization of this latter, the 2-points function $\langle a^X_{\ell_1 m_1} a^Y_{\ell_2 m_2}\rangle_{CMB}$, averaged over CMB realizations, is given by:

$$\langle a^X_{\ell_1 m_1} a^Y_{\ell_2 m_2}\rangle_{CMB} \equiv \sum_{\ell m} \Gamma^{XY}_{\ell_1 \ell_2 \ell} \begin{pmatrix} \ell_1 & \ell_2 & \ell \\ m_1 & m_2 & m \end{pmatrix} \Phi^*_{\ell m} \tag{C.6}$$

where $X, Y \in \{T, E, B\}$ and Γ functions are given in Smith et al. (126). Following the optimal quadratic estimator formalism (64), and following the notations of (126), the estimator of the gravitational potential, $\hat{\Phi}_{\ell m}$, is given by:

$$\hat{\Phi}_{\ell m} = \frac{N^{\Phi\Phi}_\ell}{2} \sum_{\ell_1 \ell_2 m_1 m_2} \Gamma^{XY}_{\ell_1 \ell_2 \ell} \begin{pmatrix} \ell_1 & \ell_2 & \ell \\ m_1 & m_2 & m_3 \end{pmatrix} \left(\mathbf{C^{-1}} a\right)^{X*}_{\ell_1 m_1} \left(\mathbf{C^{-1}} a\right)^{Y*}_{\ell_2 m_2} \tag{C.7}$$

where

$$N^{\Phi\Phi}_\ell \equiv \left[\frac{1}{2(2\ell+1)} \sum_{\ell_2 \ell_1} \sum_{XX'YY'} \Gamma^{XY}_{\ell_1 \ell_2 \ell_3} \left(C_{\ell_1} + N_{\ell_1}\right)^{-1}_{XX'} \Gamma^{X'Y'}_{\ell_1 \ell_2 \ell_3} \left(C_{\ell_1} + N_{\ell_1}\right)^{-1}_{YY'} \right]^{-1} \tag{C.8}$$

Dominant terms of the covariance of the estimated $\hat{\Phi}_{\ell m}$ are:

$$\langle \hat{\Phi}^*_{\ell_1 m_2} \hat{\Phi}_{\ell_2 m_2}\rangle_{CMB} = \left(C^{\Phi\Phi}_{\ell_1} + N^{\Phi\Phi}_{\ell_1}\right) \delta^{\ell_2}_{\ell_1} \delta^{m_2}_{m_1} \tag{C.9}$$

C.2.2 Estimation of lensing related cosmological parameters

As one can see in Eq. 3.30, $C^{\Phi\Phi}_\ell$ can be written as a line-of-sight integral including geometric distances and the power spectrum of the evolving potential, P_Ψ, and therefore depends on distances and growth of large scale structures. Especially, it is sensitive to late universe parameters such as the neutrino mass, the geometry of the universe and the dark energy equation of state, respectively parametrized in the following by $\Omega_\nu h^2$, Ω_K and w. The dependence of $C^{dd}_\ell \equiv (\ell(\ell+1))^2 C^{\Phi\Phi}_\ell / 2\pi$ on some cosmological parameters is illustrated in Fig. C.3.

Fisher approach

For the purpose of Fisher Matrix calculations, it is useful to assume that the lensing reconstruction has been used to delens the temperature and polarization fields, yielding four Gaussian independent variables $\{\tilde{T}^m_l, \tilde{E}^m_l, \tilde{B}^m_l, d^m_l\}$, which are the unlensed

C. QUANTITATIVE DISCUSSION ABOUT OPTIMUM OBSERVATION: THE CASE OF POLARBEAR

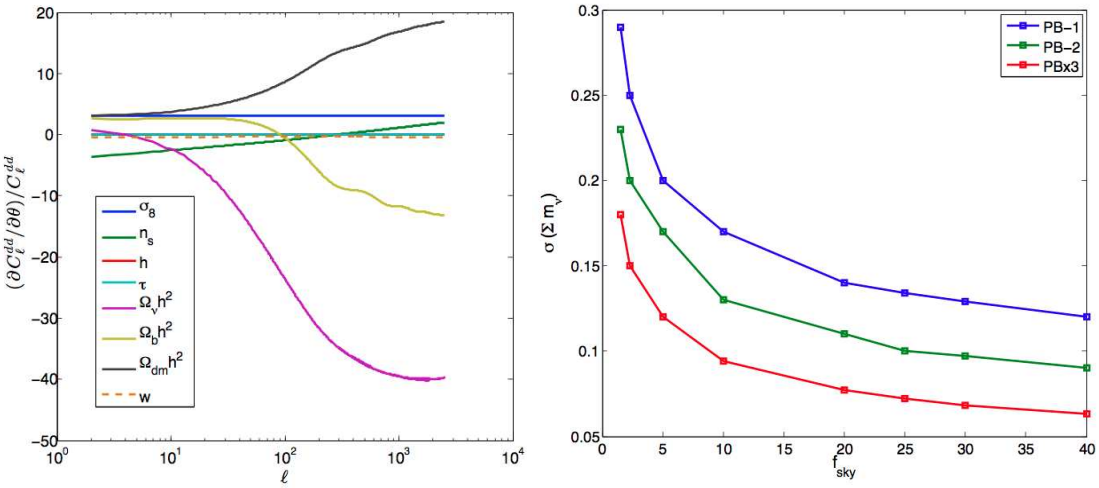

Figure C.3: **Left panel**: relative derivative of $C_\ell^{dd} \equiv (\ell(\ell+1))^2 C_\ell^{\Phi\Phi}/2\pi$ with respect to some cosmological parameters θ. **Right panel**: behavior of $\sigma\left(\sum m_\nu\right)$ as a function of the observed fraction of the sky in the case of the three versions of POLARBEAR.

CMB fields and the deflection modes. Omitting primordial B-modes from the Fisher calculation, the data covariance matrix reads,

$$\mathbf{C}_\ell^{-1} = \begin{bmatrix} C_\ell^{\tilde{T}T} + N_\ell^{TT} & \tilde{C}_\ell^{\,TE} & \tilde{C}_\ell^{\,Td} \\ C_\ell^{\tilde{T}E} & C_\ell^{\tilde{E}E} + N_\ell^{EE} & 0 \\ C_\ell^{\tilde{T}d} & 0 & \tilde{C}_\ell^{\,dd} + N_\ell^{dd} \end{bmatrix}, \tag{C.10}$$

where $\tilde{C}_\ell^{XY}$ correspond to the unlensed power spectra and N_ℓ^{XX} denote the noise power spectra. The deflection field noise power spectrum N_ℓ^{dd} is computed in the context of a quadratic estimator for the deflection field, cf. section C.2.1.

Under these assumptions, the Fisher Matrix, already defined in Eq. (B.1), reads

$$F_{ij} = \sum_\ell \frac{2\ell+1}{2} f_{sky} \mathrm{tr}\left(\mathbf{C}_\ell^{-1}\frac{\partial \mathbf{C}_\ell}{\partial\theta_i}\mathbf{C}_\ell^{-1}\frac{\partial \mathbf{C}_\ell}{\partial\theta_j}\right), \tag{C.11}$$

where θ_i denotes the i^{th} cosmological parameter and the lower bound on the error on θ_i after marginalization over all other free parameters is given by,

$$\sigma(\theta_i) = \sqrt{(F^{-1})_{ii}} \tag{C.12}$$

I consider height cosmological parameters of the ΛCDM cosmology, extended with a massive neutrino density and a dark energy equation of state w,

$$\mathbf{\Theta} \equiv \{\Omega_b h^2, \Omega_{dm} h^2, \tau, Y_{He}, n_s, \sigma_8, \Omega_\nu h^2, w, h\}.$$

	$\sigma\left(\sum m_\nu\right)$	$\sigma\left(w\right)$
POLARBEAR alone	0.184	0.0413
POLARBEAR and Planck combined	0.0762	0.0260
POLARBEAR alone with w = -1	0.0831	0
POLARBEAR and Planck combined with w = -1	0.0319	0

Table C.1: Summary of the errors on the neutrino mass and w we could reach with the POLARBEAR-I experiment, depending on a potential combination with Planck and a marginalization over w.

Besides, I chose a fiducial model given by

$$\boldsymbol{\Theta}_{fid} \equiv \{0.0226, 0.114, 0.09, 0.24, \sigma_8, 3 \times 10^{-3}, -1, 70\},$$

assuming three massive neutrino species.

I depict in the right panel of Fig. C.3 the behavior of the error on the estimation of the total neutrino mass. This shows that, for the typical noise levels of the POLARBEAR experiments, larger observed sky fraction result in better constraints on neutrino mass. This is due, as detailed in paragraph C.2.3, to the fact that the reconstruction process is based on both total intensity and polarization informations. However, even if we would like, POLARBEAR could not cover the whole sky from Chile, cf. chapter 14 and as I said previously, the experiments aims at observing ~ 2.3 % of the sky, in order to increase the polarization signal over noise ratio. This gives errors on the late universe parameters which are given in table C.1.

C.2.3 Extension of the study

In collaboration with G. Fabbian, we looked at the performance of POLARBEAR-II with respect to the estimation of the total neutrino mass, for different fraction of the sky. Our work is well summarized in Fig. C.4. This latter shows the constraint on total neutrino mass as a function of the observed fraction of the sky.

The estimation of the lensing based only on the polarization information (denoted E+B) has a minimum and is driven by the same factors as the ones I mentioned in paragraph C.1.2 about the detection of the primordial tensor-to-scalar ratio r: at low f_{sky}, the error on the estimation is dominated by the cosmic variance and for large f_{sky}, the estimator is noise dominated. Adding the T information results in the T+E+B curves which are monotonically decreasing as I stated before. It is remarkable to see that the combination of POLARBEAR-II and Planck would lead to a $\sigma\left(\sum m_\nu\right) \lesssim 50$ meV, below the inverted hierarchy predictions.

Besides, we looked at the case of a degraded noise on the T power spectrum, due to e.g. atmospheric contamination. We choose a shape for the noise such as

$$N_\ell^{TT} \equiv w^{-1} \left[1 + \left(\frac{\ell_{knee}}{\ell}\right)^\alpha\right] W_\ell \tag{C.13}$$

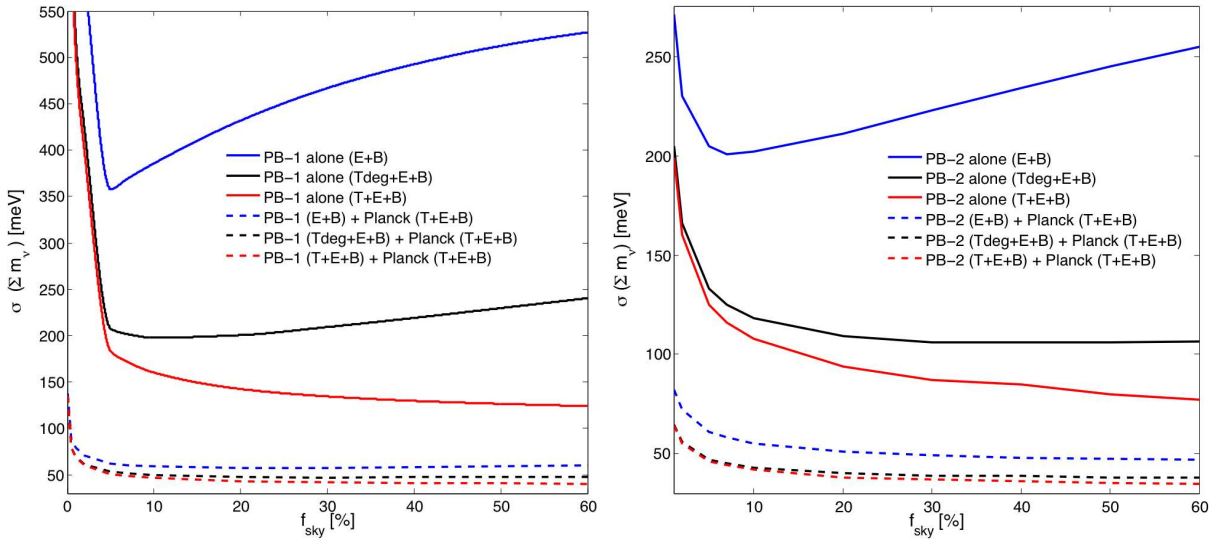

Figure C.4: **Left panel**: constraint on total neutrino mass, in the case of the POLARBEAR-II experiment, as a function of the observed fraction of the sky. **Right panel**: same as left panel but in the case of POLARBEAR-II.

where W_ℓ is the usual beam function $W_\ell \equiv \exp\left(\ell(\ell+1)\theta_b^2\right)$. Results depicted in Fig. C.4, denoted Tdeg+E+B are obtained assuming $\ell_{knee} = 1700$ and $\alpha = 3$, which match the results obtained by ACT, cf. Das et al. (29).

C.3 Summary: dealing with two science goals

As detailed in the previous paragraphs, we would like to go with POLARBEAR for the biggest fraction of the sky with the lowest noise level possible, cf. Fig C.5. But, at a fixed level of noise per angular area on the sky, this is not always true (Fig. C.2): one would like to rather find the optimal configuration between being cosmic variance dominated (small f_{sky}) and being noise dominated (large f_{sky}).

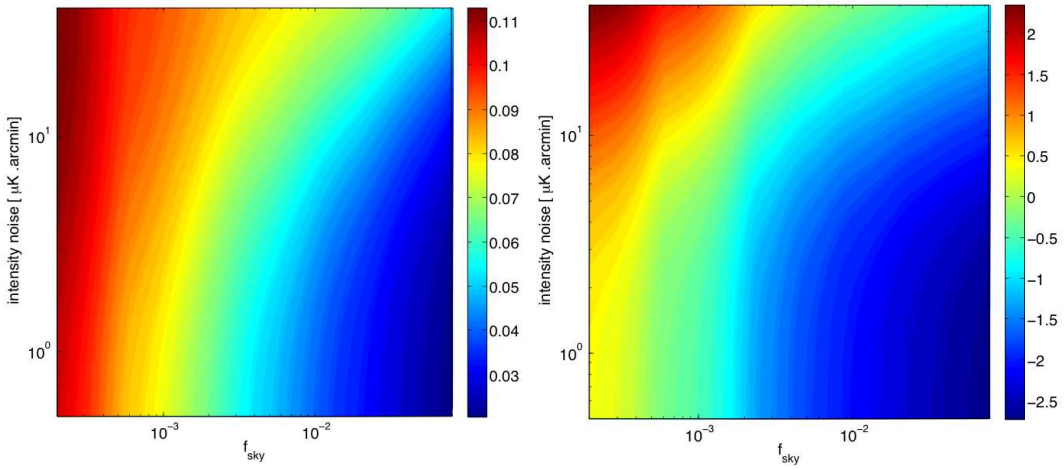

Figure C.5: **Left panel**: error in the estimation of the total neutrino mass, $\sigma(\sum m_\nu)$, in eV, as a function of the intensity noise of the detectors and fraction of the sky. **Right panel**: log of the minimum tensor-to-scalar ratio achievable at the 2-σ level as a function of the intensity noise of the detectors and fraction of the sky.

References

[1] J. Aguirre, A. Amblard, A. Ashoorioon, C. Baccigalupi, A. Balbi, J. Bartlett, N. Bartolo, D. Benford, M. Birkinshaw, J. Bock, D. Bond, J. Borrill, F. Bouchet, M. Bridges, E. Bunn, E. Calabrese, C. Cantalupo, A. Caramete, C. Carbone, S. Chatterjee, S. Church, D. Chuss, C. Contaldi, A. Cooray, S. Das, F. De Bernardis, P. De Bernardis, G. De Zotti, J. Delabrouille, F. -Xavier Dsert, M. Devlin, C. Dickinson, S. Dicker, M. Dobbs, S. Dodelson, O. Dore, J. Dotson, J. Dunkley, M. C. Falvella, D. Fixsen, P. Fosalba, J. Fowler, E. Gates, W. Gear, S. Golwala, K. Gorski, A. Gruppuso, J. Gundersen, M. Halpern, S. Hanany, M. Hazumi, C. Hernandez-Monteagudo, M. Hertzberg, G. Hinshaw, C. Hirata, E. Hivon, W. Holmes, W. Holzapfel, W. Hu, J. Hubmayr, K. Huffenberger, K. Irwin, M. Jackson, A. Jaffe, B. Johnson, W. Jones, M. Kaplinghat, B. Keating, R. Keskitalo, J. Khoury, W. Kinney, T. Kisner, L. Knox, A. Kogut, E. Komatsu, A. Kosowsky, J. Kovac, L. Krauss, H. Kurki-Suonio, S. Landau, C. Lawrence, S. Leach, A. Lee, E. Leitch, R. Leonardi, J. Lesgourgues, A. Liddle, E. Lim, M. Limon, M. Loverde, P. Lubin, A. Magalhaes, D. Maino, T. Marriage, V. Martin, S. Matarrese, J. Mather, H. Mathur, T. Matsumura, P. Meerburg, A. Melchiorri, S. Meyer, A. Miller, M. Milligan, K. Moodley, M. Neimack, H. Nguyen, I. O'Dwyer, A. Orlando, L. Pagano, L. Page, B. Partridge, T. Pearson, H. Peiris, F. Piacentini, L. Piccirillo, E. Pierpaoli, D. Pietrobon, G. Pisano, L. Pogosian, D. Pogosyan, N. Ponthieu, L. Popa, C. Pryke, C. Raeth, S. Ray, C. Reichardt, S. Ricciardi, P. Richards, G. Rocha, L. Rudnick, J. Ruhl, B. Rusholme, C. Scoccola, D. Scott, C. Sealfon, N. Sehgal, M. Seiffert, L. Senatore, P. Serra, S. Shandera, M. Shimon, P. Shirron, J. Sievers, K. Sigurdson, J. Silk, R. Silverberg, E. Silverstein, S. Staggs, A. Stebbins, F. Stivoli, R. Stompor, N. Sugiyama, D. Swetz, A. Tartari, M. Tegmark, P. Timbie, M. Tristram, G. Tucker, J. Urrestilla, J. Vaillancourt, M. Veneziani, L. Verde, J. Vieira, S. Watson, B. Wandelt, G. Wilson, E. Wollack, M. Wyman, A. Yadav, G.-H. Yannick, O. Zahn, M. Zaldarriaga, M. Zemcov, and J. Zwart. Observing the Evolution of the Universe. *ArXiv e-prints*, March 2009. xxii, 152, 163, 177

[2] M. Amarie, C. Hirata, and U. Seljak. Detectability of tensor modes in the presence of foregrounds. *Phys. Rev. D*, 72(12):123006–+, December 2005. doi: 10.1103/PhysRevD.72.123006. 140

[3] A. Amblard, A. Cooray, and M. Kaplinghat. Search for gravitational waves in the CMB after WMAP3: Foreground confusion and the optimal frequency coverage for foreground minimization. *Phys. Rev. D*, 75 (8):083508–+, April 2007. doi: 10.1103/PhysRevD.75.083508. 140, 143, 164, 183

[4] ANR MIDAS'09. Microwave data analysis for petascale computers. URL `http://www.apc.univ-paris7.fr/APC_CS/Recherche/Adamis/MIDAS09/index.html`. 77, 214

[5] K. Arnold, P. A. R. Ade, A. E. Anthony, F. Aubin, D. Boettger, J. Borrill, C. Cantalupo, M. A. Dobbs, J. Errard, D. Flanigan, A. Ghribi, N. Halverson, M. Hazumi, W. L. Holzapfel, J. Howard, P. Hyland, A. Jaffe, B. Keating, T. Kisner, Z. Kermish, A. T. Lee, E. Linder, M. Lungu, T. Matsumura, N. Miller, X. Meng, M. Myers, H. Nishino, R. O'Brient, D. O'Dea, C. Reichardt, I. Schanning, A. Shimizu, C. Shimmin, M. Shimon, H. Spieler, B. Steinbach, R. Stompor, A. Suzuki, T. Tomaru, H. T. Tran, C. Tucker, E. Quealy, P. L. Richards, and O. Zahn. The POLARBEAR CMB polarization experiment. In *Society of Photo-Optical Instrumentation Engineers (SPIE) Conference Series*, volume 7741 of *Society of Photo-Optical Instrumentation Engineers (SPIE) Conference Series*, July 2010. doi: 10.1117/12.858314. 74

[6] K. S. Arnold. *Design and Deployment of the Polarbear Cosmic Microwave Background Polarization Experiment.* PhD thesis, University of California, Berkeley, December 2010. xii, 102, 200, 204, 210

[7] E. Audit and J. F. L. Simmons. The kinematic Sunyaev-Zel'dovich effect and transverse cluster velocities. *MNRAS*, 305:L27–L30, May 1999. doi: 10.1046/j.1365-8711.1999.02647.x. 125

[8] J. Aumont, L. Conversi, C. Thum, H. Wiesemeyer, E. Falgarone, J. F. Macías-Pérez, F. Piacentini, E. Pointecouteau, N. Ponthieu, J. L. Puget, C. Rosset, J. A. Tauber, and M. Tristram. Measurement of the Crab nebula polarization at 90 GHz as a calibrator for CMB experiments. *A&A*, 514:A70, May 2010. doi: 10.1051/0004-6361/200913834. 207

[9] C. A. Beichman, G. Neugebauer, H. J. Habing, P. E. Clegg, and T. J. Chester, editors. *Infrared astronomical satellite (IRAS) catalogs and atlases. Volume 1: Explanatory supplement*, volume 1, 1988. 122

[10] A. Benoît, P. Ade, A. Amblard, R. Ansari, É. Aubourg, S. Bargot, J. G. Bartlett, J.-P. Bernard, R. S. Bhatia, A. Blanchard, J. J. Bock, A. Boscaleri, F. R. Bouchet, A. Bourrachot, and et al. First detection of polarization of the submillimetre diffuse galactic dust emission by Archeops. *A&A*, 424:571–582, September 2004. doi: 10.1051/0004-6361:20040042. 122

[11] F. Bernardeau, S. Colombi, E. Gaztañaga, and R. Scoccimarro. Large-scale structure of the Universe and cosmological perturbation theory. *Phys. Rep.*, 367:1–248, September 2002. doi: 10.1016/S0370-1573(02)00135-7. 21

[12] M. Betoule, E. Pierpaoli, J. Delabrouille, M. Le Jeune, and J.-F. Cardoso. Measuring the tensor to scalar ratio from CMB B-modes in the presence of foregrounds. *A&A*, 503:691–706, September 2009. doi: 10.1051/0004-6361/200911624. 140, 155

[13] C. Bischoff, L. Hyatt, J. J. McMahon, G. W. Nixon, D. Samtleben, K. M. Smith, K. Vanderlinde, D. Barkats, P. Farese, T. Gaier, J. O. Gundersen, M. M. Hedman, S. T. Staggs, B. Winstein, and CAPMAP Collaboration. New Measurements of Fine-Scale CMB Polarization Power Spectra from CAPMAP at Both 40 and 90 GHz. *ApJ*, 684:771–789, September 2008. doi: 10.1086/590487. 62

[14] C. Bischoff, A. Brizius, I. Buder, Y. Chinone, K. Cleary, R. N. Dumoulin, A. Kusaka, R. Monsalve, S. K. Næss, L. B. Newburgh, R. Reeves, K. M. Smith, I. K. Wehus, J. A. Zuntz, J. T. L. Zwart, L. Bronfman, R. Bustos, S. E. Church, C. Dickinson, H. K. Eriksen, P. G. Ferreira, T. Gaier, J. O. Gundersen, M. Hasegawa, M. Hazumi, K. M. Huffenberger, M. E. Jones, P. Kangaslahti, D. J. Kapner, C. R. Lawrence, M. Limon, J. May, J. J. McMahon, A. D. Miller, H. Nguyen, G. W. Nixon, T. J. Pearson, L. Piccirillo, S. J. E. Radford, A. C. S. Readhead, J. L. Richards, D. Samtleben, M. Seiffert, M. C. Shepherd, S. T. Staggs, O. Tajima, K. L. Thompson, K. Vanderlinde, R. Williamson, and B. Winstein. First Season QUIET Observations: Measurements of Cosmic Microwave Background Polarization Power Spectra at 43 GHz in the Multipole Range $25 < l < 475$. *ApJ*, 741:111, November 2011. doi: 10.1088/0004-637X/741/2/111. 62, 257

REFERENCES

[15] L. Bleem, P. Ade, K. Aird, J. Austermann, J. Beall, D. Becker, B. Benson, J. Britton, J. Carlstrom, C. L. Chang, H. Cho, T. de Haan, T. Crawford, A. Crites, A. Datesman, M. Dobbs, W. Everett, A. Ewall-Wice, E. George, N. Halverson, N. Harrington, J. Henning, G. Hilton, W. Holzapfel, S. Hoover, J. Hubmayr, K. Irwin, R. Keisler, J. Kennedy, A. Lee, E. Leitch, D. Li, M. Lueker, D. P. Marrone, J. McMahon, J. Mehl, S. Meyer, J. Montgomery, T. Montroy, T. Natoli, J. Nibarger, M. Niemack, V. Novosad, S. Padin, C. Pryke, C. Reichardt, J. Ruhl, B. Saliwanchik, J. Sayre, K. Schafer, E. Shirokoff, K. Story, K. Vanderlinde, J. Vieira, G. Wang, R. Williamson, V. Yefremenko, K. W. Yoon, and E. Young. An Overview of the SPTpol Experiment. *Journal of Low Temperature Physics*, 167:859–864, June 2012. doi: 10.1007/s10909-012-0505-y. 74

[16] J. Bock, A. Aljabri, A. Amblard, D. Baumann, M. Betoule, T. Chui, L. Colombo, A. Cooray, D. Crumb, P. Day, C. Dickinson, D. Dowell, M. Dragovan, S. Golwala, K. Gorski, S. Hanany, W. Holmes, K. Irwin, B. Johnson, B. Keating, C.-L. Kuo, A. Lee, A. Lange, C. Lawrence, S. Meyer, N. Miller, H. Nguyen, E. Pierpaoli, N. Ponthieu, J.-L. Puget, J. Raab, P. Richards, C. Satter, M. Seiffert, M. Shimon, H. Tran, B. Williams, and J. Zmuidzinas. Study of the Experimental Probe of Inflationary Cosmology (EPIC)-Intemediate Mission for NASA's Einstein Inflation Probe. *ArXiv e-prints*, June 2009. xiii, xxi, 71, 74, 79, 129, 153

[17] A. Bonaldi and S. Ricciardi. Forecast of B-mode detection at large scales in the presence of noise and foregrounds. *MNRAS*, pages 449–+, March 2011. doi: 10.1111/j.1365-2966.2011.18425.x. 144, 155

[18] J. Borrill. Power spectrum estimators for large CMB datasets. *Phys. Rev. D*, 59(2):027302, January 1999. doi: 10.1103/PhysRevD.59.027302. 240

[19] W. N. Brandt, C. R. Lawrence, A. C. S. Readhead, J. N. Pakianathan, and T. M. Fiola. Separation of foreground radiation from cosmic microwave background anisotropy using multifrequency measurements. *ApJ*, 424:1–21, March 1994. doi: 10.1086/173867. 131

[20] M. L. Brown, P. Ade, J. Bock, M. Bowden, G. Cahill, P. G. Castro, S. Church, T. Culverhouse, R. B. Friedman, K. Ganga, W. K. Gear, S. Gupta, J. Hinderks, J. Kovac, A. E. Lange, E. Leitch, and et al. Improved Measurements of the Temperature and Polarization of the Cosmic Microwave Background from QUaD. *ApJ*, 705:978–999, November 2009. doi: 10.1088/0004-637X/705/1/978. 62

[21] R. S. Bussmann, W. L. Holzapfel, and C. L. Kuo. Millimeter Wavelength Brightness Fluctuations of the Atmosphere above the South Pole. *ApJ*, 622:1343–1355, April 2005. doi: 10.1086/427935. 116

[22] Caltech. Bicep-2 experiment public website, . URL `http://www.astro.caltech.edu/~lgg/bicep2`. 74

[23] Caltech. Keck-array experiment public website, . URL `http://www.astro.caltech.edu/~lgg/keck`. 74

[24] H. C. Chiang, P. A. R. Ade, D. Barkats, J. O. Battle, E. M. Bierman, J. J. Bock, C. D. Dowell, L. Duband, E. F. Hivon, W. L. Holzapfel, V. V. Hristov, W. C. Jones, B. G. Keating, J. M. Kovac, C. L. Kuo, A. E. Lange, E. M. Leitch, P. V. Mason, T. Matsumura, H. T. Nguyen, N. Ponthieu, C. Pryke, S. Richter, G. Rocha, C. Sheehy, Y. D. Takahashi, J. E. Tolan, and K. W. Yoon. Measurement of Cosmic Microwave Background Polarization Power Spectra from Two Years of BICEP Data. *ApJ*, 711:1123–1140, March 2010. doi: 10.1088/0004-637X/711/2/1123. x, 62, 63

[25] G. Chon, A. Challinor, S. Prunet, E. Hivon, and I. Szapudi. Fast estimation of polarization power spectra using correlation functions. *MNRAS*, 350:914–926, May 2004. doi: 10.1111/j.1365-2966.2004.07737.x. 241

[26] S. E. Church. Predicting residual levels of atmosphereic sky noise in ground based observations of the cosmic microwave background radiation. *MNRAS*, 272:551–569, February 1995. 81, 104, 105, 107, 117

[27] D. T. Chuss, P. A. R. Ade, D. J. Benford, C. L. Bennett, J. L. Dotson, J. R. Eimer, D. J. Fixsen, M. Halpern, G. Hilton, J. Hinderks, G. Hinshaw, K. Irwin, M. L. Jackson, M. A. Jah, N. Jethava, C. Jhabvala, A. J. Kogut, L. Lowe, N. McCullagh, T. Miller, P. Mirel, S. H. Moseley, S. Rodriguez, K. Rostem, E. Sharp, J. G. Staguhn, C. E. Tucker, G. M. Voellmer, E. J. Wollack, and L. Zeng. The Primordial Inflation Polarization Explorer (PIPER). In *Millimeter, Submillimeter, and Far-Infrared Detectors and Instrumentation for Astronomy V. Edited by Holland, Wayne S.; Zmuidzinas, Jonas. Proceedings of the SPIE, Volume 7741, pp. 77411P-77411P-11 (2010).*, volume 7741, July 2010. doi: 10.1117/12.857119. 74

[28] E. Collett. *Field Guide to Polarization*, volume FG05. John E. Greivenkamp, Series Editor, 2009. 91

[29] S. Das, T. A. Marriage, P. A. R. Ade, P. Aguirre, M. Amiri, J. W. Appel, L. F. Barrientos, E. S. Battistelli, J. R. Bond, B. Brown, B. Burger, J. Chervenak, M. J. Devlin, S. R. Dicker, W. Bertrand Doriese, J. Dunkley, R. Dünner, T. Essinger-Hileman, R. P. Fisher, J. W. Fowler, A. Hajian, M. Halpern, M. Hasselfield, C. Hernández-Monteagudo, G. C. Hilton, M. Hilton, A. D. Hincks, R. Hlozek, K. M. Huffenberger, D. H. Hughes, J. P. Hughes, L. Infante, K. D. Irwin, J. Baptiste Juin, M. Kaul, J. Klein, A. Kosowsky, J. M. Lau, M. Limon, Y.-T. Lin, R. H. Lupton, D. Marsden, K. Martocci, P. Mauskopf, F. Menanteau, K. Moodley, H. Moseley, C. B. Netterfield, M. D. Niemack, M. R. Nolta, L. A. Page, L. Parker, B. Partridge, B. Reid, N. Sehgal, B. D. Sherwin, J. Sievers, D. N. Spergel, S. T. Staggs, D. S. Swetz, E. R. Switzer, R. Thornton, H. Trac, C. Tucker, R. Warne, E. Wollack, and Y. Zhao. The Atacama Cosmology Telescope: A Measurement of the Cosmic Microwave Background Power Spectrum at 148 and 218 GHz from the 2008 Southern Survey. *ApJ*, 729:62, March 2011. doi: 10.1088/0004-637X/729/1/62. 233, 239, 264

[30] S. Das, B. D. Sherwin, P. Aguirre, J. W. Appel, J. R. Bond, C. S. Carvalho, M. J. Devlin, J. Dunkley, R. Dünner, T. Essinger-Hileman, J. W. Fowler, A. Hajian, M. Halpern, M. Hasselfield, A. D. Hincks, R. Hlozek, K. M. Huffenberger, J. P. Hughes, K. D. Irwin, J. Klein, A. Kosowsky, R. H. Lupton, T. A. Marriage, D. Marsden, F. Menanteau, K. Moodley, M. D. Niemack, M. R. Nolta, L. A. Page, L. Parker, E. D. Reese, B. L. Schmitt, N. Sehgal, J. Sievers, D. N. Spergel, S. T. Staggs, D. S. Swetz, E. R. Switzer, R. Thornton, K. Visnjic, and E. Wollack. Detection of the Power Spectrum of Cosmic Microwave Background Lensing by the Atacama Cosmology Telescope. *Physical Review Letters*, 107(2):021301, July 2011. doi: 10.1103/PhysRevLett.107.021301. 65

[31] F.-X. Desert, F. Boulanger, and J. L. Puget. Interstellar dust models for extinction and emission. *A&A*, 237: 215–236, October 1990. 121

[32] M. A. Dobbs, M. Lueker, K. A. Aird, A. N. Bender, B. A. Benson, L. E. Bleem, J. E. Carlstrom, C. L. Chang, H.-M. Cho, J. Clarke, T. M. Crawford, A. T. Crites, D. I. Flanigan, T. de Haan, E. M. George, N. W. Halverson, W. L. Holzapfel, J. D. Hrubes, B. R. Johnson, J. Joseph, R. Keisler, J. Kennedy, Z. Kermish, T. M. Lanting, A. T. Lee, E. M. Leitch, D. Luong-Van, J. J. McMahon, J. Mehl, S. S. Meyer, T. E. Montroy, S. Padin, T. Plagge, C. Pryke, P. L. Richards, J. E. Ruhl, K. K. Schaffer, D. Schwan, E. Shirokoff, H. G. Spieler, Z. Staniszewski, A. A. Stark, K. Vanderlinde, J. D. Vieira, C. Vu, B. Westbrook, and R. Williamson. Frequency Multiplexed SQUID Readout of Large Bolometer Arrays for Cosmic Microwave Background Measurements. *ArXiv e-prints*, December 2011. 205

[33] S. Dodelson, R. Easther, S. Hanany, L. McAllister, S. Meyer, L. Page, P. Ade, A. Amblard, A. Ashoorioon, C. Baccigalupi, A. Balbi, J. Bartlett, N. Bartolo, D. Baumann, M. Beltran, D. Benford, M. Birkinshaw, J. Bock, D. Bond, J. Borrill, F. Bouchet, M. Bridges, E. Bunn, E. Calabrese, C. Cantalupo, A. Caramete, C. Carbone, S. Carroll, S. Chatterjee, X. Chen, S. Church, D. Chuss, C. Contaldi, A. Cooray, P. Creminelli, S. Das, F. D. Bernardis, P. de Bernardis, J. Delabrouille, F. X. Dsert, M. Devlin, C. Dickinson, S. Dickler, M. DiPirro, M. Dobbs, O. Dore, J. Dotson, J. Dunkley, C. Dvorklin, H. K. Eriksen, M. C. Falvella, D. Finley, D. Finkbeiner, D. Fixen, R. Flauger, P. Fosalba, J. Fowler, S. Galli, E. Gates, W. Gear, Y. Giraud-Heraud, K. Gorski, B. Greene, A. Gruppuso, J. Gundersen, M. Halpern, C. Hirata, E. Hivon, R. Holman, W. Holmes, W. Hu, J. Hubmayr, K. Huffenberger, H. Hui, L. Hui, K. Irwin, M. Jackson, A. Jaffe, B. Johnson, D. Johnson, W. Jones, S. Kachru, K. Kadota, J. Kaplan, M. Kaplinghat, B. Keating, R. Keskitalo, J. Khoury, W. Kinney, T. Kisner, L. Knox, H. Kodama, A. Kogut, E. Komatsu, R. Kosowsky, J. Khoury, W. Kinney, T. Kisner, H. Kurki-Suonio, J.-M. Lamarre, S. Landau, S. Leach, L. Leblond, A. Lee, E. Leitch, R. Leonardi, J. Lesgourgues, A. Liddle, E. Lim, M. Limon, M. Loverde, P. Lubin, E. Lunghi, J. Lykken, C. MacTavish, A. Magalhaes, D. Maino, V. Martin, S. Matarrese, J. Mather, H. Mathur, T. Matsumura, P. Meerburg, A. Melchiorri, L. Mersini-Houghton, A. Miller, M. Milligan, K. Moodley, M. Neimack, H. Nguyen, A. Nicolis, I. O'Dwyer, A. Olinto, L. Pagano, E. Pajer, B. Partridge, T. Pearson, H. Peiris, M. Peloso, F. Piacentini, M. Piat, L. Piccirillo, E. Pierpaoli, D. Pietrobon, G. Pisano, L. Pogosian, D. Pogosyan, N. Ponthieu, L. Popa, C. Pryke, C. Raeth, S. Ray, C. Reichardt, S. Ricciardi, P. Richards, A. Riotto, G. Rocha, J. Ruhl, B. Rusholme, R. Scherrer, C. Scoccola, D. Scott, C. Sealfon, E. Sefusatti, N. Sehgal, M. Seiffert, P. Serra, S. Shandera, M. Shimon, P. Shirron, J. Sievers, J. Silk, K. Sigurdson, R. Silverberg, E. Silverstein, S. Staggs, G. Starkman, A. Stebbins, F. Stivoli, R. Stompor, N. Sugiyama, D. Swetz, A. Tartari, M. Tegmark, P. Timbie, M. Titov, M. Tristram, M. Trodden, G. Tucker, J. Urrestilla, M. Veneziani, L. Verde, J. Vieira, T. Walker, D. Wands, S. Watson, S. Weinberg, R. Weiss, B. Wandelt, B. Winstein, E. Wollack, M. Wyman, A. Yadav, K. Won Yoon, O. Zahn, M. Zaldarriage, M. Zemcov, and J. Zwart. The Origin of the Universe as Revealed Through the Polarization of the Cosmic Microwave Background. In *astro2010: The Astronomy and Astrophysics Decadal Survey*, volume 2010 of *Astronomy*, pages 67–+, 2009. 152

[34] B. T. Draine and A. A. Fraisse. Polarized Far-Infrared and Submillimeter Emission from Interstellar Dust. *ApJ*, 696:1–11, May 2009. doi: 10.1088/0004-637X/696/1/1. 122

[35] B. T. Draine and A. Li. Infrared Emission from Interstellar Dust. IV. The Silicate-Graphite-PAH Model in the Post-Spitzer Era. *ApJ*, 657:810–837, March 2007. doi: 10.1086/511055. 121

[36] J. Dunkley, A. Amblard, C. Baccigalupi, M. Betoule, D. Chuss, A. Cooray, J. Delabrouille, C. Dickinson, G. Dobler, J. Dotson, H. K. Eriksen, D. Finkbeiner, D. Fixsen, P. Fosalba, A. Fraisse, C. Hirata, A. Kogut, J. Kristiansen, C. Lawrence, A. M. Magalha˜Es, M. A. Miville-Deschenes, S. Meyer, A. Miller, S. K. Naess, L. Page, H. V. Peiris, N. Phillips, E. Pierpaoli, G. Rocha, J. E. Vaillancourt, and L. Verde. Prospects for polarized foreground removal. In S. Dodelson, D. Baumann, A. Cooray, J. Dunkley, A. Fraisse, M. G. Jackson, A. Kogut, L. Krauss, M. Zaldarriaga, & K. Smith , editor, *American Institute of Physics Conference Series*, volume 1141 of *American Institute of Physics Conference Series*, pages 222–264, June 2009. doi: 10.1063/1.3160888. 140, 155

[37] A. Einstein. Die Grundlage der allgemeinen Relativitätstheorie. *Annalen der Physik*, 354:769–822, 1916. doi: 10.1002/andp.19163540702. 16

[38] H. K. Eriksen, C. Dickinson, C. R. Lawrence, C. Baccigalupi, A. J. Banday, K. M. Górski, F. K. Hansen, P. B. Lilje, E. Pierpaoli, M. D. Seiffert, K. M. Smith, and K. Vanderlinde. Cosmic Microwave Background Component Separation by Parameter Estimation. *ApJ*, 641:665–682, April 2006. doi: 10.1086/500499. 131

[39] J. Errard. Polarbear-2 science forecast. Presented at the Polarbear-2 meeting, UC Berkeley, October 2011. 68

[40] J. Errard and R. Stompor. Astrophysical foregrounds and primordial tensor-to-scalar ratio constraints from cosmic microwave background *b*-mode polarization observations. *Phys. Rev. D*, 85:083006, Apr 2012. doi: 10.1103/PhysRevD.85.083006. URL `http://link.aps.org/doi/10.1103/PhysRevD.85.083006`. 79, 129, 179

[41] J. Errard, F. Stivoli, and R. Stompor. Framework for performance forecasting and optimization of CMB B-mode observations in the presence of astrophysical foregrounds. *Phys. Rev. D*, 84(6):063005, September 2011. doi: 10.1103/PhysRevD.84.063005. 79, 129, 139, 179, 183

[42] T. Essinger-Hileman, J. W. Appel, J. A. Beal, H. M. Cho, J. Fowler, M. Halpern, M. Hasselfield, K. D. Irwin, T. A. Marriage, M. D. Niemack, L. Page, L. P. Parker, S. Pufu, S. T. Staggs, O. Stryzak, C. Visnjic, K. W. Yoon, and Y. Zhao. The Atacama B-Mode Search: CMB Polarimetry with Transition-Edge-Sensor Bolometers. In B. Young, B. Cabrera, & A. Miller, editor, *American Institute of Physics Conference Series*, volume 1185 of *American Institute of Physics Conference Series*, pages 494–497, December 2009. doi: 10.1063/1.3292387. 205

[43] Y. Fantaye, F. Stivoli, J. Grain, S. M. Leach, M. Tristram, C. Baccigalupi, and R. Stompor. Estimating the tensor-to-scalar ratio and the effect of residual foreground contamination. *J. Cosmology Astropart. Phys.*, 8:1–+, August 2011. doi: 10.1088/1475-7516/2011/08/001. 140

[44] Y. Fantaye, F. Stivoli, J. Grain, S.M. Leach, M. Tristram, C. Baccigalupi, and R. Stompor. Estimating the tensor-to-scalar ratio and the effect of residual foreground contamination. *Journal of Cosmology and Astroparticle Physics*, 2011(08):001, 2011. 183, 188

[45] L. Fauvet, J. F. Macías-Pérez, J. Aumont, F. X. Désert, T. R. Jaffe, A. J. Banday, M. Tristram, A. H. Waelkens, and D. Santos. Joint 3D modelling of the polarized Galactic synchrotron and thermal dust foreground diffuse emission. *A&A*, 526:A145, February 2011. doi: 10.1051/0004-6361/201014492. 122

[46] P. G. Ferreira and A. H. Jaffe. Simultaneous estimation of noise and signal in cosmic microwave background experiments. *MNRAS*, 312:89–102, February 2000. doi: 10.1046/j.1365-8711.2000.03108.x. 222, 225

[47] D. P. Finkbeiner, M. Davis, and D. J. Schlegel. Extrapolation of Galactic Dust Emission at 100 Microns to Cosmic Microwave Background Radiation Frequencies Using FIRAS. *ApJ*, 524:867–886, October 1999. doi: 10.1086/307852. 122, 151

[48] D. J. Fixsen, E. S. Cheng, J. M. Gales, J. C. Mather, R. A. Shafer, and E. L. Wright. The Cosmic Microwave Background Spectrum from the Full COBE FIRAS Data Set. *ApJ*, 473:576, December 1996. doi: 10.1086/178173. 11

[49] P. Fosalba, A. Lazarian, S. Prunet, and J. A. Tauber. Statistical Properties of Galactic Starlight Polarization. *ApJ*, 564:762–772, January 2002. doi: 10.1086/324297. 122

REFERENCES

[50] A. A. Fraisse, J.-A. C. Brown, G. Dobler, J. L. Dotson, B. T. Draine, P. C. Frisch, M. Haverkorn, C. M. Hirata, R. Jansson, A. Lazarian, A. M. Magalha˜Es, A. Waelkens, and M. Wolleben. Foreground Science Knowledge and Prospects. In S. Dodelson, D. Baumann, A. Cooray, J. Dunkley, A. Fraisse, M. G. Jackson, A. Kogut, L. Krauss, M. Zaldarriaga, and K. Smith, editors, *American Institute of Physics Conference Series*, volume 1141 of *American Institute of Physics Conference Series*, pages 265–310, June 2009. doi: 10.1063/1.3160889. 119

[51] A. A. Fraisse, P. A. R. Ade, M. Amiri, S. J. Benton, J. J. Bock, J. R. Bond, J. A. Bonetti, S. Bryan, B. Burger, H. C. Chiang, C. N. Clark, C. R. Contaldi, B. P. Crill, G. Davis, O. Doré, M. Farhang, J. P. Filippini, L. M. Fissel, N. N. Gandilo, S. Golwala, J. E. Gudmundsson, M. Hasselfield, G. Hilton, W. Holmes, V. V. Hristov, K. Irwin, W. C. Jones, C. L. Kuo, C. J. MacTavish, P. V. Mason, T. E. Montroy, T. A. Morford, C. B. Netterfield, D. T. O'Dea, A. S. Rahlin, C. Reintsema, J. E. Ruhl, M. C. Runyan, M. A. Schenker, J. A. Shariff, J. D. Soler, A. Trangsrud, C. Tucker, R. S. Tucker, A. D. Turner, and D. Wiebe. SPIDER: Probing the Early Universe with a Suborbital Polarimeter. *eprint arXiv:1106.3087*, June 2011. 74

[52] G. Giardino, A. J. Banday, K. M. Górski, K. Bennett, J. L. Jonas, and J. Tauber. Towards a model of full-sky Galactic synchrotron intensity and linear polarisation: A re-analysis of the Parkes data. *A&A*, 387:82–97, May 2002. doi: 10.1051/0004-6361:20020285. 151

[53] B. Gold, C. L. Bennett, R. S. Hill, G. Hinshaw, N. Odegard, L. Page, D. N. Spergel, J. L. Weiland, J. Dunkley, M. Halpern, N. Jarosik, A. Kogut, E. Komatsu, D. Larson, S. S. Meyer, M. R. Nolta, E. Wollack, and E. L. Wright. Five-Year Wilkinson Microwave Anisotropy Probe Observations: Galactic Foreground Emission. *ApJS*, 180:265–282, February 2009. doi: 10.1088/0067-0049/180/2/265. 123

[54] B. Gold, N. Odegard, J. L. Weiland, R. S. Hill, A. Kogut, C. L. Bennett, G. Hinshaw, X. Chen, J. Dunkley, M. Halpern, N. Jarosik, E. Komatsu, D. Larson, M. Limon, S. S. Meyer, M. R. Nolta, L. Page, K. M. Smith, D. N. Spergel, G. S. Tucker, E. Wollack, and E. L. Wright. Seven-year Wilkinson Microwave Anisotropy Probe (WMAP) Observations: Galactic Foreground Emission. *ApJS*, 192:15, February 2011. doi: 10.1088/0067-0049/192/2/15. 12, 62, 123

[55] P. F. Goldsmith. Radiation patterns of circular apertures with Gaussian illumination. *International Journal of Infrared and Millimeter Waves*, 8:771–781, July 1987. doi: 10.1007/BF01013128. 200

[56] J. Grain, M. Tristram, and R. Stompor. Polarized CMB power spectrum estimation using the pure pseudo-cross-spectrum approach. *Phys. Rev. D*, 79 (12):123515–+, June 2009. doi: 10.1103/PhysRevD.79.123515. 154, 155, 241

[57] A. H. Guth. Inflationary universe: A possible solution to the horizon and flatness problems. *Phys. Rev. D*, 23:347–356, January 1981. doi: 10.1103/PhysRevD.23.347. 26, 31

[58] J. L. Han, R. N. Manchester, A. G. Lyne, G. J. Qiao, and W. van Straten. Pulsar Rotation Measures and the Large-Scale Structure of the Galactic Magnetic Field. *ApJ*, 642:868–881, May 2006. doi: 10.1086/501444. 121, 122

[59] S. Hanany and D. P. Marrone. Comparison of designs of off-axis Gregorian telescopes for millimeter-wave large focal-plane arrays. *Appl. Opt.*, 41:4666–4670, August 2002. doi: 10.1364/AO.41.004666. 201

[60] S. Hanany and P. Rosenkranz. Polarization of the atmosphere as a foreground for cosmic microwave background polarization experiments. *New A Rev.*, 47: 1159–1165, December 2003. doi: 10.1016/j.newar.2003.09.017. 102

[61] S. Hanany, P. Ade, A. Balbi, J. Bock, J. Borrill, A. Boscaleri, P. de Bernardis, P. G. Ferreira, V. V. Hristov, A. H. Jaffe, A. E. Lange, A. T. Lee, P. D. Mauskopf, C. B. Netterfield, S. Oh, E. Pascale, B. Rabii, P. L. Richards, G. F. Smoot, R. Stompor, C. D. Winant, and J. H. P. Wu. MAXIMA-1: A Measurement of the Cosmic Microwave Background Anisotropy on Angular Scales of 10-5 deg. *ApJ*, 545:L5–L9, December 2000. doi: 10.1086/317322. 56

[62] G. Haslam, R. Wielebinski, and W. Priester. Radio maps of the sky. *S&T*, 63:230–232, March 1982. 151

[63] M. Hazumi. Future CMB Polarization Measurements and Japanese Contributions. *Progress of Theoretical Physics Supplement*, 190:75–89, 2011. doi: 10.1143/PTPS.190.75. 74

[64] W. Hu and T. Okamoto. Mass Reconstruction with Cosmic Microwave Background Polarization. *ApJ*, 574: 566–574, August 2002. doi: 10.1086/341110. 71, 189, 260, 261

[65] W. Hu and N. Sugiyama. Toward understanding CMB anisotropies and their implications. *Phys. Rev. D*, 51: 2599–2630, March 1995. doi: 10.1103/PhysRevD.51.2599. 42

[66] W. Hu, N. Sugiyama, and J. Silk. The physics of microwave background anisotropies. *Nature*, 386:37–43, March 1997. doi: 10.1038/386037a0. 45

[67] E. Hubble. A Relation between Distance and Radial Velocity among Extra-Galactic Nebulae. *Proceedings of the National Academy of Science*, 15:168–173, March 1929. doi: 10.1073/pnas.15.3.168. 11

[68] B. R. Johnson, J. Collins, M. E. Abroe, P. A. R. Ade, J. Bock, J. Borrill, A. Boscaleri, P. de Bernardis, S. Hanany, A. H. Jaffe, T. Jones, A. T. Lee, L. Levinson, T. Matsumura, B. Rabii, T. Renbarger, P. L. Richards, G. F. Smoot, R. Stompor, H. T. Tran, C. D. Winant, J. H. P. Wu, and J. Zuntz. MAXIPOL: Cosmic Microwave Background Polarimetry Using a Rotating Half-Wave Plate. *ApJ*, 665:42–54, August 2007. doi: 10.1086/518105. 223, 224

[69] Z. Kermish, P. A. R. Ade, A. E. Anthony, K. Arnold, F. Aubin, D. Boettger, J. Borrill, C. Cantalupo, M. A. Dobbs, J. Errard, D. Flanigan, A. Ghribi, N. Halverson, M. Hazumi, W. L. Holzapfel, J. Howard, P. Hyland, A. Jaffe, B. Keating, T. Kisner, A. T. Lee, E. Linder, M. Lungu, T. Matsumura, N. Miller, X. Meng, M. Myers, H. Nishino, R. O'Brient, D. O'Dea, C. Reichardt, I. Schanning, A. Shimizu, C. Shimmin, M. Shimon, H. Spieler, B. Steinbach, R. Stompor, A. Suzuki, T. Tomaru, H. T. Tran, C. Tucker, E. Quealy, P. L. Richards, and O. Zahn. The POLARBEAR experiment. In *SPIE proceedings*, July 2012. xvii, 210, 211

[70] M. Kesden, A. Cooray, and M. Kamionkowski. Separation of Gravitational-Wave and Cosmic-Shear Contributions to Cosmic Microwave Background Polarization. *Physical Review Letters*, 89(1):011304, July 2002. doi: 10.1103/PhysRevLett.89.011304. 185

[71] L. Knox and Y.-S. Song. Limit on the Detectability of the Energy Scale of Inflation. *Physical Review Letters*, 89(1):011303, July 2002. doi: 10.1103/PhysRevLett.89.011303. 185

[72] A. Kogut, A. J. Banday, C. L. Bennett, K. M. Gorski, G. Hinshaw, G. F. Smoot, and E. I. Wright. Microwave Emission at High Galactic Latitudes in the Four-Year DMR Sky Maps. *ApJ*, 464:L5, June 1996. doi: 10.1086/310072. 121

[73] E. W. Kolb and M. S. Turner. *The early universe.* 1990. 18, 31, 36

[74] J. M. Kovac, E. M. Leitch, C. Pryke, J. E. Carlstrom, N. W. Halverson, and W. L. Holzapfel. Detection of polarization in the cosmic microwave background using DASI. *Nature*, 420:772–787, December 2002. doi: 10.1038/nature01269. x, 62

[75] C. L. Kuo, J. J. Bock, J. A. Bonetti, J. Brevik, G. Chattopadhyay, P. K. Day, S. Golwala, M. Kenyon, A. E. Lange, H. G. LeDuc, H. Nguyen, R. W. Ogburn, A. Orlando, A. Transgrud, A. Turner, G. Wang, and J. Zmuidzinas. Antenna-coupled TES bolometer arrays for CMB polarimetry. In *Society of Photo-Optical Instrumentation Engineers (SPIE) Conference Series*, volume 7020 of *Society of Photo-Optical Instrumentation Engineers (SPIE) Conference Series*, August 2008. doi: 10.1117/12.788588. 205

[76] Kuo Lab. Polar experiment public website. URL `http://polar-array.stanford.edu`. 74

[77] A. E. Lange, P. A. Ade, J. J. Bock, J. R. Bond, J. Borrill, A. Boscaleri, K. Coble, B. P. Crill, P. de Bernardis, P. Farese, P. Ferreira, K. Ganga, M. Giacometti, E. Hivon, V. V. Hristov, A. Iacoangeli, A. H. Jaffe, L. Martinis, S. Masi, P. D. Mauskopf, A. Melchiorri, T. Montroy, C. B. Netterfield, E. Pascale, F. Piacentini, D. Pogosyan, S. Prunet, S. Rao, G. Romeo, J. E. Ruhl, F. Scaramuzzi, and D. Sforna. Cosmological parameters from the first results of Boomerang. *Phys. Rev. D*, 63(4):042001, February 2001. doi: 10.1103/PhysRevD.63.042001. 56

[78] D. Langlois. Inflation and Cosmological Perturbations. In G. Wolschin, editor, *Lecture Notes in Physics, Berlin Springer Verlag*, volume 800 of *Lecture Notes in Physics, Berlin Springer Verlag*, pages 1–57, March 2010. doi: 10.1007/978-3-642-10598-2_1. 36

[79] O. P. Lay and N. W. Halverson. The Impact of Atmospheric Fluctuations on Degree-Scale Imaging of the Cosmic Microwave Background. *ApJ*, 543:787–798, November 2000. doi: 10.1086/317115. xii, 102, 109, 110

[80] A. Lazarian. Tracing magnetic fields with aligned grains. *J. Quant. Spec. Radiat. Transf.*, 106:225–256, July 2007. doi: 10.1016/j.jqsrt.2007.01.038. 121

[81] S. M. Leach, A. R. Liddle, J. Martin, and D. J. Schwarz. Cosmological parameter estimation and the inflationary cosmology. *Phys. Rev. D*, 66(2):023515, July 2002. doi: 10.1103/PhysRevD.66.023515. 36

[82] G. Lemaître. Un Univers homogène de masse constante et de rayon croissant rendant compte de la vitesse radiale des nébuleuses extra-galactiques. *Annales de la Societe Scietifique de Bruxelles*, 47:49–59, 1927. 11

[83] A. Lewis and S. Bridle. Cosmological parameters from CMB and other data: A Monte Carlo approach. *Phys. Rev. D*, 66(10):103511–+, November 2002. doi: 10.1103/PhysRevD.66.103511. 241

[84] A. Lewis and A. Challinor. Weak gravitational lensing of the CMB. *Phys. Rep.*, 429:1–65, June 2006. doi: 10.1016/j.physrep.2006.03.002. 64

[85] A. R. Liddle and D. H. Lyth. *Cosmological Inflation and Large-Scale Structure.* April 2000. 36

[86] J. E. Lidsey, A. R. Liddle, E. W. Kolb, E. J. Copeland, T. Barreiro, and M. Abney. Reconstructing the inflaton potential-an overview. *Reviews of Modern Physics*, 69:373–410, April 1997. doi: 10.1103/RevModPhys.69.373. 36

[87] A. Linde. *Inflation and quantum cosmology*, page 604. 1989. 32

[88] D. H Lyth and A. A Liddle. The Spectral Index in the CDM Cosmogony. *Astronomy*, September 1992. 36

[89] J. C. Mather, D. J. Fixsen, R. A. Shafer, C. Mosier, and D. T. Wilkinson. Calibrator Design for the COBE Far-Infrared Absolute Spectrophotometer (FIRAS). *ApJ*, 512:511–520, February 1999. doi: 10.1086/306805. 11

[90] T. Matsumura. *A cosmic microwave background radiation polarimeter using superconducting magnetic bearings.* PhD thesis, University of Minnesota, Minnesota, USA, 2006. 90

[91] J. J. McMahon, K. A. Aird, B. A. Benson, L. E. Bleem, J. Britton, J. E. Carlstrom, C. L. Chang, H. S. Cho, T. de Haan, T. M. Crawford, A. T. Crites, A. Datesman, M. A. Dobbs, W. Everett, N. W. Halverson, G. P. Holder, W. L. Holzapfel, D. Hrubes, K. D. Irwin, M. Joy, R. Keisler, T. M. Lanting, A. T. Lee, E. M. Leitch, A. Loehr, M. Lueker, J. Mehl, S. S. Meyer, J. J. Mohr, T. E. Montroy, M. D. Niemack, C. C. Ngeow, V. Novosad, S. Padin, T. Plagge, C. Pryke, C. Reichardt, J. E. Ruhl, K. K. Schaffer, L. Shaw, E. Shirokoff, H. G. Spieler, B. Stadler, A. A. Stark, Z. Staniszewski, K. Vanderlinde, J. D. Vieira, G. Wang, R. Williamson, V. Yefremenko, K. W. Yoon, O. Zhan, and A. Zenteno. SPTpol: an instrument for CMB polarization. *THE THIRTEENTH INTERNATIONAL WORKSHOP ON LOW TEMPERATURE DETECTORS-LTD13. AIP Conference Proceedings, Volume 1185, pp. 511-514 (2009).*, 1185:511–514, December 2009. doi: 10.1063/1.3292391. 74

[92] N. J. Miller, M. Shimon, and B. G. Keating. CMB beam systematics: Impact on lensing parameter estimation. *Phys. Rev. D*, 79(6):063008, March 2009. doi: 10.1103/PhysRevD.79.063008. 206

[93] T. E. Montroy, P. A. R. Ade, J. J. Bock, Bond, and et al. A Measurement of the CMB <EE> Spectrum from the 2003 Flight of BOOMERANG. *ApJ*, 647:813–822, August 2006. doi: 10.1086/505560. 62

[94] V. Mukhanov. *Physical Foundations of Cosmology.* November 2005. doi: 10.2277/0521563984. 18, 32

[95] M. J. Myers, W. Holzapfel, A. T. Lee, R. O'Brient, P. L. Richards, D. Schwan, A. D. Smith, H. Spieler, and H. Tran. Arrays of antenna-coupled bolometers using transition edge sensors. *Nuclear Instruments and Methods in Physics Research A*, 520:424–426, March 2004. doi: 10.1016/j.nima.2003.11.351. 204, 205

[96] P. C. Myers, A. A. Goodman, R. Gusten, and C. Heiles. Observations of magnetic fields in diffuse clouds. *ApJ*, 442:177–185, March 1995. doi: 10.1086/175433. 121

[97] K. Nakamura and Particle Data Group. Review of Particle Physics. *Journal of Physics G Nuclear Physics*, 37(7):075021, July 2010. doi: 10.1088/0954-3899/37/7A/075021. 65

[98] M. Niemack, J. Appel, H. M. Cho, T. Essinger-Hileman, J. Fowler, M. Halpern, K. D. Irwin, T. A. Marriage, L. Page, L. P. Parker, S. Pufu, S. T. Staggs, K. Visnjic, K. W. Yoon, and Y. Zhao. The Atacama B-mode Search: An Experiment to Probe Inflation by Measuring the Cosmic Microwave Background Polarization. In *American Astronomical Society Meeting Abstracts 213*, volume 213 of *American Astronomical Society Meeting Abstracts*, page 480.05, December 2009. 74

[99] M. D. Niemack, P. A. R. Ade, J. Aguirre, F. Barrientos, J. A. Beall, J. R. Bond, J. Britton, H. M. Cho, S. Das, M. J. Devlin, S. Dicker, J. Dunkley, R. Dünner, J. W. Fowler, A. Hajian, M. Halpern, M. Hasselfield, G. C. Hilton, M. Hilton, J. Hubmayr, J. P. Hughes, L. Infante, K. D. Irwin, N. Jarosik, J. Klein, A. Kosowsky, T. A. Marriage, J. McMahon, F. Menanteau, K. Moodley, J. P. Nibarger, M. R. Nolta, L. A. Page, B. Partridge, E. D. Reese, J. Sievers, D. N. Spergel, S. T. Staggs, R. Thornton, C. Tucker, E. Wollack, and K. W. Yoon. ACTPol: a polarization-sensitive receiver for the Atacama Cosmology Telescope. In *Millimeter, Submillimeter, and Far-Infrared Detectors and Instrumentation for Astronomy V. Edited by Holland, Wayne S.; Zmuidzinas, Jonas. Proceedings of the SPIE, Volume 7741, pp. 77411S-77411S-21 (2010).*, volume 7741, July 2010. doi: 10.1117/12.857464. 74

[100] Bojan Nikolic. Atm software presentation. URL `hhttp://www.mrao.cam.ac.uk/~bn204/alma/atmomodel.html`. xii, 103, 104

[101] S. Nojiri and S. D. Odintsov. Introduction to Modified Gravity and Gravitational Alternative for Dark Energy. *eprint arXiv:hep-th/0601213*, January 2006. 12

[102] P. Oxley, P. A. Ade, C. Baccigalupi, P. deBernardis, H.-M. Cho, M. J. Devlin, S. Hanany, B. R. Johnson, T. Jones, A. T. Lee, T. Matsumura, A. D. Miller, M. Milligan, T. Renbarger, H. G. Spieler, R. Stompor, G. S. Tucker, and M. Zaldarriaga. The EBEX experiment. In M. Strojnik, editor, *Society of Photo-Optical Instrumentation Engineers (SPIE) Conference Series*, volume 5543 of *Presented at the Society of Photo-Optical Instrumentation Engineers (SPIE) Conference*, pages 320–331, November 2004. doi: 10.1117/12.563447. 74

[103] L. Page, G. Hinshaw, E. Komatsu, M. R. Nolta, D. N. Spergel, C. L. Bennett, C. Barnes, R. Bean, and et al. Three-Year Wilkinson Microwave Anisotropy Probe (WMAP) Observations: Polarization Analysis. *ApJS*, 170:335–376, June 2007. doi: 10.1086/513699. 123, 151

[104] J. A. Peacock. *Cosmological Physics*. January 1999. 32

[105] A. A. Penzias and R. W. Wilson. A Measurement of Excess Antenna Temperature at 4080 Mc/s. *ApJ*, 142: 419–421, July 1965. doi: 10.1086/148307. 11

[106] S. Perlmutter, S. Gabi, G. Goldhaber, A. Goobar, D. E. Groom, I. M. Hook, A. G. Kim, M. Y. Kim, J. C. Lee, R. Pain, C. R. Pennypacker, I. A. Small, R. S. Ellis, R. G. McMahon, B. J. Boyle, P. S. Bunclark, D. Carter, M. J. Irwin, K. Glazebrook, H. J. M. Newberg, A. V. Filippenko, T. Matheson, M. Dopita, W. J. Couch, and Supernova Cosmology Project. Measurements of the Cosmological Parameters Omega and Lambda from the First Seven Supernovae at z $>$ 0.35. *ApJ*, 483:565, July 1997. doi: 10.1086/304265. 56

[107] S. Perlmutter, G. Aldering, G. Goldhaber, R. A. Knop, P. Nugent, P. G. Castro, S. Deustua, S. Fabbro, A. Goobar, D. E. Groom, I. M. Hook, A. G. Kim, M. Y. Kim, J. C. Lee, N. J. Nunes, R. Pain, C. R. Pennypacker, R. Quimby, C. Lidman, R. S. Ellis, M. Irwin, R. G. McMahon, P. Ruiz-Lapuente, N. Walton, B. Schaefer, B. J. Boyle, A. V. Filippenko, T. Matheson, A. S. Fruchter, N. Panagia, H. J. M. Newberg, W. J. Couch, and Supernova Cosmology Project. Measurements of Omega and Lambda from 42 High-Redshift Supernovae. *ApJ*, 517:565–586, June 1999. doi: 10.1086/307221. 12

[108] Planck Collaboration, A. Abergel, P. A. R. Ade, N. Aghanim, M. Arnaud, M. Ashdown, J. Aumont, C. Baccigalupi, A. Balbi, A. J. Banday, and et al. Planck early results. XXIV. Dust in the diffuse interstellar medium and the Galactic halo . *A&A*, 536:A24, December 2011. doi: 10.1051/0004-6361/201116485. xiii, 120

[109] Planck Collaboration, P. A. R. Ade, N. Aghanim, M. Arnaud, M. Ashdown, J. Aumont, C. Baccigalupi, A. Balbi, A. J. Banday, R. B. Barreiro, and et al. Planck early results. VII. The Early Release Compact Source Catalogue. *A&A*, 536:A7, December 2011. doi: 10.1051/0004-6361/201116474. 124

[110] Planck Collaboration, P. A. R. Ade, N. Aghanim, M. Arnaud, M. Ashdown, J. Aumont, C. Baccigalupi, A. Balbi, A. J. Banday, R. B. Barreiro, and et al. Planck early results. XVIII. The power spectrum of cosmic infrared background anisotropies. *A&A*, 536:A18, December 2011. doi: 10.1051/0004-6361/201116461. 124

[111] N. Ponthieu. *Polarisation du Fond diffus cosmologique et de l'Émission des Poussières Galactiques*. PhD thesis, Université Joseph Fourier, Grenoble, July 2003. 229

[112] J.-L. Puget, A. Abergel, J.-P. Bernard, F. Boulanger, W. B. Burton, F.-X. Desert, and D. Hartmann. Tentative detection of a cosmic far-infrared background with COBE. *A&A*, 308:L5, April 1996. 124

[113] A. G. Riess, A. V. Filippenko, P. Challis, A. Clocchiatti, A. Diercks, P. M. Garnavich, R. L. Gilliland, C. J. Hogan, S. Jha, R. P. Kirshner, B. Leibundgut, M. M. Phillips, D. Reiss, B. P. Schmidt, R. A. Schommer, R. C. Smith, J. Spyromilio, C. Stubbs, N. B. Suntzeff, and J. Tonry. Observational Evidence from Supernovae for an Accelerating Universe and a Cosmological Constant. *AJ*, 116:1009–1038, September 1998. doi: 10.1086/300499. 12

[114] G. B. Rybicki and A. P. Lightman. *Radiative processes in astrophysics*. 1979. 123

[115] B. D. Savage and J. S. Mathis. Observed properties of interstellar dust. *ARAandA*, 17:73–111, 1979. doi: 10.1146/annurev.aa.17.090179.000445. 120

[116] S. Y. Sazonov and R. A. Sunyaev. Microwave polarization in the direction of galaxy clusters induced by the CMB quadrupole anisotropy. *MNRAS*, 310:765–772, December 1999. doi: 10.1046/j.1365-8711.1999.02981.x. 125

[117] D. J. Schlegel, D. P. Finkbeiner, and M. Davis. Maps of Dust Infrared Emission for Use in Estimation of Reddening and Cosmic Microwave Background Radiation Foregrounds. *ApJ*, 500:525–+, June 1998. doi: 10.1086/305772. 151

[118] B. P. Schmidt, N. B. Suntzeff, M. M. Phillips, R. A. Schommer, A. Clocchiatti, R. P. Kirshner, P. Garnavich, P. Challis, B. Leibundgut, J. Spyromilio, A. G. Riess, A. V. Filippenko, M. Hamuy, R. C. Smith, C. Hogan, C. Stubbs, A. Diercks, D. Reiss, R. Gilliland, J. Tonry, J. Maza, A. Dressler, J. Walsh, and R. Ciardullo. The High-Z Supernova Search: Measuring Cosmic Deceleration and Global Curvature of the Universe Using Type IA Supernovae. *ApJ*, 507:46–63, November 1998. doi: 10.1086/306308. 56

[119] U. Seljak and C. M. Hirata. Gravitational lensing as a contaminant of the gravity wave signal in the CMB. *Phys. Rev. D*, 69(4):043005, February 2004. doi: 10.1103/PhysRevD.69.043005. 185

[120] K. Serkowski, D. S. Mathewson, and V. L. Ford. Wavelength dependence of interstellar polarization and ratio of total to selective extinction. *ApJ*, 196:261–290, February 1975. doi: 10.1086/153410. 121

[121] N. Seto and E. Pierpaoli. Probing the Largest Scale Structure in the Universe with Polarization Map of Galaxy Clusters. *Physical Review Letters*, 95(10): 101302, September 2005. doi: 10.1103/PhysRevLett.95.101302. 125

[122] C. D. Sheehy, P. A. R. Ade, R. W. Aikin, M. Amiri, S. Benton, C. Bischoff, J. J. Bock, J. A. Bonetti, J. A. Brevik, B. Burger, C. D. Dowell, L. Duband, J. P. Filippini, S. R. Golwala, M. Halpern, M. Hasselfield, G. Hilton, V. V. Hristov, K. Irwin, J. P. Kaufman, B. G. Keating, J. M. Kovac, C. L. Kuo, A. E. Lange, E. M. Leitch, M. Lueker, C. B. Netterfield, H. T. Nguyen, R. W. Ogburn, IV, A. Orlando, C. L. Pryke, C. Reintsema, S. Richter, J. E. Ruhl, M. C. Runyan, Z. Staniszewski, S. Stokes, R. Sudiwala, G. Teply, K. L. Thompson, J. E. Tolan, A. D. Turner, P. Wilson, and C. L. Wong. The Keck Array: a pulse tube cooled CMB polarimeter. *ArXiv e-prints*, April 2011. 74

[123] M. Shimon, B. Keating, N. Ponthieu, and E. Hivon. CMB polarization systematics due to beam asymmetry: Impact on inflationary science. *Phys. Rev. D*, 77(8): 083003, April 2008. doi: 10.1103/PhysRevD.77.083003. 206

[124] J. L. Sievers, B. S. Mason, L. Weintraub, C. Achermann, P. Altamirano, J. R. Bond, L. Bronfman, R. Bustos, C. Contaldi, C. Dickinson, M. E. Jones, J. May, S. T. Myers, N. Oyarce, S. Padin, T. J. Pearson, M. Pospieszalski, A. C. S. Readhead, R. Reeves, M. C. Shepherd, A. C. Taylor, and S. Torres. Cosmological Results from Five Years of 30 GHz CMB Intensity Measurements with the Cosmic Background Imager. *eprint arXiv:0901.4540*, January 2009. 62

[125] K. M. Smith. Pure pseudo-C estimators for CMB B-modes. *New A Rev.*, 50:1025–1029, December 2006. doi: 10.1016/j.newar.2006.09.015. 241

[126] K. M. Smith, A. Cooray, S. Das, O. Doré, D. Hanson, C. Hirata, M. Kaplinghat, B. Keating, M. Loverde, N. Miller, G. Rocha, M. Shimon, and O. Zahn. Gravitational Lensing. In S. Dodelson, D. Baumann, A. Cooray, J. Dunkley, A. Fraisse, M. G. Jackson, A. Kogut, L. Krauss, M. Zaldarriaga, & K. Smith, editor, *American Institute of Physics Conference Series*, volume 1141 of *American Institute of Physics Conference Series*, pages 121–178, June 2009. doi: 10.1063/1.3160886. xi, 69, 71, 119, 189, 261

[127] Y. Sofue, M. Fujimoto, and R. Wielebinski. Global structure of magnetic fields in spiral galaxies. *ARAandA*, 24:459–497, 1986. doi: 10.1146/annurev.aa.24.090186.002331. 122

[128] S. Spinelli, G. Fabbian, A. Tartari, M. Zannoni, and M. Gervasi. A template of atmospheric O_2 circularly polarized emission for cosmic microwave background experiments. *MNRAS*, 414:3272–3280, July 2011. doi: 10.1111/j.1365-2966.2011.18625.x. 102

[129] E. D. Stewart and D. H. Lyth. A more accurate analytic calculation of the spectrum of cosmological perturbations produced during inflation. *Physics Letters B*, 302:171–175, March 1993. doi: 10.1016/0370-2693(93)90379-V. 36

[130] F. Stivoli, J. Grain, S. M. Leach, M. Tristram, C. Baccigalupi, and R. Stompor. Maximum likelihood, parametric component separation and CMB B-mode detection in suborbital experiments. *MNRAS*, 408:2319–2335, November 2010. doi: 10.1111/j.1365-2966.2010.17281.x. 136, 137, 140, 151, 155, 157, 179, 181, 188

[131] V. Stolyarov, M. P. Hobson, A. N. Lasenby, and R. B. Barreiro. All-sky component separation in the presence of anisotropic noise and dust temperature variations. *MNRAS*, 357:145–155, February 2005. doi: 10.1111/j.1365-2966.2005.08610.x. 176, 187

[132] R. Stompor, A. Balbi, J. Borrill, P. Ferreira, S. Hanany, A. Jaffe, A. Lee, S. Oh, B. Rabii, P. Richards, G. Smoot, C. Winant, and J.-H. P. Wu. Maps of the CMB Temperature Anisotropy: from the Time-Ordered Data to the Maximum-Likelihood Solution. In A. J. Banday, S. Zaroubi, & M. Bartelmann, editor, *Mining the Sky*, page 414, 2001. doi: 10.1007/10849171_52. 213

[133] R. Stompor, S. Leach, F. Stivoli, and C. Baccigalupi. Maximum likelihood algorithm for parametric component separation in cosmic microwave background experiments. *MNRAS*, 392:216–232, January 2009. doi: 10.1111/j.1365-2966.2008.14023.x. 131, 132, 135, 180, 232

[134] A. Suzuki, K. Arnold, J. Edwards, G. Engargiola, A. Ghribi, W. Holzapfel, A. Lee, X. Meng, M. Myers, R. O'Brient, E. Quealy, G. Rebeiz, and P. Richards. Multi-chroic Dual-Polarization Bolometric Focal Plane for Studies of the Cosmic Microwave Background. *Journal of Low Temperature Physics*, page 152, March 2012. doi: 10.1007/s10909-012-0602-y. 74, 211

[135] Y. D. Takahashi, P. A. R. Ade, D. Barkats, J. O. Battle, E. M. Bierman, J. J. Bock, H. C. Chiang, C. D. Dowell, L. Duband, E. F. Hivon, W. L. Holzapfel, V. V. Hristov, W. C. Jones, B. G. Keating, J. M. Kovac, C. L. Kuo, A. E. Lange, E. M. Leitch, P. V. Mason, T. Matsumura, H. T. Nguyen, N. Ponthieu, C. Pryke, S. Richter, G. Rocha, and K. W. Yoon. Characterization of the BICEP Telescope for High-precision Cosmic Microwave Background Polarimetry. *ApJ*, 711:1141–1156, March 2010. doi: 10.1088/0004-637X/711/2/1141. 74

[136] J. A. Tauber, N. Mandolesi, J.-L. Puget, T. Banos, M. Bersanelli, F. R. Bouchet, R. C. Butler, J. Charra, G. Crone, J. Dodsworth, and et al. Planck pre-launch status: The Planck mission. *A&A*, 520:A1, September 2010. doi: 10.1051/0004-6361/200912983. 74

[137] The COrE Collaboration. COrE (Cosmic Origins Explorer) A White Paper. *ArXiv e-prints*, February 2011. xxi, xxii, 71, 74, 79, 152, 153, 155, 162, 166, 177, 188

[138] H. T. Tran. Polarization comparison between on-axis and off-axis dual reflector telescopes: Zemax and Grasp8 simulations. *New A Rev.*, 47:1091–1096, December 2003. doi: 10.1016/j.newar.2003.09.035. 201

[139] M. Tucci, E. Martínez-González, P. Vielva, and J. Delabrouille. Limits on the detectability of the CMB B-mode polarization imposed by foregrounds. *MNRAS*, 360:935–949, July 2005. doi: 10.1111/j.1365-2966.2005.09123.x. xvi, 192, 193

[140] B. L. Ulich. Millimeter wave radio telescopes - Gain and pointing characteristics. *International Journal of Infrared and Millimeter Waves*, 2:293–310, March 1981. doi: 10.1007/BF01007036. 219

[141] A. van Engelen, R. Keisler, O. Zahn, K. A. Aird, B. A. Benson, L. E. Bleem, J. E. Carlstrom, C. L. Chang, H. M. Cho, T. M. Crawford, A. T. Crites, T. de Haan, M. A. Dobbs, J. Dudley, E. M. George, N. W. Halverson, G. P. Holder, W. L. Holzapfel, S. Hoover, Z. Hou, J. D. Hrubes, M. Joy, L. Knox, A. T. Lee, E. M. Leitch, M. Lueker, D. Luong-Van, J. J. McMahon, J. Mehl, S. S. Meyer, M. Millea, J. J. Mohr, T. E. Montroy, T. Natoli, S. Padin, T. Plagge, C. Pryke, C. L. Reichardt, J. E. Ruhl, J. T. Sayre, K. K. Schaffer, L. Shaw, E. Shirokoff, H. G. Spieler, Z. Staniszewski, A. A. Stark, K. Story, K. Vanderlinde, J. D. Vieira, and R. Williamson. A measurement of gravitational lensing of the microwave background using South Pole Telescope data. *ArXiv e-prints*, February 2012. 65

[142] L. Verde, H. V. Peiris, and R. Jimenez. Considerations in optimizing CMB polarization experiments to constrain inflationary physics. *Journal of Cosmology and Astro-Particle Physics*, 1:19–+, January 2006. doi: 10.1088/1475-7516/2006/01/019. 140

[143] D. Vey. space-time-matter. URL `http://mayaloop.gie.im/`. 18

[144] M. S. Vogeley and A. S. Szalay. Eigenmode Analysis of Galaxy Redshift Surveys. I. Theory and Methods. *ApJ*, 465:34–+, July 1996. doi: 10.1086/177399. 255

[145] Pat Wallace. Tpoint model. URL http://www.tpsoft.demon.co.uk/index.html. 218

[146] S. Weinberg. *Gravitation and Cosmology: Principles and Applications of the General Theory of Relativity*. July 1972. 13

[147] E. L. Wright, X. Chen, N. Odegard, C. L. Bennett, R. S. Hill, G. Hinshaw, N. Jarosik, E. Komatsu, M. R. Nolta, L. Page, D. N. Spergel, J. L. Weiland, E. Wollack, J. Dunkley, B. Gold, M. Halpern, A. Kogut, D. Larson, M. Limon, S. S. Meyer, and G. S. Tucker. WMAP five-year source catalog (Wright+, 2009). *VizieR Online Data Catalog*, 218:283, October 2009. 124

[148] J. H. P. Wu, J. Zuntz, M. E. Abroe, P. A. R. Ade, J. Bock, J. Borrill, J. Collins, S. Hanany, A. H. Jaffe, B. R. Johnson, T. Jones, A. T. Lee, T. Matsumura, B. Rabii, T. Renbarger, P. L. Richards, G. F. Smoot, R. Stompor, H. T. Tran, and C. D. Winant. MAXIPOL: Data Analysis and Results. *ApJ*, 665:55–66, August 2007. doi: 10.1086/518112. 62

[149] O. Zahn, M. Zaldarriaga, L. Hernquist, and M. McQuinn. The Influence of Nonuniform Reionization on the CMB. *ApJ*, 630:657–666, September 2005. doi: 10.1086/431947. 53

[150] O. Zahn, C. L. Reichardt, L. Shaw, A. Lidz, K. A. Aird, B. A. Benson, L. E. Bleem, J. E. Carlstrom, C. L. Chang, H. M. Cho, T. M. Crawford, A. T. Crites, T. de Haan, M. A. Dobbs, O. Dore, J. Dudley, E. M. George, N. W. Halverson, G. P. Holder, W. L. Holzapfel, S. Hoover, Z. Hou, J. D. Hrubes, M. Joy, R. Keisler, L. Knox, A. T. Lee, E. M. Leitch, M. Lueker, D. Luong-Van, J. J. McMahon, J. Mehl, S. S. Meyer, M. Millea, J. J. Mohr, T. E. Montroy, T. Natoli, S. Padin, T. Plagge, C. Pryke, J. E. Ruhl, K. K. Schaffer, E. Shirokoff, H. G. Spieler, Z. Staniszewski, A. A. Stark, K. Story, A. van Engelen, K. Vanderlinde, J. D. Vieira, and R. Williamson. Cosmic microwave background constraints on the duration and timing of reionization from the South Pole Telescope. *ArXiv e-prints*, November 2011. 53

[151] M. Zaldarriaga and U. Seljak. All-sky analysis of polarization in the microwave background. *Phys. Rev. D*, 55:1830–1840, February 1997. doi: 10.1103/PhysRevD.55.1830. 52

Josquin Errard

La chasse aux modes-B du fond diffus cosmologique dans la jungle des contaminations systématiques

Résumé – Cette thèse présente une étude de certains effets systématiques instrumentaux et astrophysiques, pouvant affecter les performances des nouvelles et futures générations d'observations de la polarisation du fond diffus cosmologique (CMB). Nous étudions l'impact de ces effets sur les objectifs scientifiques de ces observations, ainsi que les techniques pour leur élimination. Ce travail se concentre sur les problèmes généraux que rencontrent les expériences de manière générale, mais se penche également sur les questions plus spécifiques soulevées dans le cadre de l'expérience d'observation des modes-B du CMB, POLARBEAR.

L'objectif principal de l'effort actuel pour l'étude de la polarisation du CMB est une détection des anisotropies primordiales appelées modes-B — une signature des théories inflationnaires non détectée à ce jour. Cela aurait un grand impact sur notre compréhension de l'univers, mais aussi des lois fondamentales de la physique. Comprendre, modéliser, et, finalement, éliminer ces effets systématiques sont des éléments indispensables pour tout pipeline d'analyse moderne du CMB. Sa réussite, de concert avec une haute sensibilité instrumentale, décidera du succès final des efforts entrepris.

Dans cette thèse je décris tout d'abord l'optique des expériences typiques d'observation du CMB et propose un paramétrage des polarisations instrumentale et croisée. Deuxièmement, je présente un modèle décrivant la contamination atmosphérique et utilise celui-ci afin de donner quelques aperçus sur le rôle et l'impact de l'atmosphère sur les performances des expériences au sol. J'indique également comment ces résultats peuvent être utilisés pour améliorer le contrôle des effets atmosphériques dans l'analyse des données CMB. Ensuite, je discute d'une autre source d'effets systématiques venant du ciel — les avants-plans astrophysiques polarisés. Dans ce contexte, je présente d'une part une nouvelle approche pour prédire les performances des futures expériences prenant en compte la présence des avant-plans, et d'autre part je propose un cadre pour l'optimisation des expériences afin qu'elles puissent atteindre de meilleures performances. Cette partie de la thèse est issue d'un travail commun avec F. Stivoli et R. Stompor. Je présente enfin une expérience phare pour l'observation de la polarisation du CMB, POLARBEAR, dans laquelle j'ai été impliqué au cours de mes études doctorales. Je décris le statut actuel et les performances de l'instrument ainsi que quelques étapes de son pipeline d'analyse des données. En particulier, je montre des méthodes d'estimation de certains des paramètres introduits pour la modélisation d'effets systématiques, à partir de données simulées. Ce travail a été réalisé en collaboration avec les membres de l'équipe POLARBEAR.

A hunt for Cosmic Microwave Background B-modes in the systematic contaminants jungle

Abstract – This thesis presents a study of selected instrumental and astrophysical systematics, which may affect the performance of new generation of future observations of the Cosmic Microwave Background (CMB) polarization. It elaborates on their impact on the science goals of those observations and discusses techniques and approaches for their removal. Its focus is on general issues typical of entire classes of experiments, but also on specific problems as encountered in the context of a CMB B-mode experiment, POLARBEAR.

The main target of the CMB polarization effort undergoing currently in the field is a detection of the primordial B-modes anisotropies — a so far undetected signature of the inflationary theories. This would have far-reaching impact on our understanding of the universe but also fundamental laws of physics. Understanding, modelling, and ultimately removal of the systematics are essential steps in any modern CMB analysis pipeline and their successful accomplishment, together with a high instrumental sensitivity, will decide of a final success of the entire effort.

In this thesis I first describe optics of typical CMB experiments and introduce a parametrization of instrumental and cross-polarization effects particularly convenient for the analysis of their impact. Second, I present a model describing the atmospheric contamination and use it to provide some insights about the atmosphere's role and its impact on performance of ground-based experiments. I also outline how it could be used further to improve control of atmospheric effects in the CMB data analysis. Then, I discuss another source of sky systematics — the polarized astrophysical foregrounds. In this context I present on the one hand a new approach to forecasting performance of the future experiments, which accounts for the presence of the foregrounds, while on the other I propose a framework for optimizing hardware of such experiments to let them achieve better performance. This part of thesis stems from a common work with drs. F. Stivoli and R. Stompor. I finally present one of the leading CMB polarization experiment POLARBEAR, in which I have been involved in over the course of my PhD studies. I describe its current status and performance as well as selected steps of its data analysis pipeline. In particular, I show methods to estimate some of the parameters introduced for the systematics modeling from simulated data. This work has been performed in collaboration with members of the POLARBEAR team.